Aix*Marseille université
Socialement engagée

NNT : 0000AIXM0000

THÈSE DE DOCTORAT

Soutenue à Aix-Marseille Université
le 18 décembre 2024 par

Fabriziofranco ANAK MORRIS

Influence de la réduction des dimensions sur la formation et la dégradation des films ultra-fins de siliciure de Nickel: applications aux technologies 28 nm et en deçà.

Discipline
Physique et Science de la Matière

Spécialité
Matière Condensée et Nanosciences

École doctorale
ED 352 Physique et science de la matière

Laboratoire/Partenaires de recherche
STMicroelectronics
IM2NP
CEA-Leti

Composition du jury

Christophe DETAVERNIER	Rapporteur
Professeur d'Université, Université de Ghent	
Rémi LAZZARI	Rapporteur
Directeur de recherche, INSP-CNRS	
Claudia WIEMER	Examinatrice, Présidente
Directrice de recherche, IMM-CNR	
Dominique MANGELINCK	Directeur de thèse
Directeur de recherche, IM2NP	
Magali GREGOIRE	Co-directrice de thèse
HDR Docteure, STMicroelectronics	
Sophie GUILLEMIN	Co-encadrante, invitée
Docteure, CEA-Leti	

life.augmented

leti ceatech

Affidavit

I, undersigned, Fabriziofranco Anak Morris, hereby declare that the work presented in this manuscript is my own work, carried out under the scientific supervision of Dominique Mangelinck, in accordance with the principles of honesty, integrity and responsibility inherent to the research mission. The research work and the writing of this manuscript have been carried out in compliance with both the French national charter for Research Integrity and the Aix-Marseille University charter on the Fight against plagiarism.

This work has not been submitted previously either in this country or in another country in the same or in a similar version to any other examination body.

Place Crolles, date 18 octobre 2024



Cette œuvre est mise à disposition selon les termes de la Licence Creative Commons Attribution - Pas d'Utilisation Commerciale - Pas de Modification 4.0 International.

Liste de publications et participation aux conférences

1) Liste des publications:

1. Magali Grégoire, Fabriziofranco Morris Anak, Stéphane Verdier, Karen Dabertrand, Sophie Guillemin, and Dominique Mangelinck. **On the influence of Ni(Pt)Si thin film formation on agglomeration threshold temperature and its impact on 3D imaging technology integration**. Published. *Microelectronic Engineering*. 2023. https://doi.org/10.1016/j.mssp.2024.108806
2. Fabriziofranco Morris Anak, Andréa Campos, Magali Grégoire, Adrien Estellon, Marc Lombard, Thomas Guyot, Sophie Guillemin, and Dominique Mangelinck. **Influence of the annealing schemes on the formation and stability of Ni (Pt) Si thin films: Partial, laser, total, and one-step annealings**. Published. *Materials Science in Semiconductor Processing*. 2024. https://doi.org/10.1016/j.mee.2023.111937

2) Participation aux conférences:

1. Participation, Materials for Advanced Metallization (MAM) 2021
2. Poster presentation, European Materials Research Society Spring Meeting 2023 (https://www.european-mrs.com/meetings/archives/2023/2023-spring-meeting)
3. Oral presentation, Materials for Advanced Metallization (MAM) 2024

English summary

In microelectronics, nickel-platinum monosilicide, Ni(Pt)Si is the primary choice of materials for contact layers to improve electrical conductivity particularly for CMOS technologies with aggressive nodes beyond the 65 nm. In the latest 28 nm fully depleted silicon-on-oxide (FDSOI) technology, the thickness of the Ni(Pt)Si film is imposed to be around 11 nm (ultra-thin silicide). Moreover, recent development in the imager technologies requires the complex co-integration of the Ni(Pt)Si thin film and the $TiSi_x$ silicide, which deals with high temperature annealings after Ni(Pt)Si thin film formation. Indeed, the sensitivity of the Ni(Pt)Si film to the agglomeration phenomenon remains a key player for the next 3D integration nodes. Then, the purpose of the Ph.D. work presented in this manuscript is to determine the impact Si surface preparation treatments, annealing schemes, and the nano-confinement on the agglomeration of the ultra-thin Ni(Pt)Si film. An additional study is then dedicated on industrial wafer within a real integrated circuit including a part of experiments cited above. Several key findings have been obtained in the current work. Firstly, the different SiCoNi treatments clearly induce a difference in the thickness of the intermixing layer and the redistribution of residual fluorine, F, and oxygen, O, which play a role in the final stability of the Ni(Pt)Si thin film. Furthermore, an improvement in silicide thickness uniformity is observed when SiCoNi 2x40 is used. Secondly, four annealing approaches have been introduced in order to form the 11 nm Ni(Pt)Si thin film. The use of the millisecond laser annealing clearly improve the characteristics of the silicide thin film, including grain size, leading to a better thermal stability. Finally, Ni(Pt)Si films are also formed in confining structures with decreasing pitch size (meaning more confined structures). We report a strong impact of the interface between walls of the dielectrics structures and the silicide contact on the agglomeration of the Ni(Pt)Si film. Results on texture remains complex to analyze deeply, however, in the first stages of our analysis, we reveal no significant impact on the final texture of the Ni(Pt)Si film regardless of the confining dimensions. Finally, we also discuss the redistribution of Pt atoms during Ni(Pt)Si agglomeration through modelling in order to better understand its role in this phenomenon.

Keywords: Ultra-thin Ni(Pt)Si film, SiCoNi treatments, milliseconds laser annealings, confinement, 3D integrations, co-integration, TiSix contacts, NiSi intermixing, Pt redistribution

French summary

Dans l'industrie de la microélectronique, le siliciure de nickel, Ni(Pt)Si est le choix principal pour la siliciuration des contacts permettant d'assurer une bonne conductivité électrique notamment pour les technologies CMOS avec des nœuds agressifs au-delà de 65 nm. Dans les technologies tels que la technologie 28 nm FDSOI (pour *Fully Depleted Silicon-On-Insulator*), l'épaisseur de la couche de Ni(Pt)Si est imposée autour de 11 nm, impliquant l'utilisation des couches de siliciure dans le régime de l'ultra-mince. De plus, les développements récents dans les technologies imagers nécessitent la co-intégration du siliciure de nickel, Ni(Pt)Si, et du siliciure à base de titane, $TiSi_X$, ce qui implique des recuits à haute température après la formation de la couche de Ni(Pt)Si. En effet, la sensibilité de Ni(Pt)Si au phénomène d'agglomération constitue aujourd'hui un défi technologique majeur. L'amélioration de sa stabilité est donc un facteur clé pour les prochains nœuds plus avancés. Ainsi, l'objectif de ce travail de thèse consiste, dans un premier temps, de déterminer l'impact des traitements de préparation de surface du Si, des différents types de recuit, et du nano-confinement sur l'agglomération de la couche ultra-mince de Ni(Pt)Si. Une étude supplémentaire est ensuite dédiée aux plaques patternées (circuit intégré) utilisant l'une des solutions proposées dans les expériences mentionnées précédemment. Plusieurs résultats majeurs ont été obtenus lors de cette thèse. Tout d'abord, les différents traitements de surface de SiCoNi induisent une différence dans l'épaisseur de la couche d'intermélange (*intermixing layer*) et la redistribution du fluor résiduel, F, et de l'oxygène, O, qui jouent un rôle dans la stabilité finale du film mince de Ni(Pt)Si. De plus, une amélioration de l'uniformité de l'épaisseur du siliciure est observée lorsque SiCoNi 2x40 est utilisé. Ensuite, 4 types de recuit ont été utilisés afin de former 11 nm de film mince de Ni(Pt)Si. Une amélioration des propriétés de la couche de siliciure a été observée notamment avec le recuit laser millisecondes, entraînant une meilleure stabilité thermique. Les films de Ni(Pt)Si ont également été formés dans des structures confinées de différentes dimensions. Nous avons mis en évidence un impact significatif de l'interface de siliciure avec les parois diélectriques des structures confinées sur l'agglomération du film Ni(Pt)Si. Malgré la difficulté d'analyses de la texture dans ces structures confinées, nous avons démontré aucun impact significatif sur la texture finale du film de Ni(Pt)Si quel que soit le niveau de confinement. Enfin, nous abordons également la redistribution des atomes de Pt pendant l'agglomération du Ni(Pt)Si à travers la modélisation afin de mieux comprendre son rôle dans ce phénomène.

Mots clés: Film ultra-mince de Ni(Pt)Si, traitement SiCoNi, recuit laser millisecondes, confinement, intégrations 3D, co-intégration, contacts TiSix, intermélange de NiSi, redistribution de Pt

Extended French summary

Le transistor MOS (*Metal-Oxyde-Semiconductor*) est un élément principal constituant de nombreux dispositifs électroniques, tels que les ordinateurs, les téléphones mobiles, les microprocesseurs dans les voitures et les différents appareils ménagers que nous utilisons au quotidien [1]. L'utilisation continue et très répandue du transistor dans diverses applications a été facilitée par la miniaturisation de ces transistors, conformément à la loi de Moore, formulée par Gordon Moore en 1965. En effet, la réduction des dimensions du transistor a permis d'augmenter la densité de transistors intégrés par unité de surface sur une seule puce. Par conséquent, les dispositifs sont devenus de plus en plus performants sans augmentation des coûts de fabrication. Ainsi, ceci constitue la force motrice majeure de nombreux développements technologiques dans l'industrie semi-conducteur, à savoir la course de la miniaturisation [2].

Cependant, la réduction des dimensions de ces technologies MOS a atteint ses limites au début des années 2000, lorsque l'épaisseur des films minces utilisés dans les transistors a été contrainte à l'ordre de quelques nanomètres, équivalents à quelques couches atomiques. En conséquence, de nombreuses pistes alternatives ont été développées, conduisant à la naissance de nouvelles architectures de transistors telles que le *Fin Field-Effect Transistor* (FinFET) et les technologies *Fully Depleted Silicon-On-Insulator* (FDSOI) [3],[4], le silicium sous contrainte [5], de nouveaux matériaux tels que les oxydes à haute constante diélectrique (*high-k*) [6] et l'introduction de l'alliage NiPt permettant de stabiliser la phase de siliciure à faible résistivité, Ni(Pt)Si [7],[8].

De plus, les couches de siliciures formées sur les trois terminaux du transistor (source, drain et grille), assurant une bonne conductivité et continuité électrique, connaissent des problèmes de germination dans les petites dimensions et des problèmes de stabilité morphologique pendant des recuits à une température relativement basse. Les trois types de siliciures qui ont été utilisés dans les développements des technologies CMOS (*Complementary* MOS) sont le siliciure de titane ($TiSi_x$), le siliciure de cobalt ($CoSi_2$) et le siliciure de nickel (NiSi ou Ni(Pt)Si). Les siliciures de nickel alliés avec le platine, Ni(Pt)Si, sont

aujourd'hui utilisés dans des nœuds technologiques avancés à partir du 65 nm grâce aux différentes propriétés qu'ils présentent comparées aux deux autres siliciures.

Plus particulièrement, les siliciures de nickel, Ni(Pt)Si, sont utilisés pour les nœuds technologiques très avancés tels que la technologie 28 nm FDSOI [9],[10],[11]. Ceci constitue un vrai défi technique car l'épaisseur finale de ce type de couches minces est d'environ 11 nm. C'est pourquoi ces films sont dénommés « ultra-fins ». Les inconvénients majeurs de travailler dans le régime ultra-fin pour ce type de siliciures sont les suivants : (i) instabilité ou modification de la séquence de phase, notamment la formation de phases riches en silicium, qui sont indésirables dans les circuits de microélectronique ; (ii) une très forte sensibilité à l'agglomération, c'est-à-dire à la formation d'îlots par démouillage de la couche sur le substrat.

L'objectif de cette thèse est de proposer une compréhension fine des processus de formation et d'agglomération des films ultra-minces de Ni(Pt)Si à travers trois axes de recherche principaux. Le premier axe porte sur l'impact de la préparation de surface SiCoNi sur la formation et l'agglomération du film ultra-mince de Ni(Pt)Si. Le deuxième axe souligne l'importance du choix des types de recuit utilisés dans la formation du film de Ni(Pt)Si sur sa stabilité thermique. Enfin, un troisième axe portant sur l'étude de l'impact du confinement des structures à l'échelle nanométrique sur la stabilité thermique du film ultra-mince de Ni(Pt)Si est également présenté.

Dans le premier chapitre, nous présenterons le principe de fonctionnement et l'architecture du transistor CMOS. Cette partie sera ensuite suivie d'une présentation de la loi de Moore et des tendances émergentes à la fin de la loi de Moore, appelées aussi "More than Moore". Une vue d'ensemble des différents siliciures est ensuite présentée, évoquant à la fois des aspects historiques et techniques des siliciures dans l'industrie de la microélectronique. Les parties suivantes décriront les siliciures à base de nickel, Ni-Si, le diagramme de phases et le processus d'élaboration, appelé SALICIDE pour *Self-Aligned Silicidation*. Les défis restants liés à la stabilité thermique en lien avec l'agglomération du film de Ni(Pt)Si sont également décrits. Avant de conclure le premier chapitre, les parties

restantes décriront les différentes pistes d'améliorations existantes dans la littérature pour améliorer la stabilité du film de Ni(Pt)Si.

Le deuxième chapitre du manuscrit présentera la méthodologie de recherche et les différentes techniques de caractérisation utilisées dans le cadre de cette thèse. Ce chapitre est divisé en deux parties principales : (i) Description des procédés de fabrication des échantillons et (ii) description des différentes techniques de caractérisation. Plusieurs techniques de caractérisation seront présentées, telles que les mesures de résistance à quatre pointes (Rs), l'éllipsométrie, la microscopie électronique à balayage (MEB) et la microscopie électronique en transmission (MET), la spectroscopie des pertes d'énergie des électrons (electron energy loss spectroscopy, TEM-EELS), la diffraction des électrons rétrodiffusés (EBSD) et la diffraction des rayons X (DRX). La description de la texture pour les couches minces et les différents types de figures de pôles est également présentée.

Les principaux résultats expérimentaux seront ensuite détaillés dans le chapitre 3. Un résumé du protocole expérimental est inclus au début de ce chapitre pour donner un aperçu des processus d'élaboration des échantillons utilisés dans chaque étude. Ce chapitre commence par la première étude de l'impact des différentes préparations de surface sur la formation et l'agglomération des films ultra-minces de Ni(Pt)Si. Dans cette première étude, les résultats sur des propriétés structurelles telles que l'épaisseur de la couche d'intermélange (intermixing layer) et les propriétés chimiques telles que la composition chimique des couches et la redistribution des éléments sont présentés. Ensuite, une autre partie du chapitre 3 est consacrée à l'impact des différents types de recuit sur l'agglomération du film de Ni(Pt)Si. Les détails concernant les quatre types de recuit sont présentés au début de cette partie : recuit partiel, laser, total, et recuit « unique ».

La troisième partie du chapitre 3 est dédiée à l'impact du confinement sur la stabilité thermique du film ultra-mince de Ni(Pt)Si. Une description des étapes d'élaboration de ces structures confinées est fournie au début de cette partie, présentant les différentes étapes de photolithographie utilisant le masque DIVA. Cette partie fournira une évaluation de l'évolution morphologique du film de Ni(Pt)Si formé dans les tranchées de structures confinées pendant le phénomène d'agglomération. La dernière partie du chapitre 3

présentera ensuite l'amélioration en termes de stabilité thermique du Ni(Pt)Si dans les circuits intégrés impliquant des procédés additionnels utilisés dans la fabrication d'une puce électronique (circuit intégré réel). Ce chapitre démontrera la faisabilité de l'une des solutions proposées (le recuit laser en millisecondes en particulier), à travers des analyses électriques et morphologiques.

Le quatrième chapitre de ce manuscrit sera ensuite dédié à des discussions sur les résultats expérimentaux obtenus. Nous présenterons tout d'abord une discussion sur l'impact des paramètres structurels tels que les épaisseurs de la couche d'intermélange, la distribution de taille des grains de siliciure et la texture. Une discussion sur les résultats de l'impact du confinement sur le film de Ni(Pt)Si est également présentée. Ensuite, la deuxième partie de ce chapitre présentera des discussions sur l'impact des éléments additionnels tels que Pt, O et F. Un modèle sur la redistribution des atomes de Pt pendant l'agglomération de Ni(Pt)Si sera également présenté. Les différents environnements chimiques et la distribution des éléments résiduels sont également abordés à la fin de ce chapitre.

Le manuscrit se conclura en présentant les principales conclusions de ce travail de recherche sur l'agglomération du film ultra-mince de Ni(Pt)Si et les perspectives correspondantes pour les futurs travaux de recherche.

Résultats

a. Préparation de surface SiCoNi

Dans cette première partie, l'influence de l'étape de préparation de surface du silicium à l'aide du procédé SiCoNi sur le phénomène d'agglomération de Ni(Pt)Si est étudiée. En effet, le procédé SiCoNi est utilisé pour nettoyer la surface du silicium avant la siliciuration afin d'éliminer la couche d'oxyde natif, SiO_x ou SiO_2. Ce procédé intervient donc avant le dépôt PVD (*physical vapor deposition*) de la couche de NiPt sur le substrat Si.

Pour cette étude, deux séries d'échantillons ont été réalisées sur un substrat Si(100) non-patterné (blanket wafer) pour les deux traitements de SiCoNi étudiés, SiCoNi 80 et SiCoNi 2x40. La première série d'échantillons a été réalisée à la suite du dépôt métallique par PVD de la couche de NiPt sur le substrat Si, sans recuit et sans encapsulation TiN. La deuxième, quant à elle, correspond à la couche de Ni(Pt)Si de 11 nm post recuit haute température entre 500 et 800 °C/30 s afin d'évaluer leurs stabilités thermiques.

a.i. Impact du procédé SiCoNi sur la couche de NiPt

Les couches de NiPt déposées sur les substrats de Si traités, par le procédé de SiCoNi 80, et SiCoNi 2x40, ont été caractérisées par l'éllipsométrie, la microscopie électronique à transmission (MET), la spectroscopie photoélectronique X (XPS), la spectroscopie X à dispersion d'énergie (EDX), la spectrométrie de masse à ions secondaires à temps de vol (ToF-SIMS), et la spectroscopie de perte d'énergie électronique (EELS).

Comme illustré dans la Fig. i, les images MET mettent en évidence une épaisseur de la couche d'intermélange plus importante dans le cas de SiCoNi 2x40. De plus, l'interface entre la couche d'intermélange et le substrat de Si est plus rugueuse dans le cas de SiCoNi 80.

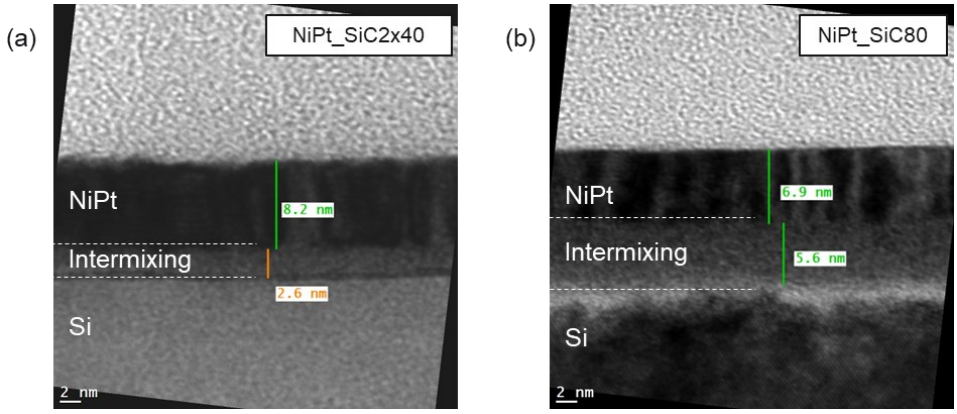


Fig. i. Images MET obtenues après dépôt de NiPt sur substrat de Si pour les échantillons (a) NiPt_SiC2x40 et (b) NiPt_SiC80.

Fig. ii présente les spectres de fluor détectés par la technique de l'XPS. Les analyses chimiques de la couche d'intermélange montrent que la concentration de fluor est plus importante lorsque le procédé SiCoNi 2x40 est utilisé. Les analyses par ToF-SIMS révèlent également deux redistributions distinctes de fluor dans la couche d'intermélange en fonction du procédé de SiCoNi utilisé (Fig. ii). En effet, le fluor présente deux pics proches des interfaces de NiPt/intermélange et intermélange/Si dans le cas du procédé SiCoNi 80.

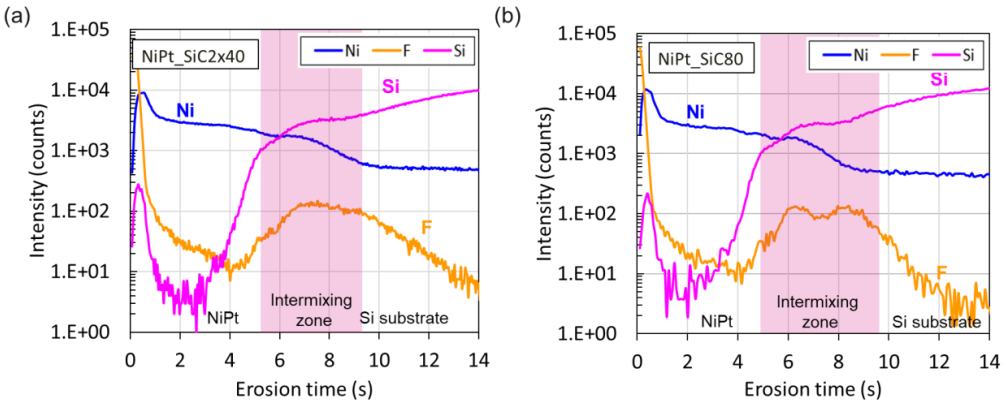


Fig. ii. Profils de profondeur ToF-SIMS de la couche de NiPt déposée sur substrat de Si pour les échantillons (a) NiPt_SiC2x40 et (b) NiPt_SiC80.

De plus, des analyses plus fines par la technique EELS ont permis de déterminer la présence d'un pic additionnel à 856 eV correspondant à un environnement chimique du type Si-F et/ou Ni-F dans le cas de SiCoNi 2x40. Ce pic additionnel n'est pas observé pour

l'échantillon préparé avec le SiCoNi 80, et ne correspond pas à une liaison du type Ni-Si ou Ni-Pt.

a.ii. Impact du procédé SiCoNi sur la couche de Ni(Pt)Si

Afin d'évaluer les impacts de ces différents procédés de SiCoNi (SiCoNi 2x40 vs. SiCoNi 80) sur la stabilité de la couche de Ni(Pt)Si, des recuits à haute température ont été réalisés entre 500 et 800 °C, notés RTAD, après la formation de la couche de Ni(Pt)Si par le procédé Salicide.

Nous avons constaté que l'agglomération de Ni(Pt)Si est moins sévère lorsque le procédé SiCoNi 2x40 est utilisé. Ceci a été attribué à une amélioration de l'uniformité de l'épaisseur de la couche finale de Ni(Pt)Si comparée à celle du procédé SiCoNi 80. Les impacts de ces procédés sur l'environnement chimique et la redistribution des éléments présentés précédemment contribuent également à l'amélioration de la stabilité thermique de la couche de Ni(Pt)Si.

b. Recuits de formation de Ni(Pt)Si

L'influence de différents types de recuits de formation sur la stabilité thermique de Ni(Pt)Si est également étudiée. Le premier recuit est appelé le recuit partiel, correspondant à une consommation partielle de la couche de NiPt lors du premier recuit, noté RTA1 pour *Rapid Thermal Annealing 1* (voir Fig. iii). Ensuite, nous étudions également le recuit laser millisecondes, noté DSA pour *Dynamic Surface Annealing*. Contrairement au recuit partiel, le recuit total transforme la totalité de la couche de métal de NiPt lors du RTA1 en siliciure riche en Ni, Ni_2Si. Enfin, le dernier recuit étudié utilise le RTAD uniquement, et est appelé recuit unique, pour sa formation et l'évaluation de sa stabilité thermique.

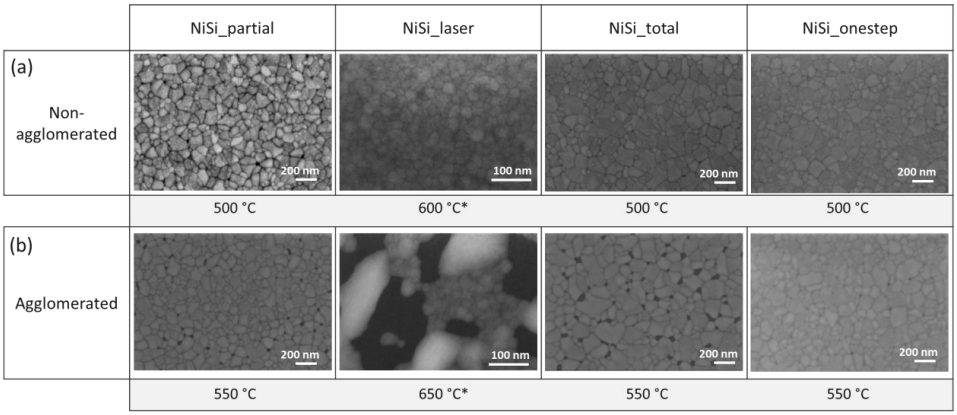


Fig. iii. Images MEB haute résolution (HRSEM) montrant les grains et les joints de grains pour des films de Ni(Pt)Si de 11 nm d'épaisseur formés par différents types de recuit de formation à l'état : (a) non aggloméré et (b) aggloméré.

En effet, les propriétés structurelles de la couche de Ni(Pt)Si sont fortement liées au choix des recuits de formation. Nous avons constaté une réduction significative de la distribution de taille de grain de Ni(Pt)Si lorsque le recuit laser est utilisé, permettant de retarder l'agglomération à un budget thermique plus élevé (une amélioration d'au moins 50 °C). Contrairement à cette observation, la couche de Ni(Pt)Si formée par le recuit total possède des gros grains de siliciure, induisant une sensibilité plus importante au phénomène d'agglomération. D'un point de vue technologique, ceci suggère fortement que le recuit total devrait être évité pour la formation de siliciure dans les intégrations 3D avancées.

Les analyses des orientations cristallines montrent que la couche de Ni(Pt)Si présente deux populations d'orientations principales, NiSi(010) et NiSi(013). Les analyses par figure de pôle permettent de confirmer la présence de la texture fibre, quel que soit le recuit utilisé. De plus, lorsque la couche de Ni(Pt)Si présente une agglomération sévère, l'intensité provenant de (010) diminue, mais ce n'est pas le cas pour les intensités de (013). Ceci suggère que l'orientation (013) est potentiellement plus stable et favorable à la stabilité de la couche de Ni(Pt)Si. En outre, les figures de pôle montrent aussi la présence d'un anneau d'axiotaxie lorsque la couche de Ni(Pt)Si est sévèrement agglomérée. Ces résultats soulignent l'importance du choix de recuit de formation pour contrôler les microstructures finales des couches de Ni(Pt)Si.

c. <u>Impact de confinement</u>

Dans cette étude, cinq séries d'échantillons ont été réalisées correspondant à des couches de Ni(Pt)Si de 11 nm formées sur un wafer non-patterné (blanket wafer) et un wafer patterné, composé de 4 structures confinées. Les 4 structures étudiées sont trois structures de champs de lignes présentant des tranchées siliciurées qui sont séparées par des lignes diélectriques avec une variation de largeur (110, 250 et 500 nm) et une structure de champ de carrés avec des plots diélectriques (cf. Fig. iv).

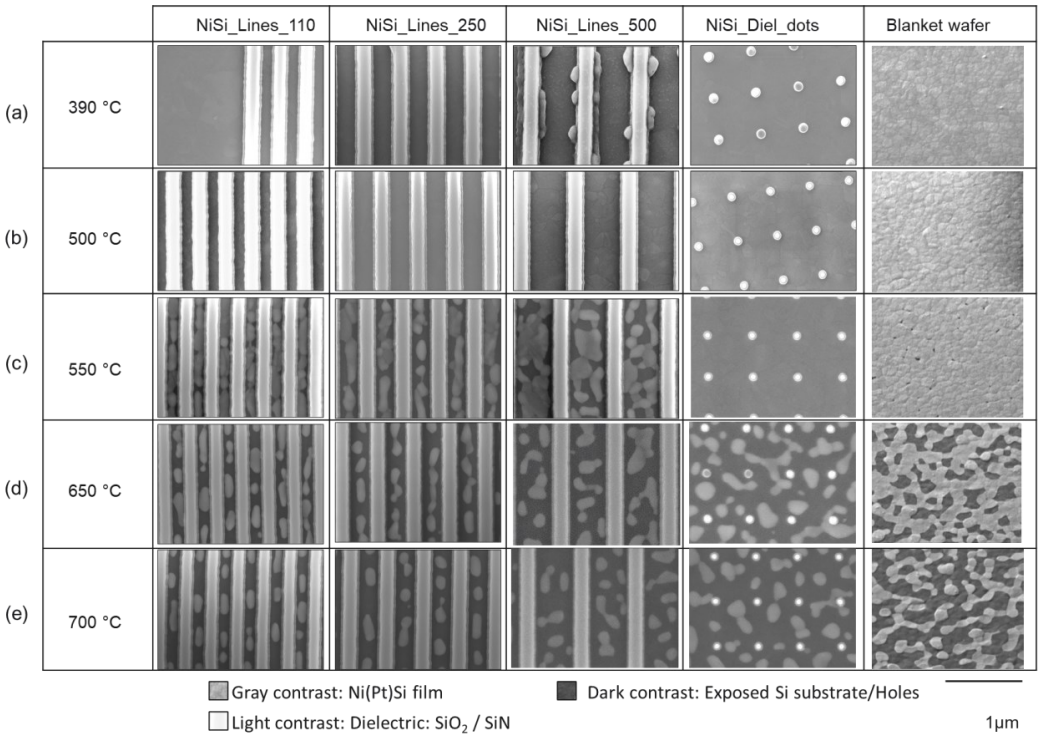


Fig. iv. Images HRSEM en vue de dessus de films de Ni(Pt)Si de 11 nm formés sur des structures confinées (NiSi_Lines_110, NiSi_Lines_250, NiSi_Lines_500, et NiSi_Diel_dots) et images MEB mesurées sur wafer non-patterné pour différentes températures de recuit, RTAD : (a) 390 °C, (b) 500 °C, (c) 550 °C, (d) 650 °C, et (e) 700 °C.

Pour les recuits à une température relativement basse, RTAD 500 °C, la couche de Ni(Pt)Si formée dans les structures les plus confinées (avec une largeur de 110 nm par exemple) présente une agglomération moins sévère parmi tous les échantillons étudiés. En effet, cette observation est inattendue. Nous attribuons cette première observation à l'hypothèse de la différence de la taille de grain lorsque la couche de Ni(Pt)Si est formée dans

des tranchées très confinées comme celles de 110 nm. En effet, la croissance latérale peut être limitée et les grains de Ni(Pt)Si sont donc plus petits.

De plus, nous avons également caractérisé la texture de ces couches de siliciures par la technique de diffusion des rayons X aux grands angles en incidence rasante, appelée GIWAXS, à l'ESRF (*European Synchrotron Research Facility*). Nous avons conclu qu'il n'y a pas de différence significative entre la texture de la couche de Ni(Pt)Si formée sur un wafer non-patterné et un wafer patterné, déterminée pour des recuits à 500 °C, c'est-à-dire avant agglomération. En effet, les analyses des figures de pôle de NiSi(002/011), NiSi(112), NiSi(202/211) et NiSi(103) montrent que les textures obtenues sont identiques, quel que soit le niveau de confinement de la couche de Ni(Pt)Si. Néanmoins, ces analyses restent très complexes lorsque la couche de Ni(Pt)Si est agglomérée et, à ce stade, il est difficile de conclure sur l'évolution de la texture de la couche de Ni(Pt)Si confinée pendant le phénomène d'agglomération.

d. <u>Résultats sur lot industriel : circuit intégré</u>

La dernière étude présentée dans le cadre de cette thèse a pour but d'évaluer la faisabilité d'une des solutions proposées (recuit laser DSA) dans la fabrication complète des circuits intégrés. Ceci implique des étapes additionnelles telles que la formation de MOS et des structures de pixels, ainsi que des procédés impliquant des budgets thermiques additionnels comme le dépôt de Ti/TiN par la technique ALD (*Atomic Layer Deposition*) et PVD (*Physical Vapor Deposition*). De plus, dans cette étude, nous évaluons également la stabilité de la couche de Ni(Pt)Si lors des recuits de formation de siliciure de titane, $TiSi_X$, autour de 550 et 650 °C.

Dans cette étude, deux types d'échantillons ont été élaborés avec les étapes de fabrication complètes des circuits intégrés. L'échantillon standard utilise le recuit de type RTA pour la formation de Ni(Pt)Si, tandis que l'autre échantillon utilise le DSA au lieu du RTA pour la formation de Ni(Pt)Si.

Nous avons constaté que le phénomène de rainurage de joints de grains (*Grain Boundary Grooving*) est plus prononcé lorsque le recuit de type RTA est utilisé dans la

formation de Ni(Pt)Si. En effet, le phénomène de rainurage de grain avec des courbures d'interfaces plus prononcées a été détecté par la caractérisation MET dans le cas de Ni(Pt)Si formé par le recuit de type RTA. Ceci suggère un stade plus avancé du phénomène d'agglomération entraînant la formation des trous à une température relativement basse.

De plus, nous avons également effectué, pour la première fois, une caractérisation électrique, notée PT pour *parametric testing*, sur des circuits intégrés réels utilisant le recuit laser DSA pour la formation des couches de siliciure de Ni(Pt)Si. Pour les recuits de $TiSi_x$ à 550 °C, nous avons constaté un impact non significatif des rainurages de joints de grains sur les propriétés électriques des circuits intégrés. Néanmoins, une augmentation drastique de la résistance a été observée par les mesures PT, lors du recuit de formation de $TiSi_x$ à 650 °C pour la couche de Ni(Pt)Si formée par le recuit de type RTA. Ceci entraîne une dégradation des performances globales du circuit intégré.

Conclusions

Dans les technologies d'imagers 3D les plus récentes, l'épaisseur du film de Ni(Pt)Si a été contrainte au régime ultra-mince, c'est-à-dire environ 11 nm d'épaisseur. La co-intégration du film ultra-mince de Ni(Pt)Si et des contacts à base de $TiSi_x$ constitue un grand défi technologique. Dans le cadre de cette thèse, nous avons étudié le phénomène d'agglomération du film ultra-mince de Ni(Pt)Si sur des wafers non-patternés et patternés à travers 4 principales études.

Le traitement de surface à l'aide du procédé SiCoNi a montré une amélioration de l'uniformité et de la stabilité par le biais de la redistribution de F et l'existence de potentielles liaisons Ni-F dans la couche intermélange. Ensuite, le choix du type de recuit, notamment le recuit laser, a permis de contrôler les microstructures finales de la couche de Ni(Pt)Si, entraînant une amélioration de 50 °C dans la stabilité thermique de Ni(Pt)Si. De plus, les études sur l'influence du confinement avec différentes dimensions ont mis en évidence l'impact significatif de l'interface avec les diélectriques. Les résultats sur les circuits intégrés réels ont également permis de confirmer l'intérêt de l'utilisation du recuit laser dans la fabrication de dispositifs microélectroniques.

Enfin, dans ces travaux de recherche, nous avons également présenté une modélisation de la redistribution de Pt lors du phénomène de rainurage de joints de grains et de l'agglomération de Ni(Pt)Si. Nous avons constaté que le Pt retarde la diffusion de Ni et/ou la diffusion de Si à l'interface de siliciure/Si dans ces phénomènes. Ceci souligne le rôle du Pt dans l'agglomération de Ni(Pt)Si

For Edward Amin, Caroline Lawi, Doris Edward and my family.

Acknowledgement

As cliché as it might sound, this Ph.D. has been a journey that constantly reminded me that growth occurs when we step out of our comfort zone. Those years of growth fostering multiple facets skillsets and competences as a young researcher would not have been possible without the numerous people that I encountered during my 3 years of Ph.D. and 6 months of internship. I would like to first dedicate these first few paragraphs to my Ph.D. supervisors who have been pivotal to the tremendous success of this research work, through their patience, pedagogy, advice, and time in ensuring quality in both my work and my growth as a young researcher in the field of silicide.

First, I thank my Ph.D. director, Dominique Mangelinck, with whom I have had the honor and privilege to work with during these 3 years, and who has been a major support behind this Ph.D. work. I extend my highest gratitude to Dominique for his constant scientific rigor, his meticulous attention to details, and most importantly, for his reliability both as a research director and as a person. Thank you for providing an environment where I was allowed to thrive, to grow, and to be independent while at the same time guided by you. It has been an immense honor for me to have had this opportunity.

I would also like to express my gratitude to Magali Grégoire, whose role has been central in the success of my Ph.D. Our story started way longer when I had the opportunity to work with Magali as an intern, and her discipline, exigences, supervision during the 6 months of internship were nothing short of impressive and excellent. Her experience in research and development (R&D) coupled with her expertise in semiconductor technologies and silicide materials have been a valuable resource to the quality reflected in the work of this Ph.D. Not only that she has been providing valuable advice and guidance in my development in STMicroelectronics, her warmth and kindness have been crucial in providing a safe, enjoyable, and a very welcoming environment for me to thrive during the 3 years of Ph.D. with her.

I would also like to thank Sophie Guillemin, for her excellent guidance and support during this Ph.D. work and her co-supervision during my internship in 2021. It was an honor to have had the opportunity to work alongside Sophie, who has been very instructive and very kind. Her guidance, advice and the discussion that we had has contributed to building the fundamental blocks that have taught me to develop my critical thinking. Thank you, Sophie, for the support and your kindness.

I extend my gratitude to members of the jury who have agreed to review this work and be part of this amazing journey: Christophe Detavernier, Claudia Wiemer, and Rémi Lazzari. I also thank my Ph.D. committee (CSI), Prof. Fiqiri Hodaj and Dr. Caroline Mauriat for their advice and guidance during this Ph.D.

I wish to also express my thanks to the numerous people I have had the chance to work with, Christophe Girardeaux, Alain Portavoce, Marion Descoins, Khalid Hoummada, Carine Perrin, Maxime Bertoglio from the IM2NP institute, and Andréa Campos from CP2M, Marseille. Thank you to all of you for being an excellent mentor, teacher and especially a

good friend to me. I would also like to extend my gratitude the Ph.D. students: Jérémy, William, Hamid, Oumaima, Gwenaël, Safae, Siham, Hamza, Karthick and a special thanks to Dr. Andréa Newman, and Dr. Réda Guelladress whom I have had the opportunity to do a Ph.D. in silicide with and who have been a good friend to me. I truly appreciate the friendly environment of the IM2NP lab, and the warm community there coupled with the sunny days, nothing less than perfect.

A special mention to Andréa Campos, who has been very diligent in her teaching of the Zeiss 500 and in transmitting her experience and expertise in the use of such high-quality measurement tools to obtain incomparable and "perfect" SEM images. Andréa, your company has always been very enjoyable despite the short moments we spent in the lab. Thank you very much for humor and your kindness.

A special thanks to those in CEA-Leti, Patrick Gergaud, Guillaume Freychet, Romane Blaise, Michel Pellat, Philippe Rodriguez, Laurent Xu, Thibaut Chêne, and many more that I would love to list here. CEA-Leti has been a great institution with competitive resources that allow young researchers to thrive and be guided properly.

As it is often said, save the best for the last, and thus, lastly, I would like to thank my second family, the *Atelier Métal 300*, who has more or less lived through my entire growth in my early years of my career. I would like to believe that every single one of you have played a role in contributing to the success of this research work. In particular, there are days I bombarded these engineers with unending questions of how the different software and web tools work.

To my "*precious"* fellowship of the Ring (*la communauté*), Sam, Hugo, Cedric, Mag, Guillaume, and Walid, thank for having given me the opportunity to discover the universe of Samwise Gamgee and Frodo Baggins. *Vous avez été tous mon Sam, comme Sam pour Frodon. Ou si vous préférez, vous étiez tous comme l'anneau pour Gollum, autrement dit, mon precious (* *). J'ai enfin compris que Gollum n'est pas le frère à Yoda.*

To *chef* Marc Lombard, you may think this line is biased, but I wish to thank you for your guidance as the silicide process engineer of Métal 300 in helping me understand the particularities of the process. You have been an amazing mentor, colleague, and moreover a friend. Wishing you a quick recovery. *Et sur l'échelle de zéro à ML, tu dépasses toujours le maximum.*

To the "*Fantastic Four*", Carine, Florian, Tselot, Marceau, and Safiya, I thank you for the horror movies in particular, which have many times become funny and have helped me to relieve stress during the writing of this manuscript. I think you have all become emotional support for me, and I have had many good memories and laughter. I am sure by now we know who the alpha of this circle is.

To the rest of the Metal, Mehdi, Fred, Sylvain, Antoine, Yannick, Elodie, Quentin, Pierre S., Pierre L., Jérôme, François, Rémi, Camille, Natalia, Magali T., Marina, Cédric M., Nidal, Bérèngère, Romaine, Jean-François R., Alexandra, Ugo, Maxence, Elisa, Agathe, Max, Denis, Carole, Yoan, Pierrick, Emmanuel, Pierre-Alexis, and Stéphane, thank you very much for these 3 years together. Special thanks to Karen Dabertrand, Jean-Gabriel Mattei, Aurore

Durel, Maxime Régé-Turo, Thibaud Fache, Maxime Dupraz, Yann Escarabajal, Rémi Beneyton, Adrien Estellon, Loan Le Duc, Antonin Zimmer, Laura Esposito, Thibaut Flacher, Damien Froger and others I may not have cited here.

Finally, thank you to my big family, for the unconditional support all the way from Malaysia, and my best friends Diana, Sabrina, Naqib, Aina, Haziq and Jing, who are also my siblings from another mother who made being far from family bearable. This may be an end to this chapter, however, I believe all the memories made during these three years and the relationships fostered, will remain for eternity.

Glossary

- **a-Si:** Amorphous Silicon
- **Agglomeration/Dewetting:** Morphological degradation of thin film resulting in the formation of small islands and film discontinuity.
- **ALD:** Atomic Layer Deposition
- **BEOL:** Back End Of Line
- **BG:** Boundary Grooving
- **BOX:** Buried Oxide
- **BSI:** Backside Illumination
- **CESL:** Contact Etch Stop Layer
- **CIS:** CMOS Image Sensor
- **CMOS:** Complementary Metal-Oxide Semiconductor
- **DSA:** Dynamic Surface Annealing
- **EBSD:** Electron Backscatter Diffraction
- **EDX:** Energy Dispersive X-ray spectrometry
- **EELS:** Electron Energy Loss Spectroscopy
- **FDSOI:** Fully Depleted Silicon-On-Insulator
- **FEOL:** Front End of Line
- **FinFET:** Fin Field-Effect Transistor
- **FSI:** Front Side Illumination
- **GB:** Grain boundary
- **GIXRD:** Grazing Incidence X-ray Diffraction
- **HAM:** High-Angle Misorientation

- **HF clean:** Hydrofluoric acid clean
- **IC:** Integrated Circuit
- **IPF:** Inverse Pole Figure
- **IPRSM:** In-Plane Reciprocal Space Mapping
- **MOSFET:** Metal-Oxide Semiconductor Field-Effect Transistor
- **NMOS:** n-channel metal-oxide semiconductor transistor is one in which n-type dopants are used in the gate region
- **PAI:** Pre-Amorphization By Implantation
- **PF:** Pole Figure
- **PMOS:** p-channel metal-oxide semiconductor transistor is one in which p-type dopants are used in the gate region
- **PVD:** Physical Vapor Deposition
- **RPC:** Remote Plasma Clean
- **Rs:** Sheet Resistance
- **RTA:** Rapid Thermal Annealing
- **RTAD:** Rapid Thermal Annealing Dewetting
- **SALICIDE:** Self Aligned Silicidation
- **SC1:** Standard Clean Particle removal
- **SCE:** Short Channel Effect
- **SE:** Selective Etch
- **SiCoNi:** Remote plasma surface treatment
- **SOI:** Silicon On Insulator
- **SPM:** Sulfuric Peroxide Mix

- **SRAM:** Static Random Access Memory
- **SEM:** Scanning Electron Microscopy
- **TEM:** Transmission Electron Microscopy
- **ToF-SIMS:** Time-of-flight Secondary Ion Mass Spectroscopy
- **XPS:** X-ray Photoelectron Spectroscopy
- **XRD:** X-ray Diffraction
- **XRR:** X-ray Reflectivity

Table of contents

AFFIDAVIT 2

LISTE DE PUBLICATIONS ET PARTICIPATION AUX CONFÉRENCES 3

ENGLISH SUMMARY 4

FRENCH SUMMARY 5

EXTENDED FRENCH SUMMARY 6

ACKNOWLEDGEMENT 18

GLOSSARY 22

GENERAL INTRODUCTION 29

CHAPTER 1: CONTEXT, STATE-OF-THE-ART, AND RESEARCH MOTIVATIONS 33

1.1 On the role of silicide in microelectronics devices 35

1.1.1 Introduction to MOSFET principles 35

1.1.2 Moore's law & "More than Moore" 40

1.1.3 Silicides for microelectronics applications 42

1.1.3.1 Early silicides 42

1.1.3.2 Integration of silicides and their purpose 43

1.2 Nickel monosilicide properties 46

1.2.1 Ni-Si systems 46

1.2.2 Introduction of alloying elements 49

1.2.3 Thin film elaboration process: SALICIDE process 51

1.3 Remaining challenge: Solid-state dewetting of Ni(Pt)Si thin films 54

1.3.1 Definition and driving force 54

1.3.2 Inverse agglomeration of Ni(Pt)Si film 60

1.4 Progress in understanding of the agglomeration of Ni(Pt)Si film 62

1.4.1 Surface preparation and SiCoNi pre-clean 63

1.4.2 Annealing techniques 66

1.5 Research axes & objectives 69

1.6 Chapter conclusions 72

CHAPTER 2: RESEARCH METHODOLOGY AND CHARACTERIZATIONS TECHNIQUES 74

2.1 Sample fabrication techniques 76

2.1.1 SiCoNi pre-clean processes 76

2.1.2 Metal deposition in Endura chambers 77

2.1.3 Thermal treatments 78

2.1.4 Selective etching 81

2.2 Characterization techniques 82

2.2.1 Four-point probe measurements for sheet resistance, Rs 82

2.2.2 Ellipsometry for thickness determination 84

2.2.3 X-ray diffraction (XRD) 85

2.2.4 Out-of-plane X-ray diffraction 87

2.2.5 In-plane X-ray diffraction 88

2.2.6 Texture analyses using pole figures 90

2.2.7 Scanning electron microscopy (SEM) 92

2.2.7.1 Tilted-SEM & High-resolution SEM 94

2.2.8 Electron backscattered diffraction (EBSD) 94

2.2.8.1 Orientation maps 95

2.2.9 Transmission electron microscopy (TEM) 96

2.2.9.1 TEM-EDX for chemical composition 97

2.2.9.2 TEM-EELS 97

2.3 Chapter conclusions 97

CHAPTER 3: EXPERIMENTAL RESULTS ON THE AGGLOMERATION PHENOMENON OF NI(PT)SI FILMS 98

3.1 List of samples, fabrication steps, and naming 101

3.2 Part 1: Different SiCoNi treatments 111

3.2.1 Experimental setup 111

3.2.2 1-A: Influence of multi-step SiCoNi process on PVD-deposited NiPt thin films 113

3.2.2.1 Observations of intermixing layer 113

3.2.2.2 Composition analyses obtained by XPS 116
3.2.2.3 EDX profiles 118
3.2.2.4 Redistribution of residual fluorine, F 121
3.2.2.5 Conclusions of part 1-A 123
3.2.3 1-B: Impact of SiCoNi treatments on the agglomeration of Ni(Pt)Si thin film 125
3.2.3.1 Investigation of the thickness uniformity post-RTA2 125
3.2.3.2 Investigation of the agglomeration of Ni(Pt)Si films (post-RTAD) 127
3.2.3.3 Conclusions of part 1-B 134
3.3 Part 2: Annealing schemes 135
3.3.1 Experimental setup 135
3.3.2 Sheet resistance, Rs 138
3.3.3 Tilted-SEM – film morphology 140
3.3.4 High-resolution SEM – grain size 144
3.3.5 Preferential orientations & textures 146
3.3.6 Conclusions of part 2 151
3.4 Part 3: Impact of confinement on Ni(Pt)Si film in regular lines 152
3.4.1 Experimental setup 152
3.4.2 Influence of confinement in regular lines on Ni(Pt)Si agglomeration 156
3.4.3 Impact of confinement on texture of Ni(Pt)Si thin films 160
3.4.4 Conclusions of part 3 167
3.5 Part 4: Results on industrial wafers (Integrated circuits) 169
3.5.1 Experimental setup 169
3.5.2 Investigation on Ni(Pt)Si thickness 172
3.5.3 Electrical characterizations 173
3.5.4 Silicide morphology 175
3.5.5 Conclusions of part 4 178
CHAPTER 4: DISCUSSIONS 179
4.1 Impact of structural parameters 181
4.1.1 Change in intermixing thickness 181

4.1.2 Role of grain size 183
4.1.3 Role of textures 186
4.1.4 Confinement of Ni(Pt)Si film 188
4.2 Impact of additional elements 194
4.2.1 Observations of Pt redistribution 194
4.2.2 Initial redistribution of Pt: before agglomeration 202
4.2.3 Pt redistribution during the agglomeration 203
4.2.4 Pt redistribution in the case of laser annealing 204
4.2.5 Modelling of the redistribution of Pt 208
4.2.6 Chemical environment 215
4.2.6.1 Residual fluoride, F and oxygen, O 215
4.2.6.2 SiCoNi treatments and Ni(Pt)Si agglomeration 217
General conclusions 219
Table of figures 233
Appendices 242

General introduction

Since its invention, transistors have served as the principal building block for many electronic devices from bulk computers, mobile phones, microprocessors found in cars to the many household appliances we interact in our day-to-day life. The widespread application of transistors in these devices has been made possible thanks to the miniaturization of these transistors, as projected by the Moore's law coined by Gordon Moore in 1965 [1]. Ever since, technological developments have seen remarkable progresses in the semiconductor industry leading to an increase in the performance of electronic devices without an increase of the manufacturing costs: as transistors are downscaled, the number of transistors that can be integrated per unit surface has exponentially increased. This has been the major driving force for technological innovations and developments in the semiconductor industry *i.e.,* the race for transistors miniaturization [2].

However, reduction of the transistor's dimensions has been pushed to physical limits in the early 2000s when the thickness of thin films within the transistor are constraint to several nanometers *i.e.,* equivalent to several atomic layers. As a consequence, numerous alternative paths have been developed leading to the birth of new transistors architectures such as the Fin Field-Effect Transistor (FinFET) and the Fully Depleted Silicon-On-Insulator (FDSOI) technologies [3], [4], strained Si [5] novel materials such as high-k oxides [6] and the introduction of the NiPt alloy allowing to stabilize the low resistivity silicide phase, Ni(Pt)Si [7], [8].

For FDSOI technologies, nickel alloyed with 10 at. % of platinum, noted Ni(10 at.% Pt) is the primary choice of industry for contact silicidation since the 65 nm technological node. A technological node is defined by the gate length of the transistor and implies different manufacturing processes and design rules. One of the technological node using the FDSOI substrates is the 28 nm [9], [10]. Introduction of a very thin Si layer on the top of embedded oxide layer (also called the BOX for Buried Oxide), led to a constraint in the thickness of the Ni(Pt)Si film at 11 nm resulting in an ultra-thin silicide film.

Similarly to the Moore's law evolution, the development of advanced imager technologies deals with the emerging 3D technologies [11], [12], [13], a complex integration requiring the use of both Ni(Pt)Si film and Ti-based contacts, $TiSi_X$. The high thermal budget used for the formation of the $TiSi_X$ layer at the bottom of W contacts, after the formation of Ni(Pt)Si thin film, is a major concern for all 3D integrations due to the fact that Ni(Pt)Si film is known to be sensitive to agglomeration phenomenon (also called solid-state dewetting) [14], [15], [16], [17], [18], [19]. Indeed, such morphological degradation of the Ni(Pt)Si film has been shown to result in severe devices yield loss and drastic increase of the silicided structures resistances in real 28 nm devices [10].

In this Ph.D. work, we aim to improve the thermal stability of the ultra-thin Ni(Pt)Si film through three major research axes. The first axis focuses on the impact of the surface preparation treatment on the formation and agglomeration of ultra-thin Ni(Pt)Si films. The second axis underlines the importance of the choice of annealing approaches used in the formation of the Ni(Pt)Si film on its agglomeration. Finally, a study on the thermal stability of ultra-thin Ni(Pt)Si films formed in nano-confined structures is also conducted through ESRF facility to determine the influence of the confinement of the Ni(Pt)Si film in more advanced technological nodes.

The first chapter is dedicated to the presentation of the basic principles and the architecture of the complementary metal-oxide-semiconductor (CMOS) transistor. This description is followed by a presentation of the Moore's law and the succeeding trends emerging during the end of the Moore's law known as More than Moore's law. A retrospective overview on silicide materials is then presented providing both historical and technical aspects of the use of silicides in the microelectronics industry. Next, the following sections provide a description on the nickel-based silicides, including their phase diagrams, and elaboration process, known as the SALICIDE process. The remaining challenges related to the thermal stability due to the agglomeration of the Ni(Pt)Si film are also described. Prior to concluding the first chapter, the remaining sections report the current existent pathways reported in the literature to improve the thermal stability of the Ni(Pt)Si film.

The second chapter of the manuscript will present the research methodology and characterization techniques used in the framework of this Ph.D. thesis. This chapter is thus divided into two main sections describing the sample fabrication techniques followed by the different characterization techniques such as four-point probe measurements for sheet resistance, Rs, ellipsometry, scanning electron microscopy (SEM), and transmission electron microscopy (TEM), electron energy loss spectroscopy (TEM-EELS), electron backscatter diffraction (EBSD), and X-ray diffraction (XRD). A particular analysis derived from either the XRD or EBSD is also presented, namely the pole figure analysis for the texture evaluation (meaning the crystal orientations).

The principal experimental results relating to the main research axes of the Ph.D. thesis are then detailed in chapter 3. The experimental set-up summary has been included at the beginning of this chapter to allow a simpler reading with an overview of the sample elaboration processes used in during this Ph.D. work.

Following the different steps in the SALICIDE process, this chapter begins with the first study of the impact of the different surface preparation treatments on the formation and agglomeration of ultra-thin Ni(Pt)Si films. Indeed, results relating to the structural properties such as the thickness of the intermixing layer, and the chemical properties *i.e.,* layer composition, and elements redistribution are presented. A second section of chapter 3 is dedicated to the impact of the annealing schemes on the agglomeration of the Ni(Pt)Si film. Details regarding the four different annealing approaches are presented at the beginning of this section called partial, laser, total and one-step annealings.

The third section of this chapter is dedicated to the impact of the nano-confinement on the thermal stability of ultra-thin Ni(Pt)Si films. The description of elaboration steps of the confined structures made using the lithography mask available at CEA-Leti is then provided. In this study, we evaluate the morphological evolution of ultra-thin Ni(Pt)Si films formed inside the confined structures during the agglomeration phenomenon. Finally, through a change in the Ni(Pt)Si film formation, we conclude the improvement in terms of Ni(Pt)Si thermal stability in real 3D integrated circuits.

The last chapter will be then dedicated to further discussions on experimental results obtained within this Ph. D work. This chapter begins with the discussion on the impact of structural parameters such as thicknesses of the intermixing layer, silicide grain size and texture. Impact of the confinement on the agglomeration of Ni(Pt)Si films is then deeply analyzed based on explicit statistics. A second section covers a deeper understanding of the impact of additional elements as well as Pt, O, and F. This includes the modeling of the redistribution of Pt atoms during agglomeration. Additionally, the different chemical environments and residual elements distributions are also discussed at the end of this chapter.

The manuscript will then conclude by giving the principal key findings of this research work on the agglomeration of ultra-thin Ni(Pt)Si films and the corresponding perspectives for future investigations.

Chapter 1: Context, state-of-the-art, and research motivations

Chapter contents

1.1 On the role of silicide in microelectronics devices 35
1.1.1 Introduction to MOSFET principles 35
1.1.2 Moore's law & "More than Moore" 40
1.1.3 Silicides for microelectronics applications 42
1.1.3.1 Early silicides 42
1.1.3.2 Integration of silicides and their purpose 43
1.2 Nickel monosilicide properties 46
1.2.1 Ni-Si systems 46
1.2.2 Introduction of alloying elements 49
1.2.3 Thin film elaboration process: SALICIDE process 51
1.3 Remaining challenge: Solid-state dewetting of Ni(Pt)Si thin films 54
1.3.1 Definition and driving force 54
1.3.2 Inverse agglomeration of Ni(Pt)Si film 60
1.4 Progress in understanding of the agglomeration of Ni(Pt)Si film 62
1.4.1 Surface preparation and SiCoNi pre-clean 63
1.4.2 Annealing techniques 66
1.5 Research axes & objectives 69
1.6 Chapter conclusions 72

Foreword

The first chapter is dedicated to the presentation of the research frameworks and context of the PhD thesis. It begins with the presentation of the basic principles of transistors and the miniaturization trends in the microelectronics industry. Next, a retrospective overview of the evolution of silicides and their role in microelectronics industry is presented. The following sections introduce in further details the nickel monosilicide, Ni(Pt)Si thin film and the remaining challenges associated with the new integration requirements for the recent imager technologies. Then, the current progress in understanding the morphological degradation of the Ni(Pt)Si film, and the extensive efforts that have been made to improve the extendibility of Ni(Pt)Si thin films are explained. The last section outlines the challenges of the formation of Ni(Pt)Si thin film in confined dimensions, and in particular, related to the agglomeration phenomenon. The chapter ends by an outline of the objectives and research axes of this thesis.

1.1 On the role of silicide in microelectronics devices

In this section, relevant insights on *metal–oxide–semiconductor field-effect transistor* (MOSFET) and the use of silicide layers in microelectronics industry are detailed. An overview of the historical and technical aspects of the silicide materials is also presented.

1.1.1 Introduction to MOSFET principles

The *metal–oxide–semiconductor field-effect transistor* (MOSFET) is one of the most utilized types of transistors in microelectronics industry . It serves as a fundamental building block for many modern microelectronics devices ranging from mobile phones, household electrical appliances to microcontrollers used in cars and airplanes [20], [21].

The working principle of the *field-effect transistor* (FET) was patented in the 1925 by Julius Edgar Lilienfeld [22]. However, a fully functional semiconductor device based on this principle could not yet be developed at that time. It was only 30 years later that the first functional transistor was developed by J. Bardeen, W. Brattain, and W. Shockley, and this work was awarded by the Nobel prize in Physics in 1956 [23]. The MOSFET was then developed by D. Kahng and M. Atalla in the 60s [24]. MOSFET derived its name from its particular architecture which is characterized by the stacking of **m**etal, **o**xide, and **s**emiconductor materials in vertical direction. From this architecture, the MOSFET terminals can be constructed.

Fig. 1 illustrates a schematic of a (a) MOSFET structure, composed of a gate terminal, source/drain terminals, and the substrate and (b) the equivalent electrical schematic.

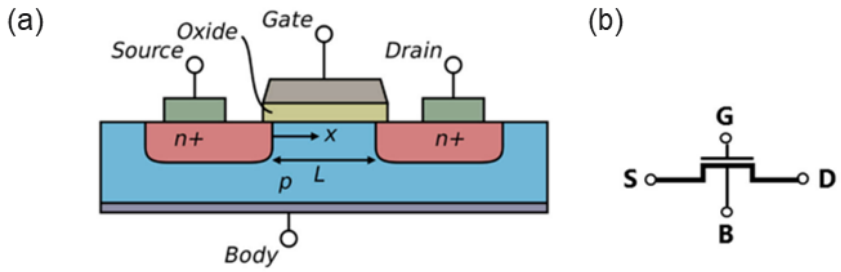


Figure 1. Schematic diagram of (a) an n-type MOSFET formed on a p-doped Si substrate and (b) its equivalent electrical diagram, from [25].

The principle of a MOSFET is hereafter presented by considering the transistor as an electrical switch. Semiconductor materials such as silicon and germanium are typically used as the substrate. For an n-type MOS, the source and drain are strongly doped with n-type dopants with electrons as charge carriers while it is the reverse for p-type MOS (with holes as charge carriers).

The source and drain terminals are as charge reservoirs. These terminals are separated by a channel under the gate, the amount of current traveling though it being controlled by the tension applied to the gate (*i.e.,* field effect). The gate is composed of a highly doped polycrystal silicon or a metallic electrode, separated from the channel by a dielectric layer usually called the gate oxide.

Upon the application of a sufficiently high voltage, the channel can be created under the gate oxide layer. This means that current can flow between the source and drain terminals and the transistor is considered to be in ON state. However, in the absence of voltage, the gate is grounded, and thus, the transistor is considered to be in OFF state. Thus, MOS transistor state can be modulated by the gate voltage, and this demonstrates high suitability for the creation of a circuitry with logic functions.

For this purpose, a *complementary metal-oxide-semiconductor* (CMOS) technology has been fabricated through the pairing of two MOSFETs with opposite conduction mode (n-type and p-type) [26]. Today, CMOS serves as the principal building block for the fabrication of integrated circuits (IC) such as memory chips, microcontrollers, and microprocessors due its reliability, manufacturability and particularly, its scalability [27].

This has been made possible thanks to the continual development of complementary metal–oxide–semiconductor (CMOS) Image Sensor (called CIS) allowing improvement on both functional capabilities and flexibility during the last years [28]. Then, CIS have emerged as a strong alternative to Charge Camera Detector (CCD) and present a very promising functionality. The CIS is generally made up of 2D array of pixels containing each a photodetector and several transistors.

Fig. 2 presents the vertical pn junction which allows photo-electronic current generation from incident light reaching the pixel area (Fig. 2(a)). An NMOS transistor (located near the photodiode inside the pixel area, named “transfer gate”) allows the transfer of “photo current”.

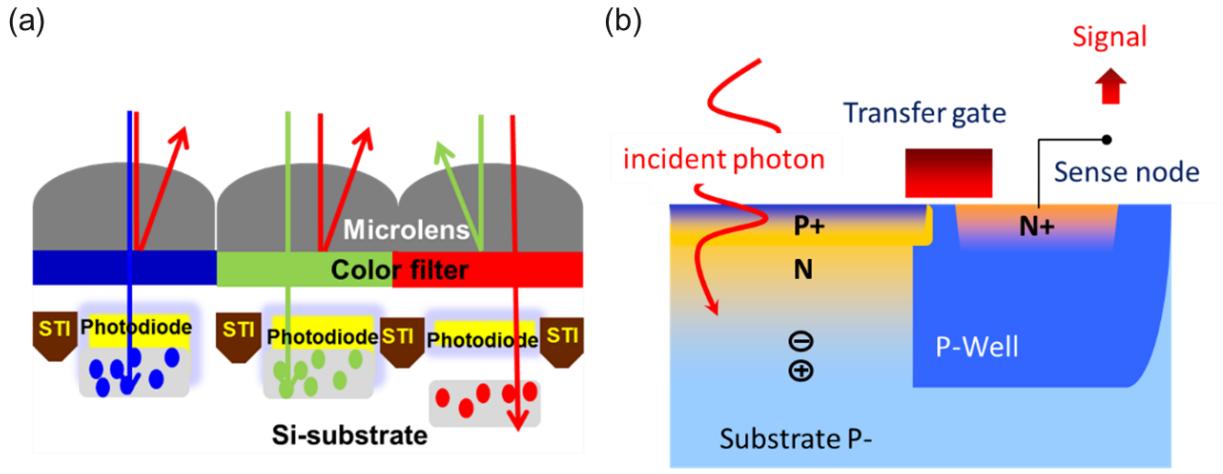


Figure 2. (a) Schematics of CMOS Image Sensor (CIS) including micro-lens and color filters on the top of the photodiode inside the pixel area. (b) Schematics of the photodiode as a vertical pn-junction in which the photo-electronic current is generated under illumination and then gathered by the transfer gate to the sense node [28].

Further innovations in the imager technologies also lead to the development of the promising 3D integration allowing drastic improvements in overall performances. This is achieved through the wafer stacking as shown in Fig. 3.

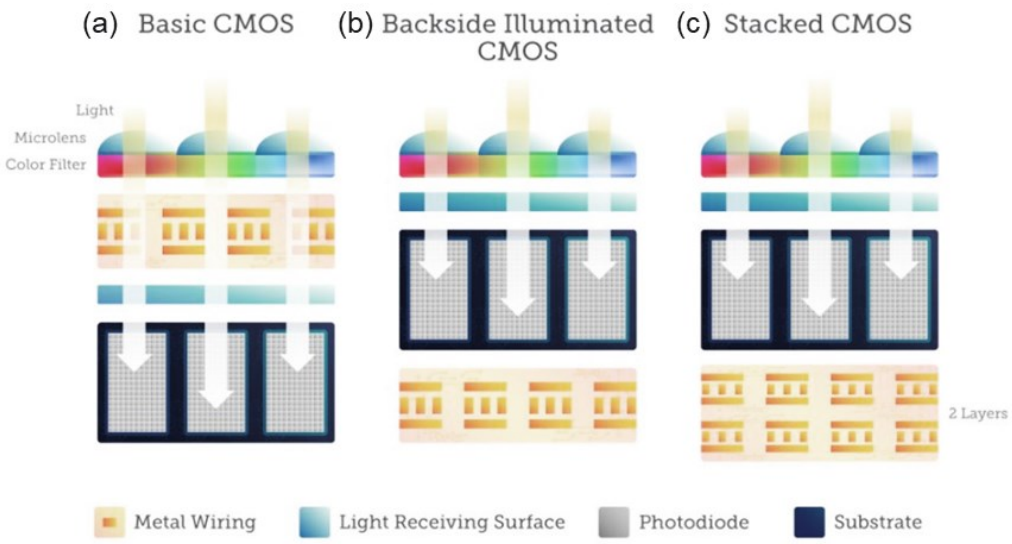


Figure 3. Evolution of imager technologies with (a) Front-side illuminated (FSI), (b) Back-side illuminated (BSI), and (c) a more recent 3D stacked BSI (3D-BSI) [28].

The evolution of the imager technologies as shown in the Fig. 3(a) starts with a photodiode embedded in the substrate with an illumination from the front side of the wafer (usually called front-side illumination, FSI). Next, in Fig. 3(b), the on-chip lens is directly integrated on the backside of the photodiode through hybrid bonding allowing to improve the image quality (called the backside illumination, BSI). Finally, in Fig. 3(c) shows the stacking of the CMOS imager sensor on top of the logic CMOS device forming the 3D stacked Back-Side Illuminated (3D-BSI) imagers. Such 3D integration deals with two wafers bonded together: one is dedicated to photo-electronic current gathering (“pixel layer” *or* “top tier”) and the second one to signal computing (“bottom tier”) [28].

For this new 3D-sequencial technologies, the co-integration between Ti-silicided contacts formed on the transfer gates and Ni-silicided in the CMOS devices implies a particular process integration as described in the Fig. 4 below. This process flow is also named monolithic approach [13], [28].

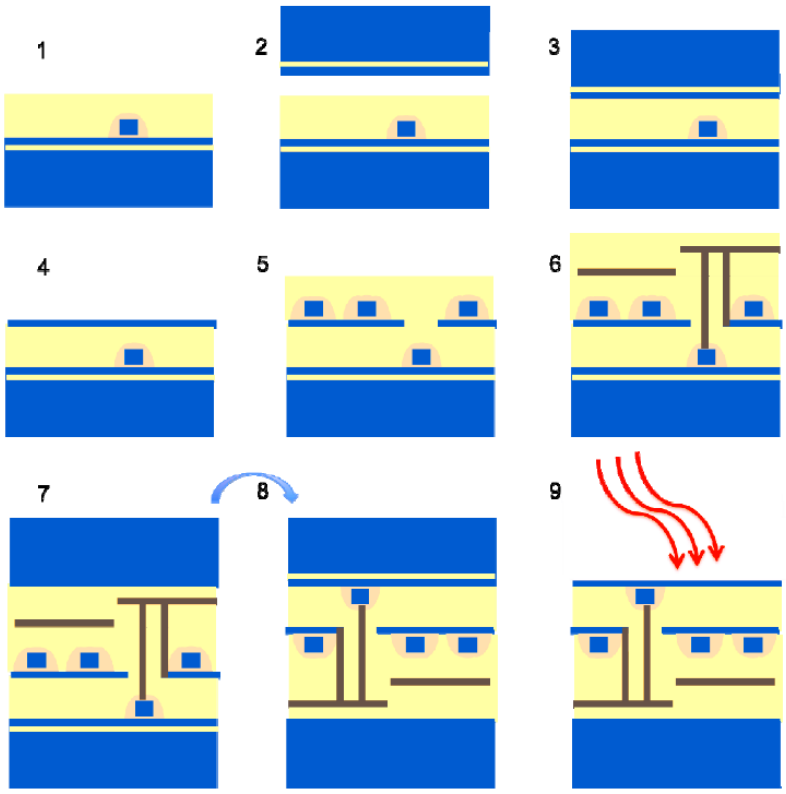


Figure 4. Process flows of the 3D sequential integration involving (1) fabrication of the embedded photodiode, (2-4) transfer of a second SOI layer by direct bonding, (5) processing of the low temperature transistor, (6) contacts formation and BEOL steps, and (7-9) Backside illumination is performed [29].

The 3D sequential integration process flow starts with the fabrication of the embedded photodiode in step 1, followed by transfer of SOI layer by direct bonding in step 2 to 4, processing of low temperature transistor in step 6, and contacts definition followed by BEOL processes (7 to 9) [29].

Thus, a low-resistive Ti-silicide phase is necessary in the photosensitive regions while an ultra-thin NiSi layer is already in place below the contacts. Such co-integration remains a challenge since formation of low-resistive Ti-silicide phase requires higher thermal budgets which further increase the risk of degrading the Ni(Pt)Si films leading to detrimental agglomeration phenomenon. Section 1.4 of this chapter will further details regarding the challenges related to such complex co-integration associated with the thermal stability of the NiSi film.

1.1.2 Moore's law & "More than Moore"

For almost half a century, the semiconductor industry has been driven by dimensional downscaling of transistors, defined by the Moore's law [1]. This trend, forecasted by Gordon Moore in 1965, states that the number of transistors per unit of surface (IC) will double every 12-18 months (ITRS, 2007). For at least a decade, the Moore's law has served as a roadmap for the technological developments for many companies in the semiconductor industry [2]. Following the scaling law, defined by R. H Dennard in 1974, MOSFETs were shrink to the micrometric and even nanometric scales [30], [31]. CMOS technologies are thus defined by their technological node which corresponds to the gate width of the transistor. For each technological node, specific semiconductor manufacturing process and design rules are developed [30].

However, multiple issues begin to rise due to the miniaturization trends in particular, issues associated with the transistor current leakage, and heat dissipation [32]. As of today's technology, the gate width has been reduced to sub-10 nm [33]. At this range, several problems have arisen affecting the proper functioning of the transistor. For example, for reduced gate widths, the channel length is in the order of magnitude of the dimensions of the surrounding depletion layer of the source/drain terminals. Consequently, this leads to an "off-state" leakage current. This parasitic effect is the known as the Short Channel Effect (SCE) [34].

These critical issues have motivated the emergence of a new trends called "More than Moore", where the focus in technology development shifted towards new MOSFET architectures and development of novel materials [35]. In particular, this led to the development of the FinFET (*fin field-effect* transistor) and FDSOI (*fully depleted silicon-on-insulator*) architectures [3], [4]. In this way, new gate materials (such as high-k oxides, including hafnium dioxide, and zirconium dioxide for the dielectric layer) [6], and strained Si channel such as the Si-Ge compressively strained channel [5] have emerged as industry standards.

Ever since the 28 nm technological node, FDSOI have been adopted as an alternative to the bulk Si-MOSFET thanks to the large performance boost and low mismatch variability of this new architecture [9]. As shown in Fig. 5, the FDSOI architecture remains a planar technology and can be distinguished from bulk Si-MOSFET by the presence of thin silicon layer on top of an insulator (the *buried oxide* BOX) at the bottom of the channel, formed by a silicon oxide. This constitutes what is known as the *silicon-on-insulator* (SOI) substrate.

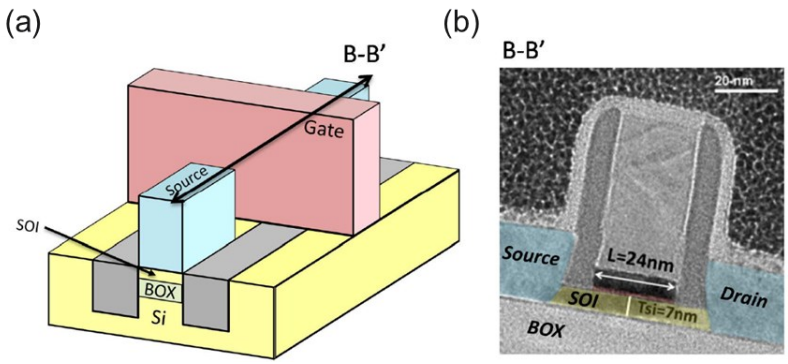


Figure 5. (a) Schematics of the FDSOI architecture with corresponding (b) TEM cross-section views between B-B' from [9].

The SOI layer is thus very thin (thickness less than 15 nm) and the active zones are very well isolated from the bulk substrate by the BOX. This results in better control over the whole depth of the channel by the gate and eliminates leakage current contributions [9].

1.1.3 Silicides for microelectronics applications

For the past four decades, silicide layers have been widely used in the semiconductor industry thanks to their interesting properties and their capacity to assist large-scale integration of downscaled CMOS technologies [36], [37], [38], [39]. Silicide is a functional material that is an intermetallic compound containing Si and can be typically constituted of a binary, ternary or quaternary phase. Its formation occurs through the application of energy (often heat) on a metal layer deposited on top of a Si substrate.

Currently, the primary role of the silicide layer is to reduce the overall contact resistance and to allow good electrical conduction between the interconnection levels and the active part of a device. An example is given in Fig. 6, where a silicide layer is formed on the three terminals of the transistor *i.e.,* source, drain and gate.

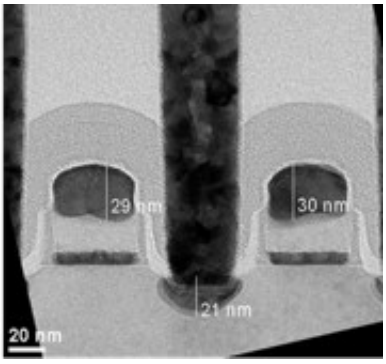


Figure 6. TEM cross-section of a 28 nm FDSOI technology with silicided gate and source/drain terminals (STMicroelectronics internal data).

1.1.3.1 Early silicides

The first silicides were introduced in the 1970s, with a major interest for the purpose of ohmic contacts, Schottky barriers, and gate electrodes. In the 1980s, the silicides were used to prevent the formation of aluminum spikes during the development of ohmic contacts for integrated circuits [40]. Historically, aluminum was deposited on top of Si substrate, and this led to the formation of aluminum spikes inside the Si substrate. Early solution such as doping the aluminum with low concentration of Si has allowed to suppress these spikes [41].

However, severe issues began to arise due to the decrease of feature size, and thus, silicide materials were needed as contact materials between the aluminum and Si substrate [41].

Nevertheless, an extensive number of papers exists on the wide variety of refractory metals considered for formation of the silicide materials thanks to their low resistivity and high thermal stability [38], [39], [40], [42]. These early silicides include, notably, platinum silicide (PtSi), palladium silicide (Pd_2Si), molybdenum disilicide ($MoSi_2$), tungsten disilicide (WSi_2), and tantalum disilicide ($TaSi_2$).

By the early 1990s, titanium disilicide, $TiSi_2$ emerged as the standard choice within the semiconductor industry [39]. However, the use of $TiSi_2$ rapidly faced major challenges related to the complex nucleation of the low-resistive C54-$TiSi_2$ phase in narrow lines lower than 250 nm in the active regions [39].

Reduction of transistors' dimensions induces the replacement of $TiSi_2$ by the cobalt disilicide, $CoSi_2$. Similarly, the integration of $CoSi_2$ layer presents a clear limitation for the technological nodes under 90 nm and the formation of voids in the gate structure during silicide process was then underlined as a major issue [43].

Due to these challenges, and with the introduction of SiGe substrates in the upcoming nodes, the interest in $CoSi_2$ began to decline from the 65 nm node and beyond [36], [44], [45]. Indeed, it has been observed that the formation of $CoSi_2$ phase is delayed to higher temperature when SiGe substrate is used [46]. As a consequence, the choice of materials used for contacts shifted towards nickel monosilicide, NiSi, in the semiconductor industry for technological nodes under 65 nm [36], [37], [47], [48], [49].

1.1.3.2 Integration of silicides and their purpose

In addition to the historical metric of presenting a low intrinsic resistivity and following Moore's law, several other criteria are nowadays considered in the selection of silicides as contacting materials:

1. Low silicon consumption versus junction depth is requested to be reduced in aggressively downscaled transistors. This means that silicides depth in the substrate must not exceed the depth of the junction to prevent any risk of short-circuit. Moreover, with the introduction of the SOI substrate, the amount of available Si for the formation of silicide is limited to 15 to 18 nm as well [3], [9], [47].
2. Low formation temperature to form silicide is performed after the formation of ultra shallow and usually highly doped junction in Si or FDSOI substrates. This allows to limit dopant redistribution during the formation of silicides.
3. Thermal and morphological stability to avoid any degradations during further processing of the back end of the line (BEOL) steps, that typically involve numerous thermal budgets for dielectric and Cu interconnects fabrications and mechanical strain.

Table 1 summarizes the properties of the previously mentioned silicides (C54-$TiSi_2$, $CoSi_2$, and NiSi) as regard to these various criteria.

Table 1. Properties of principal silicides used for CIS technologies [50].

Silicide	ρ (μΩ.cm)	T_f (°C)	T_m (°C)	t_{Si}/t_M (nm)	Mode of growth
C54-$TiSi_2$	13-16	750	1540	2.2	Germination-controlled
$CoSi_2$	15	800	1330	3.6	Mixed
NiSi	10-20	250-400	1000	1.83	Diffusion-controlled (Ni)

ρ – resistivity of silicide layer (μΩ.cm)
T_f – formation temperature of silicide phase (°C)
T_m – melting temperature of silicide phase (°C)
t_{Si}/t_M – consumption of Si per unit metal (nm)

However, each of these silicides present different difficulties related to the downscaling of CMOS technologies. Some of these issues have been previously discussed in

section 1.1.3.1 (nucleation issues in narrow lines, severe voiding in gate structures, and compatibility with SiGe substrates) in particular, for both C54-$TiSi_2$ and $CoSi_2$.

The silicides used for each generation of CMOS technologies are presented in Fig. 7, and plotted as a function of their respective diffusion coefficient in silicide at 500 °C. Indeed, NiSi presents the highest coefficient diffusion as compared to two previous silicides, C54-$TiSi_2$ and $CoSi_2$. Furthermore, interest in the NiSi and Ni(Pt)Si as contact materials is also driven by two other advantages: the relatively low silicon consumption and diffusion-controlled growth (which allow to suppress nucleation issue seen in C54-$TiSi_2$ [51] and obtain smooth interfaces).

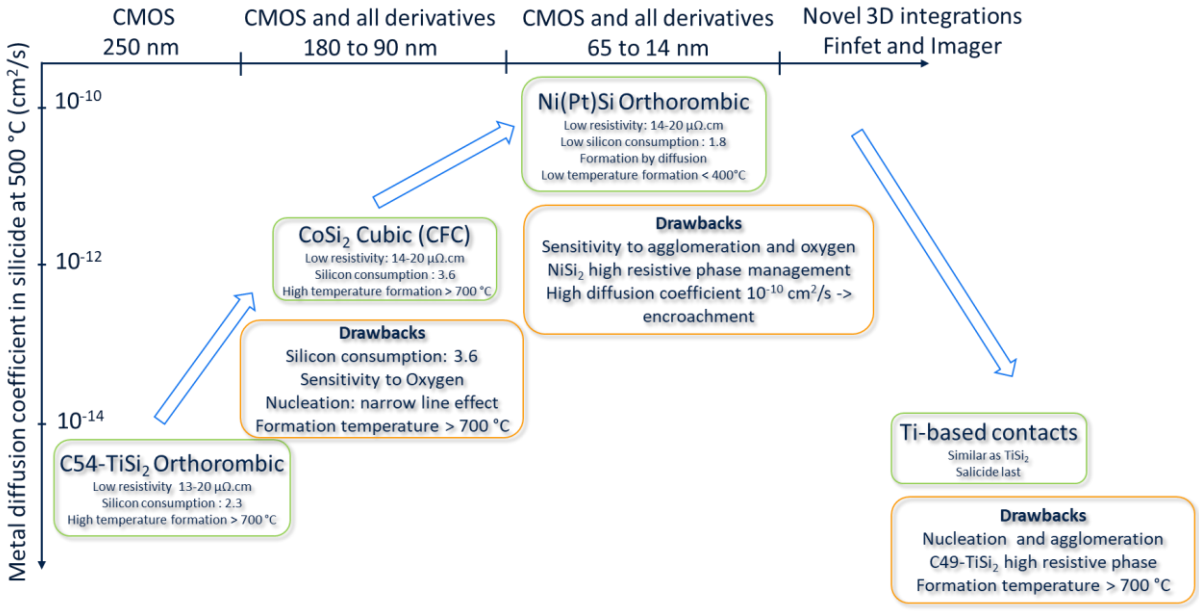


Figure 7. Evolution of "salicide" integration from C54-$TiSi_2$ to Ni(Pt)Si and recent Ti-based contacts dedicated to 3D integrations based on [44], [52], and STMicroelectronics internal data. The X-axis presents the technology node and the referred integration. The Y-axis shows the metal diffusion coefficient in silicide at 500 °C is given for Ti, Co and Ni silicide. The dominant diffusing species for each system are Si for Ti-Si, Co for Co-Si, and Ni for Ni(Pt)-Si respectively, based on [44].

Despite being the standard choice of silicide for CMOS technologies from the 65 nm node, NiSi *or* Ni(Pt)Si presents some remaining challenges, particularly associated with its low thermal stability resulting in the formation of holes, electrical discontinuities, and formation of isolated NiSi islets inside the Si substrates [16], [53]. This degradation of the

Ni(Pt)Si layer leads to severe yield loss [10] and will be covered in further detail in section 1.3.

1.2 Nickel monosilicide properties

In the framework of this Ph.D. thesis, we focus on the platinum-alloyed nickel monosilicide, Ni(Pt)Si as the unique silicide used for FDSOI technology. The relatively high Ni coefficient diffusion in the forming silicide phase allows a lower formation temperature of the lowest resistivity NiSi phase [40]. Moreover, this phase has a stoichiometry of 1 to 1 between the Ni and the Si, resulting in lower Si consumption needed during its formation when compared to the $CoSi_2$ phase, for example. Phase growth of the Ni-based silicide, including both Ni_2Si and NiSi, are primarily controlled by diffusion, suppressing the issues related to phase formation by nucleation in narrow lines as seen in the case of C54-$TiSi_2$. This section will begin by a brief introduction of Ni-Si and Ni(Pt)-Si systems followed by the SALICIDE process.

1.2.1 Ni-Si systems

The formation of metal silicide layers involves solid-state reactions between a metal and a silicon substrate through diffusion or nucleation mechanisms. After the deposition of the Ni layer on the Si substrate, the application of heat treatment will result in the interdiffusion of Ni and Si leading to the formation of new phases. Experimental results have demonstrated that Ni is the predominant diffusing species in the Ni silicides and thus the growth of these phases is usually controlled by Ni diffusion [54]. The phase diagram of the Ni-Si system (Fig. 8) is composed by four stoichiometric phases (γ-Ni_3Si, δ-Ni_2Si, NiSi and $NiSi_2$) and three non-stoichiometric ones (β-Ni_2Si, ϵ-Ni_3Si_2 and θ-Ni_2Si).

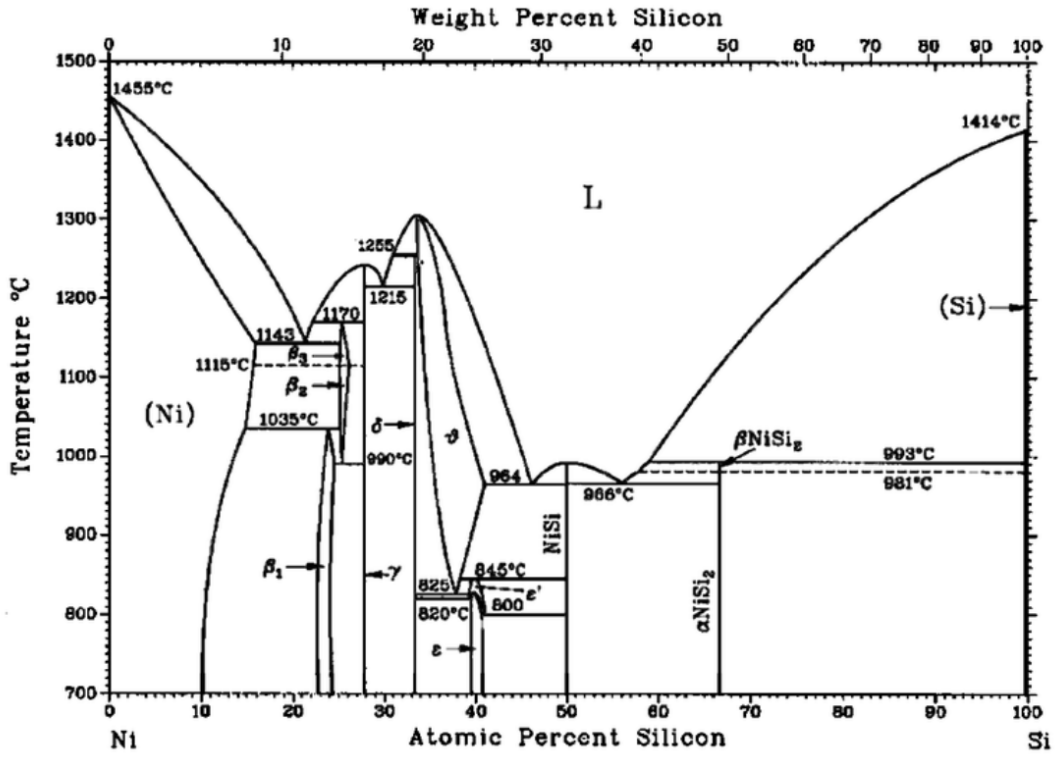


Figure 8. Phase diagram of Ni-Si system [55].

As a first approach, the phase diagram can be used to deduce the phase sequence for the thin layer materials despite it being experimentally determined for bulk materials. For silicide thin films, phase formation occurs sequentially, and this can be determined, for example, through in-situ measurements by X-ray diffraction (XRD) technique. Such measurements have allowed the identification of the phases with respect to the annealing temperature [56].

In the case of Ni-based silicides, the phase sequence is usually as follows [57]:

$$Ni/a\text{-}NiSi/Si \rightarrow Ni_2Si \rightarrow NiSi \rightarrow NiSi_2$$

Firstly, at room temperature, the Ni/Si diffusion couple forms an amorphous interlayer, a-NiSi after the deposition of the Ni *or* NiPt metal by PVD deposition (see Fig. 9)

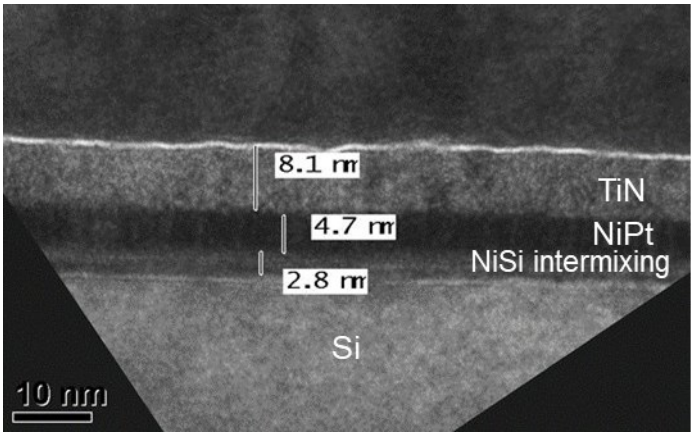


Figure 9. TEM cross-sections of NiPt layer showing the presence of the amorphous NiSi interlayer (also called intermixing layer) after metal deposition steps (STMicroelectronics internal data).

As shown on Figure 9, in the case of NiPt alloy, an interlayer of around 3 nm of thickness is formed between the metal and the substrate post-PVD deposition. Next, further annealing leads to the formation of the Ni-rich phases. The formation of the first phases is a subject of an extensive research and presents a great interest to understand the microstructural properties of the final NiSi phase [17], [54], [56], [58], [59].

The principal characteristics of each phase in the Ni-Si system is detailed in Table 2.

Table 2. Crystal structure, phase composition, and reported intrinsic resistivities for the stable phases in the Ni-Si system adapted from [37].

Phase	Crystal structure	ρ (μΩ.cm)	Lattice parameters (Å)			Si at. %
			a	*b*	*c*	
Ni	FCC	8	3.52			<10
β-Ni_3Si	Cubic	85	3.50			25
β-$Ni_{31}Si_{12}$	Hexagonal	120	6.68		12.29	27.9
δ-Ni_2Si	Orthorhombic	27	5.00	3.37	7.04	33.33
θ-Ni_2Si	Hexagonal	27	3.80		4.89	33-42
ε-Ni_3Si_2	Orthorhombic	65	12.29	10.80	6.92	39-41
NiSi	**Orthorhombic**	**17**	**5.23**	**3.25**	**5.62**	**50**
$NiSi_2$	FCC	40	5.40			66.66

Once the low resistive phase NiSi is formed, two primary degradation mechanisms have been reported: nucleation of the $NiSi_2$ phase which presents higher resistance than that of NiSi [60], [61], and the morphological degradation of the NiSi thin film due to the agglomeration phenomenon [14], [15], [18], [36], [62], [63], [64], [65].

Indeed, looking at the phase diagram previously presented in Fig. 8, one can notice that NiSi is not the final stable phase (*i.e.,* the phase in equilibrium with Si). Thus, upon the application of further thermal budgets, the system will evolve towards the $NiSi_2$ phase. In addition to the increased phase resistivity, the transition towards $NiSi_2$ on Si(100) substrate often results in the formation of inverted $NiSi_2$ pyramids inducing very rough silicide/substrate interface as illustrated in the Fig. 10 [66], [67], [68], [69], [70], [71].

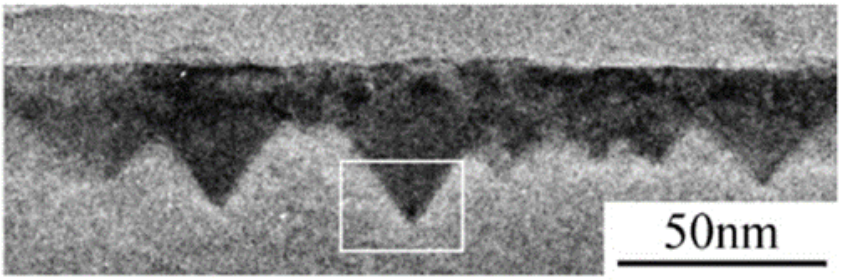


Figure 10. Example of the inverted pyramidal $NiSi_2$ formed on Si(100) substrate from [67].

1.2.2 Introduction of alloying elements

One of the widely adopted strategy to prevent the unwanted formation of $NiSi_2$ phase is to alloy the pure Ni metal layer with other metals such as Pt, Ti, W, Ta, Pd, or Zr [7], [8], [72], [73], [74]. For the industry, the introduction of Pt (ranges between 5 and 15 at. %) has emerged as the standard choice for the contact metallization [7], [8], [61], [64], [75]. Mangelinck *et al.* [7] have shown that the agglomeration is delayed for NiSi films with 5 at. % Pt compared to the pure NiSi ones as shown in Fig. 11. The stabilization of the NiSi phase at higher temperatures *i.e.,* beyond 700 °C can be understood as a result of Pt segregation at the silicide/Si interface and at grain boundaries [76] during NiSi formation.

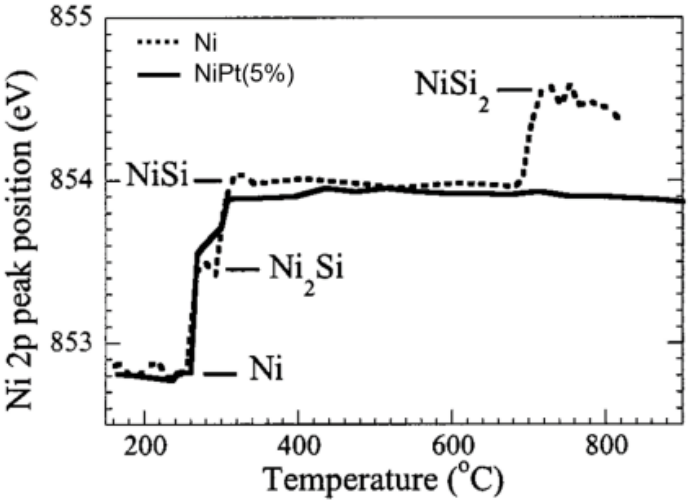


Figure 11. In-situ XPS analysis as function of the annealing temperature showing the variation of the Ni 2p peak position comparing Ni and Ni(5 at.% Pt) films on Si(100) substrates [61].

Indeed, Pt was found to distribute at the grain boundaries and silicides interfaces, hindering diffusion of Ni and thus stabilizing the NiSi phase to higher temperature. Kittl *et al.* [48] have reported similar observations by using Rs measurements. Figure 12 demonstrates that the addition of Pt delays the drastic increase in the Rs of the NiSi film alloyed with Pt.

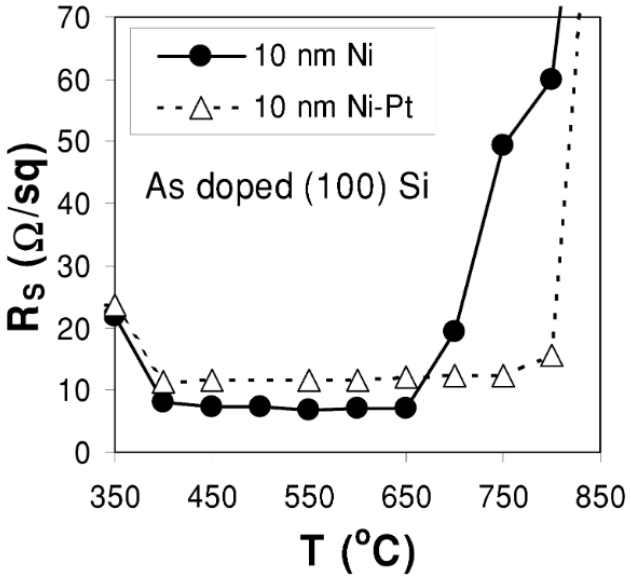


Figure 12. Sheet resistance, Rs, evolution of NiSi and Ni(Pt)Si thin films for increasing annealing temperatures post silicide films formation [48].

Moreover, further inspection of the Ni(Pt)Si layer morphology with SEM analysis (Fig. 13) demonstrated that the film is not agglomerated at 700 °C / 30 s whereas without Pt the film is agglomerated.

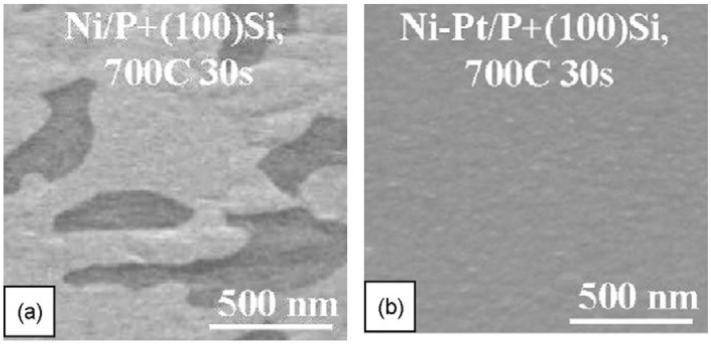


Figure 13. SEM images of the reaction of (a) 10 nm Ni and of (b) 10 nm Ni–Pt with p+ (100)Si after submitted to an annealing of 700 °C/30 s [48];

Detavernier *et al.* [77] have reported that the addition of Pt as an alloying element appears to reduce the axiotaxial relation between the NiSi grains and the substrate which proves to be beneficial for the stability of the NiSi thin film. The change in texture is a consequence of the expansion of the NiSi lattice due to presence of Pt atoms leading to the suppression of the 1D-periodicity of the axiotaxy texture [77]. The addition of Pt proves therefore crucial in controlling NiSi thin film as it affects both the grain size and the grain texture.

Nevertheless, the second degradation mechanism relating to the thermal stability of the Ni(Pt)Si still remains. Indeed, the agglomeration of the NiSi has been observed to occur at as low as 550 °C for Ni(Pt)Si film below 20 nm [10].

1.2.3 Thin film elaboration process: SALICIDE process

The current formation process of silicide layers is known as SALICIDE for the “Self-Aligned Silicidation” process. First developed in the early 1980s [78], this process allows to form silicide layer simultaneously on the three terminals of the transistor without the need of an additional lithography mask.

This process can be divided into two sub-groups, “salicide first” and “salicide last” which refers to the formation of the silicide layers before or after the tungsten, W contact patterning, respectively. For Co and Ni-based silicides, the salicide first scheme is usually chosen whereas for Ti-based silicides, the silicide formation follows the salicide last process. In the salicide first scheme, five main steps could be highlighted such as in Fig. 14.

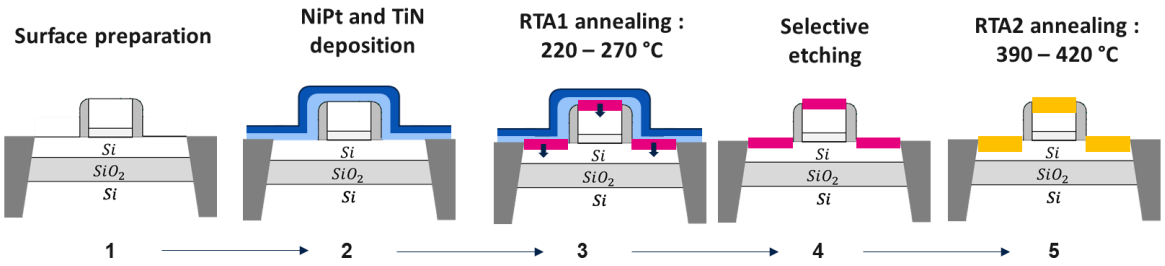


Figure 14. Steps in the salicide first process flow for the formation of the Ni(Pt)Si layer on the terminals of a transistor with SOI substrate. The Ni(Pt)Si layer is formed before contact patterning as opposed to the salicide last process for Ti-based silicide (Adapted from [79]).

1. Surface preparation (HF and/or SiCoNi^{TM} pre-clean) to remove native oxide and prepare the Si substrate for metal deposition.
2. Then NiPt metal is deposited using physical vapor deposition (PVD) sputtering technique. The NiPt layer is then capped with a TiN layer to prevent oxidation.
3. The first annealing is conducted at temperatures between 220 - 270 °C using the Rapid Thermal Annealing (RTA) technique. The first annealing is noted RTA1 and the NiPt layer is partially consumed during this anneal leaving excess NiPt and unreacted TiN layer on top of the newly formed Ni-rich silicide.
4. The excess NiPt and TiN layers are then removed using a mixture of hot SPM (sulfuric peroxide mixture H_2SO_4 and H_2O_2), and SC1 (diluted H_2O_2 & NH_4OH) solution.
5. Finally, a second annealing is performed at temperatures between 390 – 420 °C for typically 30 s (RTA2) to form the desired low resistive Ni(Pt)Si layer.

On the other hand, Ti-based silicide contacts are made through the salicide last process. To briefly describe this process, it deals with a single annealing at RTA temperatures

between 600- 800 °C after contact patterning. Fig. 15 describes the four steps involve in the salicide last scheme

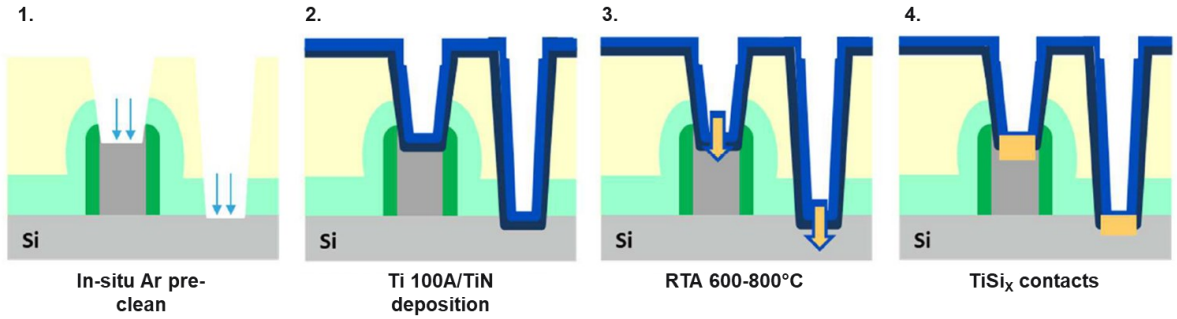


Figure 15. Steps of salicide last process flow for the formation of $TiSi_X$ layer on the terminals of a transistor for bulk Si-substrate. The $TiSi_X$ is formed after the contact patterning from [28].

1.3 Remaining challenge: Solid-state dewetting of Ni(Pt)Si thin films

The agglomeration (*or* dewetting) is a recurrent phenomenon typically observed in in thin films and particularly polycrystalline thin films [80], [81], [82], [83], [84], [85]. Such phenomenon is detrimental for microelectronics devices and remain one of the principal challenges to extend the process windows of the Ni(Pt)Si thin films for 65 nm nodes and beyond [10], [44], [62], [66], [86].

Indeed, significant reduction of the transistor dimensions implies that the junction depth is drastically decreased limiting the amount of Si available for the formation of silicide [3], [9]. In addition, the recent 28 nm FDSOI technology dealing with SOI substrate also means that the thickness Ni(Pt)Si layer is constraint to at most 11 nm thick.

At this thickness range, the capillary effect (surface and interface energies) can no longer be negligible leading to higher tendency to agglomeration in silicide films [83].

1.3.1 Definition and driving force

Agglomeration phenomenon is a process by which a continuous solid thin layer, when submitted to sufficient thermal energy, changes to form small islands (called islets) as illustrated in Fig. 16. This phenomenon is driven by the minimization of the total energy of free surfaces and film/substrate interface [83]. In the case of thin films, the large surface to volume ratio results in higher driving force for agglomeration [83].

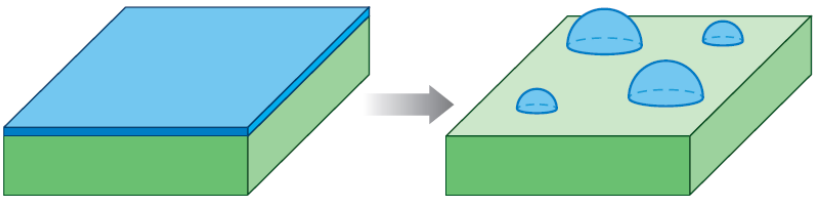


Figure 16. Schematics of the formation of isolated small islands (blue islets) on the top of rigid substrate (green) due the agglomeration phenomenon [83].

The agglomeration of these thin films may thus occur far below their melting point, in solid-state. The term of solid-state dewetting is also often used to refer to the agglomeration phenomenon of the thin film.

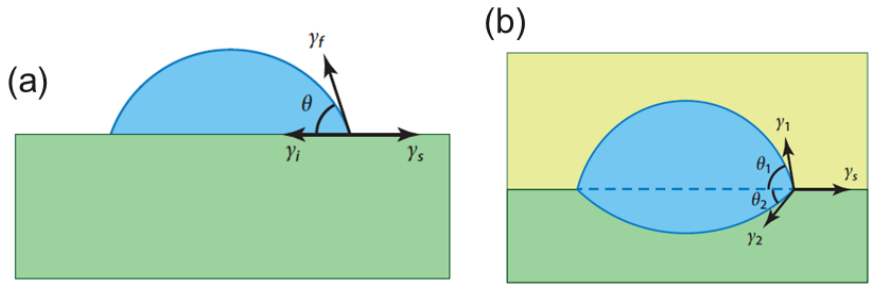


Figure 17. (a) Agglomerates formed on a rigid substrate and (b) agglomerates formed at the interface of two materials [83].

The islet can either form on the surface if the substrate is rigid, and for an isotropic surface energy, the shape of the agglomerates is theoretically a spherical cap as illustrated in Figure 17(a). The shape of the islet on the rigid substrate can be described using interfacial energy equilibrium and contact angle, θ, as deduced by Young-Laplace's equation expressed as:

$$\boldsymbol{\gamma_s = \gamma_i + \gamma_f \cos(\theta)} \qquad \textbf{Equation 1}$$

With γ_s, the surface energy of the substrate, γ_i, the interface energy of islet/substrate, and γ_f, the surface energy of the islet. When the interfacial energies γ_s, γ_i, and γ_f respect Equation 1, an equilibrium state of the agglomerates is achieved.

The film is stable if $\gamma_s > \gamma_i + \gamma_f$ and otherwise agglomerates.

For agglomeration occurring in between two non-rigid materials, the shape of the agglomerate is a lens-shaped islet as shown in Fig. 17(b). The energy equilibrium can thus be described as:

$$\boldsymbol{\gamma_s = \gamma_1 \cos(\theta_1) + \gamma_2 \cos(\theta_2)} \qquad \textbf{Equation 2}$$

$$\boldsymbol{\gamma_1 \sin(\theta_1) = \gamma_2 \sin(\theta_2)} \qquad \textbf{Equation 3}$$

With γ_1 the interface energy between the islet and phase noted A, and γ_2 the interface energy between the islet and phase noted B. Their corresponding contact angle is denoted as θ_1, and θ_2 respectively. In this case, the expressions of θ_1, and θ_2 can be deduced:

$$\cos(\theta_1) = \frac{\gamma_s^2+\gamma_1^2-\gamma_2^2}{2\gamma_s\gamma_1} \quad \textbf{Equation 4}$$

$$\cos(\theta_2) = \frac{\gamma_s^2-\gamma_1^2+\gamma_2{}^2}{2\gamma_s\gamma_2} \quad \textbf{Equation 5}$$

Agglomeration process is generally described as involving three main steps [83]:

i. Hole nucleation on available defects (film edges, triple junctions for polycrystalline films).

ii. Hole expansion, usually with a propagating rim that may be rounded or facetted.

iii. Formation of isolated islands due to Rayleigh instabilities resulting in ligament break-up.

In polycrystalline thin films, the development of the hole usually begins with the formation of grooves through boundary grooving. As shown in Fig. 18, Srolovitz and Safran [87], [88] developed a model describing the grain boundary grooving phenomenon.

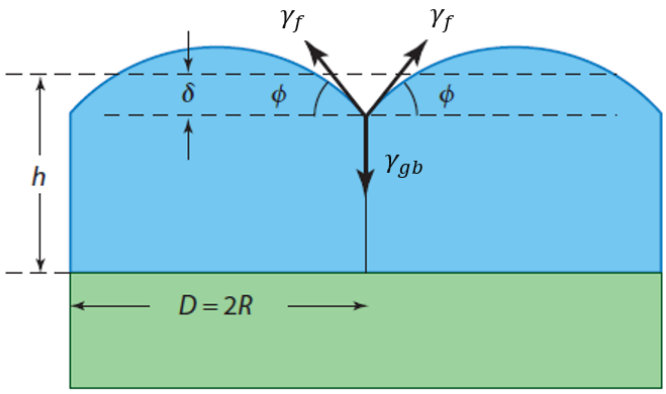


Figure 18. 2D illustration of the cross-section of two grains with diameter D on a rigid substrate at the equilibrium state during the development of grooves adapted from [83].

For a 2D grain structure on a rigid substrate as illustrated by Fig. 18, the energy balance will lead to the formation of a curved surface (boundary grooving), for which the groove angle, φ is defined as follows [89]:

$$\boldsymbol{\varphi = sin^{-1}(\frac{\gamma_{gb}}{2\gamma_f})} \qquad \textbf{Equation 6}$$

With γ_{gb}, the grain boundaries energy and γ_f, the isotropic surface energy. Under this condition, a groove can be formed, and the groove depth, δ is established as

$$\boldsymbol{\delta = D\ \frac{2-3\cos(\varphi)+cos^3(\varphi)}{3\ sin^3(\varphi)}} \qquad \textbf{Equation 7}$$

With ϕ, the groove angle and D the grain size. When the depth of the groove becomes larger than the thickness of the film, h, a hole is thus formed. The system will then follow steps ii and iii mentioned above.

The critical grain size, D_c, can be determined as function of the thin film thickness, h, and groove angle, ϕ.

$$\boldsymbol{D_c = h\ \frac{3\ sin^3(\varphi)}{2-3\cos(\varphi)+cos^3(\varphi)}} \qquad \textbf{Equation 8}$$

As stated by the Equation 8, the agglomeration phenomenon will not occur for grain size below the critical grain size ($D < D_c$). This means that polycrystalline films with small grains are more resistant to the agglomeration for a given thickness.

Numerous models have been developed to describe the boundary grooving phenomenon, including the most classical one developed by Mullins in 1956 [90], Nolan *et al.* in 1992 [84], and also Amram *et al.* in 2014 [91]. In the first approach, the grain boundary grooving was theorized to occur through a mass transport mechanism at the surface of the grains[90]. This is illustrated in the first model by Mullins as shown by Fig. 19 below. The normalized profile shape of the surface is also presented in Fig. 19(b) indicating the presence of groove.

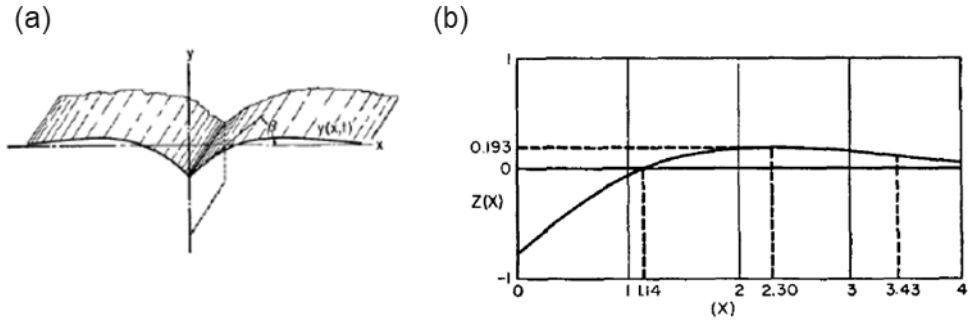


Figure 19. Mullins first model of a grain boundary grooving with (a) the boundary grooving and (b) the normalized profile shape of the surface [90].

Due to the chemical potential gradient between the rim of the hole formed via boundary grooving, the edge of the hole rim begins to recede, and this process will develop into an almost cylindrical mound or circular mound around the hole rim. Such mechanism implies a flux of mass transport, noted J due to the gradient in chemical potential [83], [91]. The steps of mass shedding are described in Figure 20(a) to Figure 20(d).

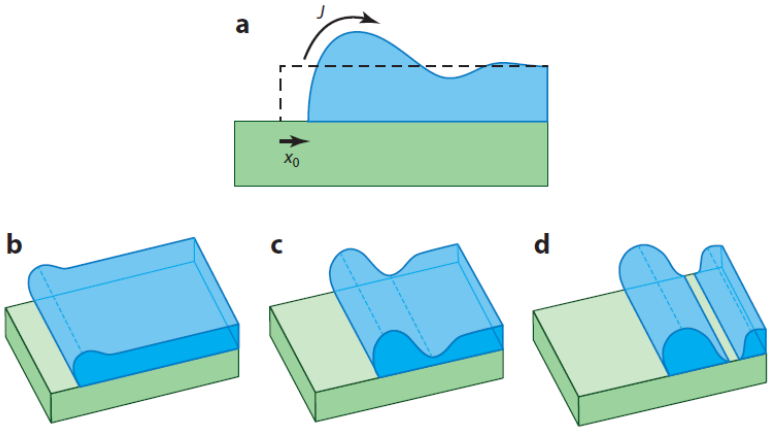


Figure 20. Mass shedding mechanisms: (a) Retraction of the thin film edge described by flux J due to chemical potential gradient. (b-c) The retraction continues and thickens the rim causing a deepening of the valley in front of the rim. (d) The valley achieved a maximum depth and in contact with the substrate, isolating the thin film, creating discontinuities [83].

While this theory remains valid for many thin films, Amram *et al.* [91] have demonstrated that the rims are nearly flat near the grain boundary grooves as shown in Fig. 21.

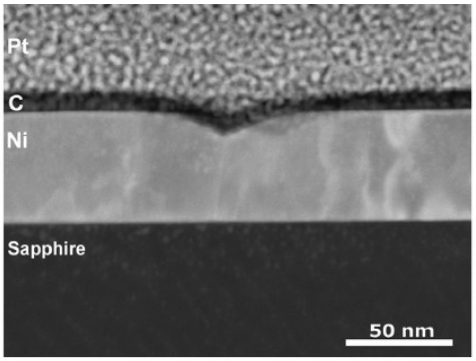


Figure 21. STEM cross-section of a Ni film on a sapphire, Al_2O_3 substrate, annealed at 700 °C for a duration of 6 mins from [91].

Such observation, schematized in the Figure 22(a), contradicts the mass balance principle as proposed by Mullins in 1956 [90]. Thus, an extension of the Mullins original model was proposed by H. Barda and E. Rabkin [85], [91], where the existence of interface diffusion of Ni at the interface of the Ni film and the sapphire substrate is no longer negligible during the boundary grooving phenomenon which leads to the film thickening.

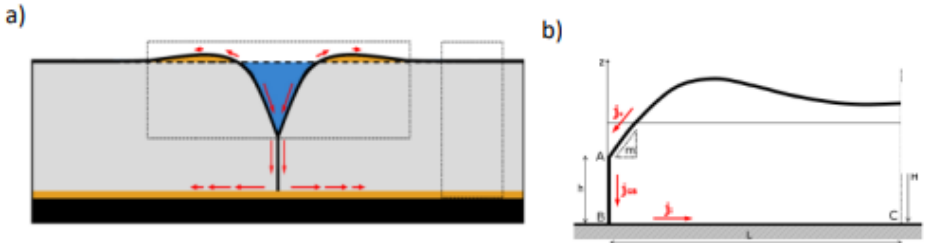


Figure 22. (a) Non-elevated rim during grain boundaries grooving, (b) Extension of Mullins original model of a grain boundary grooving with the consideration of interface diffusion [91].

Such model was validated through a Kirkendall-style marker experiment which demonstrated the thickening of the overall film during boundary grooving illustrated in Figure 23. In this figure, the Kirkendall markers are colored in pink. The thickening of overall film is demonstrated to be only possible if there are atoms diffusing between the Si substrate and silicide [85].

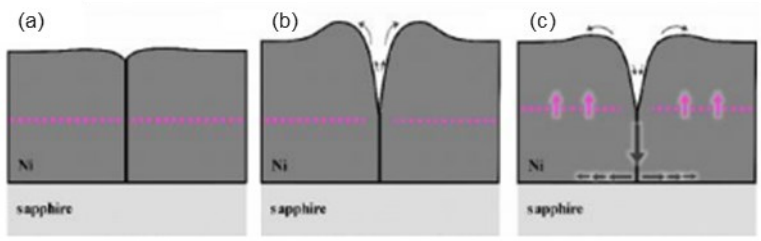


Figure 23. (a) Initial state (in pink, the Kirkendall marker). (b) Initial stage of boundary grooving without interface diffusion. (c) The presence of interface diffusion increases the height of the Kirkendall marker from [85].

1.3.2 Inverse agglomeration of Ni(Pt)Si film

A study provided by Nakatsuka *et al* [16] has demonstrated another particularity of NiSi thin films, which agglomerate inversely. That means that islands formations are inside the Si substrate in depth, as shown by TEM image in Figure 24.

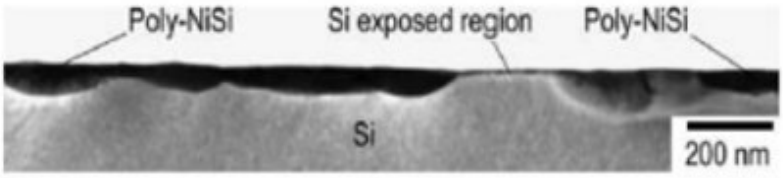


Figure 24. Cross-sectional TEM image of inverted NiSi islands formed on Si substrate post thermal annealing at 750 °C for 30 s [16].

Luo *et al.* [53] also reported similar observations regarding the agglomeration of NiSi films on Si substrate. Average roughness of the top surface of agglomerated NiSi films, after an annealing of 600 °C was reported to be around 2 nm indicating an almost flat surface despite severe agglomeration (Fig. 25(a)) [53]. The displaced NiSi volume in Fig. 25.(b) closed to the initial grain boundary is conserved and can be found at the bottom of the inverted mound of NiSi agglomerates. They explained this inverse agglomeration by the volume change associated to the reaction Ni+Si→ NiSi. Moreover, Luo *et al.* [53] demonstrated that the slow diffusion of Si at the silicide/substrate interface plays an important role in the agglomeration of NiSi by using Si isotopes enriched layers. Such observation was confirmed by atom probe tomography measurements on agglomerated NiSi film [53].

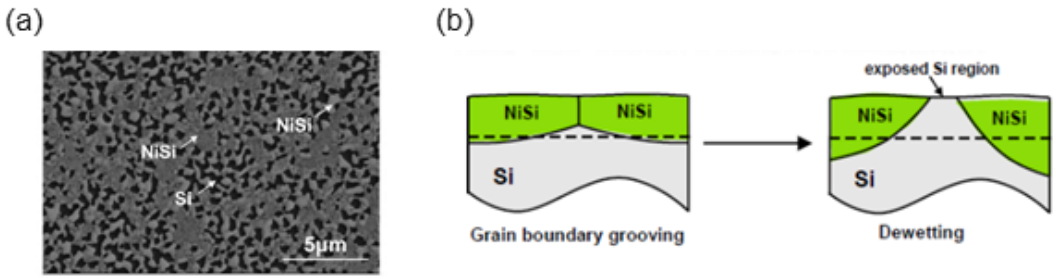


Figure 25. (a) Top-view SEM images showing agglomerated NiSi film on Si substrate. b) Cross-section schematic of the inverse agglomeration of NiSi film [53]

Assumptions based on Si diffusion at the NiSi/Si interface in a model developed by Luo *et al.* [53]. This allows to understand the diffusion of these atoms away from the top NiSi layer and towards the newly NiSi at the bottom of the inverted mound as well as the redistribution of the Si isotopes

Such discussions are of major concern as this means that there is a local thickening of the silicides film in the substrate resulting in electrical intrusion and penetration of junctions in microelectronics devices [92], [93]. The introduction SOI substrate for the 28 nm FDSOI technology is thus challenged by this phenomenon as these inverted agglomerates may reach the buried oxide and lead to overall device failure.

1.4 Progress in understanding of the agglomeration of Ni(Pt)Si film

Within the last decades, extensive research has been conducted to understand and delay the agglomeration phenomenon of nickel-based silicides. As already stated in the previous section 1.2.2, the main outcome was to alloy the used Ni metal targets with a low percentage of Pt, ranging between 5-15 at. % [7], [8], [19], [44], [64], [94]. The segregation of Pt atoms at grains boundaries and interfaces during the silicide formation, is believed to stabilize the low resistivity NiSi phase. In addition to the alloying of Ni with Pt, several approaches have been studied to limit agglomeration. Dynamic Surface Annealing (DSA) was also introduced for the 28 nm-FDSOI technologies instead of the classical Rapid Thermal Annealing (RTA) [95]. Other promising approaches are still under assessment, such as pre-amorphization implantation (PAI), doping, and surface preparation [19], [75], [95], [96], [97], [98], [99], [100], [101].

Along with the various published works, several key factors were reported to influence the agglomeration of Ni(Pt)Si films such as the film thickness, silicides grain size distribution and thin film texture. Low film thickness is associated to high driving force for agglomeration and accelerated agglomeration rate due to the increasing surface to volume ratio [83]. Meanwhile, smaller grain size is often reported to delay the agglomeration of thin film [83], [84].

The texture of the thin film also plays a significant role in the agglomeration phenomenon. Texture is usually measured by X-ray diffraction (XRD) and electron backscattered diffraction (EBSD) techniques via the generation of pole figures [102]. A pole figure gives the statistical angular distribution of a specific (hkl) crystalline plane. In general, the typical textures in thin film include random, fiber and epitaxial textures. Random texture results in a featureless pole figure as grains are oriented randomly without any preferential orientation. Fiber texture is identified by the presence of concentric rings centered around the middle of the pole figure and, for epitaxial texture, the pole figure shows well-defined spots.

However, an additional texture was observed for silicide films, known as the axiotaxy texture [82], [103], [104]. Axiotaxy is described as an atypical off-normal fiber texture characterized by a 1-D periodicity of the matching planes [104]. With regard to the agglomeration phenomenon, there is a strong correlation between the thin film/substrate interface energy and the thin film texture [105]. In random textures, as grains are randomly oriented in all directions, the interfacial energies are higher than those of fiber and epitaxial textures.

Fiber textures present grains with planes of the same family parallel to the surface but which can rotate along the surface normal axis, thus resulting in higher interfacial energies than epitaxy grown thin films. The axiotaxy texture is considered to be an intermediate case between a random and epitaxial texture [104]. Recent experimental results from Detavernier *et al.* [97] showed that the agglomeration of NiSi is related to axiotaxy. This is further corroborated by De Keyser *et al.* [17] who observed an increase in axiotaxy component as agglomeration advances. The following sections will than describe the several already existing pathways used to improve the thermal stability of the Ni(Pt)Si thin film and mitigate the agglomeration phenomenon.

1.4.1 Surface preparation and SiCoNi pre-clean

This section aims to summarize the modification relating to the substrate instead of the deposited metal as previously discussed in the case of Ni alloys. There are two principal modifications on the substrate: presence of impurities through surface preparation and substrate nature modification such as the amorphization of the top layer of the substrate. Morphological stability of Ni(Pt)Si can be affected by the presence of impurities such as oxygen, O, and fluorine, F, at the NiSi/Si substrate interface.

These contaminations often lead to anomalous NiSi growth with leads to a high roughness at the final NiSi/Si substrate interface and to the presence of a high density of defects which results in an increase of the final NiSi layer resistance [106]. Both Wong *et al.* [107] and Tsuchiaki *et al.* [108] have reported that fluorine reduces the diffusion kinetics of

Ni, thus leading to a drastic decrease of leakage in the Si substrate. However, not many papers were published that allow to further analyze this point. The understanding of the role of F in the context of agglomeration remains to be demonstrated and elucidated.

Huang *et al.*[100] have studied the impact of surface preparation on Ni(Pt) silicide oxidation. They reported that the silicide oxidation can be reduced by using a remote plasma clean[1] (RPC) as opposed to the traditional pre-silicide HF treatment. Furthermore, Lei *et al.* [109] have shown improvement of NiSi Rs values for substrate pre-cleaned with SiCoNi™ process. Surface preparation thus constitutes another interesting point in the context of this thesis.

Another technique dealing with the modification of the substrate that has been extensively studied is the pre-amorphization by ion implantation (PAI). The objective of PAI is to create a thin layer of amorphous Si (noted "a-Si" for **a**morphous **Si**) on top of the substrate by bombarding it with ions on the sub-surface level. The improvement due to the formation of silicide thin film in an a-Si substrate may be explained by a change in crystallographic orientation of NiSi grains. Stiphout *et al.* [110] reported the reduction of axiotaxy feature in NiSi grains for NiSi thin film grown on a-Si. Fig. 26(a) illustrates the correlation between an X-ray diffraction (XRD) measurements and square resistance, Rs, of samples with and without the axiotaxial texture.

[1] Remote plasma clean (RPC) is a similar process to SiCoNi™ pre-clean that involves in the removal of native oxide on Si substrate by using a plasma during the pre-clean process.

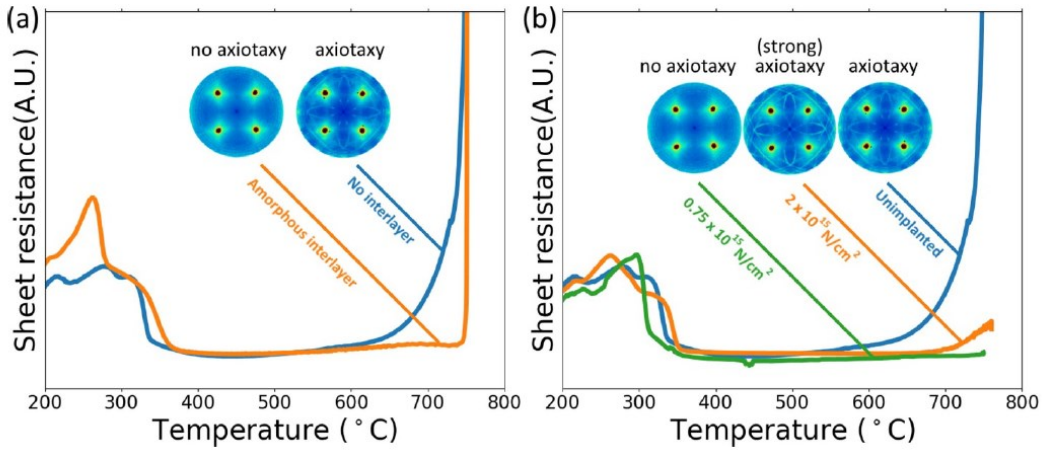


Figure 26. Sheet resistance measurements of 13 nm Ni films on Silicon-on-insulator (SOI) substrates. The samples were annealed at 1 °C/s up to 750 °C and kept at this temperature for 10 minutes. (a) A Ni film on Si(100), with and without an amorphous Si interlayer. (b) Ni films on Si(100), implanted with 20 keV/atom of nitrogen [110].

However, similar improvements were also observed for PAI with nitrogen ions but with an opposite effect on the axiotaxy texture (Fig. 26(b)). Nitrogen ions are reported to segregate at the grain boundaries and NiSi/Si substrate which hinders agglomeration kinetics of NiSi thin film. It is important to emphasize that NiSi thin film final properties may largely vary according to the implantation conditions.

The implantation parameters that allow to control the quality of NiSi thin films formed on a-Si are the choice of the implanted ions and the implantation dose, energy, orientation (tilt and twist), temperature and rate. The resulting thickness of the sub a-Si layer on the surface of crystalline Si is claimed to influence the resistivity of the obtained NiSi thin film. Lachal *et al.* [111] have demonstrated that there exists a range of a-Si for which the resistivity is the lowest as shown in Fig. 27.

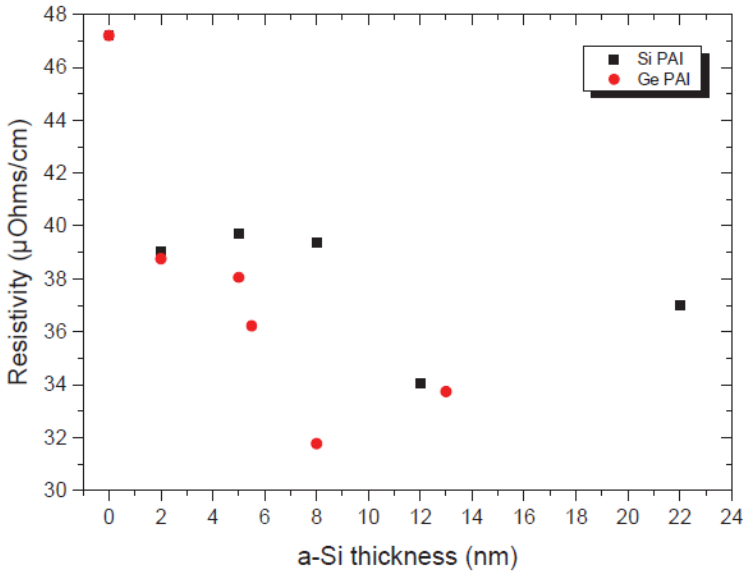


Figure 27. Evolution of the NiPt-silicide resistivity with the a-Si thickness generated for both types of PAI, Si and Ge atoms [111].

This implies that there is a need to control the thickness of a-Si through implantations parameters. Ions such as carbon and nitrogen have already demonstrated to improve the morphological stability of NiSi layers. However, the related fundamental mechanisms remain to be clarified. Additionally, in both cases, the implantation leads to an increase of the final NiSi thin film square resistance. A PAI solution that would alloy to stabilize Ni(Pt)Si layers without being detrimental in terms of layer resistivity is still yet to be found.

1.4.2 Annealing techniques

Up until this section, we have cover mostly modification relating to the intrinsic properties of both the metal layer and the substrate. Beyond these two levers to improve NiSi morphological stability, substantial research has also been carried out in order to optimize the fabrication process.

One of the interesting option is the used of laser annealing known as Dynamic Surface Annealing (DSA) instead of the conventional RTA annealing [95], [112], [113], [114]. DSA annealing is a process that has been introduced in the standard CMOS processing with the

principal objective of improving dopant activation [115]. The choice between DSA and RTA has demonstrated to affect the microstructural property of NiSi thin films [116], [117]. RTA process typically deals with annealing for a duration of tens of seconds [114], [118]. As opposed to RTA annealing, DSA annealing is often characterized by the use of laser at a very short annealing time *e.g.,* in the order of few milliseconds.

Recent results by Feautrier *et al.* [95] have demonstrated that replacing the second annealing (RTA2) in the SALICIDE process with DSA annealing results in the improvement of NiSi morphological stability. The improvement associated with the use of DSA is correlated to the reduction in the NiSi grain size and the strengthening of the epitaxial features of NiSi grains. Fig. 28 shows pole figures of NiSi(011)/(002) corresponding to two NiSi films formed by 2-steps RTA and RTA+DSA respectively on n and p-type substrates. They reported a decrease by at least 3 orders of magnitudes for the grain size when using DSA annealings (see Figs. 28 (ii) – (a) RTA, and (b) DSA annealings).

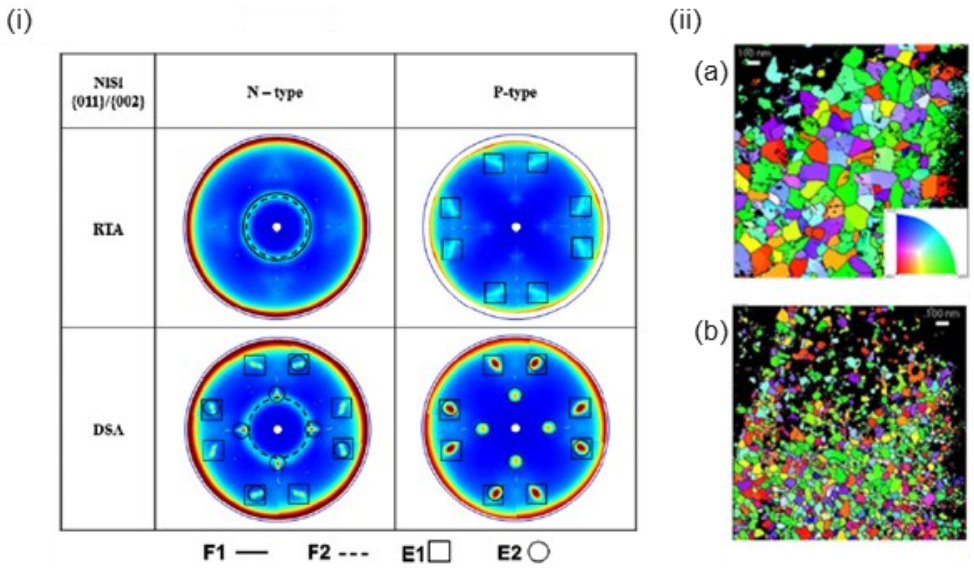


Figure 28. (i) Pole Figure of NiSi thin film with F1 and F2 representing fiber texture and E1 and E2 epitaxial one. (ii) Electron backscattered diffraction (EBSD) analysis demonstrating reduction in grain size between a) RTA and b) DSA-type annealing [95].

Another interesting process modification is the used of spike annealing. Fig. 29 shows that the used of spike annealing instead of the conventional soak annealing as RTA2 in the SALICIDE process was also reported to prevent the agglomeration of NiSi thin films [99].

Delay in the agglomeration phenomenon in this case is associated to NiSi grain size reduction [99].

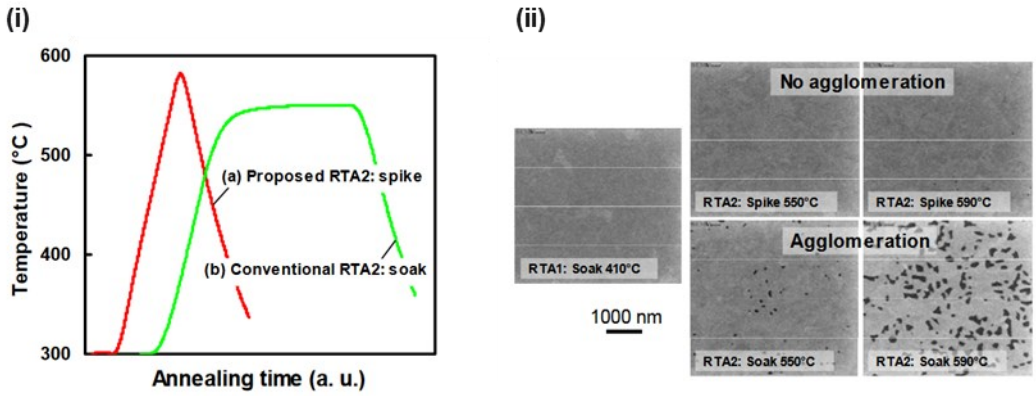


Figure 29. (i) Annealing profile of RTA2 comparison between conventional RTA2 and spike RTA2. (ii) The morphology of NiSi film for spike and soak RTA annealings at 550 and 590 °C [99].

1.5 Research axes & objectives

It has been around three decades since the introduction of Ni(Pt)Si silicide layers in the microelectronics industry. Nevertheless, despite being an interesting choice for contacts in advanced CMOS technologies *i.e.,* nodes below 65 nm, and widely used in the microelectronics industry, Ni(Pt)Si layer presents some remaining challenges relating to its formation and especially morphological instability due to the agglomeration phenomenon. Indeed, the agglomeration phenomenon of Ni(Pt)Si layers leads to the formation of holes and electrical discontinuity that are detrimental to device performances.

The latest CIS technology based on 3D-sequential process (as described in section 1.1.1.) includes the bonding of a MOS transistors fabricated on FDSOI substrate (as shown in Fig. 4) that integrated an ultra-thin Ni(Pt)Si layer, with an imager wafer. The contact between the two tiers (CMOS and pixel) is obtained through a TiSi-based contacts formed at a temperature above 600 °C, as illustrated in Fig. 30. This implies the co-integration of the two silicides in this sequential process flow

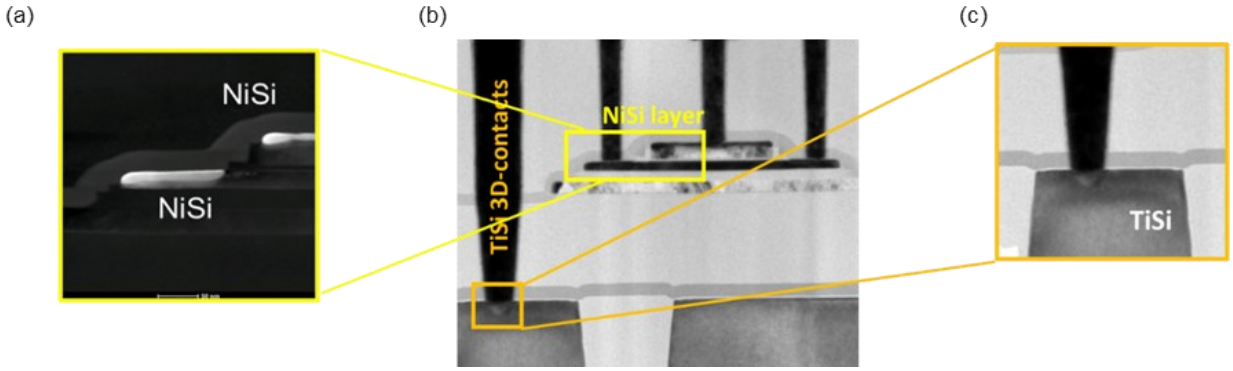


Figure 30. Co-integration of nickel silicide, Ni(Pt)Si and titanium silicide, TiSi for imager technologies. (a) TEM cross-section image of the CMOS part of the device with Ni(Pt)Si layer highlighted in yellow, (b) Schematics of the integration of silicides in CMOS on the left and in imager on the right, and (c) TEM cross-section of a part of the imager containing the TiSi layer (reproduced from [95]).

In order to form the TiSi layer at the interface of the bonded wafers, the thermal budget required to be applied is around 650 °C. Such thermal budget is already high for the Ni(Pt)Si layer as it has been reported that the Ni(Pt)Si layer begins to agglomerate at thermal budget of 550 °C [10].

Furthermore, in the development of new technologies for better speed and performance, the 28 nm FDSOI technologies have emerged as an interesting architecture. Indeed, the dimensions for the 28 nm are already challenging as it imposes constraints on the thickness of Ni(Pt)Si silicide layers. FDSOI technology dealing with the SOI substrate implies that the junction depth is shallow. This imposes a silicide thickness around 10 nm for such architecture and node (*i.e.,* ultra-thin silicide film that are prone to agglomeration).

In this context, Cavalcante *et al.* [10] have recently reported a severe yield loss in the 28 nm FDSOI devices linked to the agglomeration of the Ni(Pt)Si layer. This phenomenon is further exacerbated with decreasing line width, noted usually W, as shown in Fig. 31.

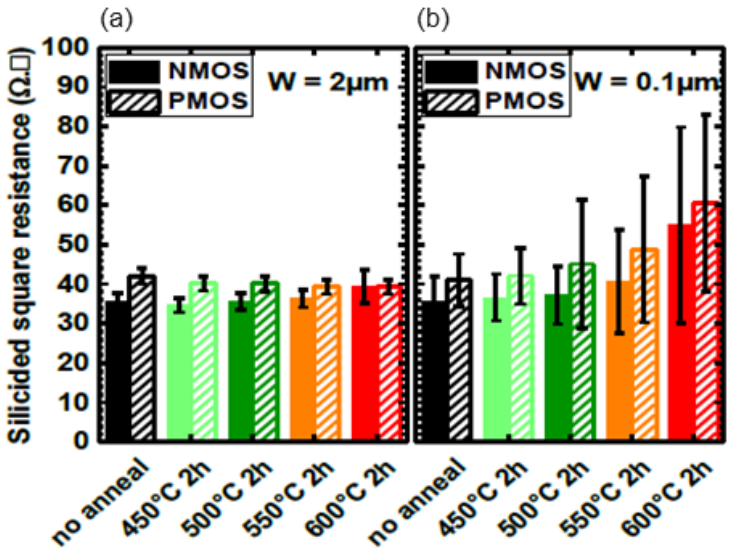


Figure 31. Square resistance[2], Rs, of the Ni(Pt)Si layer with increasing thermal budget for line width, (a) w=2 µm and (b) w=0.1 µm on the right [10].

The drastic increase in resistance observed for 550 °C is a clear indication that the Ni(Pt)Si layer is agglomerated Nonetheless, the aggravation of the agglomeration phenomenon driven by the reduction of the line width indicate that there is a downscaling

[2] *Square resistance, noted as Rs (SI unit : ohm/square) is the measure of a resistance for very thin layer of materials and express as the relation between intrinsic resistivity, ρ and thickness, t – i.e., Rs =ρ/t It is measured using a four-point probes.*

effect or more precisely in this case, a nano-scaling effect on the morphological stability of the Ni(Pt)Si layer.

When comparing experiments without any lithography patterns *i.e.,* blanket wafers, this agglomeration thermal budget appears to be lower. This underlines the preponderance of the potential influence of the confinement on the agglomeration of the silicide film.

Motivated by these challenges and questions, the principal objective of this Ph. D thesis is therefore to further deepen the understanding of the mechanisms involved in the agglomeration process of ultra-thin Ni(Pt)Si layers. This research can be divided into three principal axes:

1. Identification of the influence of additional processes on the agglomeration of Ni(Pt)Si. This includes different types of annealing, PAI, and surface preparation such as SiCoNi.
2. Understanding the influence of thickness reduction and Pt behavior during agglomeration.
3. Evaluation of the impact of structures confinement on the agglomeration of Ni(Pt)Si thin films.

Since Ni(Pt)Si has become the standard material for contacts in the state-of-the-art CMOS technology, overcoming morphological degradation far outweighs the phase transition ($NiSi_2$ formation) problem in the context of this Ph.D. thesis.

1.6 Chapter conclusions

For the development of the advanced 3D-sequential imager technologies, platinum-alloyed nickel monosilicide, Ni(Pt)Si is implemented as the silicide layer for the contacts on the three terminals of the CMOS transistors, formed on FDSOI substrate. Ni(Pt)Si layer is indeed the most suitable candidate for this technology thanks to the low formation temperature and especially the low silicon consumption as this technology deals with SOI substrate presenting a shallow junction. The SALICIDE process involved in the fabrication of this silicide layer deals with two surface preparations (HF and SiCoNi) pre-clean, metallic deposition, RTA1 at 230 °C/20 s, selective etching and a second annealing RTA2 at 390 °C/30 s.

The silicidation of the 28 nm FDSOI CMOS is particularly difficult because the Ni(Pt)Si layer is highly sensitive to the agglomeration phenomenon which degrades its morphology and drastically impacts technological performance and yield. At the current stage, the Ni is alloyed with 10 at. % of Pt which have allowed to delay the phase transition into $NiSi_2$ and improve the morphological stability. However, solutions beyond the addition of Pt is required as recent results from Cavalcante *et al.* demonstrated agglomeration-associated degradation at around 550 °C. This results also shows that the co-integration of Ni(Pt)Si layer with the TiSi contacts, required for imager is very challenging since the formation temperature of the TiSi induces the agglomeration of the Ni(Pt)Si layers. Moreover, the order of the formation of these silicide layers cannot be interchanged since TiSi follows the salicide last schemes, meaning after contact is patterned. Furthermore, the reduction of the dimensions also aggravated the agglomeration of the Ni(Pt)Si. This demonstrates the preponderance of the reduction of the dimension in the context of the study around the agglomeration of the Ni(Pt)Si layer.

Founded by this literature review, we proposed in the frame of this research work, a study on the influence of the nano-sizing on ultra-thin Ni(Pt)Si films formation and degradation for applications to 28 nm-node technologies and below. Our main objectives are therefore to provide a more thorough understanding of the mechanisms of agglomeration of the Ni(Pt)Si layer through study of the influence of additional processes

(surface preparation, types of annealings etc.) and of the formation and stability of contacts in confined structures with varying dimensions.

Chapter 2: Research methodology and characterizations techniques

Chapter contents

2.1 Sample fabrication techniques 76
2.1.1 SiCoNi pre-clean processes 76
2.1.2 Metal deposition in Endura chambers 77
2.1.3 Thermal treatments 78
2.1.4 Selective etching 81
2.2 Characterization techniques 82
2.2.1 Four-point probe measurements for sheet resistance, Rs 82
2.2.2 Ellipsometry for thickness determination 84
2.2.3 X-ray diffraction (XRD) 85
2.2.4 Out-of-plane X-ray diffraction 87
2.2.5 In-plane X-ray diffraction 88
2.2.6 Texture analyses using pole figures 90
2.2.7 Scanning electron microscopy (SEM) 92
2.2.7.1 Tilted-SEM & High-resolution SEM 94
2.2.8 Electron backscattered diffraction (EBSD) 94
2.2.8.1 Orientation maps 95
2.2.9 Transmission electron microscopy (TEM) 96
2.2.9.1 TEM-EDX for chemical composition 97
2.2.9.2 TEM-EELS 97
2.3 Chapter conclusions 97

Foreword

The samples used in the framework of this Ph. D. thesis are nickel-platinum (10 at. %) monosilicide film, Ni(Pt)Si, formed on 300 mm silicon, Si (100) wafers (patterned and non-patterned). These samples are fabricated in the clean room of STMicroelectronics at Crolles and CEA-Leti 300 mm platform at Grenoble implies good sample quality and low contaminations.

The fabrication of these samples deals with several processes including surface preparation techniques, metal sputtering, and different heat treatments. Details regarding these processes are presented in the first section of this chapter. The rest of the chapter is dedicated to the different characterization techniques used.

The fabrication steps will be elaborated in deeper details as function of the different studies conducted in this work.

2.1 Sample fabrication techniques

2.1.1 SiCoNi pre-clean processes

As illustrated in the previous chapter, the elaboration process of Ni(Pt)Si films *i.e.,* the SALICIDE process begins with a wet clean followed by the SiCoNi pre-clean step, which is performed in-situ, inside the same equipment of depositions. The objective of the SiCoNi pre-clean is to remove native oxide from the surface of the silicon substrate before metal deposition, without air-break. The introduction of SiCoNi pre-clean was demonstrated to be highly efficient in minimizing the loss of Si and Ni while reducing several process defects such as spiking and piping defects [119].

The working principle of the SiCoNi process relies on the chemical etching by remote plasma of SiO_2 and SiO_x. This implies that plasma is not in direct contact with wafer surface. However, the plasma participates in the generation of the etching precursor, named ammonium fluoride, NH_4F [115], [120].

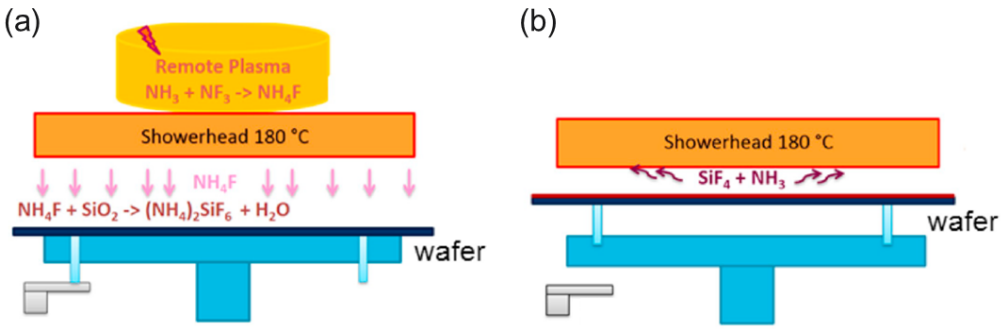


Figure 32. Schematics of the SiCoNi process illustrating (a) the generation of ammonium fluoride, NH_4F, by remote plasma and the subsequent reaction with SiO_2 to form fluoride salts. (b) Sublimation process of the $(NH_4)_2SiF_6$ salts [121].

As shown in Figure 32, the SiCoNi process involves in three main steps:

(i) The remote plasma generates etching precursors. The corresponding reaction is given by:

$$NH_3 + NF_3 \rightarrow NH_4F + NH_4F.HF \qquad \textbf{Equation 9}$$

(ii) Etching precursors pass through the showerhead (Fig. 32(a)) and react with the native oxide on Si substrates resulting in the following reaction:

$$\mathbf{2}\boldsymbol{NH_4F} + \mathbf{4HF} + \boldsymbol{SiO_2} \rightarrow (\boldsymbol{NH_4})_2\mathbf{Si}\boldsymbol{F_6} + \boldsymbol{H_2O} \qquad \textbf{Equation 10}$$

This leads to the creation of the $(NH_4)_2SiF_6$ salts on the wafer.

(iii) The next step (Fig. 32(b)) deals with the removal of these salts through sublimation process. This is achieved by raising the wafer near the heated showerhead (180 °C). The surface temperature of the wafer is estimated to be 100 °C. The sublimation of the $(NH_4)_2SiF_6$ salt gives the following reaction leaving the Si surface free of oxide:

$$(\boldsymbol{NH_4})_2\mathbf{Si}\boldsymbol{F_6} \rightarrow \mathbf{Si}\boldsymbol{F_2}\ (\mathbf{gas}) + \boldsymbol{NH_3}\ (\boldsymbol{gas}) \qquad \textbf{Equation 11}$$

2.1.2 Metal deposition in Endura chambers

Under a secondary vacuum, the subsequent steps after the cleaning of the substrate surface are the deposition of NiPt layer followed by the deposition of TiN capping layer. The NiPt layer is deposited through physical vapor deposition (PVD) technique. Next, the TiN capping layer is deposited on top of the NiPt layer to prevent metal oxide formation.

As depicted in Fig. 33, the SiCoNi pre-clean chamber is integrated inside the same equipment of metal deposition chambers.

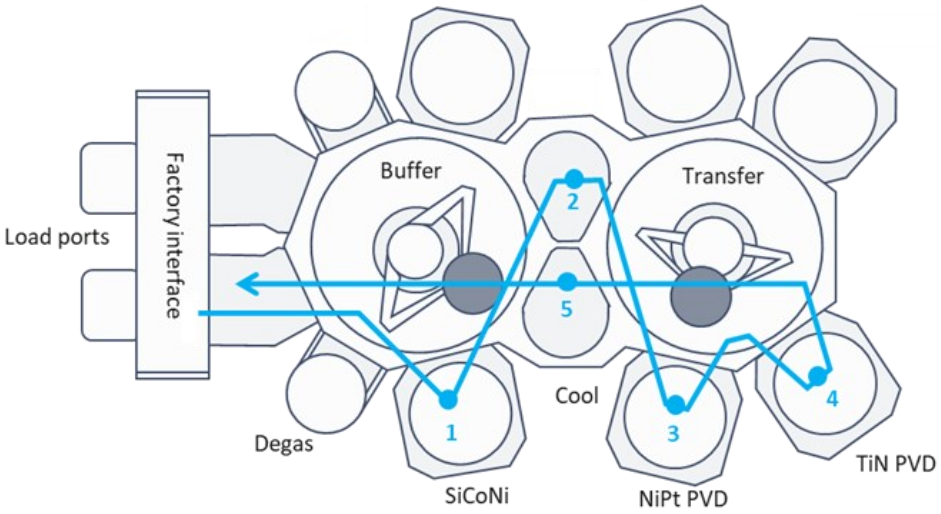


Figure 33. Schematics of the Endura equipment by *Applied Materials* illustrating the process sequence for the deposition of NiPt film (denoted by blue arrow).

The process sequence of metal deposition within this equipment is denoted by the blue arrow and can be summarized in five primary steps: SiCoNi pre-clean as previously described, wafer cooling, NiPt deposition by PVD, TiN deposition by PVD, and another wafer cooling before exiting the equipment.

2.1.3 Thermal treatments

The thermal treatment used for contact silicidation is usually a rapid thermal annealing, RTA and/or dynamic scan annealing, DSA. These thermal annealing processes are performed on different equipment, presenting specificities on their heating source, dwelling duration, and conduction mode. In all cases, the annealings are conducted under N_2 atmosphere, or vacuum environments to prevent sample oxidation during experiments.

Firstly, for the RTA-type annealing, the formation of silicides via RTA1 and RTA2 are performed within the equipment "*Radiance*", by *Applied Materials*. The heating sources are halogen lamps in a honeycomb structure as illustrated by Fig. 34(a).

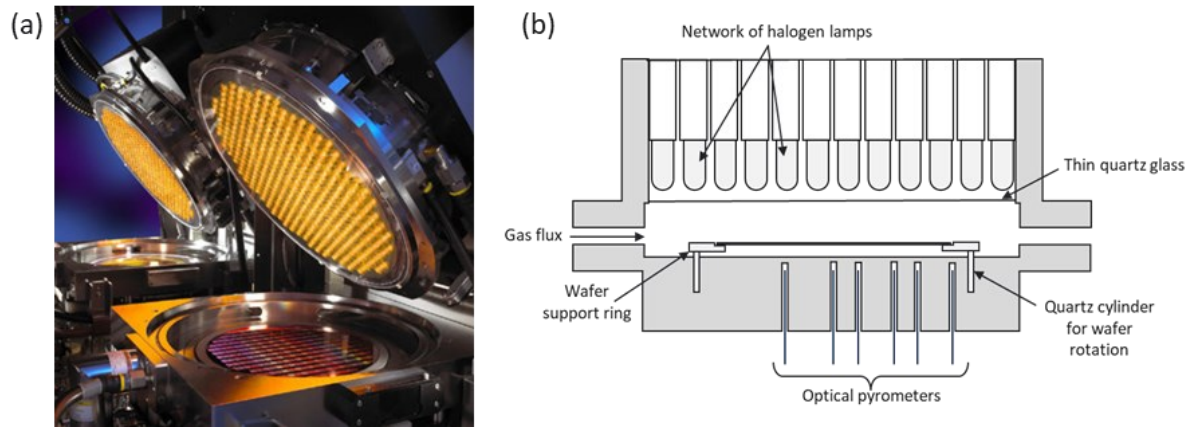


Figure 34. (a) RTA chamber for silicidation of *Radiance* by *Applied Materials* [122]. (b) Cross-sectional schematics of RTA chamber.

For the formation of the nickel-platinum monosilicide, Ni(Pt)Si, as previously described in section 1.2.3, the temperatures are comprised between 230 °C and 390 °C. In the typical formation scheme, the heating ramp (°C/s) is set between 2 and 10 °C/s with a cooling ramp of 15 °C/s. In order to regulate the temperature during the annealing, several pyrometers are placed below the wafer and are distributed along the radius of the wafer as shown in Fig. 34(b).

Another alternative to form the low resistivity phase is the use of milliseconds (ms) laser annealing, such as the DSA technique. In such a case, the RTA2 in the standard SALICIDE process is replaced by DSA2, allowing annealings at higher temperatures for a very short dwell time (*e.g., in the order of milliseconds*). In the case of Ni(Pt)Si, thermal budget is set to 815 °C with a dwell time of 0.25 ms. Table 3 summarizes the principal characteristics of the laser used for DSA process.

Table 3. Principal characteristics of the millisecond (ms) laser in Vantage Astra equipment based on STMicroelectronics internal data.

Wavelength, λ (nm)	Beam dimensions (mm x µm)	Adjacent beams overlap (%)	Scan speed (mm/s)	Surface emissivity, ε	Power (W)
810	13.5-75	50	0-300	0.88	2.2

The DSA annealing is performed within the chamber named *"Vantage Astra"*, by *Applied Materials*. The heating source is a monochromatic laser instead of halogen lamps as seen in the RTA equipment and the pyrometer is integrated in this light source (Fig. 35). The wafer is also heated to 250 °C on the backside in order to reduce the thermal shock of the wafer thus reducing the risk of wafer breakage.

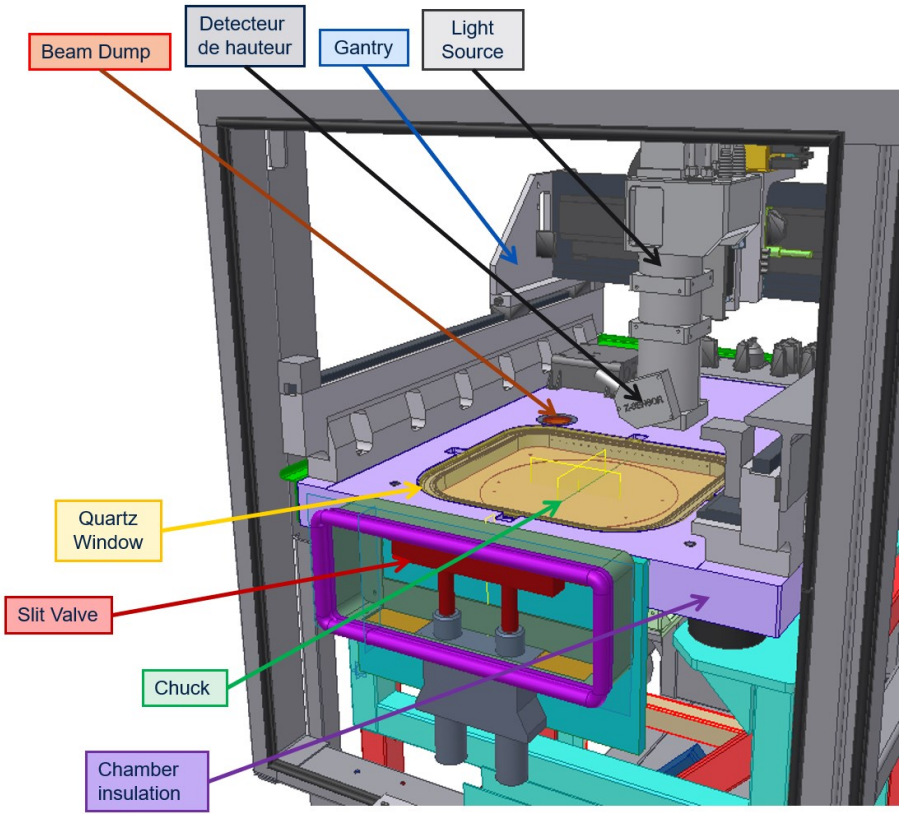


Figure 35. 3D schematics of the "Vantage Astra" chamber [123].

One of the particularities of the DSA annealing is that the wafer is annealed by the laser beam via multiple scans. One laser scan constitutes what is called the "laser strip" and illustrated in Fig. 35. This step is repeated several times on the wafer until the wafer is fully covered by the laser strips. The number of scans depends on the dimensions of the laser strip used during the annealing. For a typical 300 mm, the number of laser strips can vary between 25 to 55 strips with an overlap of 50 % between each adjacent strip.

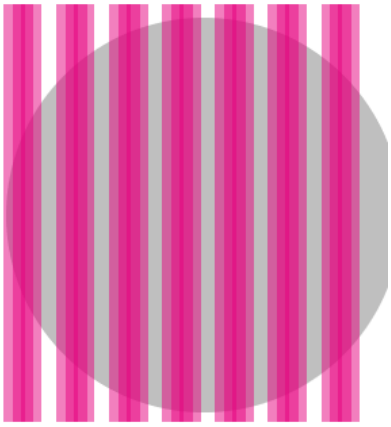


Figure 36. Schematic of "laser strips" for uncompleted coverage on a wafer during the DSA annealing.

2.1.4 Selective etching

Within the SALICIDE process, the selective etching (SE), is performed after the first annealing, RTA1 and before the second annealing, RTA2. The role of the SE is to remove the excess unreacted NiPt metal and the TiN capping layer leaving behind the silicide layer formed during the RTA1.

This selective chemical wet etching is achieved by mixing a ratio of sulfuric acid, H_2SO_4 and hydrogen peroxide, H_2O_2 (called the Piranha etch *or* sulfuric peroxide mix, SPM) [124]. Following this, another mixture is used consisting of ammonium hydroxide, NH_4OH and H_2O_2 (called SC1 for standard-clean solution).

2.2 Characterization techniques

Several characterization techniques used in the framework of this Ph. D thesis are described in this section. This includes four-point probe Rs measurements, ellipsometry, electron microscopy techniques (EBSD, SEM, and TEM), and X-ray diffraction techniques.

2.2.1 Four-point probe measurements for sheet resistance, Rs

Sheet resistance, noted Rs, is an electrical quantification of the resistance of a thin square sheet of materials measured in ohm per square (Ω/sq) as presented in Fig. 37.

The configuration of the 4-point probes measurement is illustrated in Figure 37.

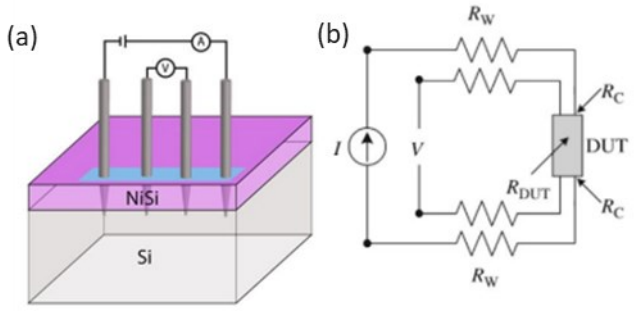


Figure 37. (a) 3D schematics of the typical setup of the four-point probe measurement. (b) Electrical representation of the contribution of the different resistances [125].

In fact, in the case of thin films, the classical resistance measurement using two probes, often used for bulk materials, is no longer adapted as the magnitude of resistance of the thin film is in the range of the resistance of the probe, noted R_W in the Fig. 37(b) [125].

A more precise method of measurement for thin film is developed known as four-point probe measurements. Since the tension and current are measured separately, this allows to completely remove the contribution of any parasitic resistances such as the influence from the cable, thus the non-negligible contribution of $R_{w.}$

The high intrinsic impedance of the voltmeter ensures that the current mainly passes in the sample and therefore the values of voltage measured is purely related to the sample, and not induced by the connecting cables. In order to obtain the value of sheet resistance,

one might consider a square sheet with a thickness t, where the length, L and width, W are equal. If the area, A, passed by the current, is defined by:

$$A = L.t \quad \textbf{Equation 12}$$

with t the thickness of the film and L the width, thus the expression of the sheet resistance, R_s, is deduced as follows:

$$R = \frac{\rho.L}{A} = \frac{\rho.L}{L.t} \quad \textbf{Equation 13}$$

$$R_s = \rho/t \quad \textbf{Equation 14}$$

With ρ the intrinsic resistivity of the film. Equation 14 holds true for a continuous single layer thin film. At STMicroelectronics Crolles, the principal characteristics of the Rs equipment are summarized in Table 4.

Table 4. Specifications of the probe used for the Rs measurements at STMicroelectronics.

Probe materials	Spacing between probe (mm)	Probe radius (µm)	Applied weight (g)
Tungsten	1	102 -203	0.1 - 100

The probe spacing refers to the distance between each probe, the radius of each probe is defined in µm. Nevertheless, in the case of severely agglomerated Ni(Pt)Si layers (Fig. 38), where inverse dewetting took place, the obtained resistance value is considered as an apparent value since the current does not only passes through the Ni(Pt)Si layer but also in the Si substrate.

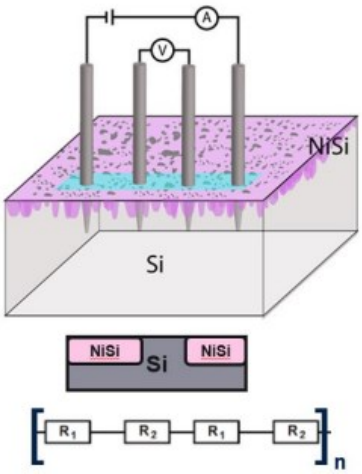


Figure 38. Apparent resistance with resistance in series model where R1 represents the resistance of Si and R2 of Ni(Pt)Si layer after the agglomeration of Ni(Pt)Si thin film.

For a 300 mm wafer, the Rs measurements is performed on equally distributed sites on the wafer. The density of the measuring sites varies between 17 sites to 121 sites, and this enables to verify the Rs variation over the entire wafer.

2.2.2 Ellipsometry for thickness determination

Ellipsometry is a non-destructive optical technique commonly used to obtain the thickness of thin films, which are transparent in a large domain of wavelength. In order to perform the measurement, an incident light beam is polarized and projected to the sample surface leading the generation of the reflected light beam that is elliptically polarized. The schematics of the measurement setup is illustrated in Fig. 39(a).

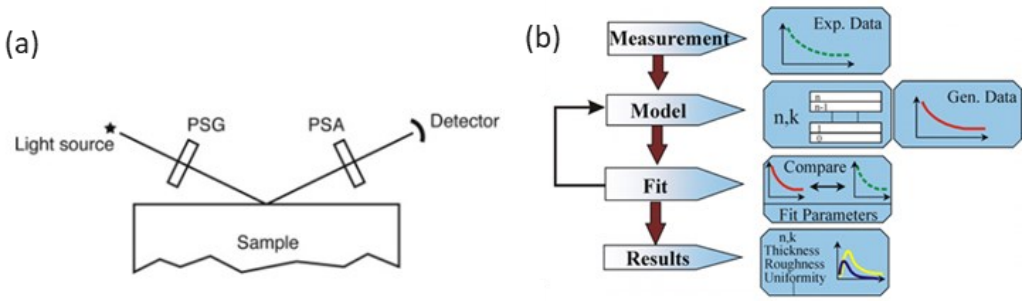


Figure 39. (a) Schematics of the working principle of ellipsometry [126]. (b) Data processing for thickness determination by comparison with mathematical model [127].

An optical instrument is used to monitor the polarization state of the reflected beam including the phase change and ratio of amplitude of incident/reflected beam [128]. Analysis of these data through fitting with mathematical models ensure the quality of the thickness measurement as can be seen in Fig. 39(b).

This technique allows the determination of thickness between 0.01 nm and a few µm. However, depending on the microstructural and optical properties of different materials, this technique may be less suitable. This can include materials that fully absorb incident light resulting in no reflected beam that is almost the case for metal film. At STMicroelectronics, this technique is calibrated by the X-ray reflectivity (XRR) technique to ensure the accuracy of thickness measurement.

2.2.3 X-ray diffraction (XRD)

X-ray diffraction (XRD) characterization is a technique relying on the Bragg diffraction conditions. The XRD technique provides several information about the material phases, grain size, crystal structure, crystal defects and material strains.

The working principle of the XRD is illustrated in Fig. 40 depicting two primary conditions leading to the diffraction of X-rays from a crystalline material: (i) Specular reflection of the X-rays beam on the crystallographic planes and (ii) X-rays wavelength in the order of magnitude of the interatomic distance.

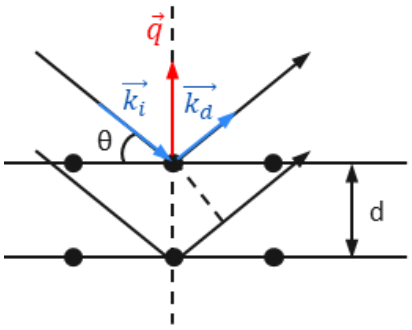


Figure 40. Schematics of x-ray diffraction concept.

This means that for a given crystal with an interplanar spacing of d, irradiated by incident X-ray beam of wavelength λ, coherent scattering results in diffracted intensity (constructive interference) at specific incident angles, θ satisfying the Bragg's law:

$$\boldsymbol{n\lambda = 2\, d_{hkl} * \sin(\theta)} \qquad \textbf{Equation 15}$$

With n, an integer representing the order of diffraction. The hkl refers to the miller indices of the crystallographic plane. A more general expression for XRD conditions is

$$\boldsymbol{\vec{q} = \vec{G}} \qquad \textbf{Equation 16}$$

Where $\vec{q}$ is the scattering vector and $\boldsymbol{\vec{G}}$ is the vector in the reciprocal space corresponding to the hkl plane.

During the scattering process, the scattering vector, $\vec{q}$ is defined as function of the incident wave vector, $\overrightarrow{k_i}$ and the diffracted wave vector, $\overrightarrow{k_d}$. The scattering vector, $\vec{q}$ is illustrated in Fig. 40, and given by the following relation:

$$\boldsymbol{\vec{q} = \overrightarrow{k_d} - \overrightarrow{k_i}} \qquad \textbf{Equation 17}$$

With $q = (4\pi/\lambda)sin(\theta)$.

Where the wave vector, $\vec{k}$ of the X-ray beam is expressed as:

$$\boldsymbol{\vec{k} = 2\pi/\lambda} \qquad \textbf{Equation 18}$$

2.2.4 Out-of-plane X-ray diffraction

As shown in Fig. 41, the experimental set-up of a conventional diffractometer is constituted of an X-ray source tilted at the angle ω (also θ) with respect to the sample surface, a sample mounted on a sample holder (*or* a goniometer), and a detector at twice the angle of θ with respect to the incident beam [129].

This geometry constitutes the conventional scan where the scan is performed about the normal of the sample surface by either rotating both the source and detector in opposite directions for a fixed sample (θ/θ scan), or by rotating the detector at twice the speed of the sample rotation for a fixed source(θ/2θ scan). This implies that the scattering vector, $\vec{q}$ is always perpendicular to the sample surface (see Fig. 41(a)).

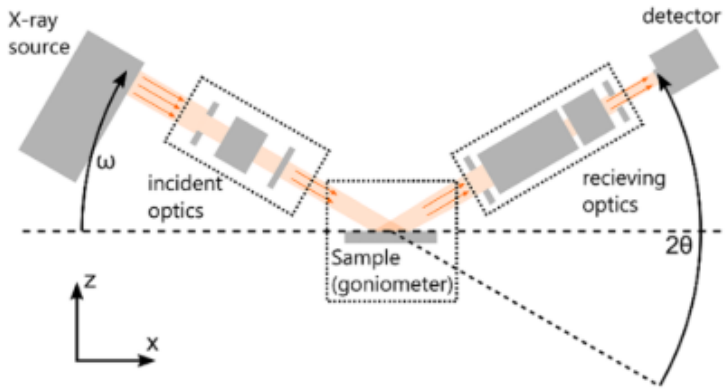


Figure 41. XRD θ-2θ geometry experimental setup [130].

In the θ-θ geometry, the XRD scan will generate diffraction patterns, called diffractograms resulting from planes that are parallel to the surface as depicted in Fig 42(a). This geometry is often applied to powder diffraction experiments coupled with the Bragg-Brentano optics providing high intensity divergent incident beam.

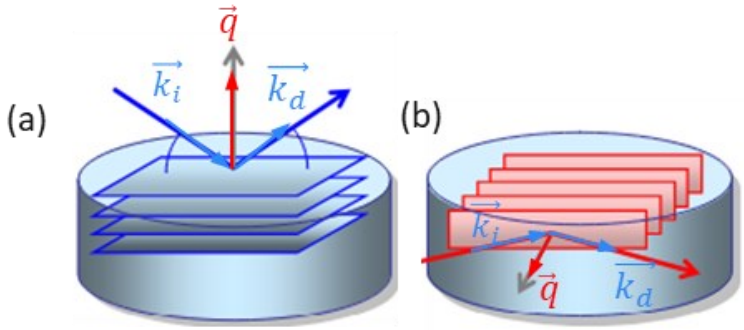


Figure 42. Schematics of the (a) out-of-plane XRD scan and (b) in-plane XRD scan adapted from [131].

For random polycrystalline powder (or thin film), all the XRD peaks belonging to the phase will appear. In the case of highly textured thin film, the θ-θ scan may not provide enough information regarding the overall thin film texture. Some complementary information such as in-plane diffraction patterns or pole figures are necessary to complete the analysis.

For example, for the fiber texture described previously, presenting mono-axial out-of-plane orientation and random in-plane orientation, the θ-2θ scan is not enough. Moreover, signal from the substrate often presents high diffraction intensity and may dominate over the peaks resulting from the thin film as penetration depth of the X-ray beam is in the range of 1 to 100 µm [130]. This constraint is relaxed with in-plane measurement where the beam is centered on the layer that is being analyzed.

2.2.5 In-plane X-ray diffraction

In the in-plane XRD configuration, both incident and reflected X-ray beams are nearly parallel to the sample surface with a penetration depth of around 100 nm from the surface.

Fig. 43 depicts experimental setup of the in-plane XRD showing a grazing incident angle, ω with respect to the sample surface.

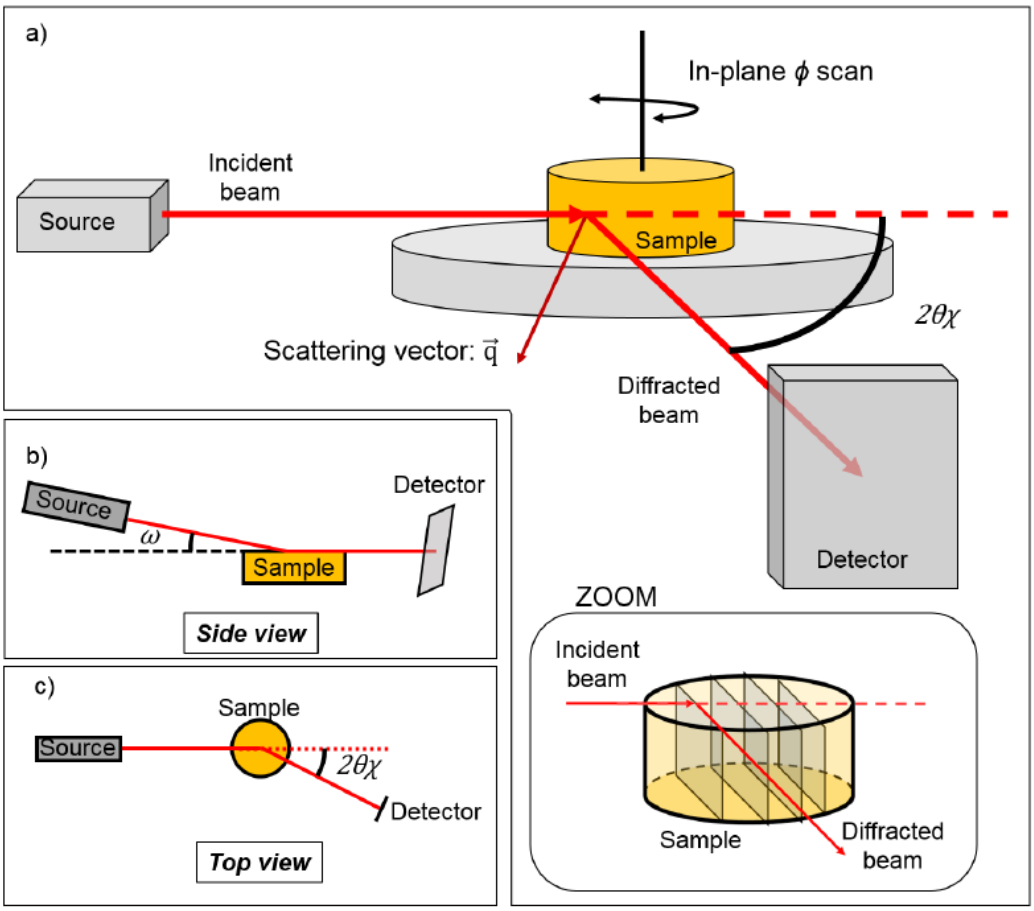


Figure 43. (a) Schematical representation of the setup of in-plane XRD with (b) side view of the setup, (c) top view and inset showing planes perpendicular to sample surface, from [132].

For in-plane XRD, the incident angle, ω is set to < 1°. This substantially minimize the diffraction peaks from the substrate.

Nevertheless, in this configuration, the resulting XRD patterns originate from planes that are normal to the sample surface as shown in Fig. 42(b). This implies that the scattering vector, $\vec{q}$ is parallel to the sample surface.

The in-plane XRD patterns are collected from a sample with a rotation of φ, using a detector positioned at $2\theta_{\chi}$ angle. Such characterization is typically done on a diffractometer equipped with a four-axis goniometer giving access to additional degrees of freedom ($\chi, 2\theta, \omega,$ and φ) illustrated in Fig. 44.

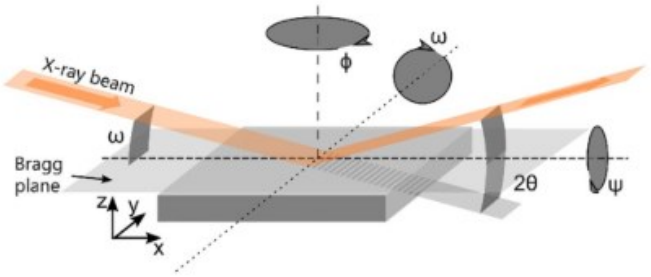


Figure 44. Schematics of a sample with four degrees of freedom in the case where four-axis goniometer is used during XRD scan [130].

Thus, complete reconstruction of a pole figure can be performed from the diffraction patterns collected using the four-axis diffractometer.

2.2.6 Texture analyses using pole figures

Polycrystalline materials consisting of numerous grains with specific orientations often present a *crystallographic texture*. The texture describes the distribution of the orientation of the grains for a given material.

The analysis of the crystallographic texture can be achieved through the extraction pole figure typically from EBSD and X-ray diffraction (XRD) measurements [77], [97], [103], [133]. A pole figure is a visual representation of the distribution of the grain orientations. The construction of the pole figure can be achieved by stereographic projection of the diffracted intensity of a given *hkl* plane. As a result, the distribution of the orientation of a family of planes can be represented and this allows texture evaluation.

For example, in the case where the *majority of grains* composing a material share a similar axis normal to the sample surface, the rotation of these grains along the normal axis will result in stereographic projections represented by the concentric rings. This particular texture is named fiber texture and is illustrated in Fig. 45.

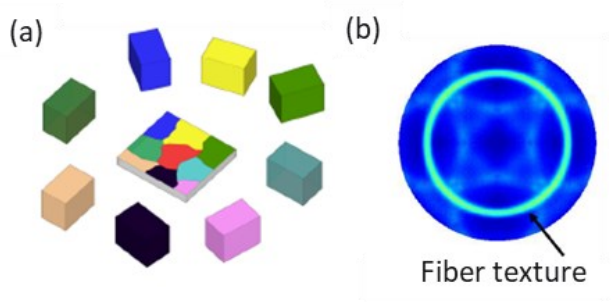


Figure 45. (a) Schematics of a polycrystalline material with grains rotating along the axis normal to the sample surface and (b) the corresponding pole figure showing a concentric ring [133].

Texture analysis allows to assess the preferential orientations of a material. Generally, preferential orientations result in materials with anisotropic properties. In addition to the previously described fiber texture, three other textures are also typically observed in thin film studies [77], [97], [133] namely random, axiotaxy, and epitaxy textures.

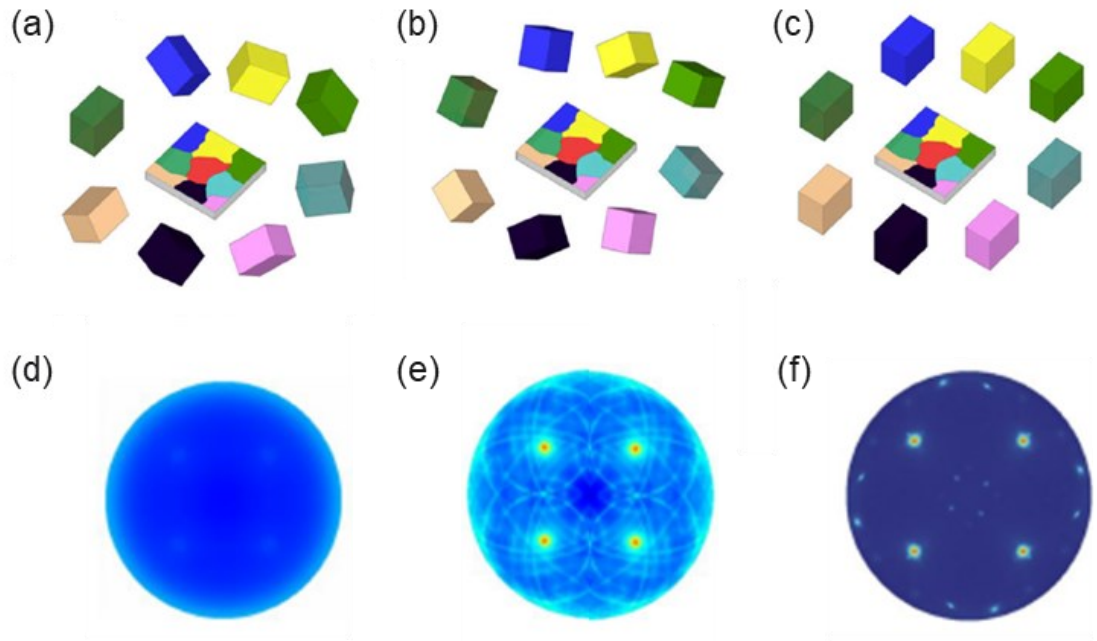


Figure 46. Schematics of polycrystalline materials with grains showing the grains orientations in top row for (a) random texture, (b) axiotaxy texture, (c) epitaxy texture, and their corresponding pole figure in bottom row (d), (e), and (f) respectively [17], [133].

As shown in Fig. 46(d), a random texture is characterized by a featureless pole figure since grains are randomly oriented and each grain orientation appears with equal possibility. In the case of an epitaxial texture, the presence of well-defined spots can be seen in the pole

figure as illustrated in Fig. 46(e). The epitaxial alignment results in 2D periodic film-substrate interface, and thus, consequently have lowest interfacial energy. This texture is typically observed for crystals with interplanar spacing closer to that of the substrates *e.g.,* $NiSi_2$ film with the Si(111) substrate [134].

Next, as previously stated in chapter 1, an additional texture was observed for the silicide films and was termed “axiotaxy”, proposed by Detavernier *et al.* [104]. The axiotaxy texture exhibits segments of rings that are not concentric and intersect with each other. This texture is described as an off-normal fiber-like texture [104]. This means that the fiber axis in the case of the axiotaxy texture is not parallel to the axis normal to the sample surface but instead is aligned with a specific orientation of the substrate, thus the name “off normal”. Moreover, this kind of texture results in a one-dimensional (1D) periodic alignment of the silicide and Si substrate interface [104]. As a comparison to the previous textures, the axiotaxy presenting the 1D periodicity alignment can be considered as an intermediate state, in terms of interfacial energy, between the random texture (high interface energy) and epitaxial texture (lowest interface energy due to 2D periodicity).

2.2.7 Scanning electron microscopy (SEM)

Scanning electron microscopy (SEM) is one of the characterization techniques that relies on the interactions between electrons and matter. This results in several types of signals such as the secondary electrons (SE) and backscattered electrons (BSE) which are the primary interactions for SEM technique as schematized in Fig. 47.

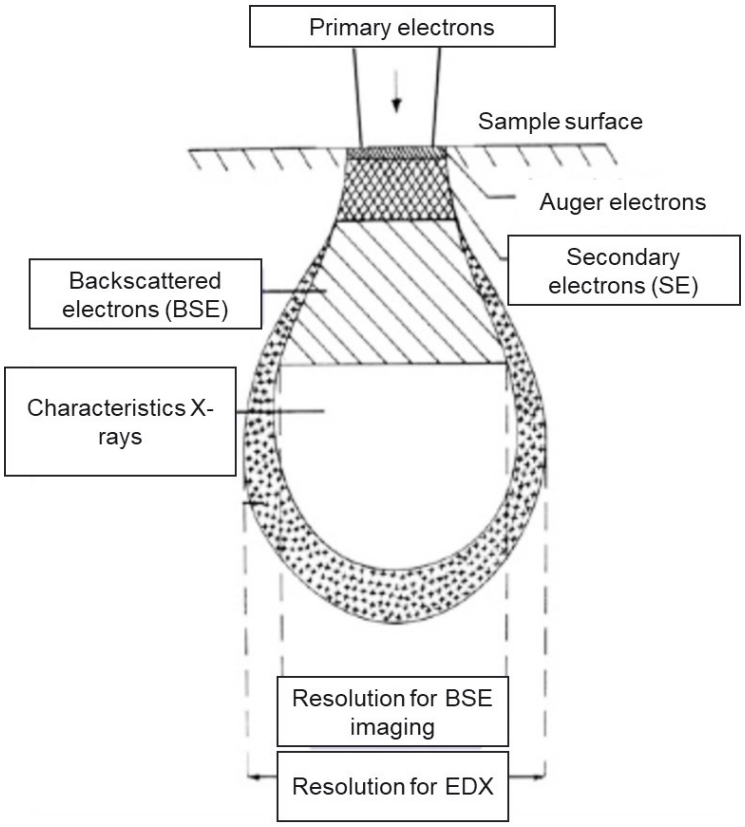


Figure 47. Interactions between electrons and matter including backscattered electrons (BSE), secondary electrons (SE), Auger electrons adapted from [135]

An electron gun is used to generate free electrons which are then accelerated in the chamber body to energies in the range of 2-40 keV before reaching the sample surface. When high energy electrons hit the sample, electron-matter interaction signals are generated, which can be monitored. For SEM application, the typical signals that are used in imaging come from BSE and SE interactions

BSE are sensitive to the atomic number of materials and originates from the elastic collisions of electrons with atoms in the deeper regions of the sample. As a result, BSE imaging is used to determine the composition of the materials.

Nevertheless, an SE detector is also used in the SEM equipment. Unlike BSE, SE originates from the surface of the sample and results from inelastic collisions of electrons with the atom. SE imaging is used for evaluation of surface topography.

2.2.7.1 Tilted-SEM & High-resolution SEM

At STMicroelectronics, the SEM equipment, SEMVision G5 by Applied Materials is adapted to receive an entire 300 mm wafer for inspection. Moreover, the electron beam can be tilted between 15 and 45 ° in order to improve the image definition by increasing topography contrast for tilted angles. Tilted-SEM in the case of the Ni(Pt)Si thin film study provides crucial information on surface roughness and improve definition of grain boundaries.

Another variant of the SEM technique is the high-resolution SEM imaging, HRSEM (also known as field emission SEM, or FESEM). The working principle of the HRSEM is similar to the conventional SEM. In that case, the electron beam is generated at higher intensity with a very small beam spot size allowing higher resolution imaging. At CP2M center in Marseille, the SEM equipment is a GeminiSEM 500 by Zeiss which is a type of FESEM allowing to produce high resolution SEM images.

2.2.8 Electron backscattered diffraction (EBSD)

Electron backscattered diffraction (EBSD) is a characterization method based on the SEM technique. Inspection of the sample using EBSD technique is often performed to acquire information regarding the crystallographic properties of the sample such as the crystal structures, orientation distribution, and texture through pole figures analyses.

In order to perform an EBSD measurement, the sample is tilted within the SEM equipment to a specific angle, typically 70 °, to maximize the intensity of the diffracted signal as shown in Fig. 48(a).

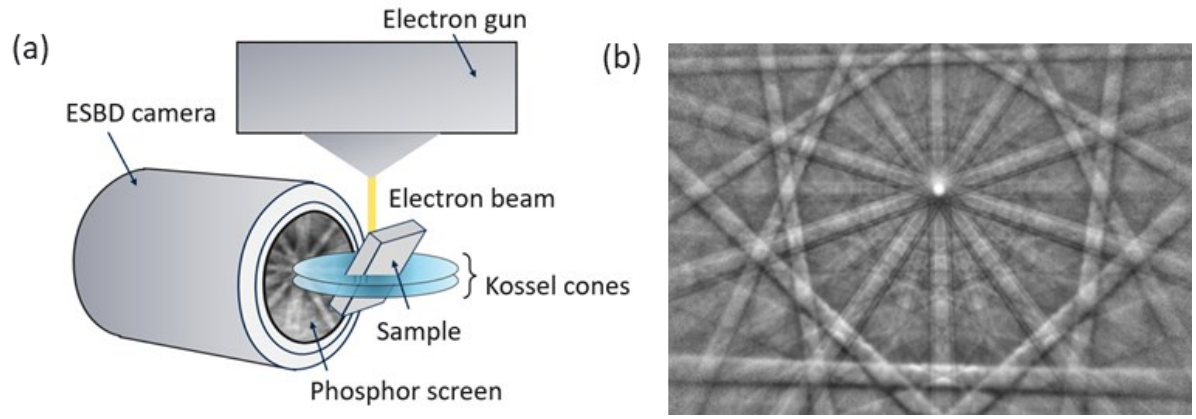


Figure 48. (a) Representation of the EBSD setup with electron beam hitting the surface of the tilted sample. (b) Example of Kikuchi bands formed from the intersection of wide-angle Kossel cones and phosphor screen [136].

As electrons reach the sample surface, they are scattered in all directions and detected using an EBSD detector consisting of electron-sensitive screen, such as phosphor and scintillator equipped with a digital camera.

The scattering of electrons in all directions results in some electrons satisfying the Bragg equation. The diffracted electrons formed diffraction cones, known as Kossel cones due to the cylindrical symmetry of the Bragg reflection condition. The intersection of the Kossel cones with the electron-sensitive screen will generate Kikuchi bands with specific geometries (band size and directions) and intensities as shown in Fig. 48(b) [136]. A Kikuchi band is constituted of a pair of Kikuchi lines and corresponds to a specific hkl plane, thus the complete EBSD pattern containing the Kikuchi bands allows the obtaining of orientation maps.

2.2.8.1 Orientation maps

EBSD orientation maps are obtained by indexing the ESBD patterns (Kikuchi bands). This orientation map provides information of the specific orientation of individual grains and their spatial distribution within the sampling area. As illustrated in Fig. 49, the orientation maps are color-coded, and each color is attributed to a specific crystal orientation. The reference color code indicator is given as a function of the material lattice.

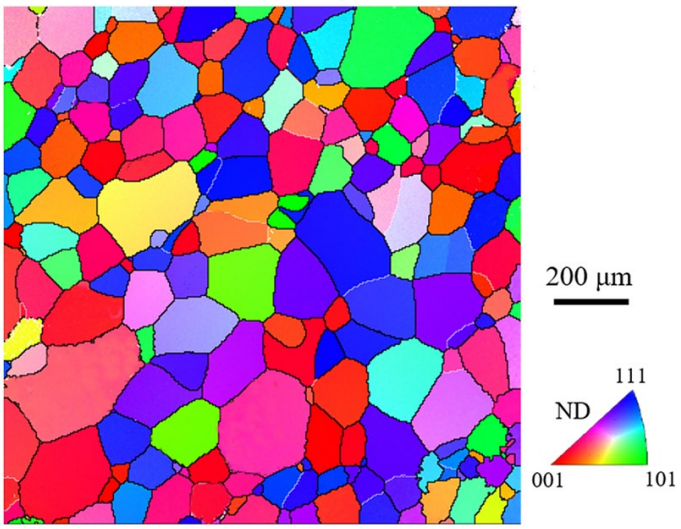


Figure 49. Example of an electron backscatter diffraction (EBSD) map of Ti-Mo alloy solution treated at 850 °C for 1 h [137]. A color code indicator is included to indicate the crystal orientation.

The orientation map allows further analysis to assess the grain size distribution, grain boundary characteristics, and misorientation evaluation. The map also provides data that can be used to obtain pole figures and inverse pole figures which correspond to the stereographic projections of the scanned surface and the texture distribution [138].

2.2.9 Transmission electron microscopy (TEM)

Transmission electron microscopy (TEM) is another electron-based imaging technique. Unlike SEM, TEM imaging relies on the electrons transmitted through a very thin sample, called TEM lamella. The thickness of a typical TEM lamellae is less than 100 nm, and the thinning process of the sample is typically achieved through an ion-bombardment technique *i.e.,* the focused-ion beam SEM (FIB-SEM), allowing site-specific ablation or material removal.

After loading the sample in the TEM tool, the electrons are produced by a heated filament at energy around 200 to 300 keV. The high energy electrons are accelerated towards the thin sample allowing electrons to pass through. The imaging is then typically performed on a phosphor screen or a photographic plate.

2.2.9.1 TEM-EDX for chemical composition

As an extension of the TEM technique, scanning TEM – energy dispersive X-ray (TEM-EDX) spectroscopy can be introduced to assess the chemical composition of the sample. This can be achieved by introducing an EDX detector within the TEM equipment. The measurements of the energy and the number of characteristic X-rays generated by the sample allows proper quantification of the atomic concentration (at. %) of each element in the sample.

2.2.9.2 TEM-EELS

Electron energy loss spectroscopy (EELS) is another technique that is an extension of the TEM characterization. In TEM-EELS, the electrons are transmitted through sample resulting either elastic or inelastic interactions with the sample, allowing to extract information from the sample. The EELS instruments are typically equipped within the TEM microscope and high energy electrons (typically between 60 to 300 kV) are used during the characterization. Typically, EELS data such as electron energy-loss near-edge structure (ELNES), allows the obtaining of information on the bonding and oxidation state of the composed elements [139].

2.3 Chapter conclusions

In this chapter, details regarding the different processes used for the formation of the sample are outlined. This includes the 300 mm silicon wafer surface preparation, the different deposition of different metal thin films, chemical etching, and heat treatments. In the second half of this chapter, the working principles of different characterization techniques are also described. The understanding of their working principles is necessary to properly analyze the obtained results that will be presented in the next chapter.

Chapter 3: Experimental results on the agglomeration phenomenon of Ni(Pt)Si films

Chapter contents

3.1 List of samples, fabrication steps, and naming 101
3.2 Part 1: Different SiCoNi treatments 111
3.2.1 Experimental setup 111
3.2.2 1-A: Influence of multi-step SiCoNi process on PVD-deposited NiPt thin films 113
3.2.2.1 Observations of intermixing layer 113
3.2.2.2 Composition analyses obtained by XPS 116
3.2.2.3 EDX profiles 118
3.2.2.4 Redistribution of residual fluorine, F 121
3.2.2.5 Conclusions of part 1-A 123
3.2.3 1-B: Impact of SiCoNi treatments on the agglomeration of Ni(Pt)Si thin film 125
3.2.3.1 Investigation of the thickness uniformity post-RTA2 125
3.2.3.2 Investigation of the agglomeration of Ni(Pt)Si films (post-RTAD) 127
3.2.3.3 Conclusions of part 1-B 134
3.3 Part 2: Annealing schemes 135
3.3.1 Experimental setup 135
3.3.2 Sheet resistance, Rs 138
3.3.3 Tilted-SEM – film morphology 140
3.3.4 High-resolution SEM – grain size 144
3.3.5 Preferential orientations & textures 146
3.3.6 Conclusions of part 2 151
3.4 Part 3: Impact of confinement on Ni(Pt)Si film in regular lines 152
3.4.1 Experimental setup 152

3.4.2 Influence of confinement in regular lines on Ni(Pt)Si agglomeration 156
3.4.3 Impact of confinement on texture of Ni(Pt)Si thin films 160
3.4.4 Conclusions of part 3 167
3.5 PART 4: RESULTS ON INDUSTRIAL WAFERS (INTEGRATED CIRCUITS) 169
3.5.1 Experimental setup 169
3.5.2 Investigation on Ni(Pt)Si thickness 172
3.5.3 Electrical characterizations 173
3.5.4 Silicide morphology 175
3.5.5 Conclusions of part 4 178

Foreword

First, a summary of all samples used in this work is given in the form of table and mind-maps describing the specificities of their elaboration steps. The samples respective naming are also included. Each mind-map is followed by a table summary for each of the study and can be printed separately to facilitate the reading.

As described in the first chapter, the principal challenge of the utilization of Ni(Pt)Si thin films for FDSOI technologies is their sensitivity to the agglomeration phenomenon. The different process steps leading to the formation of a silicide film are the key parameters driving the final microstructural properties of the thin film [7], [19], [28], [75], [95], [97]. The correlation between final microstructure of Ni(Pt)Si film and the agglomeration sensitivity allows a better understanding of thin film degradation mechanisms itself.

Within this chapter, the impacts of the different processes involved in silicide formation on the thermal stability of Ni(Pt)Si films will be presented. This chapter is divided into four main parts focusing on the principal research axes presented in chapter 1 *i.e.,* impact of the different types of SiCoNi treatments, influence of the annealing schemes, and the confinement effect on the thermal stability of Ni(Pt)Si layer (nanometric patterned structures). The final part is dedicated to results on the industrial wafers dealing with the integration processes used in the elaboration of real devices.

3.1 List of samples, fabrication steps, and naming

In this section, we will describe the experimental set-up for all of the studies. Firstly, Fig. 50 helps to understand the different processes involved in the elaboration of the four types of samples used in the study on the impact of the SiCoNi surface treatment on the agglomeration of the Ni(Pt)Si film. Their elaboration steps start with blanket 300 mm-Si wafer which then follows a similar first HF and SC1 clean. The steps are then divided into two main branches corresponding to the SiCoNi 2x40 and SiCoNi 80 treatments. Each of the branches will then generate two samples post-PVD deposition of the NiPt metal layer and post-RTAD (high temperature annealings, “D” for dewetting range). The samples are then characterized using several techniques including ellipsometry, Rs, TEM, XPS, TEM-EDX, ToF-SIMS, and TEM-EELS. The samples are then summarized in Table 5 with their respective thickness.

Next the samples elaboration steps for study 2 (impact of different annealing schemes) is described in Figure 51. Similar surface clean is applied *i.e.,* HF and SC1 followed by the SiCoNi 2x40. Next, two main branches are generated, since depending on the annealing schemes (either partial, laser, total, or one-step), the thickness of the NiPt metal layer needs to be adjusted in order to form Ni(Pt)Si film at around 11 nm in all cases. Moreover, the RTA1 is also adjusted to a higher thermal budget in the case of the total annealing (see Fig. 51). Similarly, the samples are submitted to RTAD annealings prior to the electrical and microstructural characterizations. A table is included to summarize all of the samples involved in this study.

In the third study on the impact of the confinement on the agglomeration of the Ni(Pt)Si film, both branches in Fig. 52, follow the similar standard SALICIDE process, with the exception that the lithography steps using DIVA masks are added prior to the one of the branches. This allows to create the different confinement structures. The RTAD is also applied to evaluate thin film stability prior to their characterizations.

Finally, Fig. 53 illustrates the different steps conducted in the elaboration process of an integrated circuits. This includes several new steps that was not used on the previous

studies such as the ion implantation, source/drains and gate formations, Ti/TiN deposition and the $TiSi_x$ annealings which is performed after the formation of the Ni(Pt)Si film. A complete detail regarding the sample fabrication processes will be provided at the beginning of each the study.

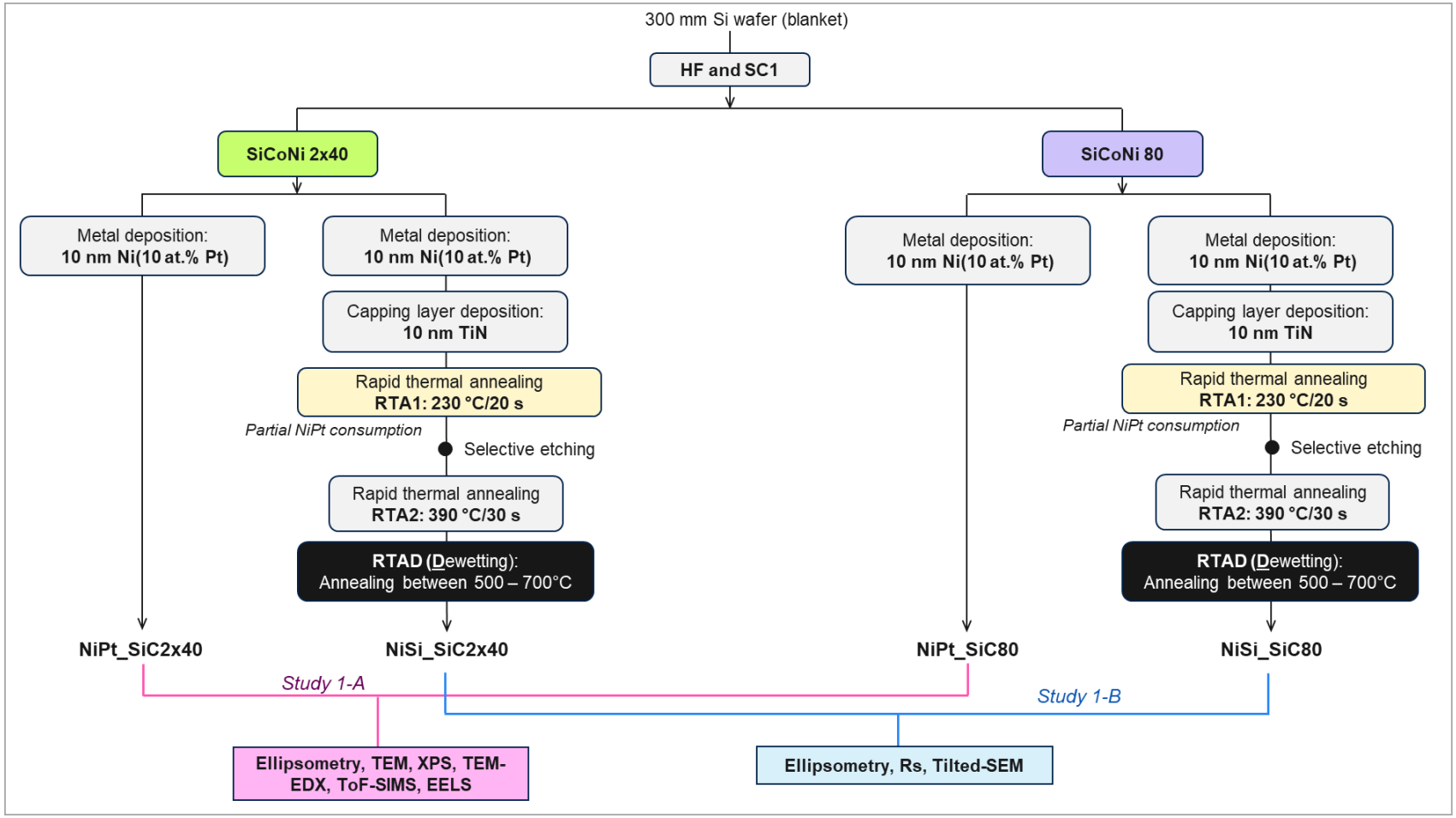


Figure 50. Study 1: Impact of different types of SiCoNi treatments on the agglomeration of the 11 nm Ni(Pt)Si thin film. In this figure the rounded rectangle refers to the main processes, words in italics to the process description, steps in bullet points to other related process, words in bold to the sample names and rectangle to different characterization techniques.

Table 5. Summary of samples used for the study on the impact of the different SiCoNi treatments on the agglomeration of Ni(Pt)Si thin film. '80' means that 80 Å of SiO_2 layer etched during SiCoNi process on blanket wafer. SiO_2 thin film composition is in that case stoichiometry.

No.	Layer	Differentiation	**Naming**
1	11.7 nm NiPt	SiCoNi 2x40	**NiPt_SiC2x40**
2	11.7 nm NiPt	SiCoNi 80	**NiPt_SiC80**
3	12.2 nm Ni(Pt)Si	SiCoNi 2x40 (*std.*)	**NiSi_SiC2x40**
4	11.5 nm Ni(Pt)Si	SiCoNi 80	**NiSi_SiC80**

Std.: Used in standard SALICIDE process (reference)

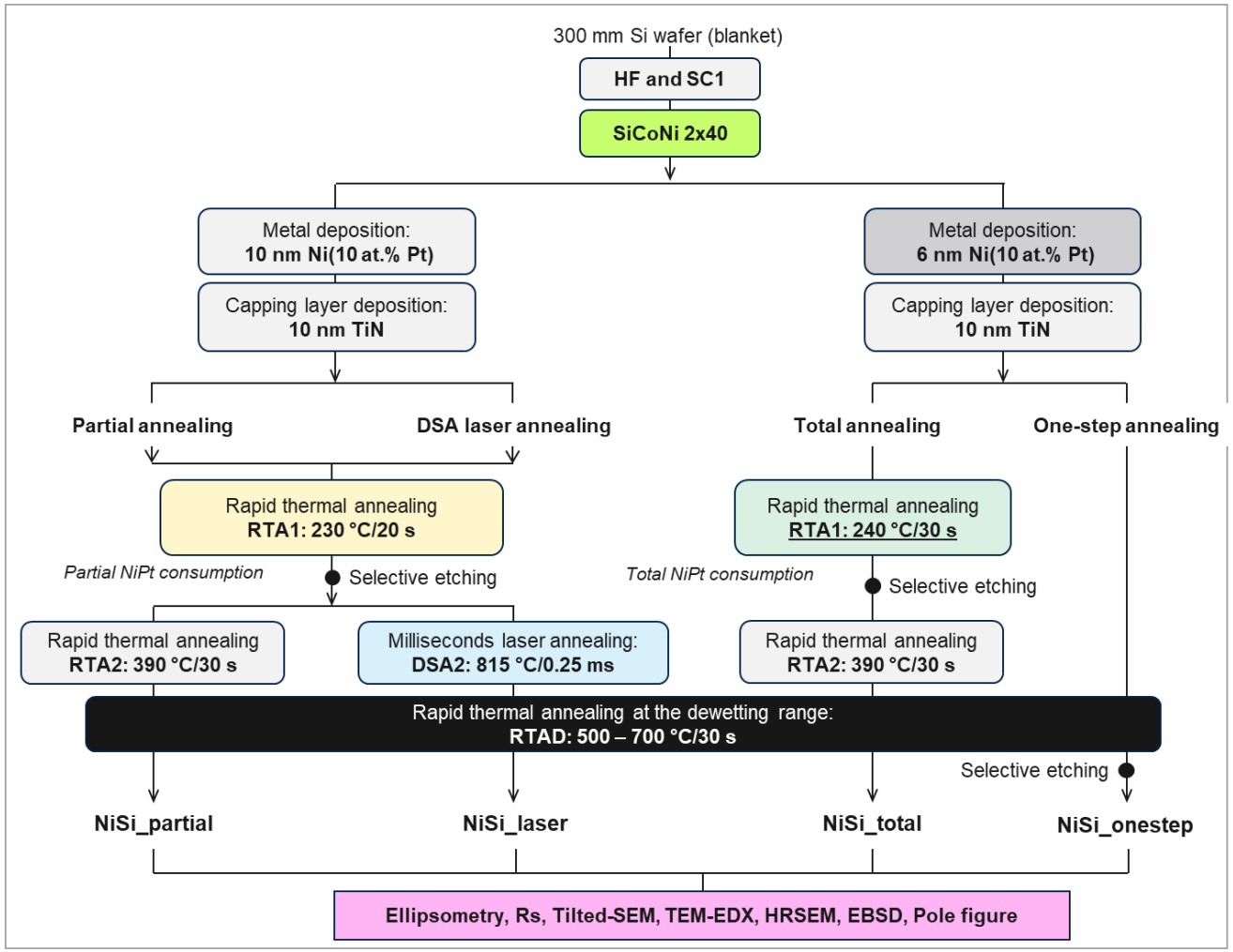


Figure 51. Study 2: Impact of the annealing schemes on the agglomeration of the 11 nm Ni(Pt)Si thin film. In this figure the rounded rectangle refers to the main processes, words in italics to the process description, steps in bullet points to other related process, words in bold to the sample names and rectangle to different characterization techniques.

Table 6. Summary of samples used for the study of the influence of the annealing schemes on the agglomeration of Ni(Pt)Si thin films. Partial means that after RTA1 annealing, excess NiPt remains on top of the newly formed silicide.

No.	Layer	Description	**Naming**
1	Ni(Pt)Si	Ni(Pt)Si layer formed using partial annealing (*std.*)	**NiSi_partial**
2	Ni(Pt)Si	Ni(Pt)Si layer formed using laser annealing	**NiSi_laser**
3	Ni(Pt)Si	Ni(Pt)Si layer formed using total annealing	**NiSi_total**
4	Ni(Pt)Si	Ni(Pt)Si layer formed using one-step annealing	**NiSi_onestep**

Std.: Used in standard SALICIDE process (reference)

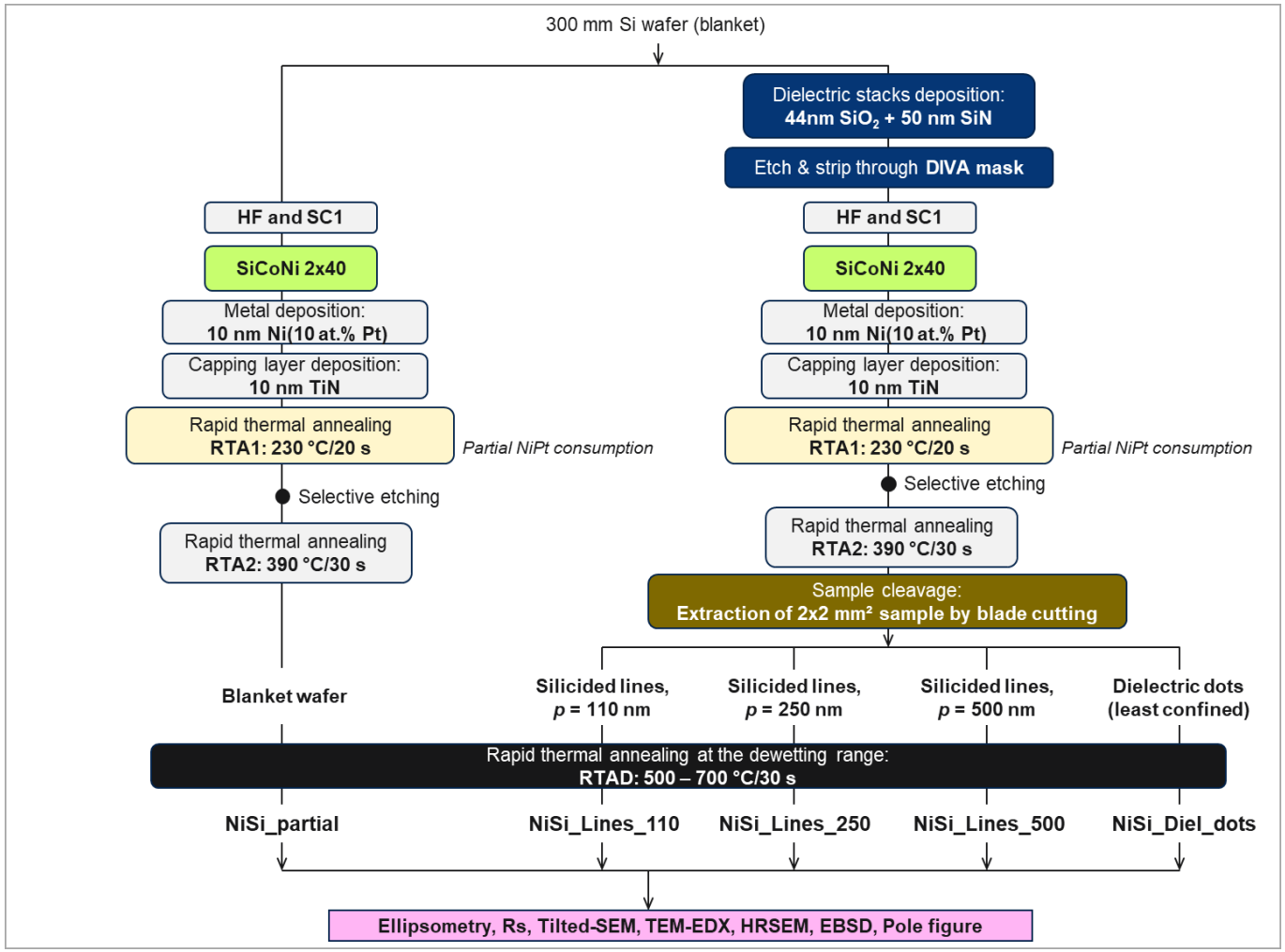


Figure 52. Study 3: Impact of confinement on the agglomeration of the 11 nm Ni(Pt)Si thin film. In this figure the rounded rectangle refers to the main processes, words in italics to the process description, steps in bullet points to other related process, words in bold to the sample names and rectangle to different characterization techniques.

Table 7. Summary of samples used for the study of the impact of confinement on the agglomeration of Ni(Pt)Si thin films. "p" refers to the pitch of the confined structures.

No.	Layer	Differentiation	**Naming**
1	11 nm Ni(Pt)Si	Silicided lines, *p*=110 nm	**NiSi_Lines_110**
2	11 nm Ni(Pt)Si	Silicided lines, *p*=250 nm	**NiSi_Lines_250**
3	11 nm Ni(Pt)Si	Silicided lines, *p*=500 nm	**NiSi_Lines_500**
4	11 nm Ni(Pt)Si	Dielectric dots	**NiSi_Diel_dots**
5	11 nm Ni(Pt)Si	Blanket wafer	**NiSi_blanket** (=NiSi_partial)

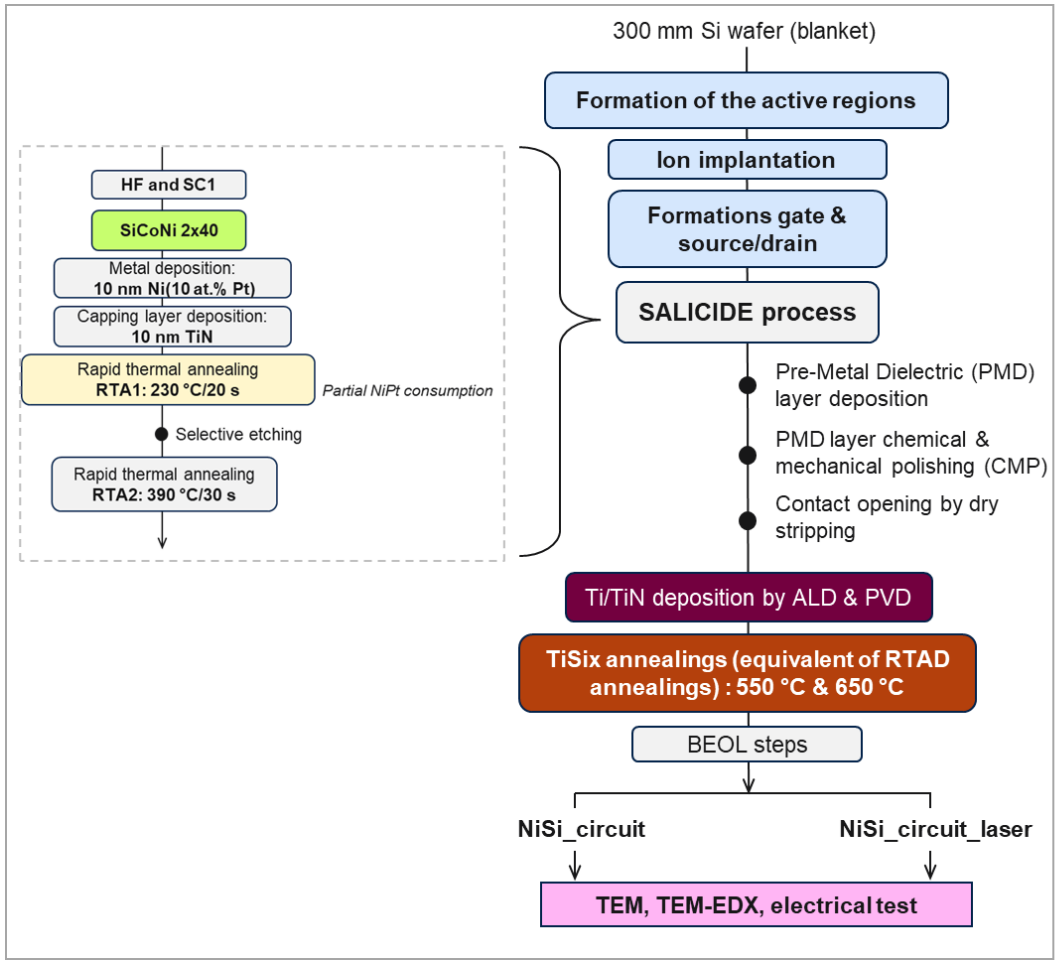


Figure 53. Study 4: Results on industrial wafers following the process flows of the integrated circuits. In this figure the rounded rectangle refers to the main processes, words in italics to the process description, steps in bullet points to other related process, words in bold to the sample names and rectangle to different characterization techniques.

Table 8. Summary of samples used for the study on the agglomeration of Ni(Pt)Si thin film in real integrated circuits.

No.	Layer	Differentiation	**Naming**
1	14 nm Ni(Pt)Si	Silicide in integrated circuit (formed by partial annealing)	**NiSi_circuit**
2	14 nm Ni(Pt)Si	Silicide in integrated circuit (formed by laser annealing)	**NiSi_circuit_laser**

3.2 Part 1: Different SiCoNi treatments

3.2.1 Experimental setup

As presented in chapter 2 (section 2.1.1), the SiCoNi treatment follows three main steps: (i) Generation of etching precursor, NH_4F by a remote plasma, (ii) interaction with the SiO_X or SiO_2 layers on top of the Si substrate leading to the formation of the $(NH_4)_2SiF_6$ salt, and finally (iii) the sublimation of the salt at 180 °C resulting in the formation of SiF_2 and NH_3 gases. The experimental setup of the study on the impact of different types of SiCoNi treatment on the thermal stability of the Ni(Pt)Si is illustrated in Figs. 50 and 54.

For this study, a blanket 300 mm-Si(100) wafer (doped p are submitted to a HF and SC1 surface clean prior to SiCoNi treatments.

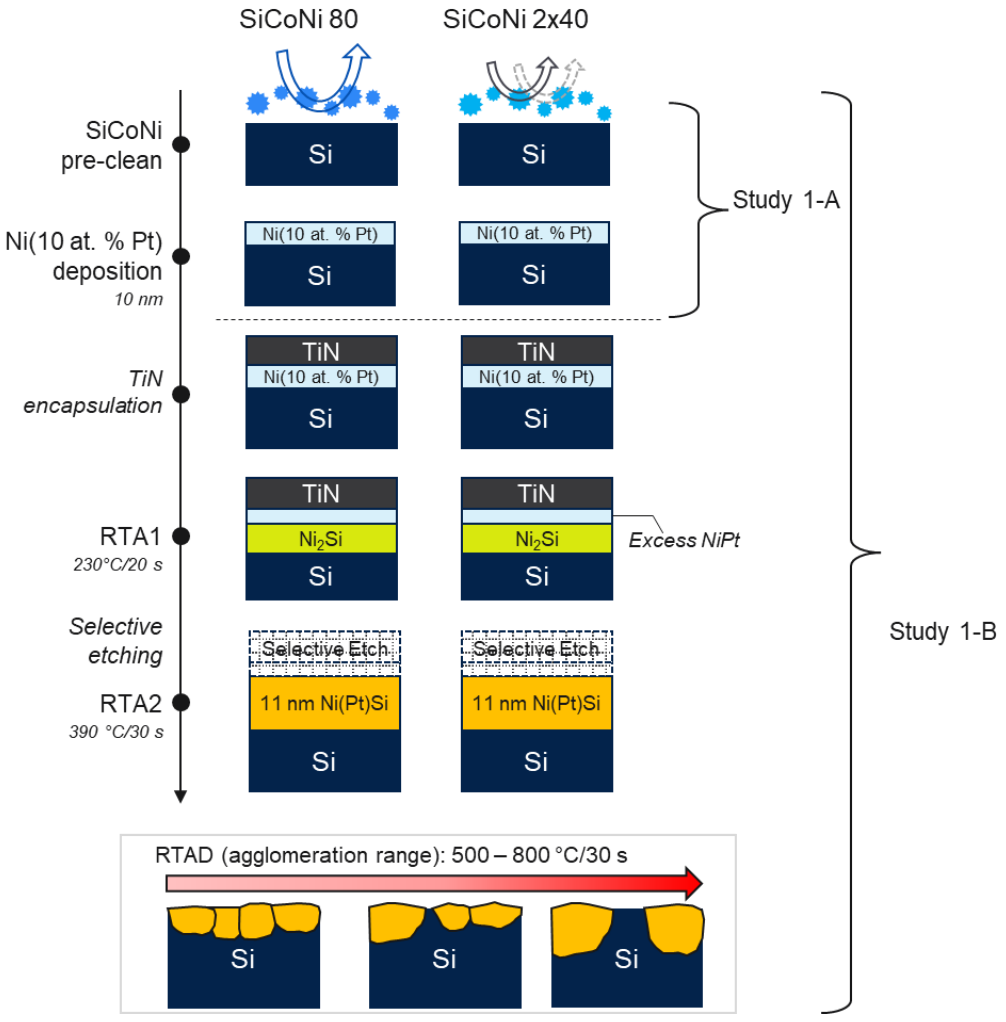


Figure 54. Schematics for the formation of 11 nm Ni(Pt)Si thin film using two different SiCoNi treatments: SiCoNi 80 (left) and 2x40 (right).

Two series of samples are introduced: (1) SiCoNi 80 and (2) SiCoNi 2x40 (Figs. 50 and 54). This corresponds to a removal of a thermal oxide layer using a single cycle of SiCoNi treatment (SiCoNi 80) or multi-cycle, or more precisely a double cycle SiCoNi treatment (SiCoNi 2x40). The etch time in each cycle of the SiCoNi 2x40 corresponds to half of the etch time in SiCoNi 80.

In other words, the total etch time remains identical in both SiCoNi treatments with the particularity of the SiCoNi 2x40 having half the etch time and repeated twice.

The rest of the process parameters are kept identical and both series are finally evaluated using a high temperature annealing, named RTAD, with “D” for the dewetting range. The associated temperature range is comprised between 500 – 800 °C and the duration of the anneal is 30 seconds.

The presentation of the experimental results for this study will be divided into two parts (see Figs. 50 and 54):

- Study 1-A addresses the impact of different SiCoNi treatments on the properties of the NiPt layer deposited during the subsequent PVD deposition.
- Study 1-B will presents the results obtained after RTA2 and RTAD annealings.

For the study 1-A, it is important to note that the NiPt layer is not encapsulated by TiN capping layer. Such approach allows the use of ellipsometry techniques.

3.2.2 1-A: Influence of multi-step SiCoNi process on PVD-deposited NiPt thin films

3.2.2.1 Observations of intermixing layer

The thicknesses of the NiPt layers measured using the ellipsometry technique are summarized in Table 9 for NiPt_SiC2x40 and NiPt_SiC80 samples. The ellipsometry measurements are performed on 49 sites equally distributed on 300 mm blanket wafers with a 3 mm edge exclusion. The measurement starts at the center of the wafer and moves further away each time. The complete coordinates for the 49-points mapping are provided in **appendix A.i**. A visual representation of the mapping is illustrated in Fig. 55.

Table 9. The thickness of the as-dep NiPt layer as measured by ellipsometry technique.

Sample	Average thickness (nm)	Range (nm)	Standard deviation (nm)
NiPt_SiC2x40	11.69	0.76	0.26
NiPt_SiC80	11.69	0.76	0.25

The average thickness is around 11.7 nm, and the standard deviation appears to be low, indicating a high thickness uniformity in both samples. Fig. 55 shows the thickness profiles of NiPt layer plotted for each of the series of samples: SiCoNi 80 and SiCoNi 2x40.

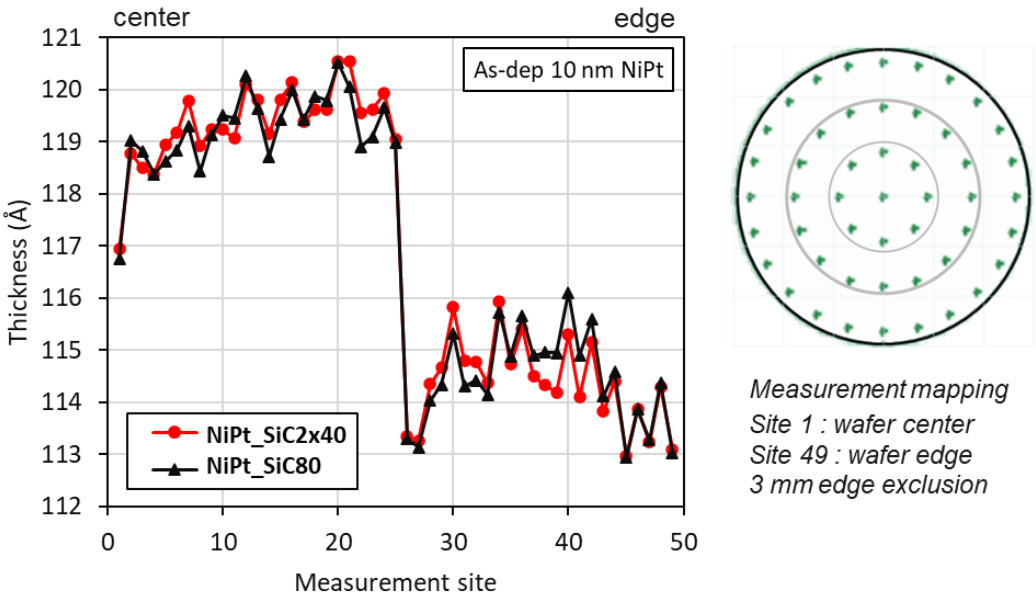


Figure 55. Thickness profile of as-dep NiPt layer on Si(100) for a 49-points measurement mapping on 300 mm wafer measured from NiPt_SiC2x40 and NiPt_SiC80 samples. Sites 1 and 49 correspond respectively to the center and the extreme edge of wafer. A 3 mm edge exclusion is considered for such mapping.

The thickness profile shows that the NiPt layer is slightly thicker at the center of the wafer as compared to the edge regardless of the SiCoNi treatments used. The thickness difference is around 5 Å between the center and the edge of the wafer. Such a profile is characteristic of the PVD sputtering technique. Indeed, for metal deposition using such technique, the thickness uniformity is defined by throw distance and deposition cone [140].

At that point, preliminary observations by ellipsometry technique appear to indicate no direct influence of the SiCoNi 2x40 treatment on the thickness and thickness uniformity of the NiPt layer after PVD deposition.

Fig. 56 shows the TEM cross-sections obtained after NiPt layers deposition for both NiPt_SiC2x40 and NiPt_SiC80 samples. The measurement is performed on TEM lamellar taken at the center of the wafer.

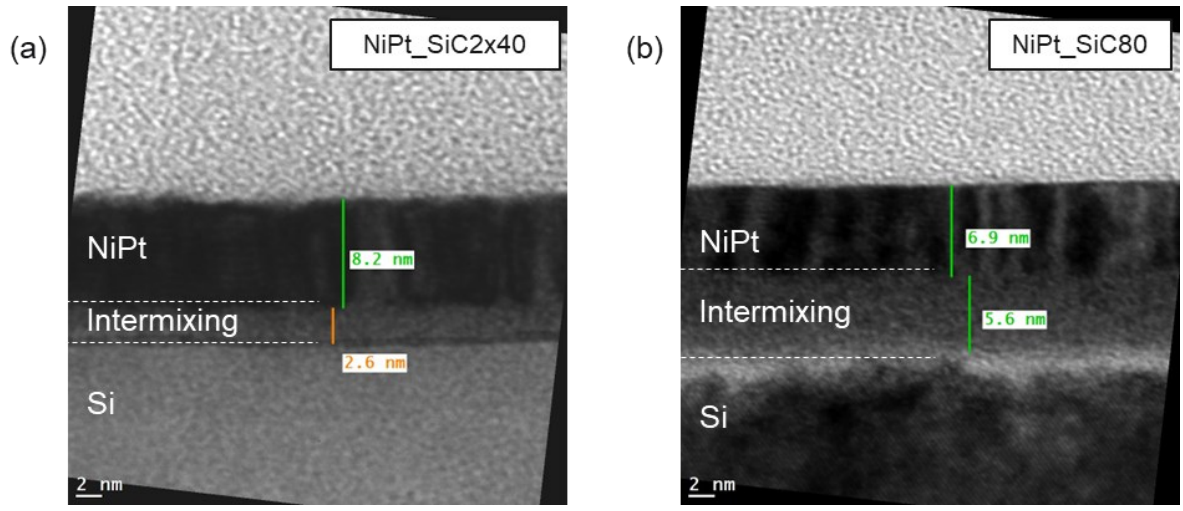


Figure 56. TEM cross-sections obtained after NiPt deposition on Si substrate for (a) NiPt_SiC2x40 and (b) NiPt_SiC80 samples.

As shown by the TEM image in Fig. 56(a) for NiPt_SiC2x40 sample, the thickness of the NiPt layer is around 8.2 nm whereas for NiPt_SiC80 sample shown in Fig. 56(b), the NiPt layer appears to be thinner, with thickness around 6.9 nm. In both cases, the NiPt thickness appears to be lower than the thickness previously measured using the ellipsometry technique.

However, the TEM images also evidence the presence of another layer in between the NiPt layer and the Si substrate. This interlayer, called intermixing layer, is often observed in the case of NiPt deposition by PVD sputtering on Si substrate [140]. This may explain the discrepancy of the thicknesses measured by the ellipsometry technique as the model used during the fit may not distinguish between the amorphous interlayer and the polycrystalline NiPt. The thickness of the intermixing may play a role in the thermal stability of the silicide thin film.

In the case of NiPt_SiC2x40 sample, the intermixing layer is thinner with a thickness of 2.6 nm. For NiPt_SiC80 sample, the thickness of the intermixing layer is 5.6 nm. Assuming the volume change remain the same as crystalline NiSi (t_{NiSi}/t_{NiPt}=1.89 [121], [141]), the theoretical thickness of the consumed NiPt layer can be calculated. This corresponds to a consumed NiPt thickness of 1.38 nm NiPt_SiC2x40 and 2.96 nm for NiPt_SiC80 sample.

This results in an overall initial metal thickness of 9.58 and 9.86 nm. Consequently, this mean that there is at least 1.8 nm difference of initial metal thickness when compared to the measurement done using the ellipsometry technique.

3.2.2.2 Composition analyses obtained by XPS

The chemical composition of the as-dep NiPt layer is determined in detail using an X-ray photoelectron spectroscopy (XPS) technique. The XPS measurements were performed at the center of the wafer.

Fig. 57 shows the XPS spectra of (a) O-1s and (b) Ni-2p3 states for NiPt_SiC2x40 and NiPt_SiC80 samples.

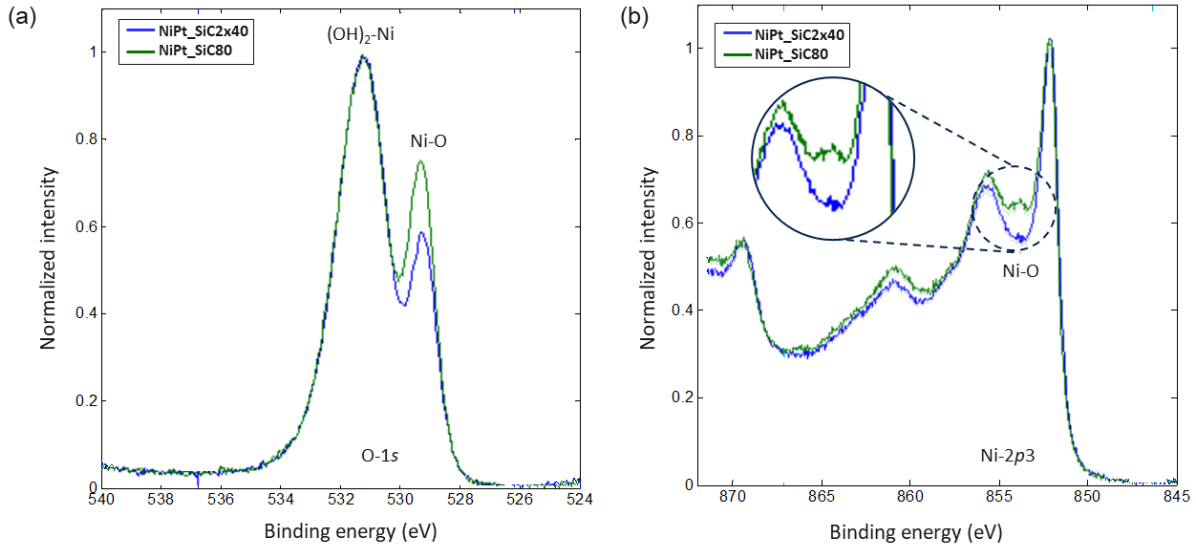


Figure 57. XPS spectra of (a) O-1s and (b) Ni-2p3 measured from NiPt layers on Si substrates for both NiPt_SiC2x40 and NiPt_SiC80 samples with a circular inset zoomed on Ni-O peaks.

As shown in Fig. 57(a), the O-1s spectra consists of two intensity maxima at around 531.2 and 529.3 eV corresponding to the bonds of oxidized nickel, $(OH)_2$-Ni and Ni-O respectively. Both peaks are observed for all samples regardless of the treatments used prior to the NiPt deposition. However, the intensity of the Ni-O peak is more significant in the NiPt_SiC80 sample compared to the NiPt_SiC2x40 one. This is a strong indication of higher oxygen content in NiPt layer deposited on Si substrate after SiCoNi 80 treatments.

As illustrated in Fig. 57(b), the Ni-2p3 spectra present a maximum at 852.2 eV corresponding to the Ni metal peak. Moreover, a small peak is also observed at around 853.7 eV corresponding to the bond of the oxidized nickel in the form of Ni-O. The Ni-O peak is observed in both NiPt_SiC2x40 and NiPt_SiC80 samples. The intensity of the Ni-O peak appears to be more significant in the case of the NiPt_SiC80 sample than that of the NiPt_SiC2x40 one as shown in the inset of Fig. 57(b). This further corroborates the previous observations on the O-1s spectra indicating higher oxygen content in the case of single-step SiCoNi treatments.

The XPS spectra of the F1s are also extracted for both samples. As shown in Fig. 58, a peak can be seen at around 684 eV corresponding to the typical chemical states of metal fluoride bonds.

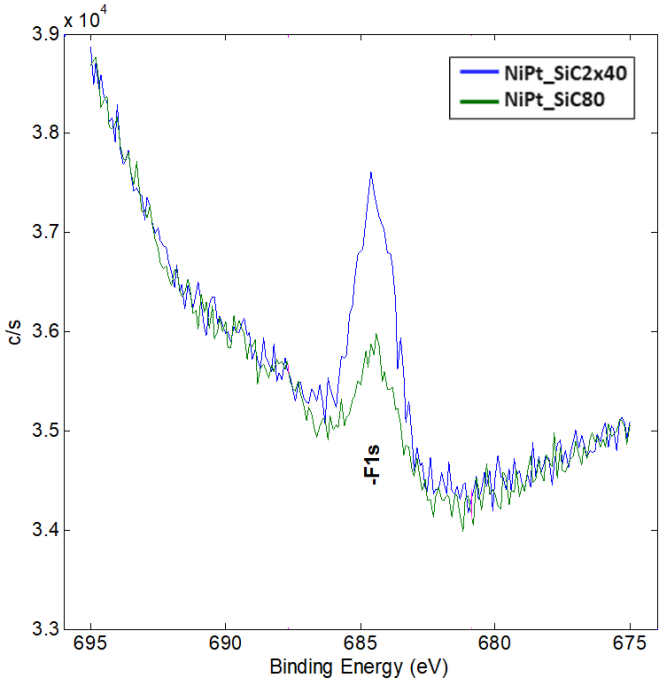


Figure 58. XPS spectra of F1s measured from NiPt layers deposited on Si substrates for NiPt_SiC2x40 and NiPt_SiC80 samples.

The intensity of such peak is more significant for NiPt_SiC2x40 as compared to that of the NiPt_SiC80 sample. The atomic concentration of each element are summarized in Table 10. The fluor concentration is doubled in the case of the NiPt_SiC2x40 compared to the that in NiPt_SiC80.

Table 10. Atomic concentrations of elements (at. %) determined by XPS technique in NiPt layers deposited on Si substrates after two different SiCoNi treatments: SiCoNi 2x40 and SiCoNi 80.

Sample	C-1*s*	O-1*s*	F-1*s*	Si-2*p*	Ni-2*p*3	Pt-4*f*
NiPt_SiC2x40	15.1	37.9	1.6	0.1	42.6	2.8
NiPt_SiC80	15.7	39.5	0.7	0.0	41.1	2.9

As depicted in Table 10, lower oxygen concentration is observed for NiPt_SiC2x40 sample, related to the contribution of the Ni-O bonds seen in both O-1*s* and Ni-2*p*3 spectra. The Pt concentration remains identical in both cases and slightly higher carbon content is detected for NiPt_SiC80 sample.

3.2.2.3 EDX profiles

Fig. 59 shows the concentration profiles of Ni, Pt, Si, O and F measured using TEM-EDX technique for both samples: NiPt_SiC2x40 and NiPt_SiC80. Line concentration profile is extracted and plotted from the top of the sample surface towards the bulk Si substrate. The bottom row represents a zoom at lower at. % concentration to better visualize the platinum, Pt and fluorine, F atoms.

The intensity is normalized using the concentration of the Si in the bulk of the substrate. Both of the samples are capped with a metal oxide layer prior to characterization, thus significant oxide concentration at low depth (*at depth inferior to 16* nm) is detected.

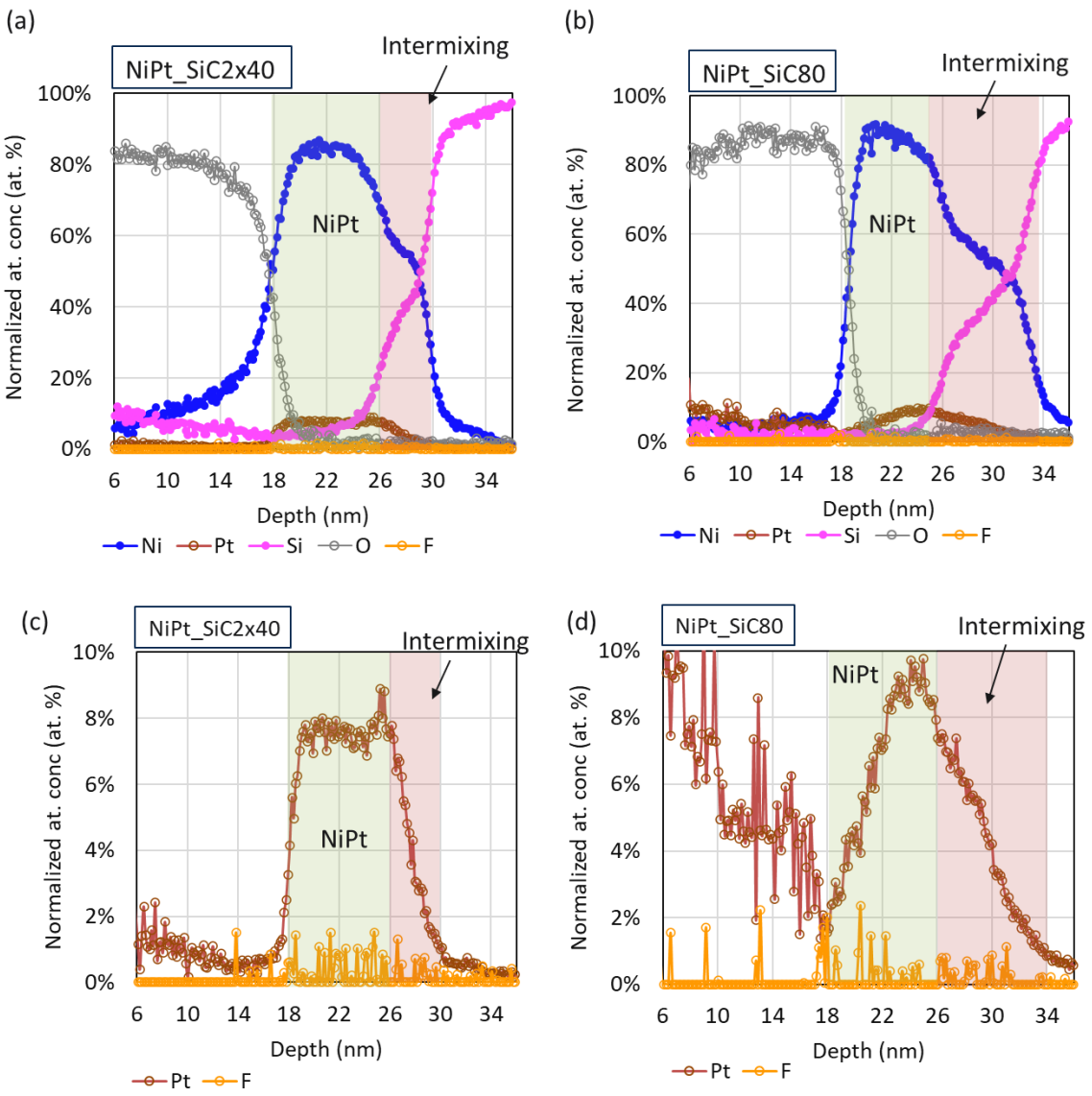


Figure 59. Concentration profiles of Ni, Pt, Si, O and F in as-dep NiPt layer for (a) NiPt_SiC2x40, and (b) NiPt_SiC80 samples measured using TEM-EDX. The corresponding zoom in (c) and (d) to better visualize both the Pt and F atoms.

As illustrated in Fig. 59, the concentration profiles can be divided into two distinct regions. The first region is comprised of the NiPt layer (green shaded region). Furthermore, this is evidenced by the concentration profiles of both Ni and Pt that remains at a constant 1/10 ratio for Pt/(Ni+Pt) (see the ratio between Figs. 59(a) and (c) for example). This observation is consistent with the PVD sputtering target used in the framework of this PhD thesis *i.e.,* Ni(10 at. % Pt).

Then, the second region corresponds to the intermixing layer (pink shaded region). The interface between NiPt and intermixing layer could be defined as the starting point of decreasing in both Ni and Pt concentrations. Then, the interface between intermixing layer and substrate is set for Ni and Pt concentrations near to 0 at. %.

As shown in Figs. 59(c) and (d), the platinum, Pt is well distributed in the NiPt layer deposited on Si substrate treated with the SiCoNi 2x40 contrarily to the Pt spatial distribution in the case of SiCoNi 80. Furthermore, Pt at. % concentration shows an increase to a maximum at the interface of the NiPt/intermixing layer in both cases.

No quantifiable variations on fluorine concentrations within NiPt and intermixing layers might be detected through EDX technique. The low concentration of fluorine is presumed to fall below the detection limit of the TEM-EDX technique as no clear pattern is observed in the redistribution of fluorine atoms.

Applying such analyses of EDX profiles, the following intermixing thicknesses could be then extracted and presented in Table 11.

Table 11. Estimated thicknesses of the intermixing layer from EDX profiles measured on NiPt layer deposited on Si substrate for NiPt_SiC2x40 and NiPt_SiC80 samples. The experimental errors are determined using the real intermixing thickness obtained by TEM in Fig. 56.

Sample	Average intermixing thickness (nm)	Experimental error (nm)
NiPt_SiC2x40	4	1.4
NiPt_SiC80	8.5	2.9

This region is characterized by the presence of a slow decrease (gradual slope) in the concentration profile of the Ni (or a slow increase in Si concentration profile). Additionally, the Si atomic concentration appears to increase starting from the interface of NiPt/intermixing to the interface of intermixing/Si. This region is then followed by the abrupt increase of Si at. % concentration and the subsequent decrease of Ni at. % concentration, corresponding to the bulk of the substrate.

3.2.2.4 Redistribution of residual fluorine, F

ToF-SIMS analyses are conducted to further characterize the redistribution of the residual fluorine in the NiPt and intermixing layers after SiCoNi treatments. Fig. 60 shows the ToF-SIMS profiles of Ni, Si, and F elements obtained for NiPt layers after deposition for (a) NiPt_SiC2x40 and (b) NiPt_SiC80 samples.

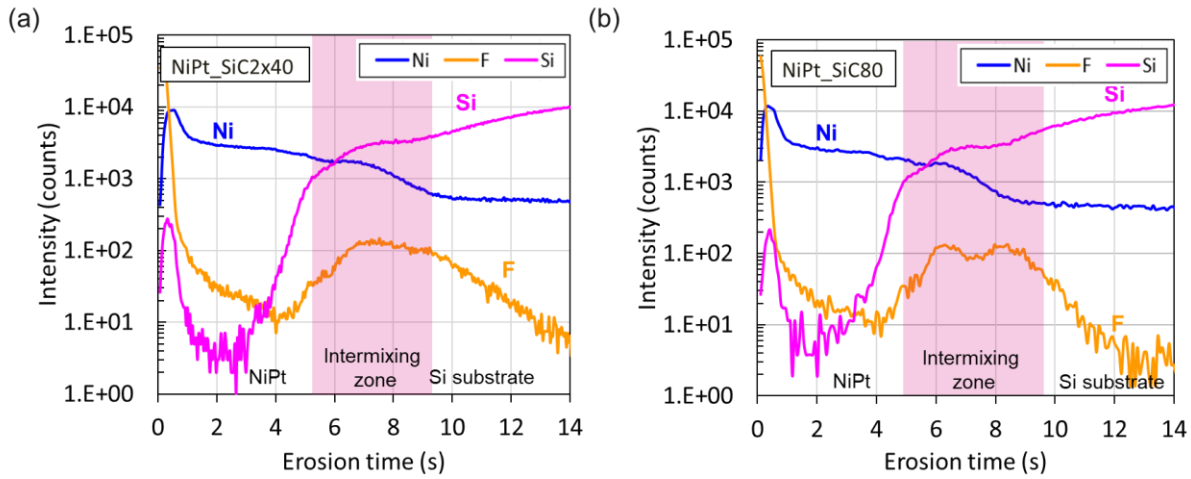


Figure 60. ToF-SIMS depth profiles of as-dep NiPt layer deposited on Si substrate for (a) NiPt_SiC2x40 and (b) NiPt_SiC80 samples.

Similar to previous observations by TEM and TEM-EDX, several regions can be identified by distinguishing the NiPt/intermixing and intermixing/Si substrate interfaces using the relative intensity profiles of Ni and Si. The NiPt/intermixing is set for Si at relative intensity of 1000 while the intermixing/Si interface is set for Ni at relative intensity of 300. The redistribution of both Ni and Si is identical regardless of the choice of the SiCoNi treatments used. However, ToF-SIMS depth profiles of fluorine element clearly show two different fluorine redistributions as function of SiCoNi treatments.

As depicted in Fig. 60(b), the fluorine profile contains two maxima at both edges of the intermixing zone *i.e.,* the NiPt/intermixing and intermixing/Si interfaces for NiPt_SiC80 sample. Contrarily, the ToF-SIMS profile of fluorine in the case of NiPt_SiC2x40 sample is characterized by a single maximum represented by a broad peak in the intermixing region.

This indicates that the fluorine atoms are homogenously distributed within the depth of the intermixing layer.

In order to investigate the bonding environments in core of these layers and their respective interfaces, electron energy loss spectroscopy (EELS) analyses are performed, focusing on the nickel $L_{2,3}$ ionization edge (855 eV). Fig. 61 shows the energy loss near edge structure (ELNES) signatures of nickel (Ni-$L_{2,3}$), extracted from the interfaces between the NiPt/NiSi/Si stack and in the core of each layer. The Ni-$L_{2,3}$ edges are characterized by the presence of two sharp peaks as can be seen in the ELNES signatures in Figs. 61(a) and (b), corresponding to the L_3 and L_2 Ni-edges. The level of background noise may appear to differ causing a slight fluctuation. However, this remains negligible.

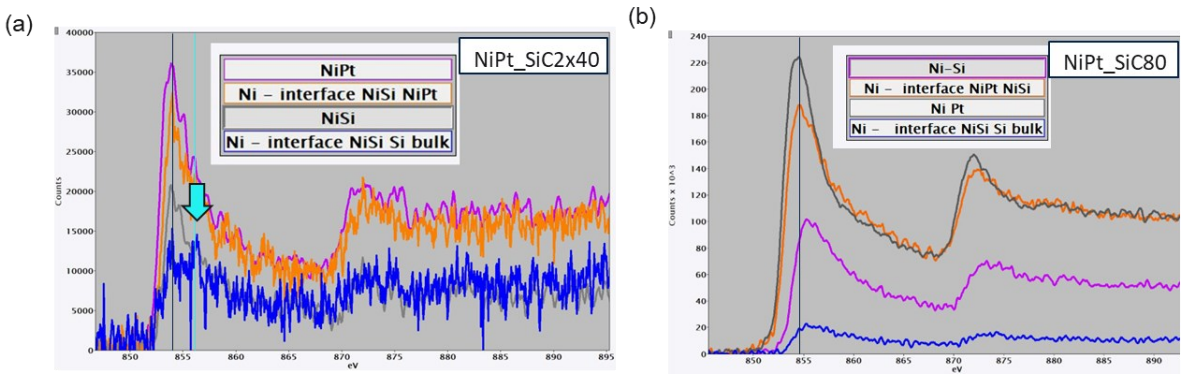


Figure 61. EELS spectra of nickel $L_{2,3}$ ionization edge extracted from line profiles at different regions: interfaces between the NiPt/NiSi/Si bulk and in the core of each layer for (a) NiPt_SiC2x40 and (b) NiPt_SiC80 samples. Cyan-colored arrow is used to indicate the presence of additional peak.

Nonetheless, a chemical shift towards higher energy loss is observed, in particular for the Ni-$L_{2,3}$ ELNES signatures extracted from the core of the intermixing layer, and the interfaces of NiPt/intermixing and intermixing/Si substrate due to the bonding between Ni and Si. However, Pt bonding to Ni in the core of the NiPt layer does not induce any chemical shift as the onset of Ni-$L_{2,3}$ edge remains identical to that of the Ni at around 855 eV.

Moreover, the Ni-$L_{2,3}$ ELNES signature extracted from intermixing layer revealed the presence of an additional peak at 856 eV (cyan arrow) for NiPt_SiC2x40 sample (plotted in dark blue in Fig. 61(a)). The presence of such additional peak does not correspond to the bonding of either Ni-Pt or Ni-Si.

This additional peak is not observed in the Ni-$L_{2,3}$ ELNES signature of the intermixing layer of NiPt_SiC80 samples. This strongly suggests the presence of a different bonding environment within the intermixing layer depending on the choice of the SiCoNi treatment. The presence of the additional peak might be attributed to the possible bonds of Ni-F and/or Ni-O. Previous observations on the redistribution of fluorine in the intermixing layer by ToF-SIMS technique may further confirm this hypothesis. Indeed, fluorine redistribution in the intermixing layer of NiPt_SiC80 sample could explain the absence of the additional peak.

On one hand, for the NiPt_SiC80 sample, a potential segregation of fluorine at the interface of the intermixing layer could induce the loss of Ni-F bonds. On the other hand, as observed on XPS profile, we estimate that for NiPt_SiC2x40 sample the Ni-O bonds are also representative than for NiPt_SiC80 sample. This last point must indicate the presence of Ni-F bonds inside the intermixing layer for the multistep SiCoNi process.

3.2.2.5 Conclusions of part 1-A

For the two series of samples, thicker NiPt layer at the center of the film is ascribed to the PVD sputtering technique for thin metal film deposition. TEM cross-sections evidenced that the intermixing layer is thicker when the SiCoNi treatment used is SiCoNi 80 instead of the SiCoNi 2x40 one, even though no clear change in the NiPt layer thickness has been pointed out by ellipsometry measurements. Elements redistribution analyzed through TEM-EDX and ToF-SIMS demonstrated a region with a more gradual slope between the NiPt layer, and the Si substrate further confirming the presence of the intermixing layer.

Pt redistribution within the NiPt layer reveals to be dependent on the SiCoNi treatments. However, both series of samples present an accumulation of Pt at the interface of the NiPt/intermixing. In addition, the concentration is identical in both SiCoNi treatments. Lower oxygen content has also been detected via the XPS technique for multi-step SiCoNi. In addition, the XPS spectra of the F1s also demonstrates a higher fluorine content for this sample.

The concentration depth profile measured using the ToF-SIMS technique showed a difference in the redistribution of the fluorine atoms inside the intermixing layer depending

on the SiCoNi treatment. Fluorine is demonstrated to be incorporated in the intermixing layer in the case of the multi-step SiCoNi treatment whereas two distinct fluorine peaks are observed in the case of the single-step one. Finally, the EELS spectra consisting of the Ni-$L_{2,3}$ edges showed a clear change in the bonding environment within the intermixing layer between the two series of samples. The presence of an additional peak at 856 eV is observed in the case of the sample treated with the SiCoNi 2x40 process. Indeed, further analyses are required as residual F are difficult to detect. The change in the bonding environment is hypothesized to be due to the presence of Ni-F bonds.

3.2.3 1-B: Impact of SiCoNi treatments on the agglomeration of Ni(Pt)Si thin film

This section is dedicated to studying the impact of different surface treatments, SiCoNi 2x40 and SiCoNi 80, on the agglomeration of the Ni(Pt)Si thin film. Ni(Pt)Si films are annealed to high temperature, in the dewetting range, noted RTAD, to evaluate their thermal stability after the silicide formation (see Fig. 50, 54, and Table 5).

3.2.3.1 Investigation of the thickness uniformity post-RTA2

For a NiPt layer of 10 nm, the standard SALICIDE process typically results in 11 nm Ni(Pt)Si films since the RTA1 is set to partially consume the NiPt metal layer. Table 12 summarizes the thickness of the nickel monosilicide, Ni(Pt)Si film measured by ellipsometry technique after its formation by RTA2 annealing. Similar measurements mapping (49-points) are used for all of the samples.

Table 12. The thickness of Ni(Pt)Si thin film formed after RTA2 annealing measured by ellipsometry technique for NiSi_SiC2x40 and NiSi_SiC80 samples.

Sample	Average thickness (nm)	Range (nm)	Standard deviation (nm)
NiSi_SiC2x40	12.2	0.41	0.11
NiSi_SiC80	11.5	1.52	0.53

The average thickness of the silicide film is 12.2 nm by applying SiCoNi 2x40 treatment prior NiPt deposition and 11.5 nm for NiSi_SiC80 sample. The thickness of the silicide film is slightly lower for the NiSi_SiC80 sample as compared to the NiSi_SiC2x40 ones.

In order to better visualize the thickness uniformity, the thickness maps are presented in Fig. 62. The color marker indicator is set to a similar thickness range for better comparison. As shown in Fig. 62(a), the Ni(Pt)Si film is very uniform within the wafer for NiSi_SiC2x40 samples.

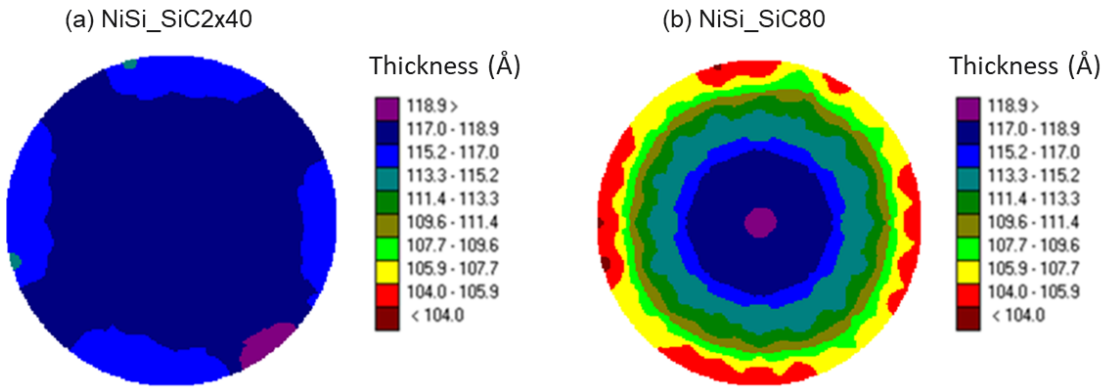


Figure 62. The thickness uniformity of Ni(Pt)Si film measured by ellipsometry after RTA2 annealing for (a) NiSi_SiC2x40, and (b) NiSi_SiC80 samples.

Contrarily, sample NiSi_SiC80 showed significant difference in thickness between the center and the edge of the wafer. The thickness difference between the center and the edge of the wafer is estimated to be at least 12 Å (1.2 nm) for Ni(Pt)Si film formed on Si substrate prepared using SiCoNi 80. The thickness profile of the Ni(Pt)Si film plotted in Fig. 63 further confirms such observations.

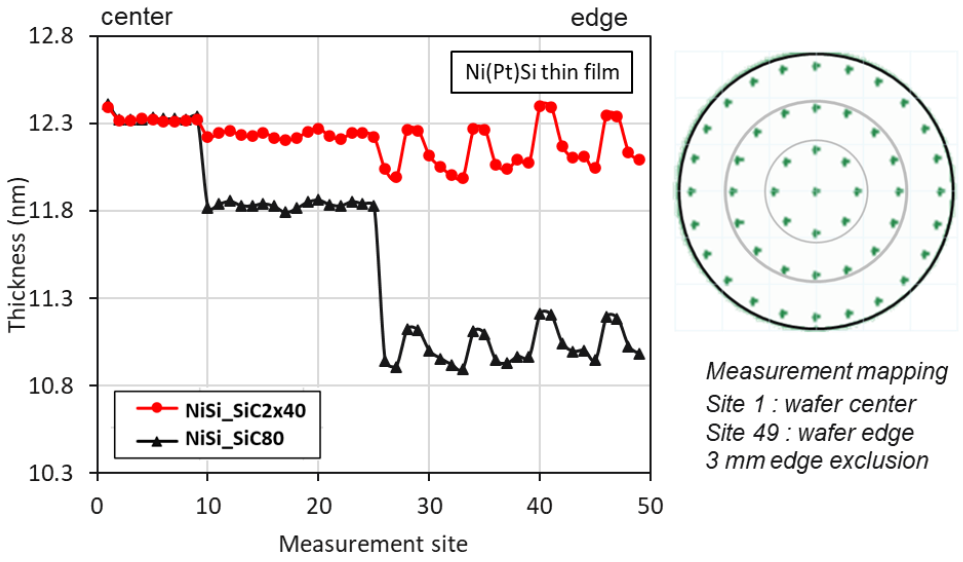


Figure 63. Thickness profile of the Ni(Pt)Si film formed on Si(100) substrate for a 49-points measurement mapping on the 300 mm wafer for the different SiCoNi treatments: SiCoNi 2x40 and SiCoNi 80. Site 1 corresponds to the center of the wafer and site 49, to the edge.

The SiCoNi 2x40 treatment appears to improve the thickness uniformity of the Ni(Pt)Si film between the center and the edge of the wafer. As result, higher average thickness of the Ni(Pt)Si film is obtained for the NiSi_SiC2x40 sample.

3.2.3.2 Investigation of the agglomeration of Ni(Pt)Si films (post-RTAD)

The samples obtained after the formation of the 11 nm Ni(Pt)Si thin film *i.e.,* after RTA2 annealing, are submitted to further thermal treatments at higher temperatures [121], [141]. A series of samples consisting of six different samples are prepared for each SiCoNi treatment. The six samples in each series correspond to each of the annealing temperatures in the RTAD range e.g., 500, 550, 600, 650, 700, and 800 °C with a constant dwell time of 30 seconds.

Fig. 64 illustrates the sheet resistance, Rs, evolution after high temperature thermal treatments (RTAD) of Ni(Pt)Si films for the two samples: NiSi_SiC2x40 and NiSi_SiC80.

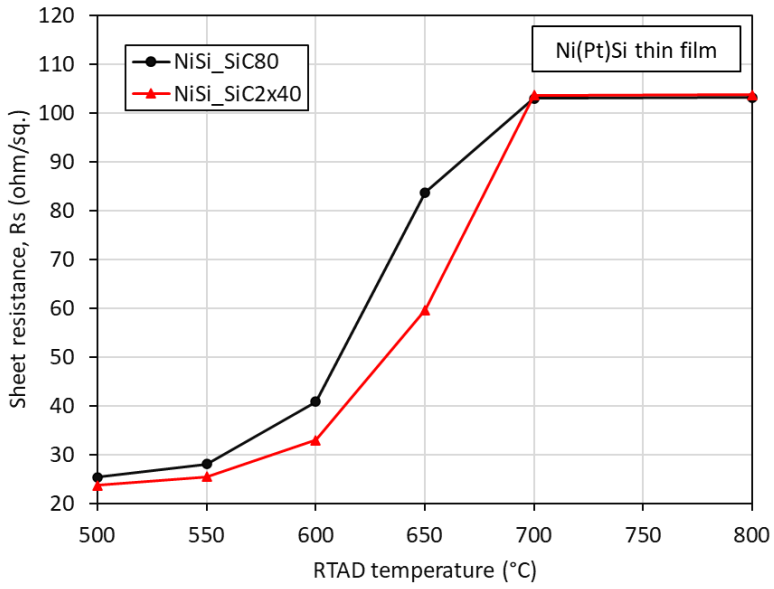


Figure 64. Sheet resistance of the 11 nm Ni(Pt)Si films formed on Si for NiSi_SiC2x40 and NiSi_SiC80 after high-temperature annealing, RTAD.

The Rs trends begins with slight increase (gradual slope) between the RTAD annealings in the range of 500 and 550 °C. The measured Rs values remain in the range of 24 – 30 Ω/sq. Moreover, the NiSi_SiC80 sample is slightly more resistive at both 500 and

550 °C. This is consistent with the silicide film thicknesses presented in Table 12 which showed a lower average thickness in the NiSi_SiC80 sample.

Between 550 and 650 °C, the Rs shows a more drastic rise as evidenced by the more abrupt slope. The Rs values increase up to 83 Ω/sq for NiSi_SiC80 sample meanwhile only up to 60 Ω/sq for NiSi_SiC2x40 sample. In addition, the slope of the Rs for NiSi_SiC2x40 samples is more gradual as compared to the NiSi_SiC80 samples between each RTAD temperature in this range.

In the range of 700 and 800 °C, the Rs shows a saturation plateau with the value of 103 Ω/sq regardless of the SiCoNi treatments. Nonetheless, the degradation of the Rs seem to be even exacerbated at higher RTAD temperatures (beyond 550 °C) in particular for the NiSi_SiC80 sample. Indeed, a relatively more gradual Rs slope is observed for the NiSi_SiC2x40 sample during the RTAD annealings.

To verify the Ni(Pt)Si film morphology at these RTAD temperatures, tilted SEM observations are performed on each sample for RTAD ranging between 500 and 650 °C. Figs. 65-(i) and (ii) show the top view SEM images tilted by 45° during acquisition in order to better account for the topology evolution. The SEM measurements are performed at the (a) center and (b) edge of the 300 mm wafers.

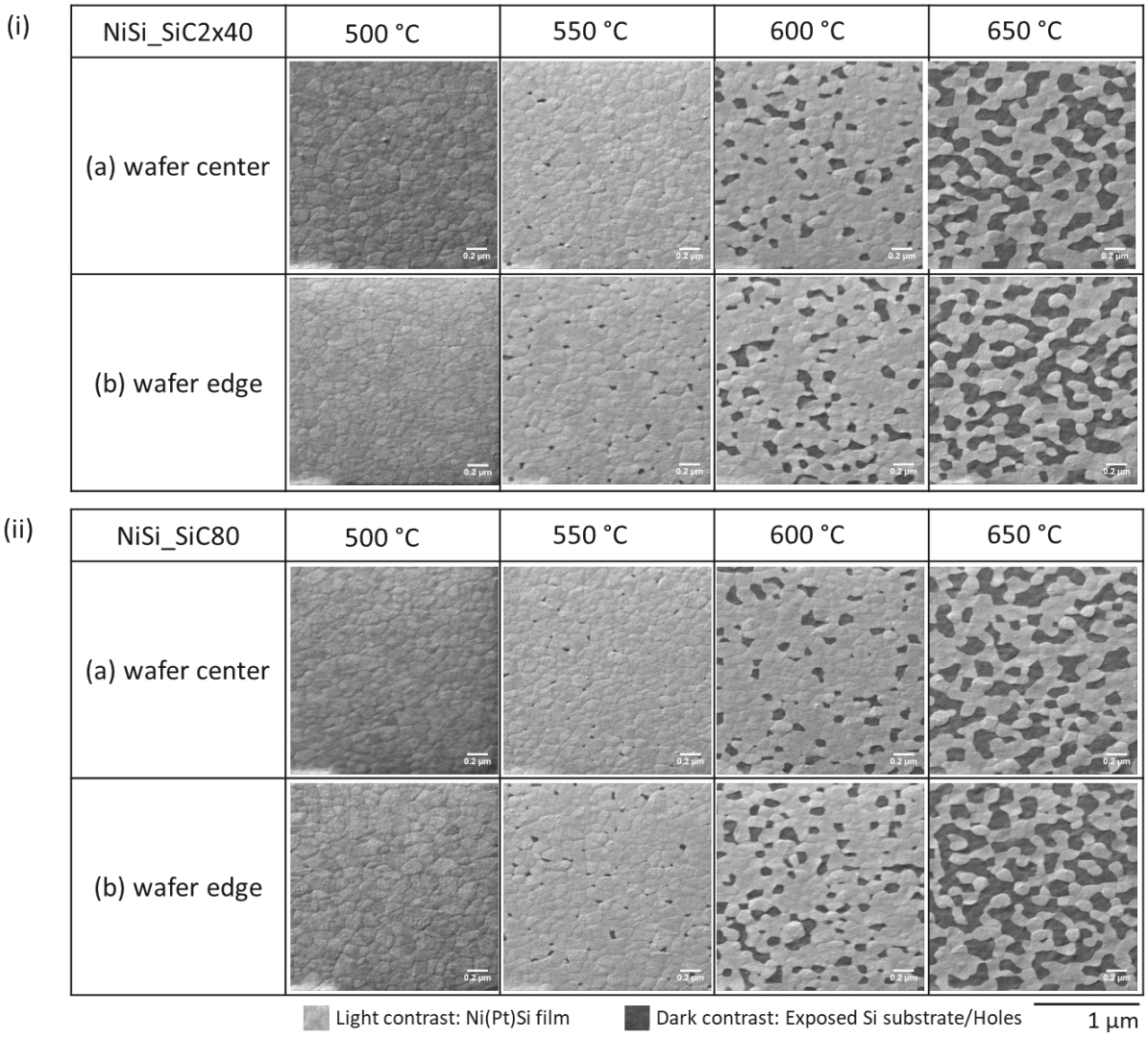


Figure 65. Top view tilted-SEM images of 11 nm Ni(Pt)Si films formed on Si substrate for (i) NiSi_SiC2x40, and (ii) NiSi_SiC80 samples, measured the (a) center and (b) edge of the 300 mm blanket wafers.

For the NiSi_SiC2x40 sample at 500 °C as shown by Figs. 65(i), the surface is fully covered by the silicide film showing visible Ni(Pt)Si grains and grain boundaries. Similar observations are shown by SEM images for the NiSi_SiC80 sample (Figs. 65(ii)). In addition, the average grain size in both cases is estimated to be around 150 nm. No significant difference is then detected from the measurements of the grain size of the Ni(Pt)Si films.

At 550 °C, there is a clear evolution of the Ni(Pt)Si film morphology for all of the samples. The SEM image at 550 °C evidenced the presence of small holes for both samples.

The quantity of holes at the edge of the wafer is more significant than that of the center of wafer in both SiCoNi treatment cases.

Further annealing at 600 °C induces the expansion of the holes size as evidenced by the SEM images in Fig. 65 (i) and (ii). Furthermore, the expanded holes appear to be connected, presenting a large area of exposed Si substrate as depicted by the dark-grey contrast in the SEM images. Nonetheless, the expansion of the holes is observed to be less severe at the center of the wafer when compared to the edge.

At 650 °C, the Ni(Pt)Si films is severely agglomerated as most of the SEM acquisition area are covered by the dark contrast, *i.e.,* a more significant area of exposed Si substrate. To properly quantify the severity of the agglomeration, the area of the exposed Si (µm²) on the surface can be extracted using post-processing software such as IP-SDK (Reactiv'IP Smart Image processing) and ImageJ. Precise segmentation using machine learning is performed to extract the surface area of the exposed Si, as illustrated in Fig. 66.

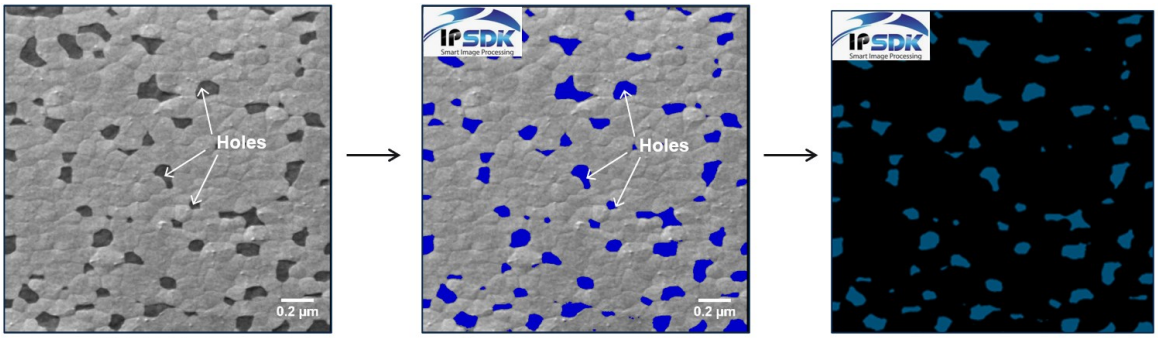


Figure 66. Examples of precise segmentation using the Smart Segmentation feature of the IP-SDK software. The surface area of exposed Si substrate, $S_{exposed_Si}$ (µm²) is extracted for 11 nm Ni(Pt)Si film post RTAD 600 °C (NiSi_SiC2x40).

The extracted surface area is then used to generate the fraction of exposed surface area of Si, f_{Si}(%), calculated using the following formula:

$$f_{Si}(\%) = \frac{S_{exposed_Si}}{S_{ROI}} * 100 \qquad \textbf{Equation 19}$$

With f_{Si}(%), the fraction of exposed Si on the surface during the agglomeration phenomenon, $S_{exposed_Si}$ (µm²), the surface area of exposed Si and S_{ROI} (µm²) is the surface of

the region of interest (ROI). The ROI is fixed to 2 x 2 µm², corresponding to the size of the acquisition area of the SEM image. The evolution of f_{Si}(%) as a function of RTAD temperatures (500 – 650 °C) is plotted in Fig. 67 and their values are summarized in Table 13. An inset is included in Fig. 67 for better evaluation of the evolution of f_{Si}(%) between 550 and 600 °C.

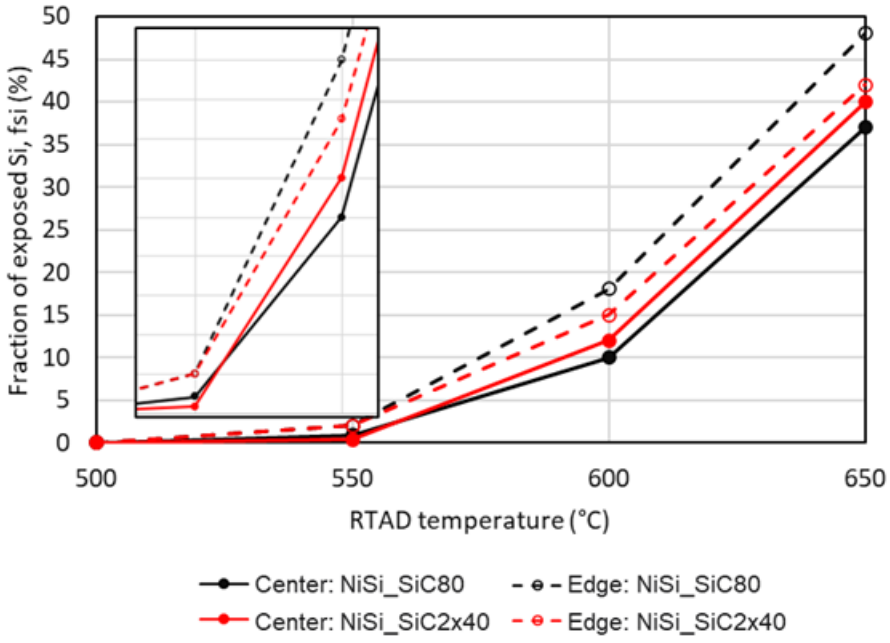


Figure 67. Top view tilted-SEM images measured the (a) center and (b) edge of the wafer for the NiSi_SiC2x40 and NiSi_SiC80 sample. An inset corresponding to a zoom of f_{Si}(%) between 550 and 600 °C is included.

For the NiSi_SiC2x40 sample, the evolution of f_{Si}(%) extracted from the center of the wafer, shown in Fig. 67, starts with a plateau between 500 and 550 °C. This is followed by a rise to 10 % of exposed Si area at 600 °C due to holes expansion. The trends continue to evolve in the same fashion, with a more abrupt slope, between 600 and 650 °C. Similar trends is observed for the NiSi_SiC80 sample.

The evolution of f_{Si}(%) at the edge of the wafer has been determined and plotted in Fig. 67 using dashed lines. The evolution of f_{Si}(%) for both of the SiCoNi treatments appears to follow similar trends at the center. However, the value of f_{Si}(%) is slightly more significant at the edge of all the samples.

Moreover, for similar RTAD temperature, the difference between the fraction of exposed Si, f_{Si}(%) at the center and the edge of the wafer can be calculated.

As shown in Table 13, the values of the $f_{Si}(\%)$ extracted from each SEM images for RTAD in the range of 500 and 650 °C using IPSDK software show significant difference between the fraction of the exposed Si at the center of the wafer, $f_{Si}(\%)_{Center}$ and the edge, $f_{Si}(\%)_{Edge}$.

Table 13. Summary of the fraction of the exposed Si, $f_{Si}(\%)$ extracted from tilted-SEM for NiSi_SiC2x40 and NiSi_SiC80 samples.

Sample	Measurement site	$f_{Si}(\%)$ 500 °C	$f_{Si}(\%)$ 550 °C	$f_{Si}(\%)$ 600 °C	$f_{Si}(\%)$ 650°C
NiSi_SiC2x40	Center	0	0.32	12	40
	Edge	0	2	15	42
NiSi_SiC80	Center	0	0.84	10	37
	Edge	0	2	18	48

For a given RTAD temperature, the $\Delta f_{Si}(\%)$ is given by:

$$\Delta f_{Si}(\%) = f_{Si}(\%)_{Edge} - f_{Si}(\%)_{Center} \quad \text{Equation 20}$$

With $f_{Si}(\%)_{Edge}$, the fraction of the exposed Si at the edge of the wafer and the $f_{Si}(\%)_{Center}$ the fraction of the exposed Si at the center of the wafer. The value of Δf_{Si} is summarized in Table 14 for each of RTAD temperature.

Table 14. Summary of the fraction of the exposed Si, $f_{Si}(\%)$ extracted from tilted-SEM images of 11 nm Ni(Pt)Si films formed on Si substrate for NiSi_SiC2x40 and NiSi_SiC80 samples.

Sample	$\Delta f_{Si}(\%)$ 500 °C	$\Delta f_{Si}(\%)$ 550 °C	$\Delta f_{Si}(\%)$ 600 °C	$\Delta f_{Si}(\%)$ 650°C
NiSi_SiC2x40	0	1.68	3	2
NiSi_SiC80	0	1.16	8	11

The Δf_{Si} at 500 °C shows no difference between the center and the edge of the wafer as no hole formation are detected at this temperature. At 550 °C, the Δf_{Si} shows a slight increase for both of the SiCoNi treatments. This is due to the presence of the small holes previously described in Figs. 65 and 67. Nonetheless, the difference between the Δf_{Si} of both

samples is quite low, indicating that the SiCoNi 2x40 may not have an impact on holes nucleation. At further RTAD temperatures, *i.e.,* 600 and 650 °C, the Δf_{Si} present a more significant values for both samples. Furthermore, when comparing the Δf_{Si} between both of the SiCoNi treatments, it is clear that the agglomeration at the edge of wafer NiSi_SiC80 is more severe.

3.2.3.3 Conclusions of part 1-B

In study 1-B, the Rs measurements demonstrated an increase towards very high resistance values (around 103 Ω/sq) for high temperatures annealing for both of the samples, *i.e.,* NiSi_SiC2x40 and NiSi_SiC80. However, depending on the SiCoNi treatments, the slope of the Rs curve is different. The slope of the silicide Rs in the case the SiCoNi 2x40 process is more gradual as compared to the SiCoNi 80, suggesting better thermal stability when SiCoNi 2x40 treatment is used.

Further inspection of the morphology of the Ni(Pt)Si films by SEM imaging showed that the holes nucleation occurs at temperatures as low as 550 °C. The size and quantity of the holes appears to be more significant at the edge of the wafer in both cases. This may indicate that there is no direct impact of the SiCoNi treatment on holes nucleation. However, upon annealing at higher temperatures, the fraction of the exposed Si, f_{Si}(%) begins to show significant differences depending on the SiCoNi treatment used.

Finally, the difference of f_{Si}(%) between the center and the edge of the wafer is estimated to be around 3 % in the case of the SiCoNi 2x40 treatment. Similar analysis in the case of SiCoNi 80 showed that the Δf_{Si} is estimated at 8 % between the center and the edge of the wafer. Further annealing at 650 °C shows similar observations, indicating that agglomeration at the edge of the wafer is more severe when the SiCoNi 80 treatment is used.

3.3 Part 2: Annealing schemes

3.3.1 Experimental setup

11 nm of Ni(Pt)Si films are formed on blanket Si(100) wafers by four different annealing schemes: partial reaction annealing, laser annealing, total reaction annealing, and one-step annealing (Figs. 51 and 68). The initial Ni(10 at. % Pt) film thickness is adjusted to 6 nm for the total and one-step annealings (10 nm instead for the partial reaction and laser annealing) due to full consumption of Ni(10 at. % Pt) film. This allowed to obtain Ni(Pt)Si thin films of equal thickness (about 11 nm), regardless of the chosen annealing scheme.

NiPt films are deposited by physical vapor deposition (PVD) sputtering of a Ni(10 at. % Pt) target. Prior to Ni(10 at. % Pt) deposition, all Si substrates are subjected to a wet clean using a HF-0.5% diluted solution followed by an in-situ remote plasma clean using NF_3/NH_3 gases to remove Si native oxide. A 10 nm TiN capping film is then deposited on top of the metal layer to prevent any oxidation.



Figure 68. Schematics of the different annealing schemes studied for the formation of 11±1 nm Ni(Pt)Si films. The obtained silicide films are then subjected to additional high-temperature annealing (RTAD) between 500 and 700 °C/30 s for agglomeration assessment.

For the first annealing scheme (partial annealing), the Ni(Pt)Si film formation followed the conventional silicide integration scheme, *i.e.,* the salicide process: after Si substrate surface cleaning and Ni(10 at. % Pt) deposition, an initial rapid thermal annealing (RTA), named RTA1, at 230 °C/20 s is carried out, to form a Ni-rich silicide phase. The remaining unreacted metal is then removed along with the TiN capping layer using a selective etching (SE) step inside a hot H_2SO_4/H_2O_2 solution. Finally, a second RTA, denoted RTA2, is applied to form the desired Ni(Pt)Si phase at 390 °C for 30 s. For an initial 10 nm-Ni(10 at. % Pt) film, this annealing scheme typically resulted in 11±1 nm thick Ni(Pt)Si film.

For the second annealing scheme (DSA laser annealing), similar steps to that of the partial annealing are carried out, except for the second annealing, as shown in Fig. 68. More precisely, a similar RTA1 thermal budget is performed, but the RTA2 is replaced with a DSA laser annealing (Vantage Astra chamber) set to a wavelength of 810 nm and annealing duration of 0.25 ms to form 11 nm-thick Ni(Pt)Si film.

For the third annealing scheme (total annealing), both the deposited Ni(10 at. % Pt) thickness and the RTA1 thermal budget are varied. The deposited metal thickness is reduced to 6 nm, while RTA1 is increased to 240 °C/30 s allowing full metal consumption during the first annealing.

In the first three schemes (partial, laser, and total annealings), an additional annealing step is implemented to evaluate the film behavior at high thermal budget, named RTAD (see Fig. 68). The range of temperatures for RTAD is between 500 and 700 °C, and the annealing duration is kept constant and fixed to 30 seconds, regardless of the scheme used.

The fourth annealing scheme (one-step annealing) involved only a single annealing step. Thus, the RTAD is directly applied to the 6 nm Ni(10 at. % Pt) film to form and evaluate Ni(Pt)Si film behavior at high temperature simultaneously. The TiN capping is removed only after RTAD in the case of one-step annealing. The list of samples used for this study is summarized in Table 6 at the beginning of this chapter.

Four-point probe measurements (Rs) are applied to all wafers using a 49-point contour map with 3 mm edge exclusion using the KLA Tencor RS100 resistivity mapping system. Both tilted and high-resolution scanning electron microscopy (SEM) are performed with the Applied Materials SemVision G5 and Gemini 500 Zeiss microscopes, to evaluate the microstructures of Ni(Pt)Si films*, e.g.,* grain size, area fraction of exposed Si (%), and grain shapes. Texture characterizations are performed using the electron backscatter diffraction (EBSD) technique via the EDAX Hikari super detector, to assess grain orientations, misorientations, and their spatial distribution. SEM images are treated using ImageJ and IPSDK software. EBSD maps are indexed using Orientation Imaging Microscopy (OIM) Analysis software.

As constant thickness is a key parameter in our study, the thickness of Ni(Pt)Si films formed by each annealing scheme is measured using the ellipsometry technique. The results are displayed in Table 15, for each annealing scheme.

Table 15. The thickness of Ni(Pt)Si films measured by ellipsometry, formed via various annealing schemes *i.e.,* for all samples: NiSi_partial, NiSi_laser, NiSi_total, and NiSi_onestep.

Sample	Ni(Pt)Si thickness (nm)	Standard deviation (nm)
NiSi_partial	11.5*3*	0.53
NiSi_laser	10.8*6*	0.14
NiSi_total	11.3*5*	0.20
NiSi_onestep	12.5*9*	0.43

The median thickness is around 11.6 nm, and the standard deviation is very low, indicating a high thickness uniformity among the studied samples.

3.3.2 Sheet resistance, Rs

In order to assess the impact of the various annealing schemes (partial, laser, total, and one-step annealings) on the stability of the Ni(Pt)Si thin film, the samples obtained after RTAD annealing (500 °C, 550 °C, 600 °C, 650 °C, and 700 °C) are characterized by Rs and tilted-SEM imaging. The RTAD annealing duration is 30 seconds for all samples.

Fig. 69 shows the sheet resistance, Rs, measurements for Ni(Pt)Si films formed by the different annealing schemes after RTAD annealing.

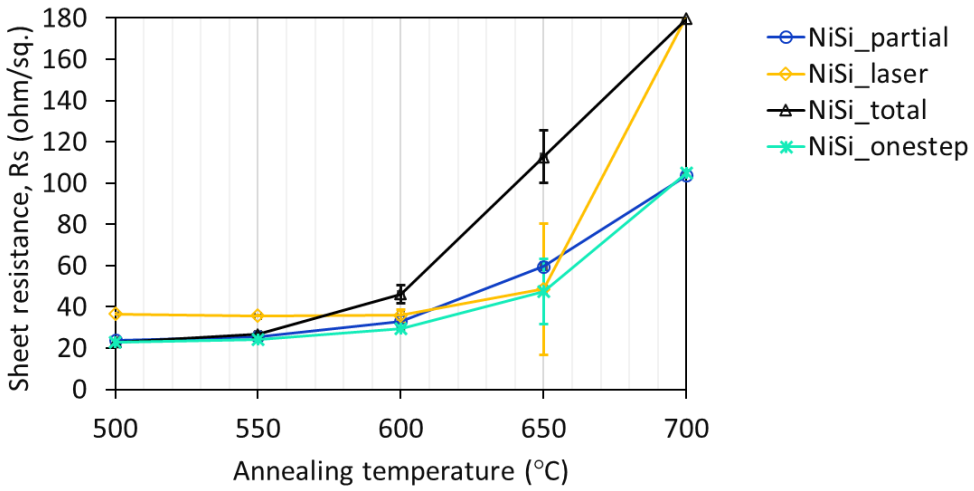


Figure 69. Sheet resistance, Rs, of 11±1 nm Ni(Pt)Si films formed by the four types of annealing schemes (NiSi_partial, NiSi_laser, NiSi_total, and NiSi_onestep) after high-temperature annealing, RTAD.

As plotted in Fig. 69, the Rs trends begin with a plateau between 500 and 550 °C. The Rs of silicide films for all annealing schemes remains between 20 and 40 Ω/sq. The silicide film formed by laser annealing exhibits a higher Rs.

Beyond 550 °C, the Rs begins to rise gradually, especially for the NiSi_partial, NiSi_total, and NiSi_onestep samples. Meanwhile, the increase of Rs for the NiSi_laser sample extends to a higher temperature (600 °C), suggesting better film stability. At 700 °C, the Rs is completely deteriorated (indicated by drastic Rs increase) for all samples.

Table 16 reports the incremental rise of Rs, noted as ΔRs, between two successive annealing temperatures to compare the degradation of the Rs of the silicide films formed by

the different annealing schemes. As an example, the ΔRs between 500 and 550 °C is obtained as follows:

$$\Delta Rs\ (550 - 500\ °C) = Rs\ (550\ °C) - Rs\ (500\ °C) \qquad \text{Equation 21}$$

This allows evaluation of the increment in Rs with respect to the RTAD temperatures.

Table 16. Calculated increment of Rs, ΔRs (Ω/sq) of 11 nm Ni(Pt)Si films formed by different annealing schemes (NiSi_partial, NiSi_laser, NiSi_total, and NiSi_onestep) for increasing RTAD temperatures.

Sample	ΔRs (Ω/sq) 500 – 550 °C	ΔRs (Ω/sq) 550 – 600 °C	ΔRs (Ω/sq) 600 – 650 °C
NiSi_partial	1.8	7	26
NiSi_laser	0	0.2	12
NiSi_total	3.8	19	66
NiSi_onestep	1.5	5	18

In the range of 550 to 600 °C, the ΔRs for the NiSi_total sample is the most significant with a $\Delta Rs^{Total}(600 - 550\ °C) = 19\ \Omega/sq$, suggesting higher sensitivity to degradation at a relatively low temperature. For the other annealing schemes, the ΔRs is less than 10 Ω/sq for the same annealing temperature range. At a higher temperature range (600 – 650 °C), a sharp Rs augmentation is observed for all samples. The lowest ΔRs is recorded for NiSi_laser sample corresponding to only 12 Ω/sq. This suggests better film stability, while the silicide films formed by the total annealing continues to show significant Rs deterioration with ΔRs of around 66 Ω/sq.

3.3.3 Tilted-SEM – film morphology

To verify the Ni(Pt)Si film morphology, SEM observations are performed on each sample after RTAD annealing. Fig. 70 shows the top view SEM image measurements tilted by 45° during acquisition in order to better reveal the thin film grain boundaries.

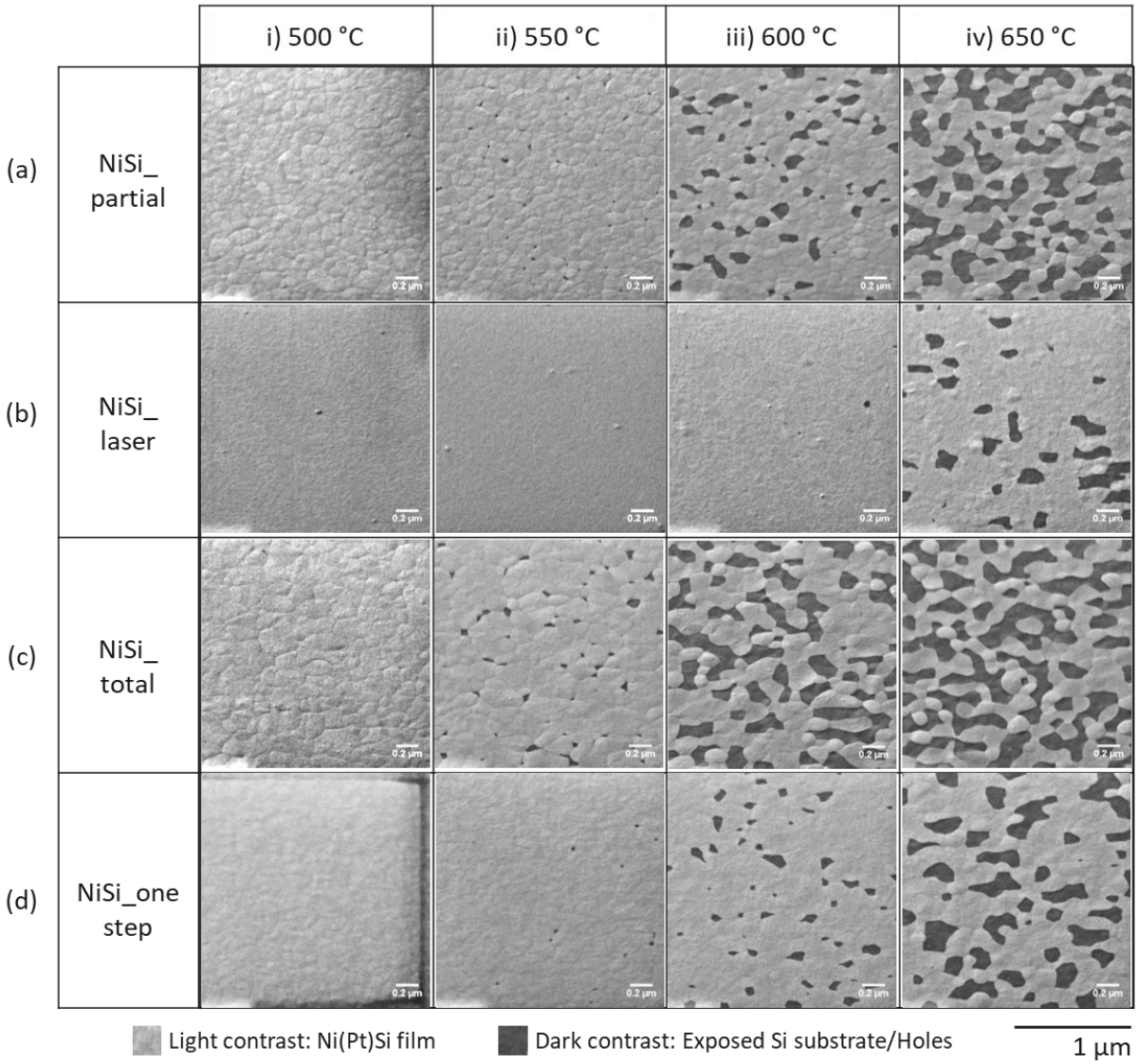


Figure 70. Top view tilted-SEM images of 11±1 nm Ni(Pt)Si films after RTAD treatments (i) 500 °C, (ii) 550 °C, (iii) 600 °C, (iv) 650 °C, for all of the samples: (a) NiSi_partial, (b) NiSi_laser, (c) NiSi_total, (d) NiSi_onestep. Light grey and dark grey contrasts represent Ni(Pt)Si and exposed Si substrate/holes respectively.

At 500 °C (Figs. 70.i – (a), (b), (c), (d)), the surface is fully covered by the silicide film with varying surface roughness and grain boundary detection. Especially for NiSi_partial and

NiSi_total samples, the grain boundaries can clearly be distinguished. However, no clear grain boundaries are detected for NiSi_laser and NiSi_onestep samples, which may indicate low average grain size.

At 550 °C (Figs. 70.ii – (a), (b), (c), (d)), there is a clear evolution of Ni(Pt)Si film morphology for all the annealing schemes, except for the NiSi_laser sample. Indeed, the associated SEM image (Fig. 70.ii – (b)) indicates no morphology degradation, *i.e.,* absence of dark grey areas indicating absence of hole formation for the silicide formed by the laser annealing. On the contrary, the apparition of holes is observed for partial, total, and one-step annealings at this RTAD temperature. Out of the three, the nucleated holes are clearly more significant in both quantity and size for the NiSi_total sample. This shows that the agglomeration of silicide film is at a slightly more advanced stage.

At 600 °C (Figs. 70.iii – (a), (b), (c), (d)), the holes continue to expand, particularly for partial, total, and one-step annealing. The agglomeration is most severe for NiSi_total sample at this RTAD temperature (Fig. 70.iii(c)). The holes appear to be connected, presenting large areas of exposed Si substrate (as represented by the dark-grey contrast), while for NiSi_laser sample (Fig. 70.iii(b)), the nucleation of small holes starts to develop, as can be seen by the presence of the small dark areas in the SEM image.

At 650 °C (Figs. 70.iv – (a), (b), (c), (d)), all the silicide films are agglomerated. The silicide films formed by the partial and total annealing (NiSi_partial and NiSi_total) exhibit the most severe agglomeration (Fig. 70.iv – (a) & (c)). Meanwhile, for NiSi_laser and NiSi_onestep samples, the agglomeration remains moderate (Figs. 70.iv – (b) & (d)).

The evolution of f_{Si}(%) as a function of RTAD temperatures (500 – 700 °C) is plotted in Fig. 71 and their values are summarized in Table 17.

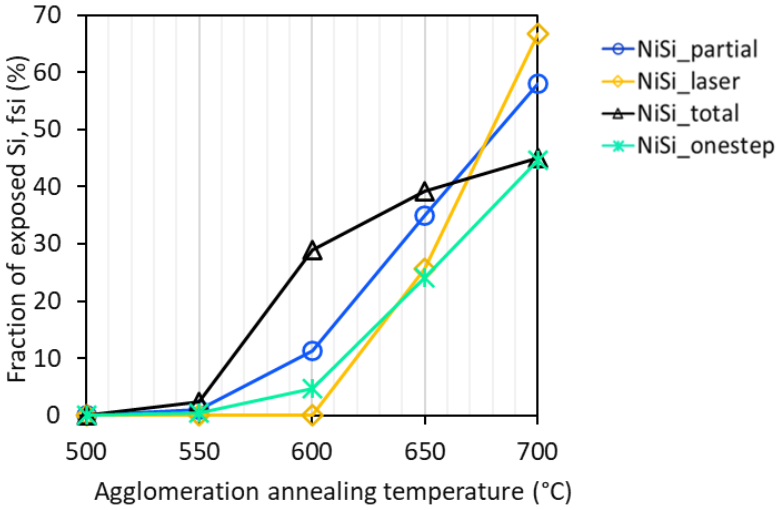


Figure 71. Evolution of the fraction of exposed Si, f_{Si}(%), during the agglomeration of 11±1 nm Ni(Pt)Si films formed by different annealing schemes (NiSi_partial, NiSi_laser, NiSi_total, and NiSi_onestep) extracted from IPSDK software.

For NiSi_partial sample, the evolution of the f_{Si}(%) in Fig. 71 starts with a plateau between 500 and 550 °C, followed by an increase to 10 % of exposed Si area at 600 °C due to the agglomeration phenomenon. The trend continues to evolve in the same fashion at 650 and 700 °C as the f_{Si}(%) continues to show an increment up to 40 and 50 %, respectively.

For NiSi_laser sample, a different evolution of f_{Si}(%) is clearly observed. As shown in Fig. 71, the f_{Si}(%) remains at 0 %, indicating the absence of holes and agglomeration up to 600 °C. As the Ni(Pt)Si film is annealed at higher RTAD temperatures, *i.e.,* 650 – 700 °C, the f_{Si}(%) rises drastically up to at least 30 %.

For NiSi_total sample, Fig. 71 shows that the evolution of the f_{Si}(%) begins with a slight increase for RTAD between 500 and 550 °C. Upon the application of a higher thermal budget of 600 °C, the f_{Si}(%) displays the most significant increment up to 30 % when compared to other schemes at this temperature range. At higher RTAD temperatures, the trends of f_{Si}(%) clearly differ to those of the other annealing schemes that show a continuous rise in f_{Si}(%). In the present case, f_{Si}(%) seems to increase only slightly beyond 600 °C, suggesting a potential saturation plateau.

As for NiSi_onestep sample, the f_{Si}(%) trends in Fig. 71 also begin with a plateau followed by a more gradual increase in f_{Si}(%) when compared to that of the annealing

schemes. Beyond 600 °C, the rise of the f_{Si}(%) is significantly more drastic and a similar trend continues up to 700 °C.

Table 17. Summary of the fraction of exposed Si, f_{Si}(%) during the agglomeration of 11±1 nm Ni(Pt)Si films formed by different annealing schemes (NiSi_partial, NiSi_laser, NiSi_total, and NiSi_onestep).

Sample	f_{Si}(%) 500 °C	f_{Si}(%) 550 °C	f_{Si}(%) 600 °C	f_{Si}(%) 650 °C	f_{Si}(%) 700 °C
NiSi_partial	0	1.0	11.0	34.9	58.1
NiSi_laser	0	0.0	0.1	25.7	66.7
NiSi_total	0	2.5	28.9	39.2	44.9
NiSi_onestep	0	0.5	4.7	24.2	44.7

The evolution of the f_{Si}(%) shows a strong correlation with the Rs measurements previously described in section 3.3.2. Moreover, the evolution of the f_{Si}(%) during the agglomeration of Ni(Pt)Si film formed by total reaction is clearly different than the other annealing schemes. Indeed, the trends of f_{Si}(%) for NiSi_total sample shows a gradual evolution beyond 600 °C, as opposed to a drastic rise in the other annealing schemes in this temperature range. The f_{Si}(%) trends for NiSi_partial and NiSi_onestep samples show similar evolution, starting with a gradual increase followed by a more drastic rise beyond 600 °C. However, as for NiSi_laser sample, the f_{Si}(%) plateau extends to higher RTAD temperature (600 °C) followed by a significant increase at higher temperatures.

3.3.4 High-resolution SEM – grain size

To evaluate the evolution of the grain size during agglomeration phenomenon, high-resolution scanning electron microscopy (HRSEM) characterizations are performed. The HRSEM images illustrated in Fig. 72 are obtained at specific RTAD temperatures for each annealing scheme corresponding to two morphological states: non-agglomerated and slightly agglomerated Ni(Pt)Si films.

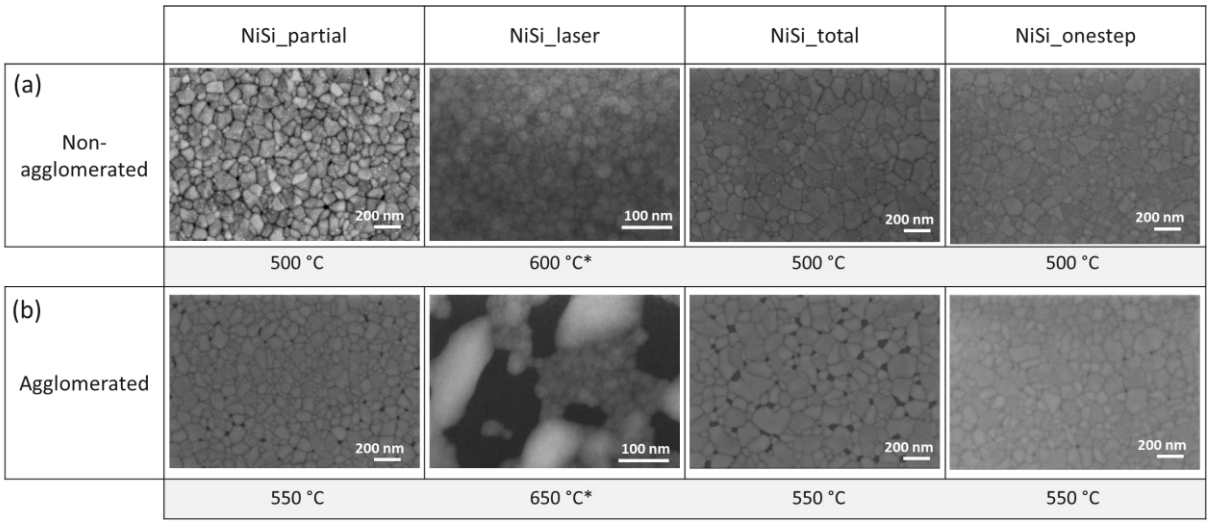


Figure 72. High-resolution SEM (HRSEM) images showing grains and grain boundaries for 11±1 nm-thick Ni(Pt)Si films formed by different annealing schemes in two states: (a) non-agglomerated and (b) agglomerated.

**Note that the HRSEM images for NiSi_laser sample are taken post-RTAD: 600 – 650 °C, since agglomeration is delayed to higher RTAD temperatures.*

As shown in Fig. 72(a), the grain boundaries are visible for all samples. In this way, the evaluation of the grain size distribution can be performed more precisely. The HRSEM image for NiSi_laser sample in Fig. 72(a) is at a higher magnification (200kX magnification instead of 50kX magnification used for other samples), due to the presence of very fine Ni(Pt)Si grains. Nevertheless, Fig. 72(b) shows the slightly agglomerated state of Ni(Pt)Si film for all samples. For both NiSi_partial and NiSi_onestep samples, the presence of small holes is observed. Meanwhile, for NiSi_total sample, the holes is larger, and more interestingly, these holes show a significant increase in size and quantity, indicating more advanced stages of morphological degradation.

For NiSi_laser sample, the agglomeration is slightly different. Indeed, the nucleation of holes can be expected to occur between 600 and 650 °C, since the agglomeration appears to be quite severe at 650 °C. Moreover, the HRSEM images also show the presence of large grains surrounding a hole as opposed to the non-agglomerated regions, which consist in fine grains. This indicates that an abnormal grain growth phenomenon may be involved.

The average if initial grain size, D (nm), is extracted for non-agglomerated Ni(Pt)Si films. Around 300 grains for each sample are measured using ImageJ software based on the HRSEM images, and the results are summarized in Table 18. The determination of the average grain size, D, consists in a contrast correction and binarization of the raw HRSEM images. The binarized images are then filtered to remove any noise. The final step consists in the extraction of the diameter length in two directions using an equivalent ellipse feature, and the mean is calculated from the two measured diameters.

Table 18. Summary of the average values of the grain size, D (nm), estimated from more than 300 grains using ImageJ software of 11±1 nm Ni(Pt)Si thin films formed by different annealing schemes (NiSi_partial, NiSi_laser, NiSi_total, and NiSi_onestep).

Sample	Initial average grain size (before agglomeration)**, D** (nm)
NiSi_partial	109
NiSi_laser	50
NiSi_total	127
NiSi_onestep	100

As illustrated in Table 18, the silicides grains in the case of NiSi_partial and NiSi_onestep samples appear to exhibit similar average grain size of around 100 nm. For NiSi_laser sample, the average grain size is drastically reduced by 50 % with respect to other annealing schemes. Large silicide grain size (average value around 127 nm) is determined after the total annealing scheme.

3.3.5 Preferential orientations & textures

To evaluate the preferential orientations and evolution of thin film textures during agglomeration, EBSD characterizations are performed to obtain orientation maps and pole figures. The ESBD orientation maps are presented in Fig. 73 and are characterized for samples at specific RTAD temperatures corresponding to non-agglomerated and moderately agglomerated states.

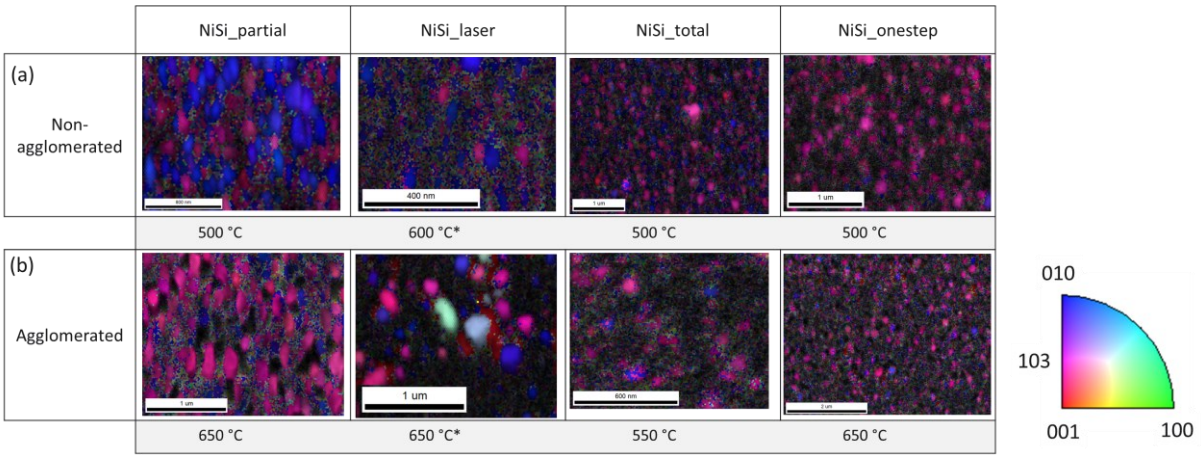


Figure 73. EBSD orientation map for (a) non-agglomerated, and (b) agglomerated 11±1 nm-thick Ni(Pt)Si films on Si(100) substrate formed by the different annealing schemes (NiSi_partial, NiSi_laser, NiSi_total, and NiSi_onestep). Pink-colored grains represent Ni(Pt)Si-(013) planes, blue-colored grains represent Ni(Pt)Si-(010) planes, and dark areas correspond to unindexable areas due to very fine grains (detection limits ≈ 40 nm).

The EBSD orientation maps are illustrated in Fig. 73 for both the non-agglomerated (Fig. 73(a)) and agglomerated (Fig. 73(b)) states of the silicide films. The colors displayed in EBSD maps are set up through the stereographic projection for orthorhombic crystal in the bottom quadrant of Fig. 73. Different colors correspond to different orientations; for example, blue, red, and green colors represent the (010), (001), and (100) orientations.

As shown in Fig. 73, the orientation maps consist of three principal colors: pink, blue, and black. The pink-colored grains correspond to the (013) orientation, while the blue-colored grains correspond to the (010) orientation. The black color represents areas with a low confidence index, indicating non-reliable indexation of the orientation due to technical limitations.

Nevertheless, for NiSi_partial sample, there is clear evidence of the evolution of the preferential orientation during agglomeration. The initial state in Fig. 73(a) shows that grains are mostly oriented in the (010) direction (represented in blue color), while in Fig. 73(b), the remaining grains after the agglomeration phenomenon are principally oriented along the (013) direction (represented in pink).

For NiSi_laser sample, the silicide film consists of mostly very fine grains (see Table 18) that are difficult to index. The film presents two principal orientations before the agglomeration phenomenon: (010) and (013). After the agglomeration, there is an increase in pink (013)-oriented grains.

For NiSi_total sample, both (010) and (013) orientations are detected, indicating that the silicide grains have two main orientations before agglomeration. After the agglomeration, the silicide films appear to have a reduced number of grains oriented along the (010) direction.

For NiSi_onestep sample, there is a clear change in the main initial orientations: the grains oriented in the (010) direction seems to be fewer in quantities. After the agglomeration phenomenon, the grains oriented along the (013) directions seem to either increase or remain the same.

Further analysis is performed by extracting inverse pole figures (IPF) from these EBSD orientation maps to qualitatively compare the intensity of the (013) and (010) orientations before and after agglomeration. Fig. 74 shows the IPF of Ni(Pt)Si films formed by different annealing at two different stages: non-agglomerated and agglomerated state.

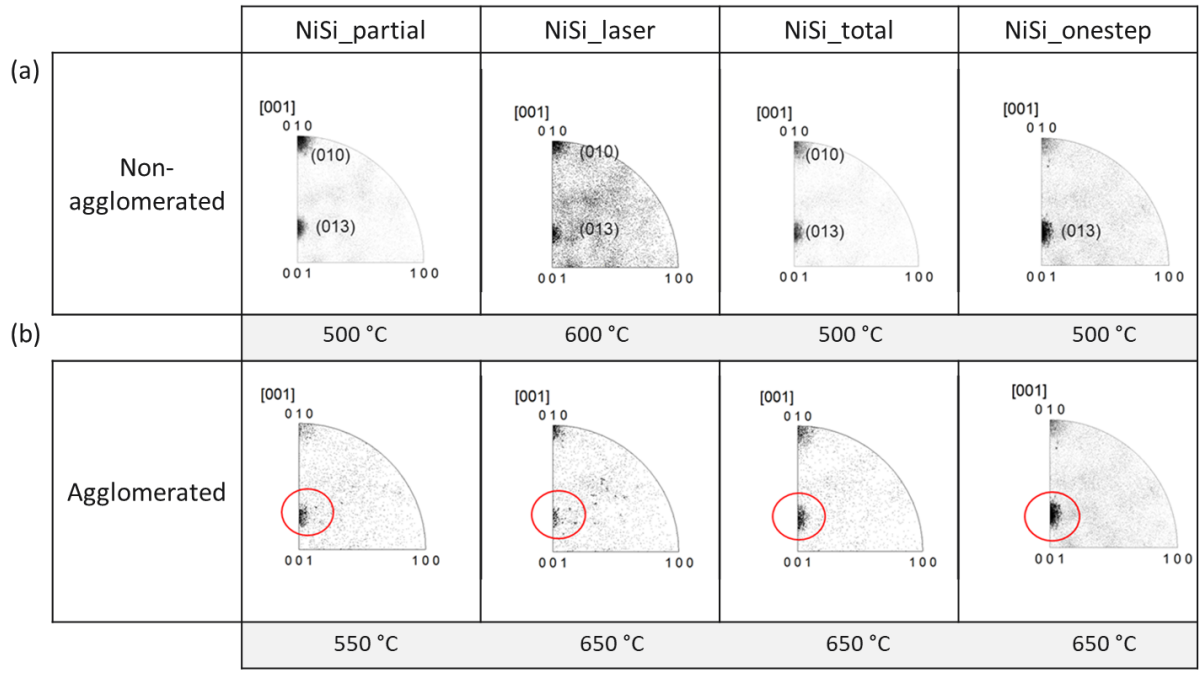


Figure 74. (a) Inverse pole figures (IPF) of Ni(Pt)Si thin films on Si(100) substrate at two different states (non-agglomerated and agglomerated) showing an evolution along the (013) orientation (red circle), while the intensity of the (010) orientation is reduced.

The evaluation of the preferential orientation may be performed using an intensity ratio between the (010) and (013) planes, since the sampling areas differ (*i.e.,* different number of grains quantified in each map), according to the annealing schemes. However, from the IPFs in Fig. 74(a), it is clear that two preferential orientations are present, and can be attributed to the (010) and (013) planes for the non-agglomerated Ni(Pt)Si films. However, in the case of NiSi_onestep, the IPF shows that the intensity of the (010) planes are significantly lower than the (013) planes.

After subsequent annealing at higher RTAD temperatures, the IPF in Fig. 74(b) shows that there is a reduction in the intensity of (010) planes for the partial annealing. Moreover, after the agglomeration, the (013)-oriented grains remain present in all cases, as circled in red in Fig. 74(b). These findings suggest that the Ni(Pt)Si-(013) grains may have a more favorable interfacial energy than the Ni(Pt)Si-(010) ones

Fig. 75 shows the pole figures (PF) of Ni(Pt)Si-(103) planes, one of the axiotaxy components typically observed in NiSi films [104].

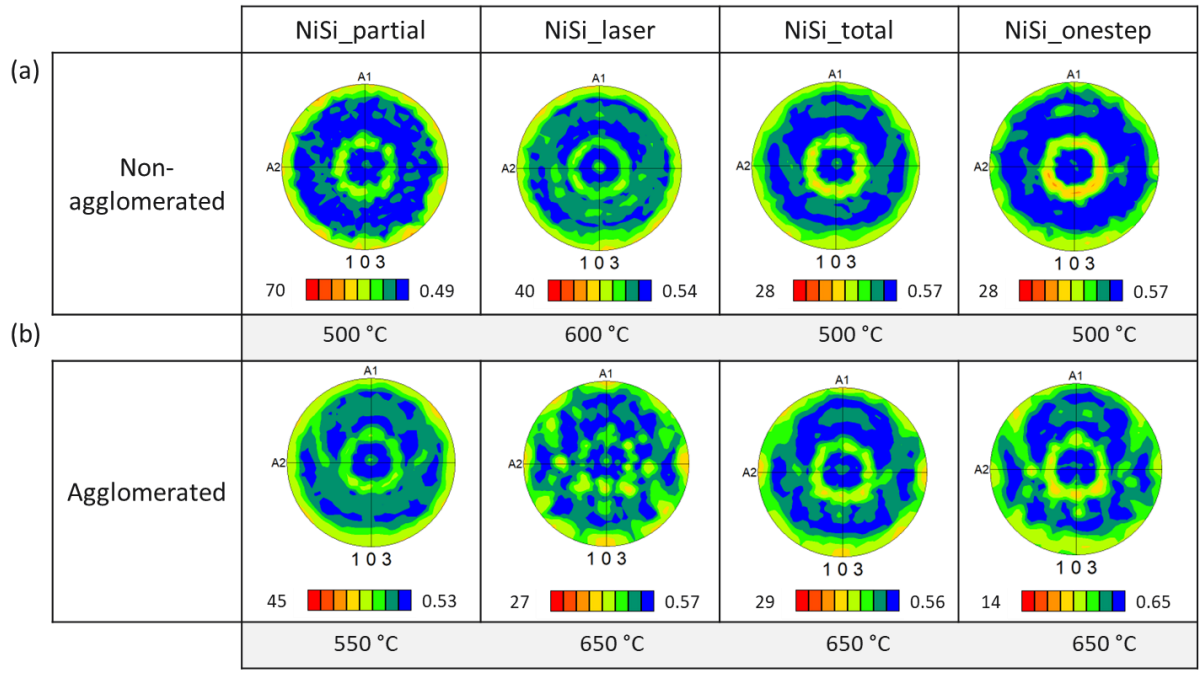


Figure 75. Pole figures (PF) of Ni(Pt)Si-(103) on Si(100) substrate at two different states: (a) non-agglomerated and (b) agglomerated illustrating the presence of fiber-like texture with off-normal axis. The color scale marker indicates red for maximum intensity, and blue for minimum.

As illustrated in Fig. 75(a), all the silicide films show a dominant fiber texture before the agglomeration phenomenon, as indicated by the presence of the concentric rings on the pole figures. Unlike the pole figures for partial, laser, and total annealings in Fig. 75(a), the pole figure of Ni(Pt)Si-(103) for NiSi_onestep sample presents a single ring. This observation is consistent with previous analysis for one-step annealing with preferential orientations along the (013) and (010) directions and a significantly lower intensity in the (010) plane.

For the agglomerated stage, there is a clear evolution of the Ni(Pt)Si film texture. In addition to the presence of the rings centered around the pole figure (fiber texture), the pole figures in Fig. 75(b) also show additional rings not centered around the pole figure. This is a strong indication of the presence of a fiber-like texture with an off-normal axis, *i.e.,* axiotaxy texture. This also suggests that there is a rise of the axiotaxy components during the agglomeration of the Ni(Pt)Si films.

Silicide textures and preferential orientations evolution are summarized in Table 19. No transrotational domains are observed in any sample.

Table 19. Summary of texture evolution before and after agglomeration of 11±1 nm Ni(Pt)Si thin films formed by different annealing schemes (NiSi_partial, NiSi_laser, NiSi_total, and NiSi_onestep), deduced from EBSD orientations maps of Figs. 73, 74, and 75.

Sample	Non-agglomerated		Agglomerated	
	Texture	Preferential orientations	Texture	Preferential orientations
NiSi_partial	fiber	010 & 013	off-normal fiber	013
NiSi_laser	fiber	010 & 013	off-normal fiber	010 & 013
NiSi_total	fiber	010 & 013	off-normal fiber	010 & 013
NiSi_onestep	fiber	010 & 013	off-normal fiber	010 & 013

3.3.6 Conclusions of part 2

For this study, four different samples following different annealing schemes (NiSi_partial, NiSi_laser, NiSi_total, and NiSi_onestep) are introduced to study their impacts on the stability of 11 nm Ni(Pt)Si films. For the first time, the thickness of the Ni(Pt)Si films is kept constant in all samples, regardless of the annealing schemes used.

Firstly, there is a strong correlation between the microstructure properties resulting from the different annealing schemes and the corresponding thermal stability of the obtained Ni(Pt)Si films. In particular, the drastic grain size reduction for NiSi_laser sample showed a significant effect on the thin film stability at higher temperature annealing. Ni(Pt)Si films formed by the laser annealing showed a delayed resistance by 50 °C, attributed to the reduction of the grain size. On the contrary, silicide films formed by the total annealing resulted in large grains, leading to higher sensitivity to agglomeration. From a technological point of view, this strongly suggests that total annealing schemes should be avoided for advanced 3D integration.

For the NiSi_onestep sample, pole figure analyses demonstrated that Ni(Pt)Si grains oriented along the (013) direction may be more beneficial to delay agglomeration. Pole figure analyses also showed a strong correlation between the agglomeration and the texture evolution. Consequently, the (103) axiotaxy components become increasingly significant during the agglomeration phenomenon. Adapting these different annealing strategies in industrial production may help improve the extendibility of the Ni(Pt)Si films in 3D advanced technologies.

3.4 Part 3: Impact of confinement on Ni(Pt)Si film in regular lines

3.4.1 Experimental setup

The experimental setup to determine the effect of confinement on the formation and agglomeration of the Ni(Pt)Si film is illustrated in Figs. 52 and 76. Cavalcante *et al.* [10] demonstrated that the degradation of the measured Rs on silicided linewidth occurs at a relatively lower temperature when the dimension of the linewidth is reduced. The Rs degradation has been correlated to the stability issue of the Ni(Pt)Si thin film.

Here, prior to the SALICIDE process, formation of confined structures is performed using photolithography steps and DIVA mask available at CEA-Leti. As presented in Fig. 76, different structures have been fabricated with a change in the distance between two dielectric lines (noted p for pitch) and schematized by an arrow. These structures are named in the following sections regular lines with specific pitch dimension, as summarized in table 7 at the beginning of this chapter.

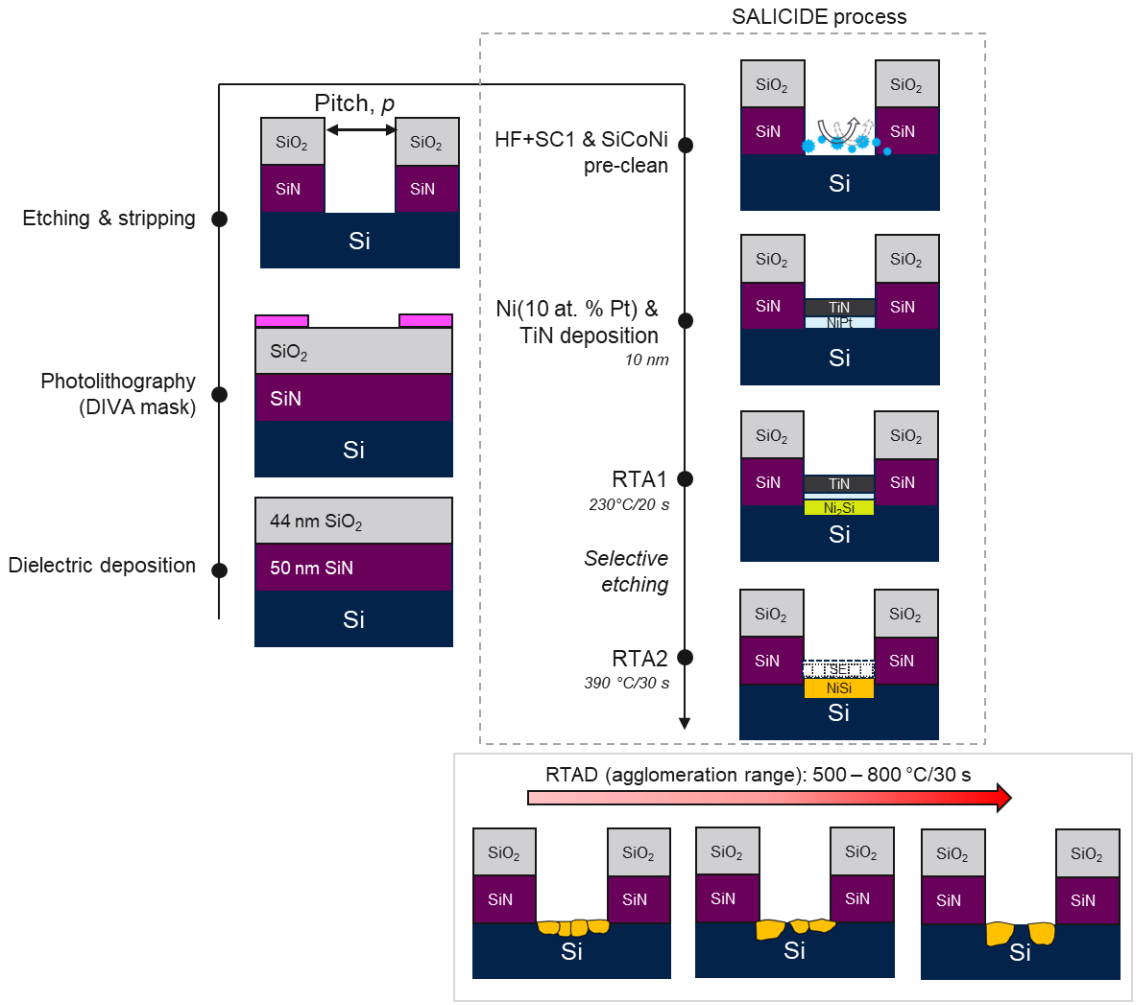


Figure 76. Schematics of the process steps used to form the regular silicided lines based on classical photolithography and SALICIDE process for the formation of 11 nm Ni(Pt)Si film on Si(100) substrate (for process details please refer to section 1.2.3).

The formation of these lines consists in the deposition of a dielectric stack of SiN and SiO_2 which will then be etched and stripped through the DIVA mask. This allows the definition of tight patterned trenches with exposed Si substrate at the bottom of the trenches. Each structure is repeated regularly within an area of 2x2 mm². Different structures with varying pitch, *p,* are available within a single wafer fabricated using the DIVA mask and this also includes the regular dielectric dots (*or squares*) as shown in Fig. 77.

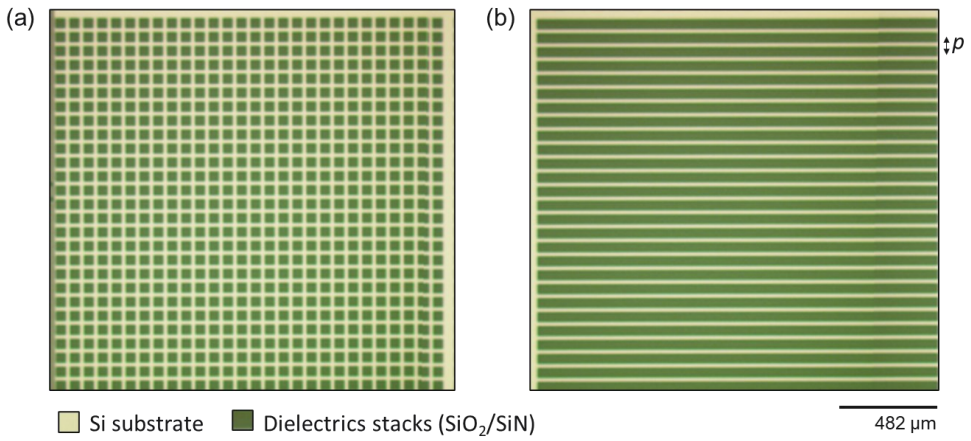


Figure 77. Top-view optical image of (a) dielectrics dots and (a) dielectrics lines regularly spaced by a pitch of *p*, repeated over an area of 2x2 mm² on a 300 mm Si wafer after patterning by DIVA mask.

A 10 nm NiPt layer is then deposited inside the trenches covered by the TiN layer after standard surface preparation steps. An 11 nm Ni(Pt)Si film is formed inside trenches following the SALICIDE process.

For better visualization, Fig. 78 shows top view SEM images of the different structures.

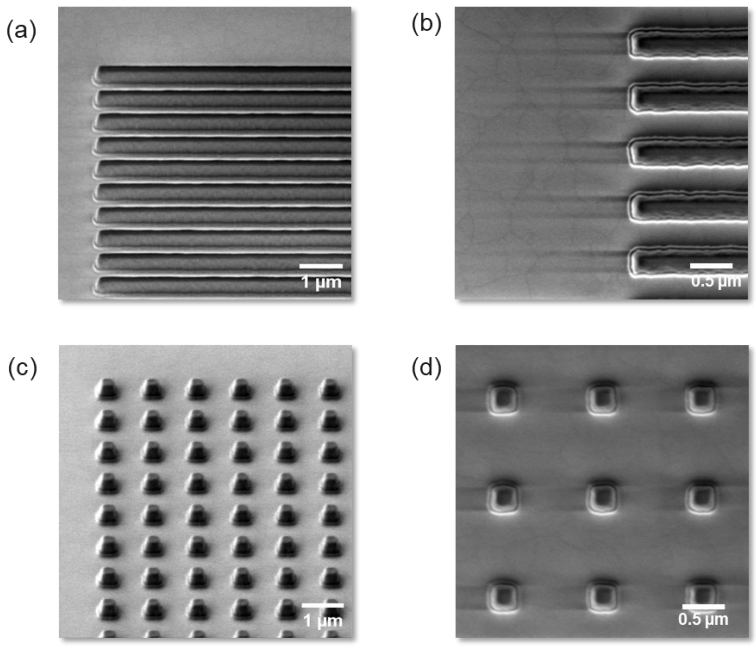


Figure 78. SEM images of two types of structures featured in the DIVA mask design presenting a regular patterning of dielectric and silicided lines in (a) and (b), and silicided substrate including some dielectrics squares in (c) and (d). Note that the (a) and (c) images are obtained through tilted SEM apparatus and (b) and (d) with a classical tool set.

In this study, we defined 4 types of structures which present typical dimensions of silicide active regions of recent microelectronics devices. A sample consisting of the square field is also introduced and could be also considered as “the least confined structure” (refer to table 7). Fig. 79 shows the four final structures after the complete SALICIDE process presenting the respective pitch of (a) 110, (b) 250, (c) 500 nm, and (d) the dielectric plots. 11 nm Ni(Pt)Si thin film is formed inside the trenches of different pitch size, *p*.

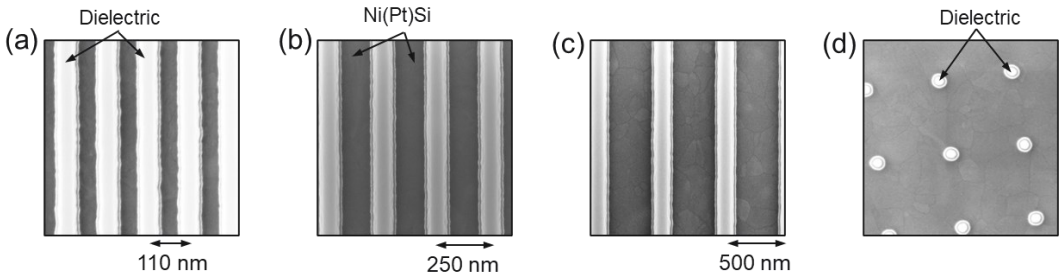


Figure 79. Top view HRSEM images of the four types of structures formed by regular silicided lines (a), (b) and (c) presenting different pitch dimensions respectively 110, 250 and 500 nm and dielectric dots (d). In the following sections these structures are named NiSi_Lines_110, NiSi_Lines_250, NiSi_Lines_500, and NiSi_Diel_dots.

The fifth sample included in this study is a blanket wafer following the SALICIDE process as previously presented in section 3.3 of this chapter. (or section 1.2.2 for a more general description)

All of the samples are then characterized post silicide formation and post-RTAD annealing using HRSEM imaging, ESBD, XRD, IPRSM, and GIWAXS measurements at European Synchrotron Research Facility (ESRF) on the BM02 beamline.

3.4.2 Influence of confinement in regular lines on Ni(Pt)Si agglomeration

Fig. 80 presents the top view SEM images showing the top surface of the 11 nm Ni(Pt)Si films after RTA2 annealing at (a) 390 °C and subsequent RTAD annealings: (b) 500 °C, (c) 550 °C, (d) 650 °C, and (e) 700 °C for all the previously presented structures. Three levels of contrast can be observed in these images corresponding to Ni(Pt)Si film in moderately light gray, dielectric stacks appearing in lightest gray, and exposed Si substrate in dark gray.

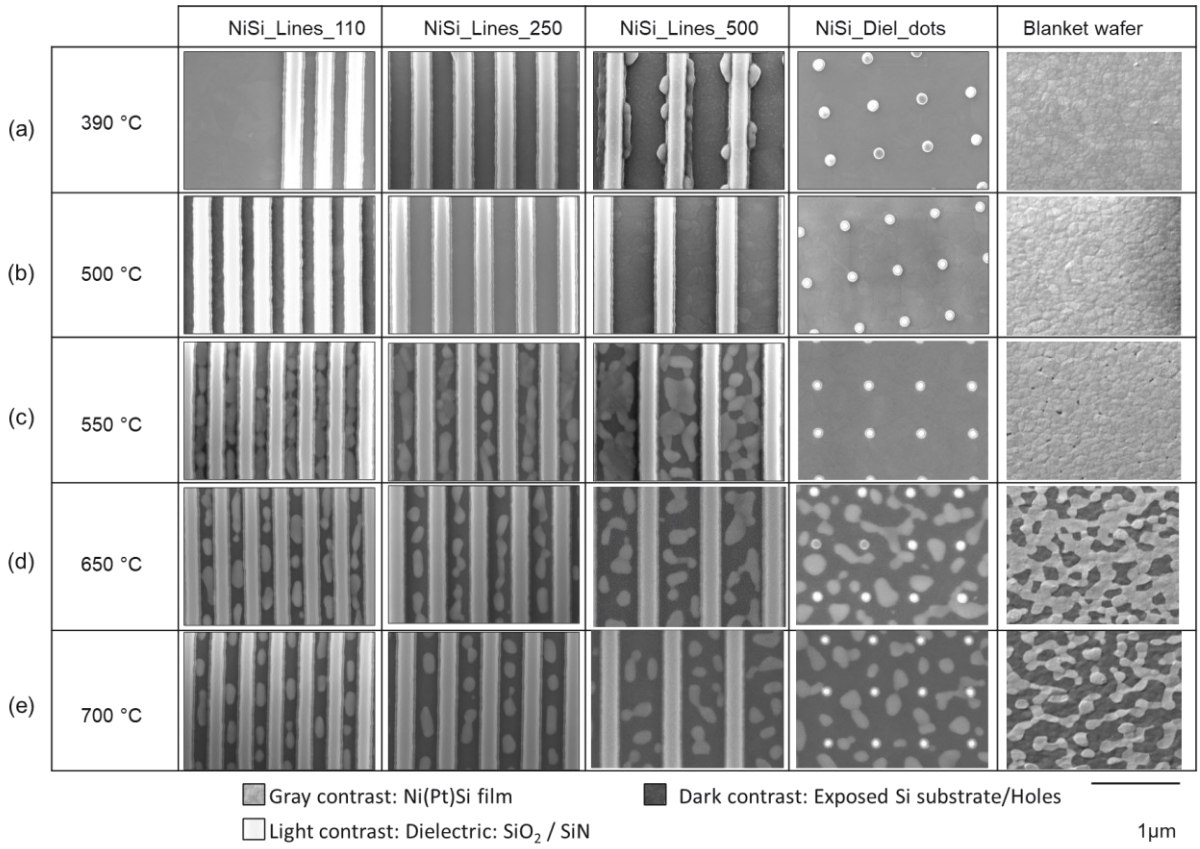


Figure 80. Top-view HRSEM images of 11 nm Ni(Pt)Si formed on confined structures (NiSi_Lines_110, NiSi_Lines_250, NiSi_Lines_500, and NiSi_Diel_dots) and top view tilted-SEM images measured on blanket wafer for different annealing temperatures (a) 390, (b) 500, (c) 550, (d) 650, and (e) 700 °C.

Further inspection of the SEM images in Figs. 80 – (a) and (b) after annealings at 390 °C and 500 °C shows minimal evolution of the morphology of the Ni(Pt)Si film as the silicide film remains continuous and uniform. The silicide film shows a complete coverage of

the surface of Si substrate inside the trenches, in between the dielectric dots, and on the blanket wafer. For NiSi_Lines_500 after annealing at 390 °C, unwanted oxide appears to be formed on the wall of the dielectric stacks.

Subsequent annealing at 550 °C induces a clear evolution of the morphology of the silicide film in all samples. Several small holes can be observed in particular for the NiSi_Diel_dots and NiSi_blanket samples, indicating the early stages of the agglomeration phenomenon. Nonetheless, hole expansion have occurred for Ni(Pt)Si film formed in the three regular lines samples: NiSi_Lines_110, NiSi_Lines_250, and NiSi_Lines_500. This suggests that agglomeration is more pronounced in regular lines compared to that of the NiSi_Diel_dots and NiSi_blanket.

At a higher annealing of 650 °C, a more advanced stage of agglomeration of the Ni(Pt)Si film can be seen in all samples. For NiSi_Lines_110 and NiSi_Lines_250, the agglomerates of Ni(Pt)Si are more elongated unilaterally with lesser connectivity (higher discontinuity). Contrarily, the agglomerates formed on NiSi_Lines_500 and NiSi_Diel_dots appear to be slightly more connected. At this annealing temperature, the agglomeration on the blanket wafer remains at a moderate stage. The exposed Si on the surface is less significant compared to silicide coverage, suggesting similarity to the stage of the expansion of holes.

Nevertheless, at 700 °C, severe agglomeration is detected for all samples as shown by the SEM images in Figs. 80(e). Isolated islands of Ni(Pt)Si can be observed particularly for NiSi_Lines_110, NiSi_Lines_250, NiSi_Lines_500 and NiSi_Diel_dots samples. The islands are more elongated unilaterally in both NiSi_Lines_110 and NiSi_Lines_250. Contrary observations are demonstrated in the SEM images of the NiSi_Lines_500, NiSi_Diel_dots, and NiSi_blanket samples. More precisely, the agglomerates remain connected in the case of the NiSi_blanket sample indicating that agglomeration may not yet achieve the final stages.

In order to precisely compare the degree of the agglomeration of both samples at each RTAD temperatures, the fractions of the exposed Si, f_{Si}(%) are extracted using IPSDK and ImageJ software as previously described in section 3.2.3.2.

Fig. 81 shows the plot of f_{Si}(%) as a function of the RTAD temperature. The values of the extracted f_{Si}(%) are summarized in Table 20.

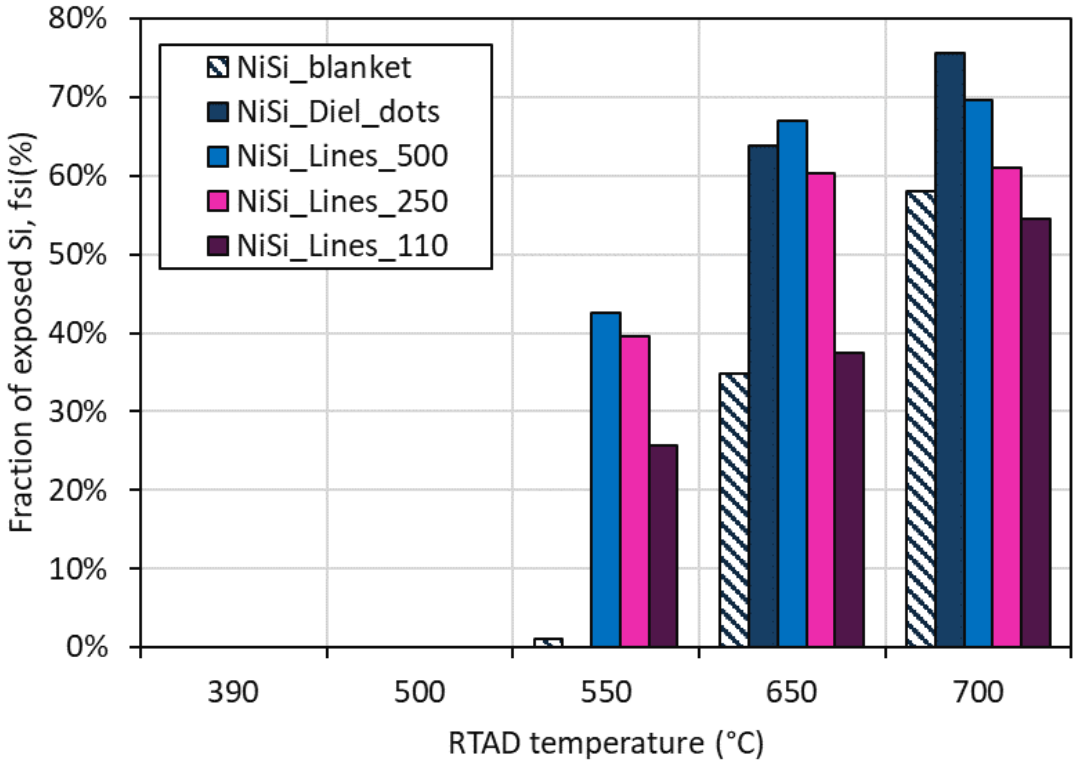


Figure 81. Evolution of the fraction of exposed Si, f_{Si}(%) during the agglomeration of 11 nm Ni(Pt)Si film formed in (in ascending order of degree of confinement) NiSi_blanket, NiSi_Diel_dots, NiSi_Lines_500, NiSi_Lines_250, and NiSi_Lines_110.

After an annealing at 500 °C, the f_{Si}(%) does not show any evolution and remains at 0 % since the formation of holes has not yet occurred. Further annealing at 550 °C induces a dramatic rise in the f_{Si}(%)for all of the samples. This is clearly demonstrated by the drastic increase up to 40 % of exposed Si surface by the NiSi_Diel_dots, NiSi_Lines_500, and NiSi_Lines_250 samples. The rising of the f_{Si}(%) in the case of the most confined sample, NiSi_Lines_110 appears to increase up to 25 % whereas for the NiSi_blanket sample, very minimal change in the f_{Si}(%) value is observed.

Nonetheless, the trends continue to increase up to 60 % of exposed Si surface after an annealing at 650 °C, for all of samples, except for the NiSi_blanket and NiSi_Lines_110 ones. For the NiSi_blanket and the NiSi_Lines_110, the f_{Si}(%) remains below 40 % after RTAD at 650 °C.

The exposition of the Si on surface is further exacerbated after an annealing at 700 °C in most of the samples and f_{Si}(%) reaches a value of 75 %. However, the f_{Si}(%) remains unchanged between 650 and 700 °C for NiSi_Lines_250 sample.

Table 20. Summary of the fraction of the exposed Si, f_{Si}(%) extracted from tilted-SEM images of 11 nm Ni(Pt)Si films formed on Si substrate confined between oxide structures of different pitch distance.

Annealing temperature (°C)	f_{Si}(%) NiSi_Lines_110	f_{Si}(%) NiSi_Lines_250	f_{Si}(%) NiSi_Lines_500	f_{Si}(%) NiSi_Diel_dots	f_{Si}(%) NiSi_blanket
390	0	0	0	0	0
500	0	0	0	0	0
550	25.6	39.7	42.6	0	1
650	34.9	60.3	67.1	63.9	34.9
700	54.5	61.1	69.6	75.6	58.1

3.4.3 Impact of confinement on texture of Ni(Pt)Si thin films

As presented in the previous study on the impact of the annealing schemes on the agglomeration of Ni(Pt)Si, the texture plays a major role in the agglomeration phenomenon. The current subsection aims to firstly investigate the impact of the confinement on texture of the Ni(Pt)Si grains. This is achieved through pole figure analyses between NiSi_blanket and Ni(Pt)Si film formed on confined structures for non-agglomerated Ni(Pt)Si film. In particular, a comparison of the pole figure analyses on NiSi_blanket and NiSi_Lines_250 will be presented in the current section.

Fig. 82 shows the pole figures of non-agglomerated 11 nm Ni(Pt)Si film formed on blanket Si(100) wafer *i.e.,* NiSi_blanket sample after an RTAD annealing at 500 °C. These pole figures are extracted for the following 2θ angles *or* hkl planes for which axiotaxy texture is typically detected [104]: (a) 2θ=31.20 °;(002/011), (b) 2θ=45.47 °;(112), (c) 2θ=46.65 °;(202/211), and (d) 2θ=51.5 °;(103).

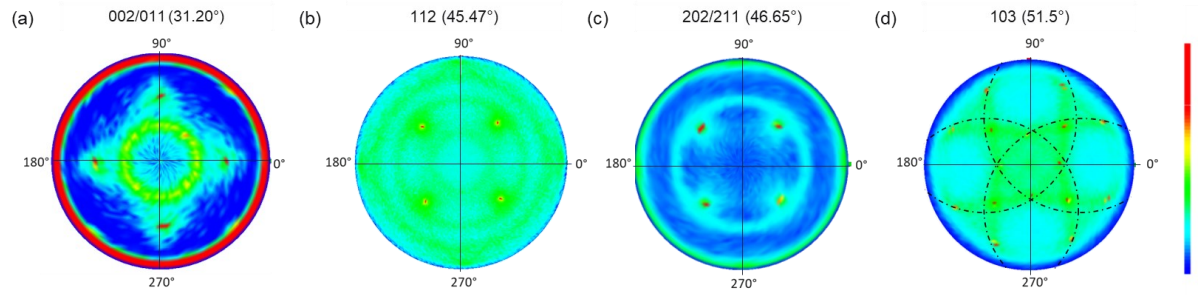


Figure 82. Pole figure of non-agglomerated 11 nm Ni(Pt)Si film formed on blanket wafer for (a) 2θ=31.20 ° (002/011), (b) 2θ=45.47 ° (112), (c) 2θ=46.65 ° (202/211), and (d) 2θ=51.5 ° (103). Dashed lines are drawn on top of the pole figure of NiSi(103) indicating the presence of ring segments.

The pole figure of the NiSi(002/011) is also included since preliminary IPRSM shows the presence of intense peak at this specific 2θ position. Nonetheless, the pole figures of NiSi (002/011), NiSi (112), and NiSi (202/211) in Figs. 83 – (a), (b), (c) exhibit the characteristics of a typical fiber texture. This is demonstrated by the presence of concentric rings in each of the pole figures. Meanwhile, the pole figure of NiSi (103) reveals a more complex texture indicated by several non-concentric and off-normal segments of fiber ring (Fig. 83(d)). This clearly indicates the presence of the axiotaxy texture.

Background subtraction have been performed on these samples to reduce contributions of the Si substrate.

As illustrated in Fig. 82(a), the pole figure of NiSi (002/011) presents a specific background intensity. When compared to other pole figures, the distribution of the background intensity of the NiSi (002/011) appears to be less homogenous. Such as can be seen in all of the pole figures, the periodic well-defined spots are also present which is the contribution of the Si(100) substrate *and probably a part of axiotaxy components.*

Similar analyses are performed in confined structures based on synchrotron experimental results. Indeed, due to lack of brilliance from the classical tool set in laboratory and lower density of diffracting planes for thin film in confined structures, pole figures extraction is performed at the European Synchrotron Research Facility (ESRF). A grazing incidence wide-angle X-ray scattering (GIWAXS) measurement is performed using the BM02 beamline at Grenoble.

This drastically improved beam brilliance in order to compensate the lower density of diffracting planes of thin film samples in confined structures. The GIWAXS experiment is performed at an energy of 17 keV, corresponding to X-ray with wavelength of 0.729319 Å. The scan is conducted between ϕ ranging from 100 to 100 °, 2θ between 0 and 60 °, and for χ values comprised between 0 and180 °.

Fig. 83 shows the (a) angular mapping of intensity, ϕ (°) vs. $2\theta_\chi$ (°) radially integrated for values of χ (°) to account for all possible peaks, and (b) extracted XRD θ-$2\theta_\chi$ scans performed on each of the value of ϕ (°) measured from the NiSi_Lines_250 sample after RTAD of 500 °C.

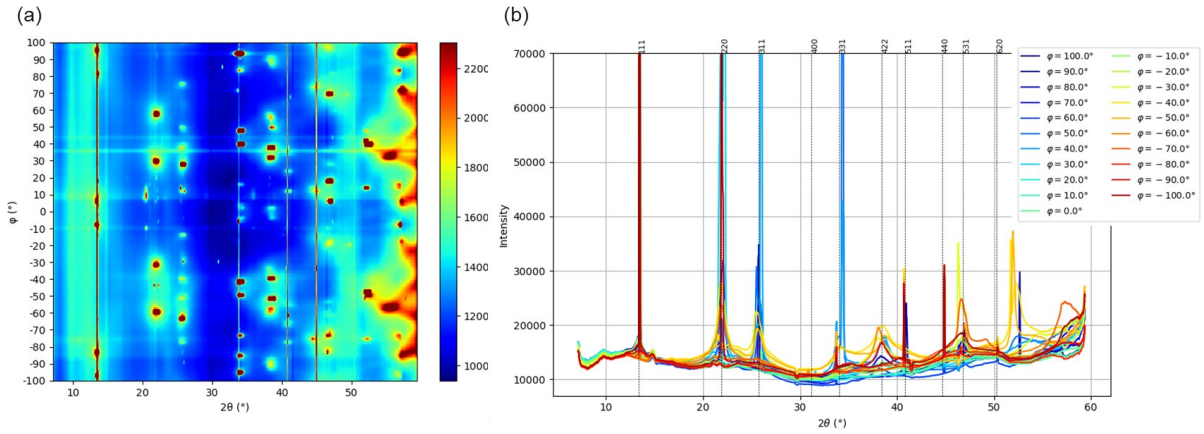


Figure 83. (a) Angular mapping of intensity, ϕ (°) vs. $2\theta_\chi$ (°) radially integrated for values of χ (°), and (b) extracted XRD θ-$2\theta_\chi$ scans performed on each ϕ (°) value measured from the NiSi_Lines_250 sample after RTAD of 500 °C.

As shown in Fig. 83(a), the angular mapping of intensity shows several periodic spots (*in dark red*) at specific 2θ positions for a given ϕ (°) value. Such intense peaks are attributed to the Si substrate as identified in Fig. 83(b). In addition, the angular mapping also reveal the presence of moderately intense vertical lines which appears at specific 2θ positions.

In order to better display the XRD patterns in Fig. 83(b), the extraction of these patterns is performed for a particular range of ϕ (°) angle avoiding the intense Si peaks. In this way, the diffracted peaks from the Ni(Pt)Si film in the confined structure is not dominated by the intense Si peaks. In addition to the selective extraction of the XRD patterns in specific ϕ range, the background contribution is also subtracted by taking background intensity at 2θ range without any prominent peaks.

Fig. 84 illustrates the resulting XRD pattern after considering the previous modification. Moreover, the 2θ range is also reduced to between 14 and 25 ° since the peaks of interest for this study is inside this range for the wavelength of 0.729319 Å. For any peaks at around 25 and 26 °, Si(311) might also become dominant.

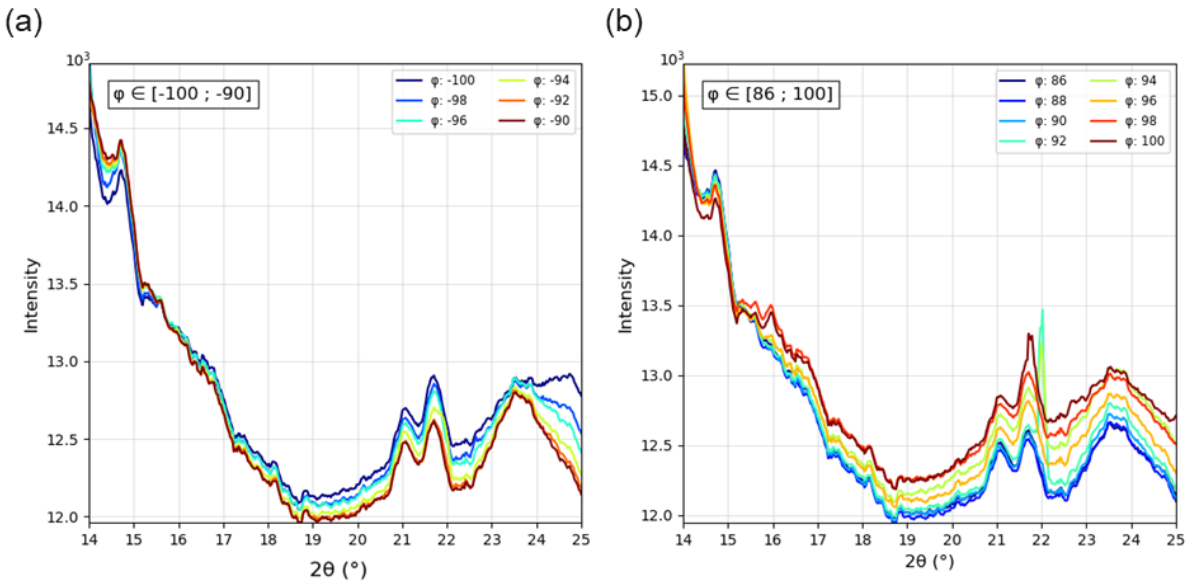


Figure 84. Extracted θ-2θ$_χ$ scans for (a) ϕ between -100 and -90 °, and (b) ϕ between 86 and 100 ° measured from the NiSi_Lines_250 sample after a RTAD annealing at 500 °C.

Several peaks can be extracted from Fig. 84 – (a) and (b). The identified peaks is summarized in Table 21 with their corresponding calculated d-spacing and miller indices. The first peak appears at 14.75 ° corresponding to either 002 or 011 planes which are impossible to dissociate due to the low difference in their d spacings. Next, a very small peak is detected at 20.4 ° attributed to the 210 planes. The following peaks detected are the typical planes that often results in the axiotaxy texture: at 21.0 ° (112), 21.70 (202/211), and 23.64 (103).

Table 21. Identified peaks and their corresponding hkl indices, 2θ positions, intensity and calculated d-spacing measured from the NiSi_Lines_250 sample.

Peak index	hkl	2θ (°)	Intensity (cps)	Calculated d-spacing (Å)
1	002/011	14.75	14428.51	2.85
2	210	20.4	12502.59	2.06
3	112	21.0	13192.24	1.99
4	202/211	21.70	13104.07	1.94
5	103	23.64	12985.14	1.79

Fig. 85 shows the poles figures (PF) at (a) 2θ=14.75 °, (b) 2θ=21.0 °, (c) 2θ=21.7 °, and (d) 2θ=23.64 ° measured the NiSi_Lines_250 sample after an annealing at 500 °C. The intensity is normalized across all samples. The missing parts of the pole figures is reconstructed with the assumption of rotation symmetry for better visualization.

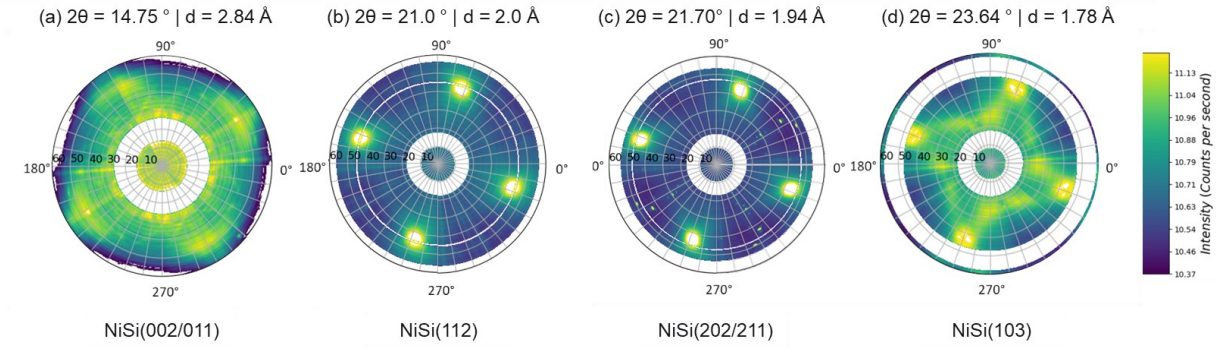


Figure 85. Extracted pole figures (PF) for (a) 2θ=14.70°, (b) 2θ=20°, (c) 2θ=22°, and (d) 2θ=24° measured from the NiSi_Lines_250 sample.

Ad depicted in Fig. 86, similar pole figures as blanket are observed for all orientations. In Fig. 85(a), NiSi(002/011) exhibits a strong background. Furthermore, further inspection of this PF also reveals several segments of off-normal non-concentric rings. The PF also demonstrates four intensity maxima (widespread) periodically spaced by Δϕ=90 ° which corresponds to the contribution of the Si substrate.

In addition, the PF of NiSi(112) and NiSi(202/211) illustrated in Fig. 85(b) and (c) respectively, are characterized by periodically well-defined spots attributed to the contribution of the Si substrate. The fiber rings previously observed in NiSi_blanket sample may not be visible due to the dominating diffraction intensity coming from the substrate.

Finally, the PF of NiSi(103) shown in Fig. 85(d) appears to exhibit segments of the off-normal fiber texture intersecting each other. This is a clear indication of the presence of the axiotaxy texture consistent with the previous observations in NiSi_blanket sample. The axiotaxial lines drawn by the dashed lines in the previous PF of NiSi(103) are superimposed on top of the NiSi(103) PF measured for NiSi_Lines_250 sample (Fig. 86).

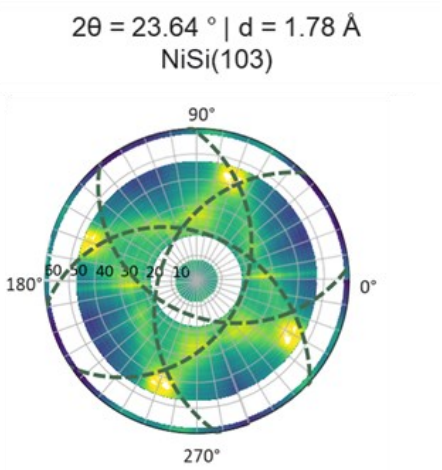


Figure 86. Superimposition of the dashed lines drawn in the NiSi(103) PF in Fig. 82(d), related to blanket experiment, on top of the pole Figures of the NiSi(103) determined for the NiSi_Lines_250 one.

The PF of the NiSi(103) is indeed the most suitable indicator for texture comparison as the other PFs are dominated by the signal of the Si. Moreover, this also suggests that Ni(Pt)Si film in confined structures maintain similar texture than the blanket wafer one. However, a complete comparative analysis of the texture remains a very complex task.

As shown in Fig. 87, the PFs of the NiSi(103) are extracted for all of the samples in the confined structures with varying pitch, *p*, at a non-agglomerated stage *i.e.,* after a RTAD annealing at 500 °C.

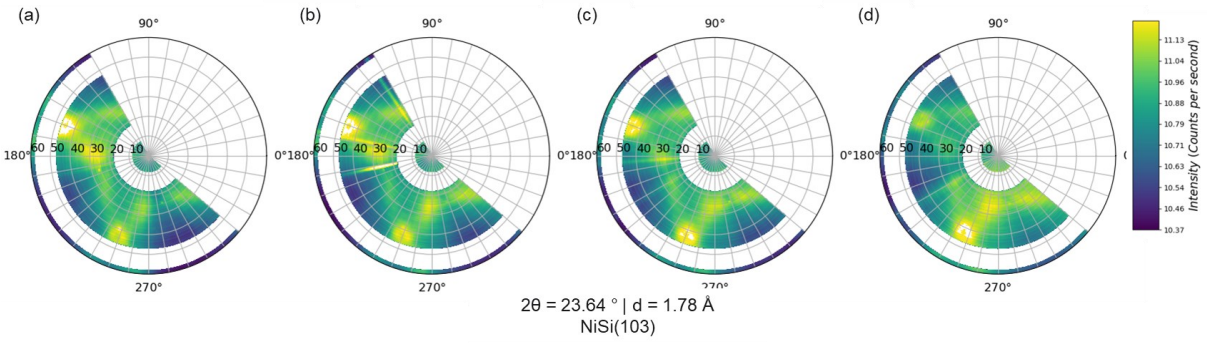


Figure 87. Pole Figures of NiSi(103) after a RTAD annealing at 500 °C of (a) NiSi_Diel_dots, (b) NiSi_Lines_500, (c) NiSi_Lines_250, and (d) NiSi_Lines_110 with normalized intensity.

All the PFs in Fig. 87 exhibit the characteristics of the axiotaxy texture as previously described in NiSi_blanket sample. Superimposition of these PFs with the one extracted for NiSi_blanket sample results in similar consistency shown in Fig. 86. In addition, very minimal

differences are observed for all of the PFs despite the different degrees of confinement of the Ni(Pt)Si thin film.

3.4.4 Conclusions of part 3

In this study, five types of samples are introduced consisting of 11 nm Ni(Pt)Si film formed on blanket wafer, and on patterned wafer in confined structures (either regular lines or dots. Morphological evolution with the RTAD temperatures and the confinement is evidenced by both the tilted and HRSEM measurements. Different stages of agglomeration are observed between all of the samples. At RTAD 550 °C, the NiSi_Diel_dots and NiSi_blanket samples exhibit very minimal changes whereas all the other samples show a more advanced stage of agglomeration. At higher temperatures, the agglomeration is severe for all the samples. Moreover, the agglomerates are clearly different for fine pitch (as 110 and 250 nm) compared to the other samples.

Indeed, inside both of these structures, higher discontinuities with elongated islets of NiSi are observed for severely agglomerated Ni(Pt)Si film. However, the agglomeration of Ni(Pt)Si formed on blanket wafer exhibit a higher degree of connectivity between NiSi agglomerates which suggest less agglomeration compared to the ones in confined structures.

A more quantitative analyses of the fraction of the exposed Si, f_{Si}(%) reveal that agglomeration changes with pitch size, *p.* For intermediate pitches, this value is maximal but the most confined structures, the NiSi_Lines_110 sample exhibits a less dramatic rise in f_{si}(%) values during subsequent RTAD annealings.

Contrarily, the least confined sample demonstrates a significant increment of the f_{Si}(%) during the subsequent RTAD annealings. Better stability for Ni(Pt)Si layer formed on the blanket wafer is observed, underlining potential impacts of the interface with the dielectric stacks.

Preliminary investigations on the texture comparison between Ni(Pt)Si film formed on blanket wafer and in confined structures have been performed through pole figures analyses, at the non-agglomerated stage (500 °C). The pole figures of the NiSi(002/011), NiSi(112), NiSi(202/211), and NiSi(103) are extracted and compared between the NiSi_blanket sample and the other four samples: PF of the NiSi(103) exhibits the characteristics of the axiotaxy texture, as evidenced by the off-normal ring segments of the

fiber texture. This observation remains consistent within all of the samples *i.e.,* regardless of whether or not the Ni(Pt)Si film is confined.

A complete analysis of the texture remains very complex and at the current stage**, no significative differences are distinguished in terms of texture between the Ni(Pt)Si thin film formed on blanket wafer and in confined structures** (*at non-agglomerated stage i.e., after a RTAD at 500 °C*). Indeed, a finer analysis is also necessary to evaluate the evolution of the texture within the confined structure during the agglomeration phenomenon.

3.5 Part 4: Results on industrial wafers (Integrated circuits)

3.5.1 Experimental setup

The final section of this chapter is dedicated to the results on industrial patterned dies that follow both front-end of the line (FEOL) and back-end of the line (BEOL) process flows for the complete elaboration of a functional integrated circuit [142]. As described in the first chapter in section 1.5 (Fig. 30), one of the principal challenges in the state-of-the-art technology is the co-integration of the Ni-based and Ti-based silicides, in particular the Ni(Pt)Si and $TiSi_x$ phases due to the thermal budget incompatibility between their formation temperature. Indeed, Ni(Pt)Si film is reported to agglomerate leading to severe yield loss during the formation of the $TiSi_x$ layer at a thermal budget of at least 650 °C [142].

Fig. 88 describes an overview of the process flows used during the elaboration of the integrated circuit.

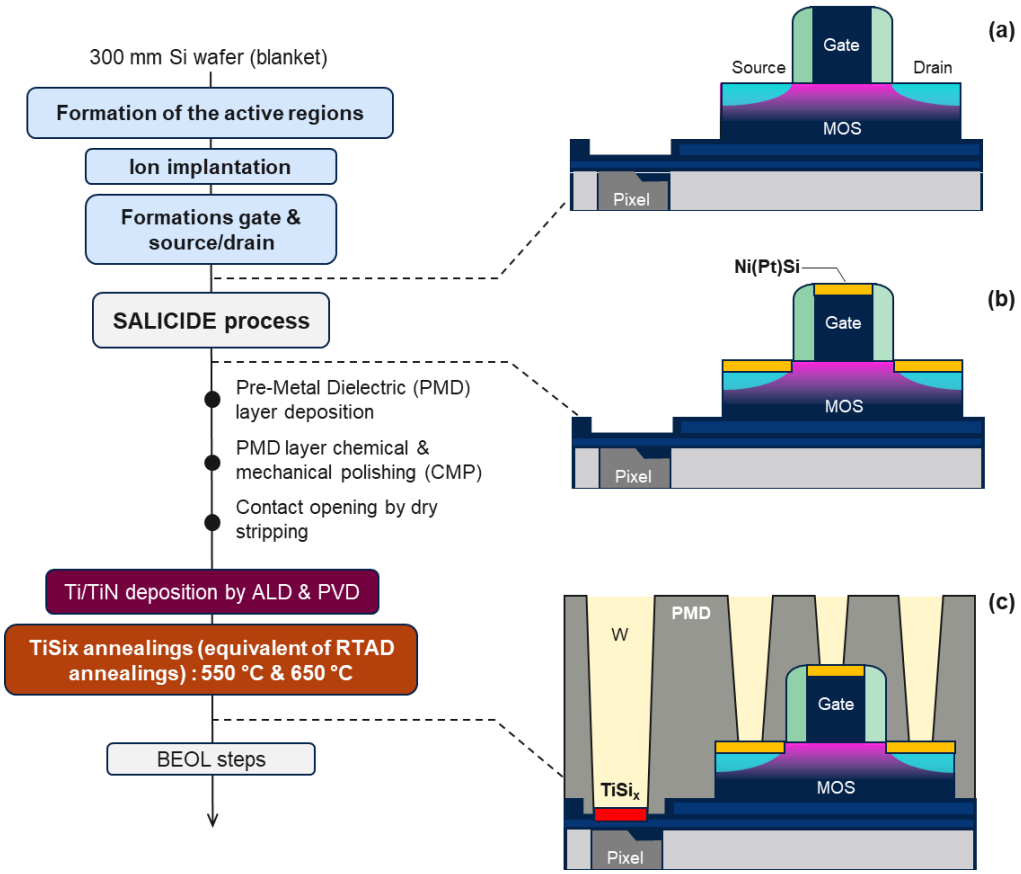


Figure 88. Description of a part of the process flow used to fabricate the integrated circuit involving the co-integration of Ni-silicide, Ni(Pt)Si and Ti-silicide, $TiSi_X$ presenting thermal budget incompatibility due to premature agglomeration of Ni(Pt)Si film during $TiSi_x$ formation.

This process flow starts with the definition of the active regions, followed by ions implantations and then the formation of the source, drain, and gate of the transistor. An additional annealing is also added in the following steps for the recrystallization of the Si substrate and to induce dopants diffusion. This results in the structure presented in Fig. 88(a), the MOS and the pixel structures.

Ni(Pt)Si thin film is formed on the active area in the MOS area following classical SALICIDE flow. Based on previous study, two different pathways have been utilized for the formation of the Ni(Pt)Si thin film (Fig. 90). This results in the structure shown in Fig. 88(b).

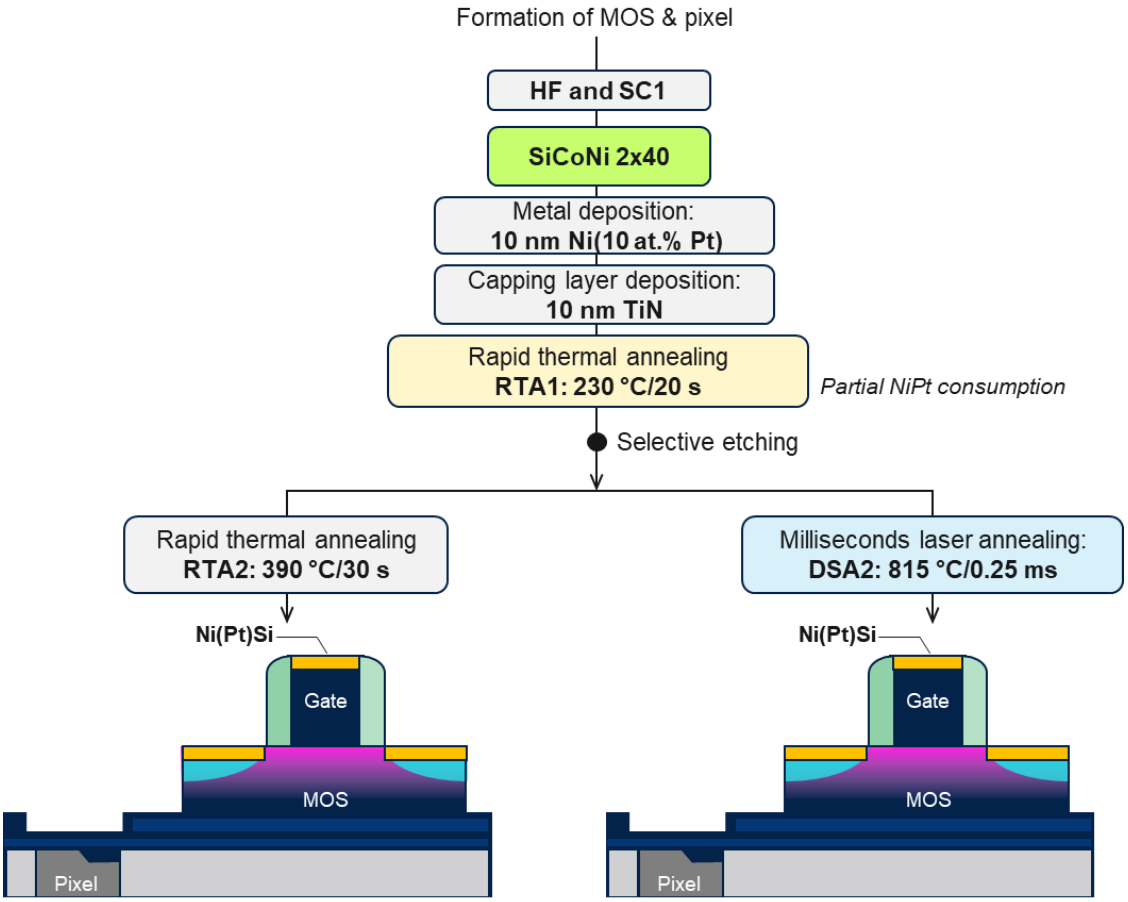


Figure 89. SALICIDE process flows illustrating two studied pathways for the formation of Ni(Pt)Si thin film dealing with millisecond laser annealing (DSA).

The subsequent steps involved the deposition of the pre-metal dielectric (PMD) layer, polishing of the PMD and dry stripping to open the contacts. Prior to contact filling with tungsten, W, a thick layer of Ti/TiN is deposited using physical vapor deposition (PVD) and atomic layer deposition (ALD) respectively (Fig. 88(c)). TiSi contacts formation in the pixel

area is thus performed by adding an RTA at high temperature (at least 550 °C). This deals with the end of FEOL process steps before the integration of Cu interconnects, known as BEOL processes.

To evaluate the thermal stability of the already formed Ni(Pt)Si film, the $TiSi_x$ annealing temperature is fixed to 550 and 650 °C for a constant dwell time of 30 s. The samples are then characterized by ellipsometry technique, electrical characterizations, and TEM. The description of the two types of Ni(Pt)Si formations studied in integrated circuits is summarized in Table 8 at the beginning of this chapter.

3.5.2 Investigation on Ni(Pt)Si thickness

The formation of the Ni(Pt)Si thin film at the source/drain and gate terminals of the CMOS transistors follows the standard SALICIDE process as described in section 1.2.3. The thermal budget of the RTA1 is always set to consume partially the NiPt metal layer. In the current technology, the RTA1 is set to 240 °C/10 s typically results in Ni(Pt)Si film of final thickness of 14.3 nm. Fig. 90 shows the thickness of the Ni(Pt)Si film measured by ellipsometry technique after its formation by either RTA2 annealing or laser annealing in integrated circuits

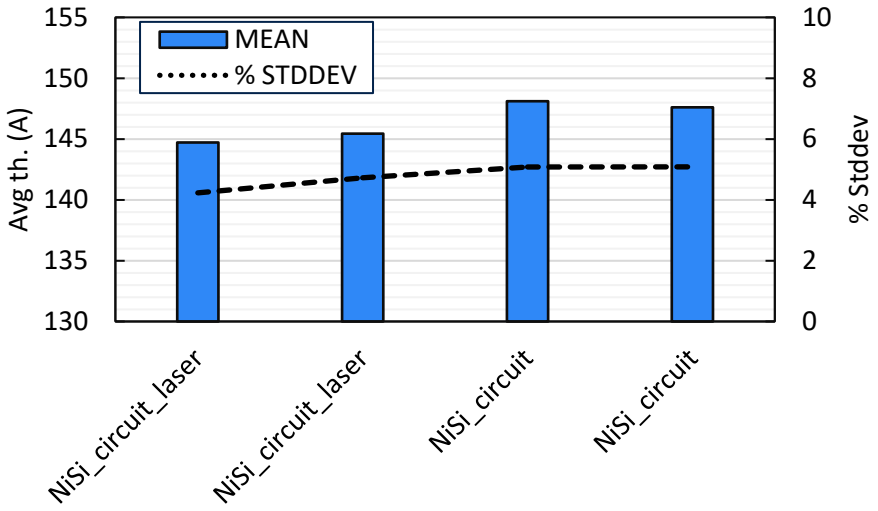


Figure 90. Thickness of Ni(Pt)Si film formed on terminals of the transistor for two types of annealing: standard RTA annealing, named NiSi_circuit, and milliseconds laser annealing, NiSi_circuit_laser.

Two wafers have been prepared for each of sample type: NiSi_circuit and NiSi_circuit_laser. The average thicknesses of the silicide film are 14.5 and 14.8 nm for NiSi_circuit_laser and NiSi_circuit, respectively. Furthermore, the relative standard deviation, σ (%) is also included in order to account for thickness dispersion within the 300 mm wafer measured based on a mapping of 17 points. The relative standard deviation, σ is calculated by the following equation:

$$\boldsymbol{\sigma}(\%) = \mathbf{100} * \left(\sqrt{\frac{\sum(x_i - \mu)^2}{N}}\right)/\mu \qquad \textbf{Equation 22}$$

With x_i, measured thickness on each point, μ, thickness mean value, and N, the size of the population (*i.e.,* 17 in our case). The relative standard deviation appears to be slightly higher for the NiSi_circuit sample as compared to the NiSi_circuit_laser sample. The improvement of the relative standard deviation for the Ni(Pt)Si film formed using the millisecond laser is a direct consequence of the use of laser strips rather than a halogen lamp used in RTA-type annealing.

3.5.3 Electrical characterizations

Electrical characterizations, usually called parametric testing (PT) is one of the important steps in the manufacturing of integrated circuits allowing to ensure the quality of the semiconductor devices. This is achieved through test structures that are specifically made for the purpose of parametric testing which can typically be found within the area of the die or between the die (scribe line). These test structures often consist of resistors and/or capacitors.

Fig. 91 illustrates the normalized resistance, R (Ω) extracted from the parametric testing performed on the N-doped gates, source/drain, and P-doped source/drain for both NiSi_circuit and NiSi_circuit_laser samples. These measurements are conducted after the annealing at the $TiSi_x$ thermal budgets of 550 and 650 °C for 30 s and the complete BEOL processes.

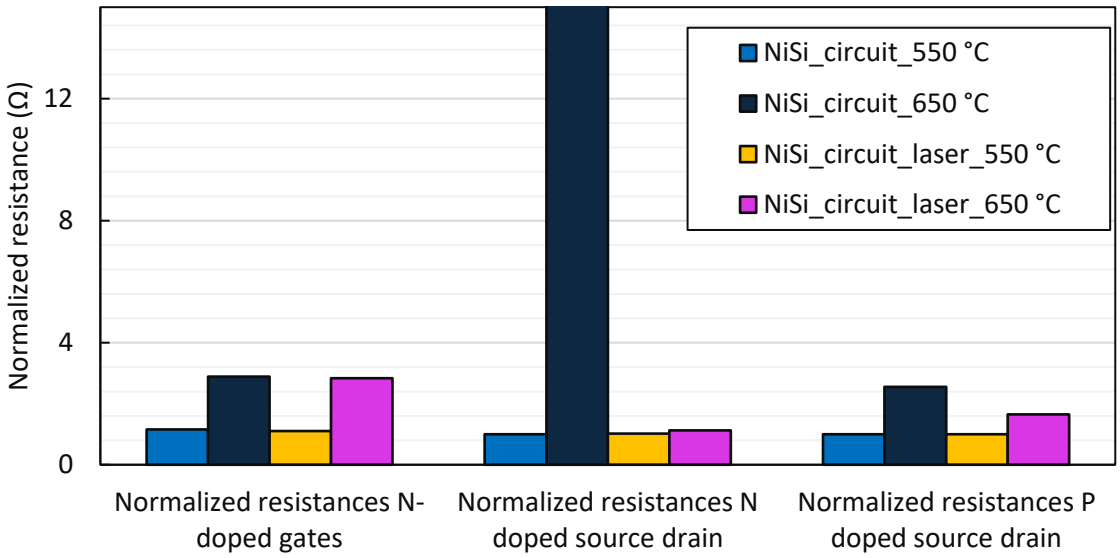


Figure 91. Normalized resistance, R (Ω), extracted from parametric tests on N-doped gates, source/drain, and P-doped source/drain for NiSi_circuit and NiSi_circuit_laser after $TiSi_x$ annealings at 550 and 650 °C.

For the N-doped gates, the normalized resistance show no significant difference between the NiSi_circuit and NiSi_circuit_laser samples after the $TiSi_x$ annealing at 550 °C. At a higher annealing of 650 °C, the resistance shows a slight increase for both NiSi_circuit and NiSi_circuit_laser samples.

For the N-doped source and drain, there is a clear difference in the trends of the normalized resistance between each $TiSi_x$ annealings. Firstly, at 550 °C, no significant change is observed for both samples. At 650 °C, the normalized resistance shows a drastic rise for NiSi_circuit sample. As for the NiSi_circuit_laser sample, the resistance appears to show no significant change after annealing at 650 °C.

Similarly, in the P-doped source/drain, the resistance also shows an increase, however not as drastic as the ones measured in the N-doped source/drain for the NiSi_circuit sample. In addition, slight resistance increase is observed for the NiSi_circuit_laser sample when the annealing temperature is changed from 550 °C to 650 °C.

3.5.4 Silicide morphology

To verify the morphology of the Ni(Pt)Si film after each of the $TiSi_x$ annealings at 550 and 650 °C, TEM observations were performed on each sample at a specific undoped active regions. These regions often consist of sufficiently large structures allowing to ensure a sufficient volume of Ni(Pt)Si film for the lamella preparation.

Fig. 92. shows the TEM cross-sections obtained after a $TiSi_x$ annealing zoomed on Ni(Pt)Si silicide film for both of the samples: (a) NiSi_circuit, and (b) NiSi_circuit_laser.

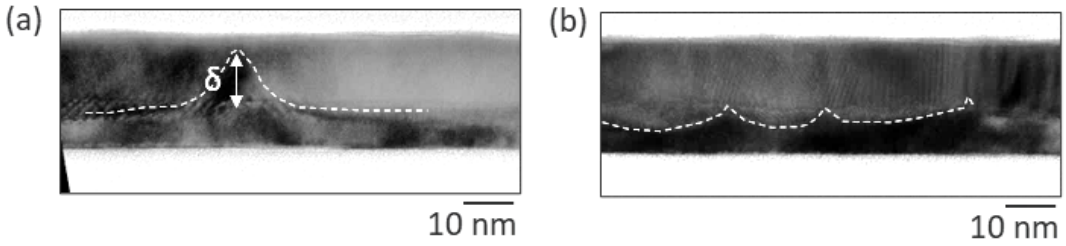


Figure 92. TEM cross-sections obtained after $TiSi_x$ annealings at 550 °C for (a) NiSi_circuit, and (b) NiSi_circuit_laser samples. White dashed lines are included to indicate the boundary grooving phenomenon, with δ, the depth of the groove.

As shown in Figs. 92 – (a) and (b), the Ni(Pt)Si grains is larger for NiSi_circuit sample compared to that of the NiSi_circuit_laser sample. Such results are consistent with the observations in part 2 (section 3.3) and our published work [141] demonstrating a reduction by 50 % of the silicide grain size when the DSA-laser annealing is used.

Moreover, both TEM images also evidenced the presence of interface curvature between the silicide film and the Si substrate due to the boundary grooving phenomenon. These curvatures are represented by the dashed white lines in Fig. 92(a) for the NiSi_circuit sample and Fig. 92(b) for the NiSi_circuit_laser sample.

The depth (*or* height), δ of the groove is more pronounced for the NiSi_circuit sample compared to that of the NiSi_circuit_laser one. This is a clear indication of a more advanced stage of GB grooving for the NiSi_circuit sample, and a subsequent hole's formation at lower temperatures for this sample.

Nonetheless, in order to further evaluate the morphology evolution of the Ni(Pt)Si film for both NiSi_circuit and NiSi_circuit_laser samples at a higher temperature $TiSi_x$ annealing, TEM measurements with lower magnification is performed at both 550 and 650 °C.

Fig. 93 shows the TEM images obtained for NiSi_circuit sample after the complete process of integrated circuit for $TiSi_x$ annealings at (a) 550 °C, and (b) 650 °C.

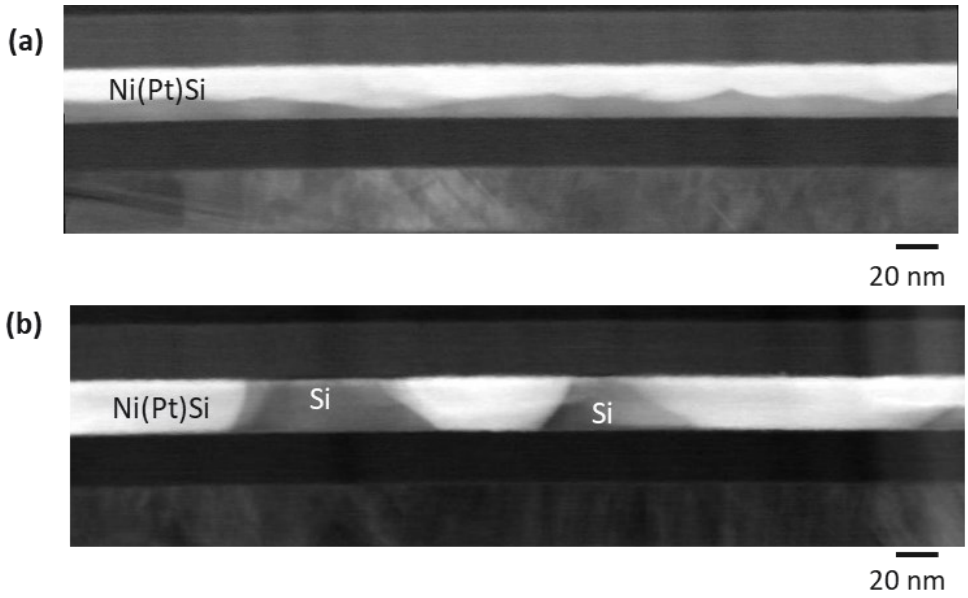


Figure 93. TEM cross-sections obtained for NiSi_circuit sample for $TiSi_x$ annealings at (a) 550 °C, and (b) 650 °C.

As shown in Fig. 93(a), the morphology of the Ni(Pt)Si film appears to remain continuous with the presence of interface curvature indicating the presence of grain boundary grooving as described previously. Moreover, the interface curvature appears to occur over a long-range corroborating the previous observation on a high magnification TEM image. As a consequence, the thickness of the Ni(Pt)Si film is less homogenous over the range of the measured area.

Consequently, after an annealing at 650 °C, as depicted in Fig. 93(b), the Ni(Pt)Si film presents discontinuities with isolated islets. The Si substrate is thus exposed to the surface. In addition, the resulting silicide agglomerates (islets) presents a higher depth within the Si substrate. Most of the Ni(Pt)Si agglomerates reach the oxide layer (*in dark contrast*).

In similar fashion, the TEM cross-sections at lower magnification are shown for the NiSi_circuit_laser sample for both $TiSi_x$ annealings as shown in Fig. 94 – (a) 550 °C, and (b) 650 °C.

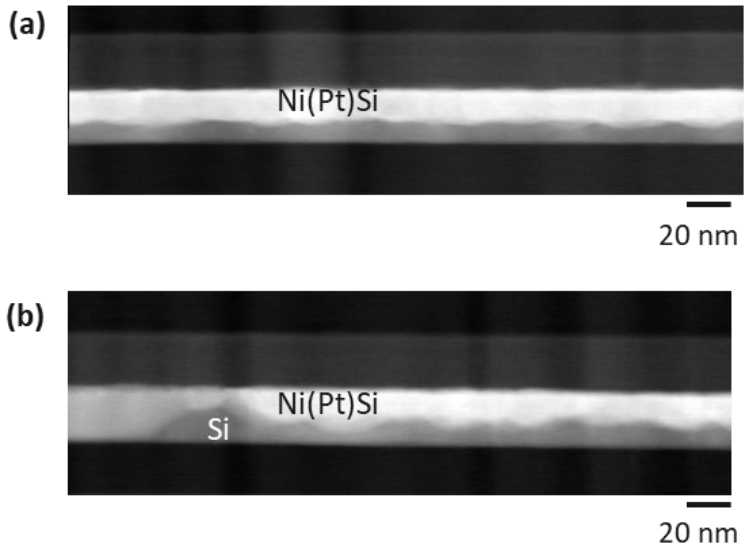


Figure 94. TEM cross-sections obtained for NiSi_circuit_laser sample for $TiSi_x$ annealings at (a) 550 °C, and (b) 650 °C.

As shown in Fig. 94(a), the morphology Ni(Pt)Si film remains continuous after an annealing at 550 °C. In addition, the grooves are less pronounced as compared to the previous NiSi_circuit sample. The Ni(Pt)Si/Si interface seems to be quite smooth in comparison to previous observations.

After annealing at higher temperatures, 650 °C, the TEM image in Fig. 94(b) evidenced a loss of the long-range layer homogeneity. Furthermore, the grooving appears to have increased significantly, suggesting a more advanced stage of grain boundary grooving. No Si substrate is exposed towards the surface and no islets are formed at this annealing temperature for the NiSi_circuit_laser sample.

This is an indication that holes have not yet reached the surface, and thus a better thermal stability compared to the NiSi_circuit sample is then demonstrated by replacing RTA by DSA as the second annealing steps in integrated circuits, as well as blanket wafers. Such results pave the route to the emergence of high performing imager sensors based on 3D integrations in the coming years.

3.5.5 Conclusions of part 4

Two different types of samples have been studied following the complete industrial elaboration process flows of the integrated circuits from the FEOL to BEOL steps. The milliseconds Dynamic Surface Annealing (DSA) laser has been utilized as an alternative to rapid thermal annealing, RTA2, during the formation of the Ni(Pt)Si thin film following the SALICIDE process.

The TEM observations are performed for both samples after annealings at 550 and 650 °C. For the NiSi_circuit sample, the Ni(Pt)Si silicide film clearly demonstrates a more advanced stage of the grain boundary grooving indicated by the more pronounced interface curvature. Moreover, the depth of the groove, δ, is very closed to the thickness of the Ni(Pt)Si thin film. This suggests that hole formation may occur at as low as 550 °C for the NiSi_circuit sample. Lower magnification TEM images demonstrates thickness uniformity is also impacted, meaning that the silicide film is less uniform for this sample. This is due to the presence of the interface curvature during the grain boundary grooving.

As for the NiSi_circuit_laser sample, the interface curvature shows minimal changes between 550 and 650 °C, or at least not as pronounced as in the NiSi_circuit sample. Better thickness uniformity is observed compared to that of the NiSi_circuit one.

Furthermore, the feasibility of the proposed alternative has been evaluated through electrical characterizations (called parametric testing, PT) accounting the overall functionality of the silicide film within a larger structure dealing with several additional thermal budgets (*i.e.,* formation of $TiSi_x$ silicide and BEOL interconnections).

The NiSi_circuit sample demonstrates a drastic resistance increase (*above the technological specifications*) after the annealing of $TiSi_x$ at 650 °C. Contrarily, the NiSi_circuit_laser sample showed very minimal resistance change between the two $TiSi_x$ annealings suggesting a better silicide stability. These findings demonstrated the feasibility of the integration of the DSA laser annealings in industrial elaboration process flows to improve the thermal stability of the Ni(Pt)Si thin film.

Chapter 4: Discussions

Chapter contents

4.1 Impact of structural parameters 181
4.1.1 Change in intermixing thickness 181
4.1.2 Role of grain size 183
4.1.3 Role of textures 186
4.1.4 Confinement of Ni(Pt)Si film 188
4.2 Impact of additional elements 194
4.2.1 Observations of Pt redistribution 194
4.2.2 Initial redistribution of Pt: before agglomeration 202
4.2.3 Pt redistribution during the agglomeration 203
4.2.4 Pt redistribution in the case of laser annealing 204
4.2.5 Modelling of the redistribution of Pt 208
4.2.6 Chemical environment 215
4.2.6.1 Residual fluoride, F and oxygen, O 215
4.2.6.2 SiCoNi treatments and Ni(Pt)Si agglomeration 217

Foreword

The experimental results of the four principal studies conducted in the framework of this Ph. D thesis have been presented in the previous chapter. This includes the study on the impact of the different SiCoNi treatments, the different annealing schemes used in the formation of the Ni(Pt)Si film, the influence of the confinement of the Ni(Pt)Si film on its thermal stability and finally, a fourth section which is dedicated to the results on wafers following the complete industrial elaboration process flows. In this chapter, deep discussions on the previously described results will be presented through combinatory analyses of the different studies and/or techniques utilized.

This chapter is divided into two main sections relating to the discussions on the impact of structural parameters and the impact of additional elements on the agglomeration of Ni(Pt)Si thin films. The first section begins by discussing the impacts of structural parameters on the agglomeration of the Ni(Pt)Si film. This includes the discussion on the change in the thicknesses of the intermixing layer, determined in chapter 3 (section 3.2.2), SiCoNi treatments, the role of grain size and textures and finally a discussion on the impact of the confinement.

In the second section, a model on the redistribution of Pt is presented. Finally, some relevant discussions on the different chemical environments and redistribution of the residual elements (fluorine, F, and oxygen, O) during the different SiCoNi treatments are provided at the end of this chapter before general conclusions of the manuscript.

4.1 Impact of structural parameters

4.1.1 Change in intermixing thickness

In the case of the deposition of NiPt metal layer on silicon substrate by PVD sputtering, an amorphous interlayer has been shown to grow between the NiPt metal and the Si substrate at room temperature *i.e.,* prior to any heat treatments [54], [143], [144]. The interlayer, also called intermixing layer, is reported to exhibit a variation of Si concentrations between 33 to 45 at. % [54]. For similar intermixing thickness, El Kousseifi *et al.* [54] demonstrated that both the Pt concentration in the intermixing layer, and the selection of the first silicide phase are primarily determined by the composition of the intermixing layer [54].

In study 1-A (chapter 3 section 3.2.2), our results revealed that the thickness of the intermixing layer depends on the choice of the SiCoNi treatments (SiCoNi 2x40 or SiCoNi 80). As shown in Fig. 56, the intermixing layer is thicker when the silicon substrate is treated with SiCoNi 80 process prior to the NiPt metal deposition. This results in intermixing layer of 5.6 nm for the NiPt_SiC80 sample versus 2.6 nm in the case of the NiPt_SiC2x40 sample.

Such finding is further corroborated by composition analysis using the TEM-EDX line profile, and ToF-SIMS depth profile, indicating a relatively larger intermixing zones for NiPt_SiC80 sample compared to the NiPt_SiC2x40 one (see Figs. 59, and 60). Even if a slight overestimation of the thickness of the intermixing layer is evidenced by the TEM-EDX technique (see experimental error in Table 11), conclusions on thicker intermixing layer for SiCoNi 80 treatment remain consistent across all of the measurements.

The thicker intermixing layer can be understood as the consequence of the higher fluorine concentration in the case of the SiCoNi 2x40 treatment. As previously shown in Fig. 58 and Table 10, the concentration of fluorine in the case of the SiCoNi 2x40 process is clearly more significant compared to that of the SiCoNi 80 one. Tsuchiaki *et al.* [108] reported that the fluoride residue at the Ni-Si interface hindered the diffusion of Ni. Thus, this implies that the diffusion of Ni is retarded in the interface in the case of the SiCoNi 2x40 treatments, and thus lead to a thinner intermixing layer as compared to the SiCoNi 80 case.

Moreover, as shown by TEM image in Fig. 56(b), we can clearly see that the intermixing/Si interface is rough. Futase *et al.*[106] have indeed reported that the presence of F at the silicide/Si interface may trigger the formation of rough interface. This interface roughness is not observed in the case of the SiCoNi 2x40 treatment. Indeed, as shown by the Figs. 60(a) and (b), one may notice that the F is redistributed differently in the intermixing zone depending on the SiCoNi treatments. For SiCoNi 2x40, the smooth interface may be explained by the homogenous distribution of F in the intermixing layer contrarily to the SiCoNi 80, where F is observed to redistribute towards the NiPt/intermixing, and intermixing/Si interfaces.

After the silicidation steps, the average silicide thickness is slightly higher in the case of the SiCoNi 2x40. Fig. 95 shows the EDX line scan of oxygen, O and platinum, Pt for the two SiCoNi treatments. The high oxygen concentration at the surface (low depth) can be ignored since the TEM lamellar is capped with chrome oxide.

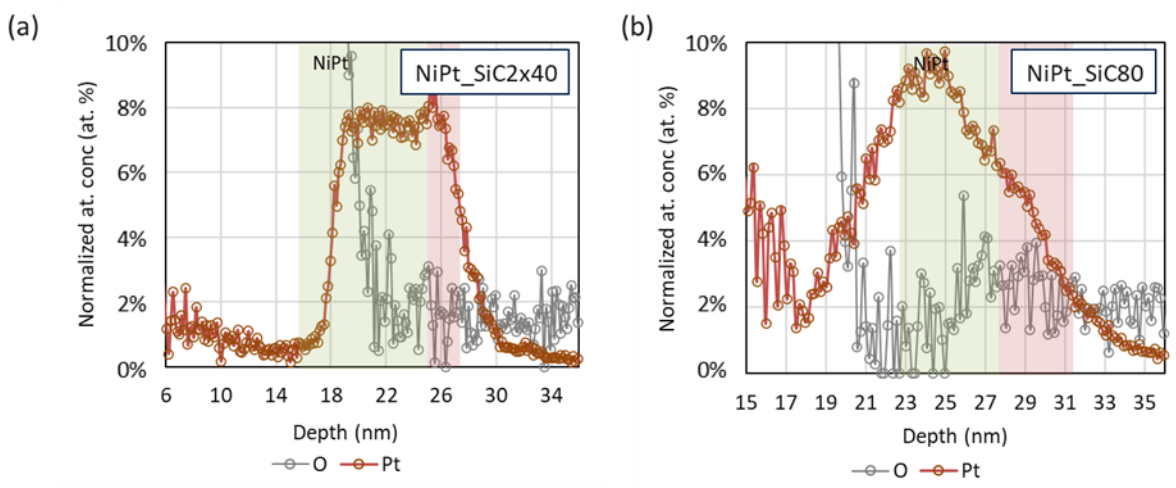


Figure 95. EDX line scan of oxygen, O and platinum, Pt for the two SiCoNi treatments: (a) SiCoNi 2x40, and (b) SiCoNi 80 treatments.

In the intermixing layer, however, a difference in the concentration of the oxygen, O, can be seen within the intermixing layer depending on the SiCoNi treatments used. The oxygen concentration is slightly higher in the case of the SiCoNi 80. This may explain the low thickness uniformity and low average thickness of the formed Ni(Pt)Si film in the case of the SiCoNi 80 treatments.

An important consideration, however, is that the XPS technique is estimated to probe very near to the sample surface. The estimated probed depth by this technique for this material is between 5 to 10 nm. Under this consideration, the concentration by XPS may originate from as deep as near the NiPt/intermixing interface. Regardless, the presence of F in the intermixing layer is confirmed as can be seen by both ToF-SIMs and TEM-EELS techniques.

4.1.2 Role of grain size

One of the key parameters that has been demonstrated to play an important role in the agglomeration of the Ni(Pt)Si films is grain size distribution [83], [84], [91]. Finer grains in polycrystalline thin films are known to improve thin film thermal stability [19], [83], [84]. The agglomeration of thin film is a phenomenon driven by the minimization of the surface and interface energies, which depend on the thin film thickness, grain size, and texture [83], [84], [91]. The following equations describe the interface energies as function of the different properties of a polycrystalline thin film (*i.e.,* thickness and grain size)[83]. For a 2D grain structure grown on a substrate, the energy balance will lead to the formation of a curved interface (boundary grooving), for which the groove angle, φ is defined as follows:

$$\boldsymbol{\varphi = sin^{-1}(\frac{\gamma_{gb}}{2\gamma_f})} \quad \textbf{[83]} \qquad \textbf{Equation 23}$$

With γ_{gb}, the grain boundaries energy and γ_f, the isotropic interface energy. Under this condition, a groove can be formed, and the groove depth, δ is established as

$$\boldsymbol{\delta = D\ \frac{2-3\cos(\varphi)+cos^3(\varphi)}{3\ sin^3(\varphi)}}\ \textbf{[83]} \qquad \textbf{Equation 24}$$

With ϕ, the groove angle and D the grain size. When the depth of the groove becomes larger than the thickness of the film, h, a hole is thus formed. Thus, the critical grain size, D_c can be determined as function of the thin film thickness, h, and groove angle, ϕ.

$$\boldsymbol{D_c = h\ \frac{3\ sin^3(\varphi)}{2-3\cos(\varphi)+cos^3(\varphi)}}\ \textbf{[83]} \qquad \textbf{Equation 25}$$

As stated by the equation 25, the agglomeration phenomenon will not occur for grain sizes below the critical grain size ($D < D_c$). Thus, the delay in agglomeration observed in the case of the Ni(Pt)Si films formed by the laser annealing should be mainly due to the presence of the small grains. Note that this critical grain size proportional to the thickness of the film, noted, h: thus, one should compare the effect of grain size for a given thickness of the film. This is indeed the case in the study on the annealing schemes, where we have kept an identical final silicide thickness.

The characteristics of the DSA-laser annealing is often a high temperature annealing at 815 °C with a very short dwell time (in order of the milliseconds). These principal particularities of the laser annealing, as opposed to the RTA annealing, may explain why the grains size is drastically lower. The Ni(Pt)Si grains are hypothesized to not have enough dwell time for lateral growth, while the high temperature should result in a high rate of grain nucleation. When compared to the agglomeration temperature of the silicide films formed by other annealing schemes, the reduction by 50 % of the grain size resulted in a delay of at least 50 °C for the agglomeration temperature.

Moreover, higher grain boundary density in the silicide films formed by the laser annealing may also lead to higher Pt concentration at the silicide-silicon interface, as the grain boundaries act as fast diffusion pathways for the Pt atoms. Indeed, high Pt concentrations at the silicide-silicon interface have been associated with an improvement of the thermal stability of the Ni(Pt)Si film [7], [19]. Nevertheless, the Pt is presumed to redistribute at the interface of the agglomerated silicide/substrate by means of interface diffusion during the agglomeration phenomenon. However, such hypothesis still need to be validated.

On the contrary, silicide films formed by the total annealing present quite large holes after RTAD annealing at 550 °C. This suggests that the agglomeration is more advanced compared to the silicide films formed by the other annealing schemes. The grain size of the Ni(Pt)Si grains formed by the total annealing appears to be the largest among all the annealing schemes studied (see Table 18). The more advanced agglomeration of silicide film in the case of the total annealing can thus be attributed to the larger mean grain size (D=127 nm).

For silicide films formed by the one-step and partial annealings, one can note that, despite their identical grain size, there is a slight difference in their thermal stability after RTAD annealing at 550 °C, as can be seen in the HR-SEM images in Fig. 72(b). Since thickness and grain size are identical for these two schemes, the slight difference in their stability may also be explained by the texture of silicide films.

4.1.3 Role of textures

Another important parameter that impacts the agglomeration of polycrystalline thin film is the distribution of the crystal orientations, *i.e.,* thin film texture. As described in chapter 2 (see section 2.2.6), the four textures typically observed in thin films are random texture (highest interfacial energy), fiber texture, axiotaxy texture, and the epitaxial texture (lowest interfacial energy). [17], [95], [97], [98], [103], [145]. Detavernier *et al.* [104] have shown that the axiotaxy texture presents a 1D periodicity at the silicide/Si substrate interface as illustrated by the Fig. 96. They reported four axiotaxial components in the case of the NiSi films of Si substrates with preferred alignments with the Si(220) planes.

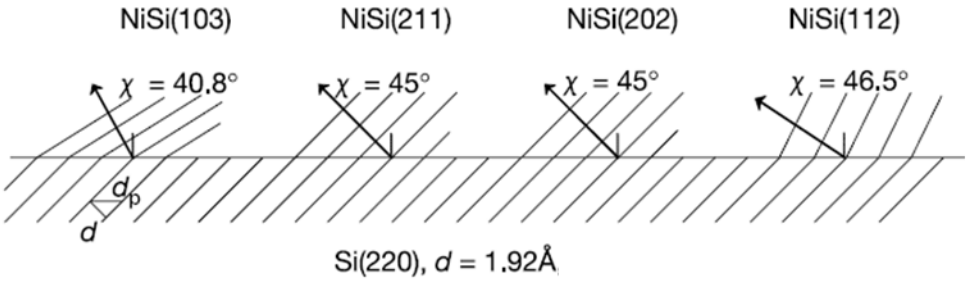


Figure 96. Illustration of the 1D periodic interface achieved for NiSi(103), NiSi(211), NiSi(202), and NiSi(112), planes parallel to Si(220), adapted from [104].

EBSD measurements in Fig. 73 allow to map the orientation distributions of the Ni(Pt)Si grains and the texture of the silicide films as evidenced by the pole figures in Fig. 75. The presence of the two preferential orientations along the (010) and (013) directions is observed in all samples. Furthermore, all samples initially present a fiber texture before agglomeration at higher RTAD temperatures. It is also important to note that the intensity of the (010) planes is clearly weaker in the IPF in Fig. 74(b) for the one-step annealing at 500 °C than the other samples.

After the agglomeration, the IPF shown in Fig. 74(b) reveals that the (013) preferential orientation remains even after the agglomeration. This is supported by the orientation maps in Fig. 73(b) showing the presence of grains color-coded in pink. This suggests that the grains oriented along the (013) direction may be more effective at delaying agglomeration, perhaps due to a lower interface energy. This may explain why silicide films formed by one-step

annealing show a slightly higher stability (see Fig. 72(b)) than the film formed by partial annealing, despite their identical thickness and grain size. Moreover, in the case of partial annealing, the intensity of the (010) planes is drastically lower (see IPF in Fig. 74(b)). This suggests that grains oriented in the (010) direction may be consumed during agglomeration. Further analysis using transmission Kikuchi diffraction may be required to validate such hypotheses.

The one-step annealing is the only scheme that deals with a single-step annealing as the as-deposited Ni(10 at.% Pt) layer is directly subjected to the RTAD treatments. Such differences in formation schemes may lead to the presence of Ni(Pt)Si grains with a more dominant orientation along the (013) directions. However, other process parameters, such as the position of the selective etch steps before and after the high-temperature RTAD annealing may also play a role.

Furthermore, the presence of either one or two dominant grain orientations may indicate a certain difference in the global grain boundary energies due to the difference in the global misorientations. However, such analysis is very complex in silicide films, with very small grains leading to a large number of unindexable grains. In fact, precise evaluation of the misorientation requires the orientation maps to show clear grain boundaries between two neighboring grains. However, in the case of very thin Ni(Pt)Si films, the EBSD orientation mapping is already difficult to obtain and misorientation is even more difficult.

Regarding the evolution of texture with respect to the agglomeration phenomenon, Fig. 75 shows that there is an increase of the axiotaxy component in the Ni(Pt)Si-(103) pole figures after agglomeration. This is evidenced by the rise in intensity of the off-normal fiber texture. Such findings support the XRD characterizations performed by De Keyser *et al.*[17], where they demonstrated an increase in the intensity of the (103) peak during the agglomeration phenomenon of 20 nm NiSi films. The superimposition between the pole figures of agglomerated Ni(Pt)Si film with the simulated axiotaxy texture by Detavernier *et al.* [104] further corroborates this observation. As an example, Fig. 97 showed the superimposition of the axiotaxy lines (in red) extracted from [104] on the pole figure of the agglomerated silicide film formed using one-step annealing.

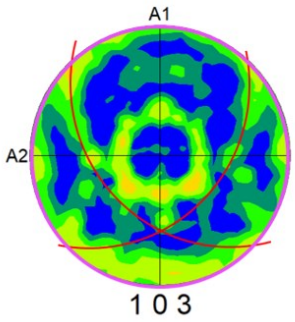


Figure 97. Pole Figures (PF) of Ni(Pt)Si-(103) on Si(100) substrate for an agglomerated silicide sample formed by one-step annealing with a superimposition of calculated axiotaxial lines from [104].

4.1.4 Confinement of Ni(Pt)Si film

Five different samples have been studied to determine the impact of the confinement of the Ni(Pt)Si film on the agglomeration phenomenon (section 3.4). These five samples correspond to blanket wafer, named NiSi_blanket (without confinement), Ni(Pt)Si film formed between dielectric dots, NiSi_Diel_dots, and inside trenches between dielectric lines, of different pitch size, *p*; NiSi_Lines_110, NiSi_Lines_250, and NiSi_Lines_500. Indeed, Cavalcante *et al.* [10] reported a severe yield loss and increase of silicide sheet resistance Rs (Ω/sq.) occurring at lower annealing temperature when Ni(Pt)Si film is formed in smaller devices.

In our study, we used the fraction of exposed Si, f_{Si} (%) as an indicator to evaluate the thermal stability of the Ni(Pt)Si film during high temperature RTAD annealings. The Rs measurement may not be adapted to these samples since we do not have connected silicided structures (meaning separated by the dielectric layers). In addition, the diameter of the Rs probe is in the order of magnitude of a few microns (µm). The f_{Si} (%) is extracted from the SEM images in Fig. 80 following the procedures described in Fig. 66 (section 3.2.3.2).

Our results reveal that the agglomeration of the Ni(Pt)Si film is exacerbated when silicide films are formed inside the line trenches *i.e.,* for NiSi_Lines_110, NiSi_Lines_250, and NiSi_Lines_500 compared to that of the NiSi_blanket and NiSi_Diel_dots samples. For example, at 500 °C, the f_{Si} (%) of the silicide film measured for the non-confined samples (NiSi_blanket and NiSi_Diel_dots) is significantly low, *i.e.,* zero percent of exposed Si indicating that the agglomeration may have not yet occurred.

In addition, when comparing the trends of only NiSi_Lines samples, the f_{Si} (%) appears to increase with increasing pitch size. This means that agglomeration is more severe when the Ni(Pt)Si film is formed in less confined structures. Such findings clearly contradict the previous observations made by Cavalcante *et al.* [10].

Additionally, our results also revealed that the agglomeration is more severe in NiSi_Diel_dots sample compared to that of the NiSi_blanket sample. Such finding is unexpected since the NiSi_Diel_dots should not induce any silicide film confinement. This means that NiSi_Diel_dots sample should be equivalent to the NiSi_blanket sample.

Moreover, the plot in Fig. 81 also shows two distinct groups of f_{Si} (%) in particular after RTAD at 650°C, between 60 to 70 % (NiSi_Diel_dots, NiSi_Lines_250, and NiSi_Lines_500), and 30 to 40 % (NiSi_blanket and NiSi_Lines_110). While the agglomeration continues to be exacerbated in the first group at such thermal budget, the f_{Si} (%) of the NiSi_blanket samples appear to have increased significantly up to 35 %, equivalent to the f_{Si} (%) of the NiSi_Lines_110 sample (see Table 21). This implies that area of the exposed Si substrate at the surface of the **non-confined sample** is **identical to that of the most-confined sample** at this particular thermal budget.

Both observations present an unexpected trend in the agglomeration of the Ni(Pt)Si film in confined structures. Several parameters need to be considered in order to provide a relevant explanation to these findings including both the presence of an additional NiSi/dielectric interface and potential grain size difference in different pitch sizes. We will first discuss the trends of agglomeration in the NiSi_Lines samples i.e., Ni(Pt)Si films formed in trenches of pitch sizes of 110, 250, and 500 nm.

Fig. 98 illustrates the schematics of the supposed Ni(Pt)Si grains (in yellow) formed inside one of the trenches for each of NiSi_Lines samples separated by dielectric walls (in grey). Their corresponding expected grain size is noted D_{Lines_110}, D_{Lines_250}, and D_{Lines_500} for (a) NiSi_Lines_110, (b) NiSi_Lines_250, and (c) NiSi_Lines_500 respectively.

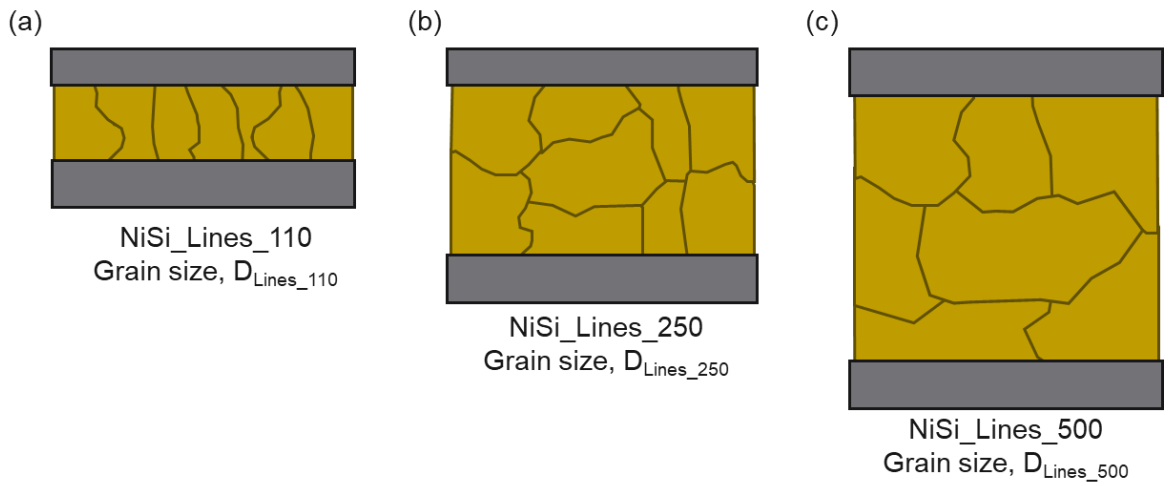


Figure 98. Schematics of the supposed of Ni(Pt)Si grains inside one trench for (a) NiSi_Lines_110, (b) NiSi_Lines_250, and (c) NiSi_Lines_500 samples.

As schematized in the Fig. 98 the silicide grain size is hypothesized to be smallest in the most confined sample, NiSi_Lines_110 implying that $D_{Lines_110} < D_{Lines_250} < D_{Lines_500}$. This hypothesis could be understood as the consequence of the lateral growth of the NiSi phase from the Ni-rich phase, θ-Ni_2Si [58].

In structures with significant confinement (low pitch size), the lateral growth is expected to be limited by the dielectric walls geometrically and hindered kinetically at the silicide/dielectric interface. This results in a more favorable lateral growth of the NiSi grains when the formation is performed in less confined structure such as in the NiSi_Lines_500 samples.

Under the above hypotheses and assuming that the contribution of the NiSi/dielectric interface is equivalent in all of the three cases, the unexpected trends in Fig. 81, can be understood as a difference in the silicide grain size. The tendency to agglomerate at the NiSi/dielectric interface can be considered to be equivalent regardless of the pitch size since total interface area with the dielectric walls is identical in all cases.

This means that the difference in the grain size could play a major role in the observed f_{Si}(%) trends in Fig. 81. The fact that the grain size, D_{Lines_110}, is the smallest the, this implies that a larger driving force is required to induce the agglomeration of the Ni(Pt)Si film in this structure (NiSi_Lines_110). As previously described by the equation 25, the formation of

holes in polycrystalline films will only occur when the grain size is larger than the critical grain size, D_c which is dependent on both the grooving angle, and film thickness [83], [84].

Next, in order to explain the unexpected difference of the Ni(Pt)Si film formed on blanket and least confined wafers, named NiSi_blanket and NiSi_Diel_dots respectively, we hypothesize that that grain size is similar for both samples. Contrary to the previous case of NiSi_Lines samples, NiSi_blanket and NiSi_Diel_dots samples do not present decreasing pitch size meaning that the Ni(Pt)Si film is not confined.

As a reminder, the dielectric dots and lines are comprised of a stacking of two layers namely, a 50 nm SiO_2 layer on top of a 44 nm SiN layer (see Fig. 76). This means that the silicide films in patterned samples (dots or lines) have a different interface compared to that of the Ni(Pt)Si film formed on blanket wafer. This additional interface is the Ni(Pt)Si/SiN interface. The silicide does not present any interface with the SiO_2 since this layer is on top of a 44 nm SiN layer.

The presence of such interface should contribute to a more severe agglomeration of the Ni(Pt)Si film. This hypothesis can be validated when investigating the HRSEM images of the NiSi_Lines samples for example, illustrated in Fig. 80(e) corresponding to the agglomerated state of the Ni(Pt)Si film after an annealing at 700 °C.

The agglomerates (islets) of NiSi appears to be localized at the middle of lines indicating that the first steps of Ni(Pt)Si dewetting occur at the Ni(Pt)Si/SiN interface. This confirms that the interface energy of Ni(Pt)Si/SiN is not favorable due to the fact this interface disappears at the early stages of agglomeration. In addition, the islets are more elongated in the direction “parallel” to the dielectric lines without any remaining interface with the SiN layer.

This could then explain the peculiar fSi(%) trends between the NiSi_blanket and NiSi_Diel_dots samples, which were expected to be equivalent samples i.e., without confinement. Under the assumption of identical grain sizes and Ni(Pt)Si thickness for the two samples (as depicted in Fig. 99), the exacerbated agglomeration in the case of the NiSi_Diel_dots sample might be a direct consequence of the presence of the NiSi/SiN interfaces.

Fig. 99 shows the schematics of the NiSi_blanket and NiSi_Diel_dots samples with $D_{blanket} = D_{Diel_dots}$.

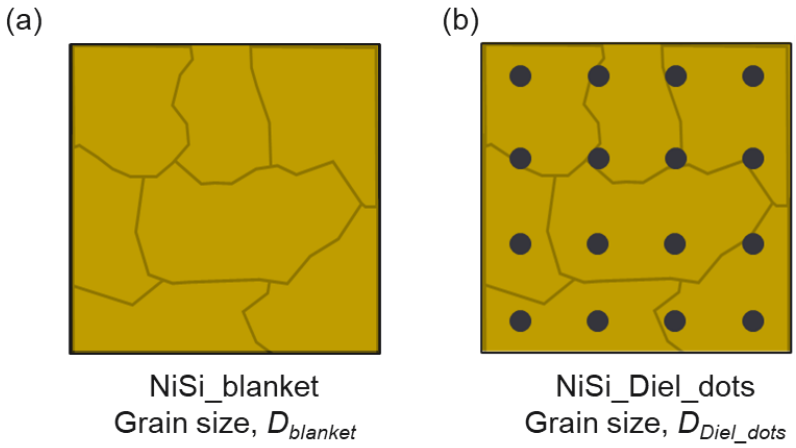


Figure 99. Top-view schematics of the (a) NiSi_blanket and (b) NiSi_Diel_dots samples with $D_{blanket} = D_{Diel_dots}$.

The agglomerated Ni(Pt)Si film in Fig. 80(e) for NiSi_Diel_dots sample clearly corroborate this hypothesis since most of the agglomerates present no more interface with SiN layers.

By combining these two explanations: (i) lower grain size in lower pitch size, and (ii) presence of the additional high interface energy terms due to the NiSi/SiN interface, a relevant explanation may be given for the identical f_{Si}(%) values between the most confined sample, NiSi_Lines_110 and the non-confined sample, NiSi_blanket after an annealing at 650 °C.

(i) Considering that grain size is smaller in lower pitch size, this implies that silicide grains are smaller in NiSi_Lines_110 sample compared to the NiSi_blanket sample, *i.e.,* $D_{Lines_110} < D_{blanket}$. Consequently, better thermal stability should be expected for NiSi_Lines_110 and one should expect $\mathbf{f_{Si}^{NiSi_Lines_110}(\%) < f_{Si}^{NiSi_blanket}(\%)}$.

(ii) Considering the presence of an additional Ni(Pt)Si/SiN interface in the NiSi_Lines_110 sample inducing a higher driving force for the minimization of the interface energy, one should then expect $\mathbf{f_{Si}^{NiSi_Lines_110}(\%) > f_{Si}^{NiSi_blanket}(\%)}$.

Under these assumptions, the expected lack of thermal stability due to the presence of the Ni(Pt)Si/SiN interface could then be compensated by the small grains size which allows

an improvement of the thermal stability of the Ni(Pt)Si film formed in the line structure of pitch, p=110 nm. This results then in similar level of agglomeration with the blanket wafer.

This study highlights the importance of the impact of the nano-confinement on the final properties of the Ni(Pt)Si film, and on the agglomeration phenomenon. Indeed, understanding the agglomeration within the confined structures remained however a complex task. At the current stage, we attribute the different observations in the part 3 of chapter 4 to the hypotheses presented above. Deeper analyses may be required to investigate the impact of the Ni(Pt)Si/SiN interface on the crystalline orientations of the silicide grains.

4.2 Impact of additional elements

4.2.1 Observations of Pt redistribution

Fig. 100 shows the TEM cross-sections of an 11 nm Ni(Pt)Si thin film after an annealing at 400 °C at three different magnifications: low magnification (a), high magnification between adjacent grains (b), and at the middle of a grain (c).

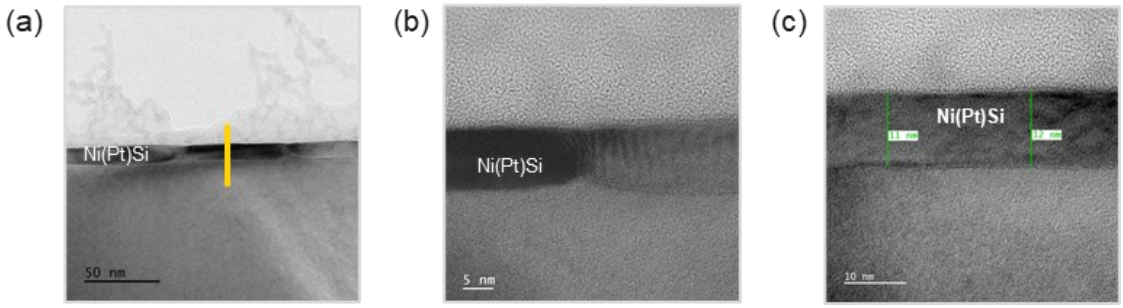


Figure 100. TEM cross sections of a 11 nm Ni(Pt)Si thin film formed using the standard SALICIDE process (identical to the NiSi_partial sample) and an additional annealing at400 °C. Three different magnifications are shown: (a) low magnification, (b) high magnification between adjacent grains, and (c) at the middle of a grain. The yellow line indicates EDX line scan.

The silicide film appears to remain continuous with over the long range as shown by the low magnification TEM image in Fig. 100(a), (c). Moreover, very minimal curvature can be seen at the grain boundary of two adjacent grains indicating the presence of a very weak groove (Fig. 100(b)). Indeed, an annealing at 400 °C may not be sufficient to induce any significant changes to the morphology of the silicide film. These results are consistent with the 11 nm Ni(Pt)Si film used in the study on the impact of the annealing schemes (see part 2, in chapter 3), indicating film stability up to 550 °C (Fig. 70(a)-(i), (ii)).

At this stage *i.e.,* we can confirm that neither the boundary grooving nor the agglomeration phenomenon has occurred. EDX measurements are then performed to account for the initial redistribution of the elements prior to any subsequent RTAD heat treatments.

Fig. 101 illustrates the STEM image (a) and the corresponding EDX mapping for Ni (b), Si (c) and Pt (d) for 11 nm Ni(Pt)Si submitted to SALICIDE process and RTAD at 400 °C.

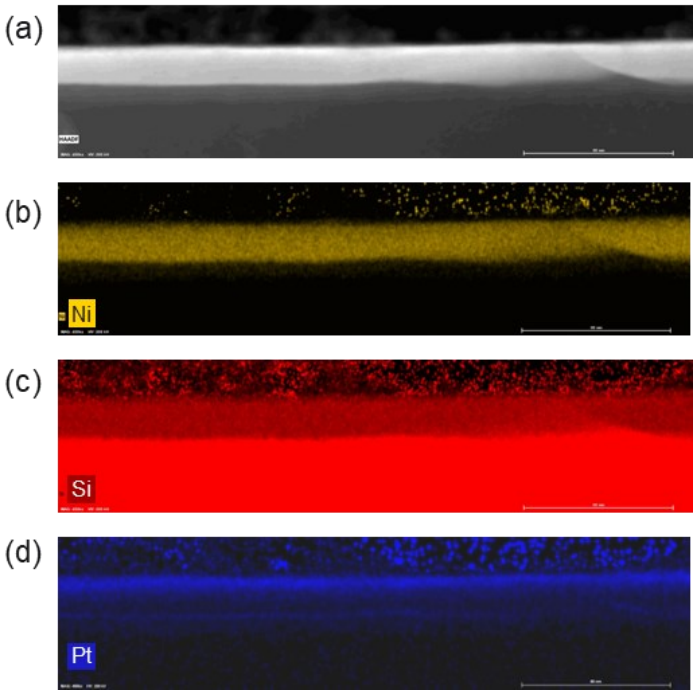


Figure 101. (a) STEM-EDX cross-sections of 11 nm Ni(Pt)Si thin film formed using standard SALICIDE (NiSi_partial) after RTAD 400 °C with the STEM image, (b) Ni EDX map, (c) Si EDX map, and (d) Pt EDX map.

As shown in Fig. 101(b) and (c), the redistribution of Ni and Si is relatively uniform within the overall thickness of the Ni(Pt)Si film. Meanwhile, most of the Pt are distributed near the surface of the silicide film with very minimal concentration at the silicide/Si interface.

To better visualize the initial Pt distribution, EDX line scan is performed along the yellow lines drawn in Fig. 100(a) and is plotted in Fig. 102 together with the distribution of Ni and Si.

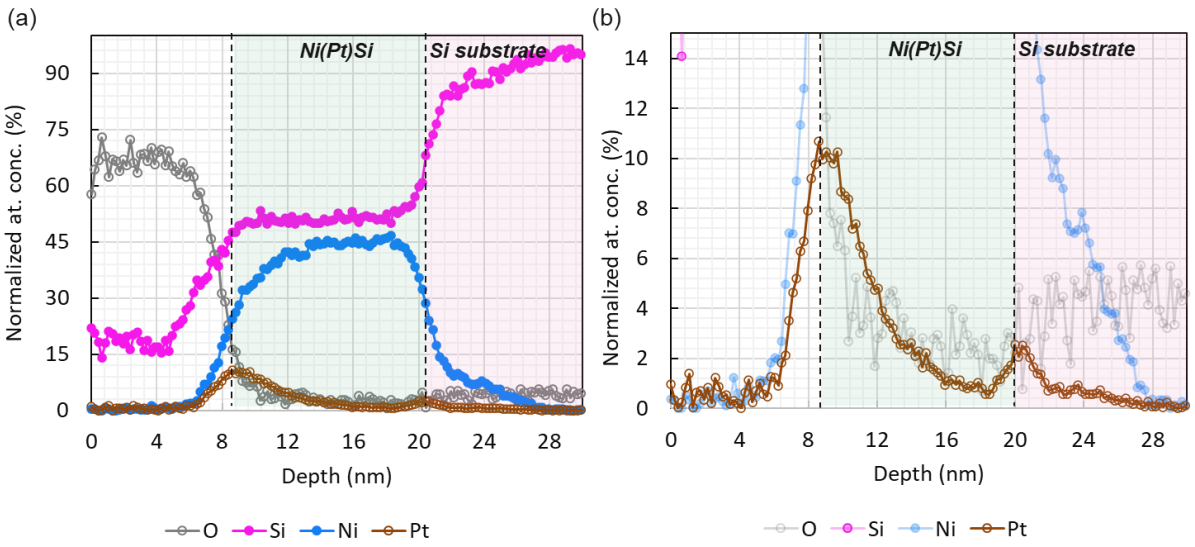


Figure 102. (a) EDX line scans of Pt concentration measured along the yellow lines in Fig. **100 and (b) zoom EDX line of the same sample for better visualization of Pt redistribution. Regions shaded in green correspond to the Ni(Pt)Si layer and pink to the Si substrate.**

As depicted in Fig. 102(a), the silicide layer can be identified by the region shaded in green corresponding to a zone where the Ni concentration is superior to 30 at.%. This is also confirmed by the plateau of the Si concentration remaining around 50 at.% indicating the 1:1 ratio between the Ni and Si. Two concentration maxima can be seen in Fig. 102(b) corresponding to the high concentration of Pt (around 10 at.%) accumulated at the top surface of the silicide film and the low concentration of Pt near the silicide/Si interface (at around 2 at. %).

Similar characterizations (TEM and STEM-EDX) are then performed on the 11 nm Ni(Pt)Si film after annealing at higher RTAD temperatures *i.e.,* 500, 550, 600 and 700 °C.

Fig. 103 shows the TEM cross-sections performed on the silicide sample after each of the RTAD temperatures for similar level of magnifications shown in Fig. 100. Yellow, cyan, and pink lines are included in the corresponding TEM images indicating the area used to perform the EDX line scan.

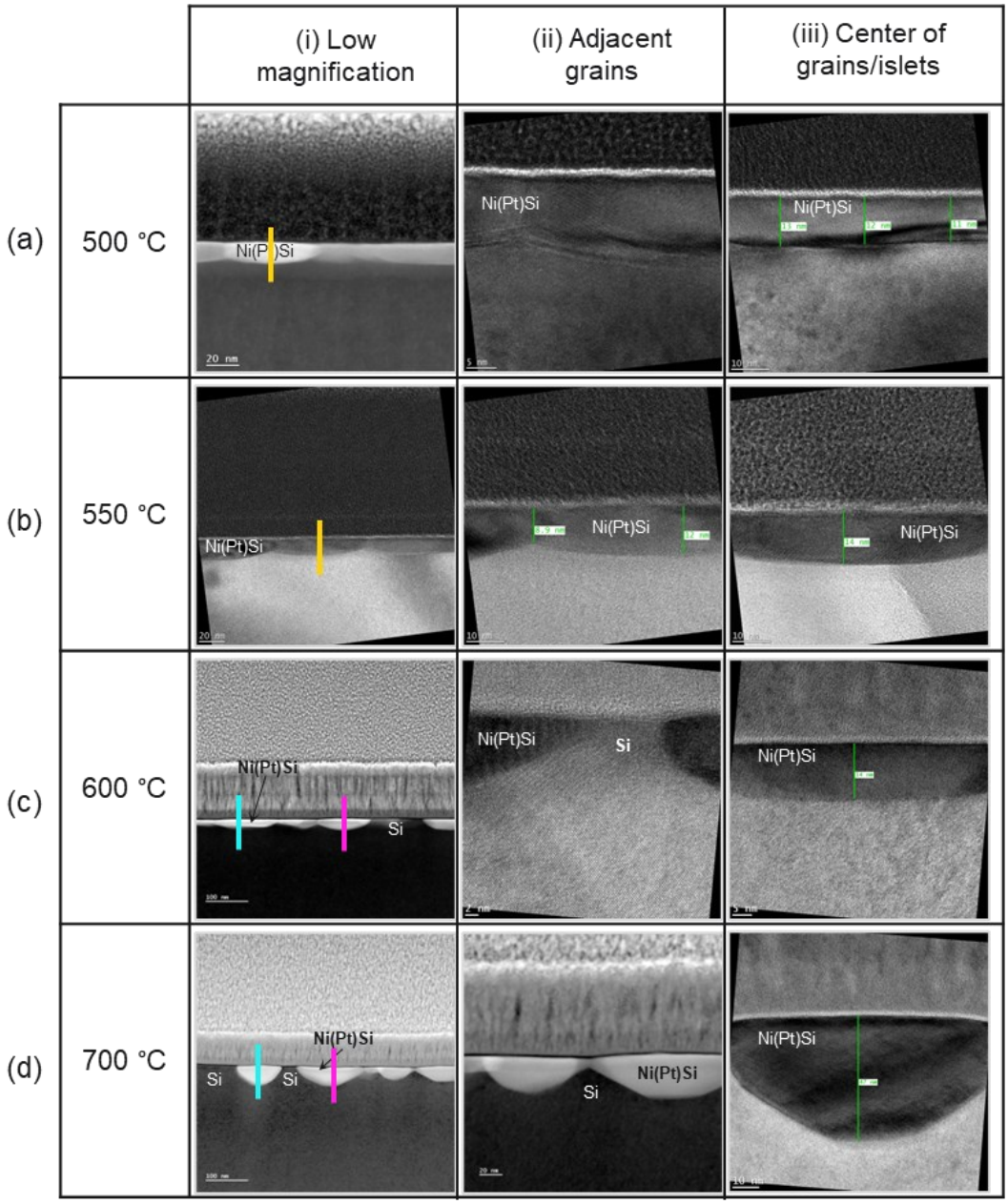


Figure 103. TEM cross-sections of the morphological evolution of the 11 nm Ni(Pt)Si thin film at each of the RTAD annealings, (a) 500, (b) 550, (c) 600, and (d) 700 °C, taken at (i) lower magnification, (ii) between adjacent grains, and (iii) at the center of a grain/islet. Note that all of the silicide films are formed using the standard SALICIDE process (equivalent to that of the NiSi_partial sample). Yellow, cyan and pink lines indicate EDX line scans.

Fig. 103(a) shows a continuous Ni(Pt)Si film after an annealing at 500 °C. However, curvature of the silicide/Si substrate interface is more pronounced compared to the previous case (after annealing at 400 °C). The formation grooves can clearly be seen between two adjacent grains. The TEM images performed after an annealing at 550 °C appears to show an almost similar morphology of the Ni(Pt)Si thin film. However, the boundary grooving

phenomenon is more exacerbated at this thermal budget. The groove depth, δ between the adjacent grains have receded as shown by the TEM image in Fig. 103(b)-(ii).

At a higher annealing temperature such as 600 °C, morphological discontinuity can be seen in the Ni(Pt)Si film. The Si substrate have displaced towards the surface as illustrated in Fig. 103(c)-(i) and (ii). Moreover, the grain near the exposed Si substrate also reveals an increase in its thickness confirming the inverse agglomeration of the Ni(Pt)Si film.

At 700 °C, formation of small NiSi islands (islets) can be observed (Fig. 103(d)). The islets exhibit increased depth compared to the initial thickness of the Ni(Pt)Si film as shown in Fig. 103(d)-(ii) and (iii). The local thickening of the islets occurs with an increase of the depth of the grooves, δ due to the NiSi displacement towards the lower portion of the grains.

Fig. 104 shows the EDX line scans of Pt performed for each of the samples previously described along the yellow, cyan, and pink lines in Fig. 103. Similar colors shading is used to indicate the Ni(Pt)Si layer and the Si substrate, separated by dashed lines for each interface.

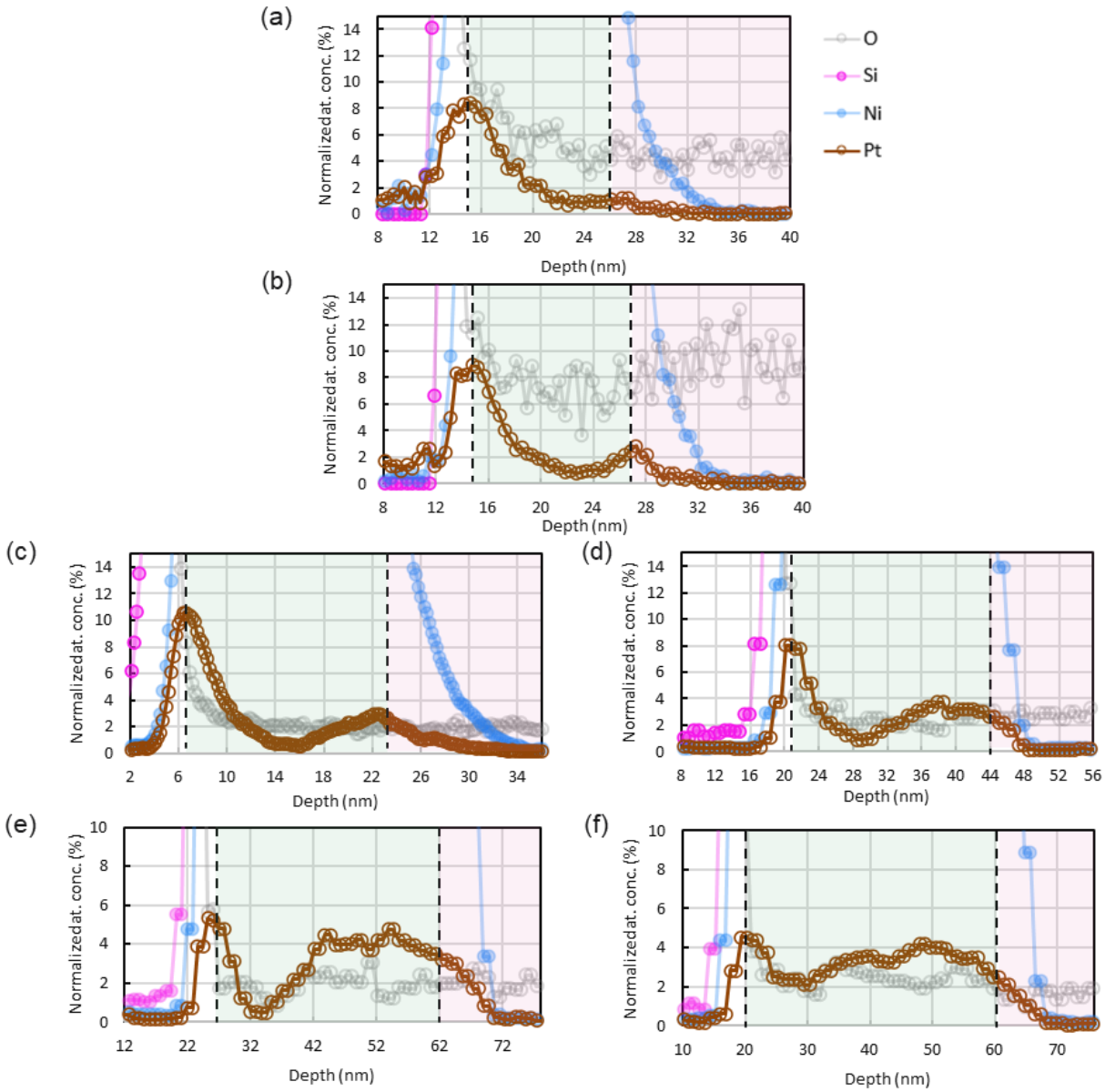


Figure 104. EDX line scans of Pt concentration measured along the yellow lines in Fig. **4.4 for each of the RTAD temperatures: (a) 500, and (b) 550 °C. Two lines scans are provided for RTAD at 600 °C corresponding to grains with boundary grooving (cyan line) (c), and grains near a hole (pink line) (d). Similarly for 700 °C: line scan for isolated islet (cyan line) (e), connected islet (pink line) (f). Regions shaded in green corresponds to Ni(Pt)Si layer and pink to Si substrate.**

As shown in Fig. 104(a), most of the Pt are located near the surface of the silicide film after an annealing of 500 °C, similar to the initial Pt distribution previously described for annealing at 400 °C. After an annealing at 550 °C, the EDX line scan in Fig. 104(b) show that there is a rise of the Pt concentration at the interface. This observation is further corroborated at higher annealing temperature (600 °C) as shown in Figs. 104(c) and (d), clearly revealing an increase of the Pt concentration at the bottom of the silicide grains.

Moreover, the Pt seems to exhibit a peculiar redistribution as the concentration profile is spread over a wider range of depth compared to that of the Pt located at the surface. Finally, after an annealing at 700 °C, the concentration of Pt at the surface is drastically reduced and redistributed over a larger range of depth *i.e.,* over the displaced NiSi forming the bottom part of the islets.

Further inspection by STEM-EDX mapping of the Pt at different RTAD temperatures is also performed. Fig. 105 shows the EDX mapping of Pt performed for Ni(Pt)Si film after annealing at 500 (a), 550 (b), 600 (c)-(d), 700 °C (e).

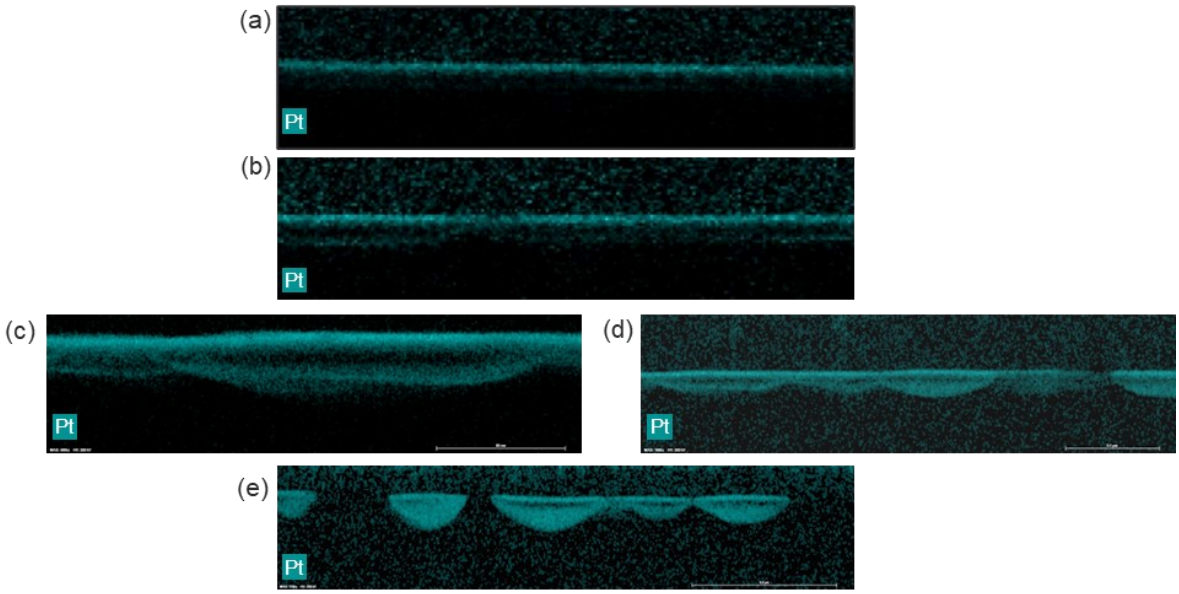


Figure 105. EDX maps of Pt measured on Ni(Pt)Si thin films after RTAD annealing at (a) 500, (b) 550, (c) 600 °C zone 1, (d) 600 °C zone 2, and (e)700 °C.

At the initial stage, the Pt redistribution near the surface of the silicide remains consistent with previous observations as can be seen in Fig. 105(a) with minimal concentration at the silicide/Si interface. Moreover, the increase of Pt concentration at the silicide/Si interface after annealing at 550 °C, can also be confirmed by the EDX mapping in Fig. 105(b). Indeed, based on these two EDX mappings, three principal regions can be identified: (i) Pt-rich near surface, (ii) Pt-depleted region within the silicide film, and (iii) Pt-rich displaced NiSi near the silicide/Si interface.

The presence of these regions is then further visible at higher annealing temperature such as 600 °C. Additionally, the third region shows an increase in depth at this thermal

budget indicating that Pt may have diffuse by means of the grain boundary and interface towards the bottom of the grains. Finally, at a more severe agglomeration stage, *i.e.,* after annealing at 700 °C, Pt seems to dominate over the bottom part of the NiSi islets corresponding to the displaced NiSi during the agglomeration phenomenon.

In order to evaluate the evolution of the Pt concentration during the agglomeration of the Ni(Pt)Si film, the ratio between the Pt concentration at the silicide surface and at the silicide/Si interface can be calculated as follows:

$$\boldsymbol{Ratio\ of\ Pt}\ (\%) = \boldsymbol{Pt}\ (\boldsymbol{conc.})_{\boldsymbol{interface}} / \boldsymbol{Pt}(\boldsymbol{conc.})_{\boldsymbol{surface}} \qquad \textbf{Equation 26}$$

Fig. 106 illustrates the evolution of the concentration of Pt at the interface at each RTAD annealing temperature *i.e.,* during the agglomeration of the Ni(Pt)Si thin film.

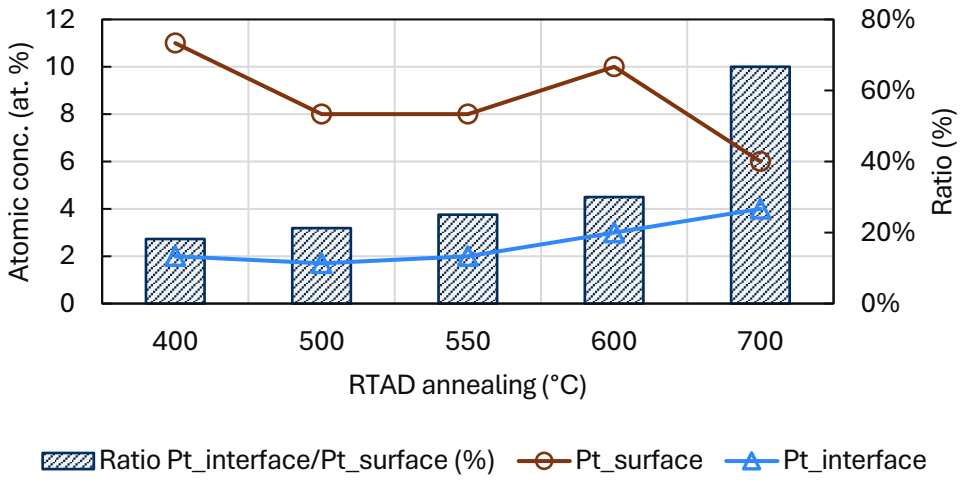


Figure 106. Evolution of the Pt concentration at the top surface of the Ni(Pt)Si thin film and at the Ni(Pt)Si/Si interface and their corresponding ratio (Pt_interface/Pt_surface) at each of the RTAD temperatures (°C).

As plotted in Fig. 106, the concentration of Pt at the silicide/Si interface shows a drastic increase during the agglomeration of the Ni(Pt)Si film consistent with the overall observations made from the EDX mapping.

4.2.2 Initial redistribution of Pt: before agglomeration

The initial redistribution of Pt revealed that the three identified regions are already present. However, most of the Pt are located near the surface of the sample and the third region is not rich in Pt at this stage. Furthermore, at the current stage (prior to high temperature annealing), the redistribution of the Pt near the surface has been reported in a previous works. Indeed, the redistribution of Pt during Ni silicide formation has been extensively studied [65], [146], [147], [148]. Different behaviors have been reported depending on the Pt content and the initial phase that forms [65], [146]. Specifically, for Ni(5%Pt), the first phase to grow is δ-Ni_2Si, in which Pt has low solubility.

Consequently, Pt is rejected from the growing δ-Ni_2Si phase by the snowplow effect [149], leading to Pt segregation at the δ-Ni_2Si grain boundaries (GB) and enrichment in Pt of the unreacted Ni(Pt) film. In contrast, for Ni(10%Pt), the first phase to grow is θ-Ni_2Si, in which Pt has relatively high solubility. Additionally, the diffusion coefficient of Pt in θ-Ni_2Si is lower than that of Ni. These two characteristics lead to the formation of a Pt-enriched region near the surface characterized by a Pt diffusion profile with the highest concentration near the surface.

During the subsequent transformation from θ-Ni_2Si to NiSi, the existing Pt gradient is incorporated into the upper portion of the NiSi film. Concurrently, Pt diffuses through the NiSi grain boundaries and accumulates at the NiSi/Si interface. However, the amount of Pt at these interfaces is very limited since lattice diffusion is very limited at low temperatures. Ultimately, most of the Pt is located near the surface of the NiSi film, with lesser amounts accumulating at the NiSi grain boundaries (GBs) and the NiSi/Si interface [146]. The EDX line scan performed after an annealing at 400 °C appears to be very consistent with that seen in the work by Panciera *et al.* [146].This means that the initial Pt redistribution is mainly due to solubility and diffusion of Pt within the Ni-silicides and is reproducible during the formation of the Ni(Pt)Si thin film.

4.2.3 Pt redistribution during the agglomeration

The previous observations clearly reveal that Pt exhibit a peculiar and complex redistribution during the boundary grooving and agglomeration phenomena. As a summary, the unusual redistribution of Pt during the grooving and agglomeration of the Ni(Pt)Si film at different thermal budgets is clearly illustrated by the EDX mapping in Figure 105. In all cases, three distinct regions are observed: a Pt-rich region near the surface, a Pt-depleted region within the silicide, and another Pt-rich region corresponding to the displaced NiSi at the silicide/Si interface.

These observations highlight the complex redistribution of Pt during the formation and agglomeration phenomena, which have been schematized in Figure 107. Several factors can contribute to this redistribution. Primarily, agglomeration involves changes in the shape of the NiSi grains/agglomerates, leading to the transfer of matter. Since matter is conserved, not only Ni and Si but also Pt atoms should be displaced during grooving and agglomeration. This is because the solubility of Pt is very limited in Si, while Pt is fully soluble in NiSi. The driving force for this redistribution is the reduction of interface energy, and the transport occurs mainly along the silicide/silicon interface, as shown by Luo *et al.* [53].

This allows the silicide grains to change shape while the Si substrate becomes uncovered by the silicide. Secondly, classical diffusion driven by the gradient of chemical potential associated with concentration differences may also be at play. This would transfer Pt atoms from the high Pt concentration region near the surface to the silicide/Si interface, which has a lower Pt concentration than the sub-surface region of NiSi. Interfaces such as the NiSi surface, NiSi grain boundaries (GB), and the NiSi/Si interface typically act as fast diffusion paths compared to lattice diffusion. Consequently, the redistribution of Pt primarily follows these paths, as indicated by the schematics in Figure 107.

However, as the temperature increases, the difference in diffusion rates between fast paths and lattice diffusion diminishes. This is because fast diffusion paths typically have lower activation energies than lattice diffusion. Therefore, at relatively high temperatures, lattice diffusion may also contribute significantly to the redistribution of Pt. This explains why at a moderate agglomeration stage (600°C/30 s), Pt concentration remains high at the

top surface of Ni(Pt)Si, with notably lower concentrations at the bottom while at 700°C, the Pt concentration at the top surface decreases significantly and the Pt concentration increases at the bottom part of the agglomerate.

Therefore, at intermediate temperatures, the Pt redistribution is mainly due to the transfer of matter by grooving and agglomeration to form the islets while, at high temperatures, lattice diffusion is also acting to transfer Pt from the Ni(Pt)Si sub-surface region to the displaced region.

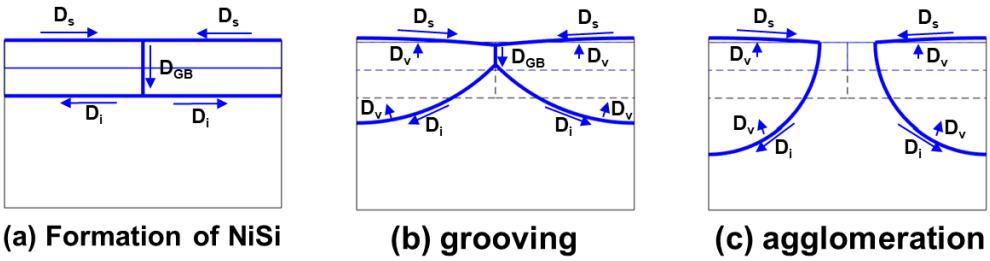


Figure 107. Schematics illustrating diffusion paths during different processing steps: (a) Formation of NiPtSi at 380 °C (b) Grooving during RTAD at 600 °C (c) Agglomeration during RTAD at 700 °C. Arrows indicate the direction of diffusion, with corresponding diffusion coefficients provided.

4.2.4 Pt redistribution in the case of laser annealing

Based on the previous discussions, a special attention needs to be given to the Ni(Pt)Si films formed using the milliseconds laser annealing (DSA) used both in part two and part four of the experimental studies in chapter three (*i.e.,* NiSi_laser and NiSi_circuit_laser). As a reminder, the laser annealing is performed at 815 °C for a dwell time of 0.25 ms instead of the classical RTA2 at 390 °C/30 s used in the SALICIDE process.

Indeed, such conditions are pre-determined based on several factors, namely surface emissivity, laser scanning speed, and wafer backside chucking temperature, and allows the complete transformation of the θ-Ni_2Si phase into NiSi. This is confirmed by the ellipsometry measurement in Table 15 showing Ni(Pt)Si thickness of 10.9 nm in the case of the laser annealing, and the Rs measurements < 40 Ω/sq indicating the Ni(Pt)Si phase is well formed regardless of the choice of the annealings used.

Nevertheless, despite the identical thickness, NiSi_laser samples showed better thermal stability up to at least 600 °C compared to 550 °C in the case of the NiSi_partial sample (Fig. 70). The HRSEM images in Fig. 72 revealed that the grain size of the silicide film is reduced by 50 % when laser annealing is used in the formation of the Ni(Pt)Si film rather than the RTA-type annealing (also reported in Table 18). The improvement of the thermal stability can thus be understood as the consequence of the grain size reduction as reported by an extensive number of literatures [83], [84], [91], [141], [145]. The role of grain size will be further discussed in the following section.

Nonetheless, as previously described in section 4.2.3, the driving force for the peculiar redistribution of Pt can be explained by two principal mechanisms: Matter transport during agglomeration and chemical potential gradient due to Pt concentration difference between the upper and lower portions of the silicide film (implying grain boundary diffusion, interface diffusion and/or lattice diffusion).

Under these assumptions and the drastically reduced silicide grain size in the case of the laser annealing, one should expect an increase of the Pt diffusion towards the lower portion of the NiSi grains, assisted by the increased quantity of fast diffusion pathways i.e., grain boundaries. Indeed, smaller grains means that the density of the grain boundary is significantly higher in the case of the NiSi_laser sample compared to that of the NiSi_partial sample (see Fig. 72(a) for example for NiSi_laser and NiSi_partial).

Fig. 108 shows the EDX line scan of Pt measured at the center of silicide or islets of NiSi for NiSi_partial and NiSi_laser samples after an annealing at 550 and 650 °C, corresponding to the state of non-agglomerated and agglomerated Ni(Pt)Si film respectively. Similar color shading is used to indicate the Si substrate (in pink), lower portion of NiSi islet *i.e.,* displaced NiSi (in yellow), and finally the Ni(Pt)Si thin film (in green).

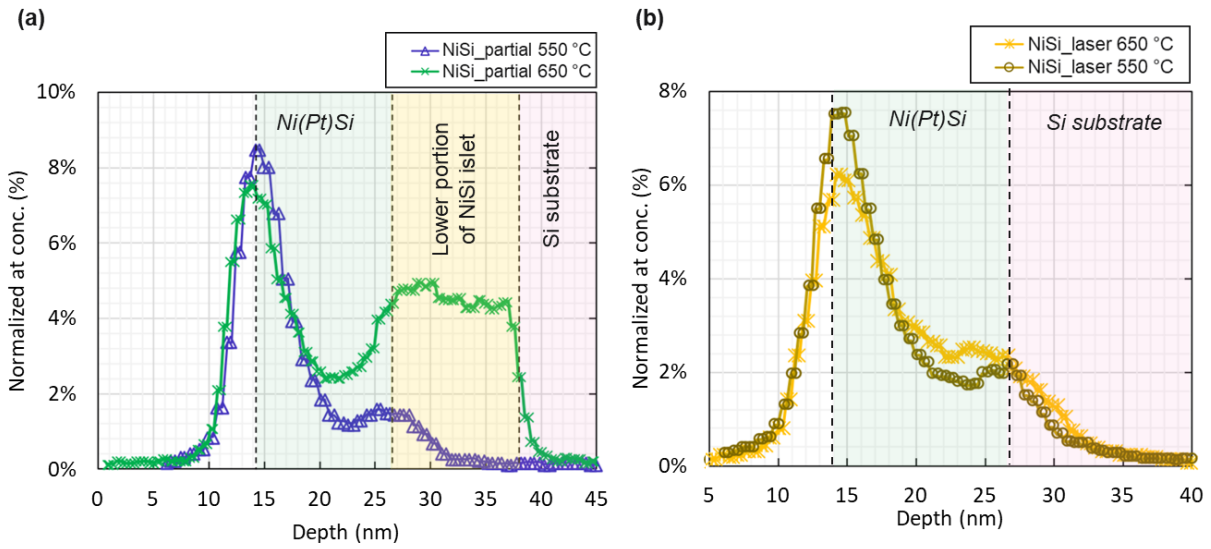


Figure 108. EDX line scans of Pt measured at the center of silicide grains/islets for (a) NiSi_partial sample, and (b) NiSi_laser sample after annealing at two RTAD temperatures corresponding to the agglomerated (650 °C) and non-agglomerated (550 °C) stage.

In both cases, the three identified Pt regions described in the previous section can be observed: Pt-accumulation at the top surface, Pt-depletion region, and Pt-rich interface. Moreover, the redistribution of Pt over a wider range of depth at lower portion of the silicide grains/islets appear to be very consistent with previous observations in both cases. The concentration of Pt at this region appears to be more significant in the case of the NiSi_partial sample after an annealing of 650 °C as depicted in Fig. 108(a). This is expected since agglomeration is more advanced for the NiSi_partial sample at this RTAD temperature.

Nonetheless, in order to better compare the redistribution of Pt between the NiSi_partial and NiSi_laser samples, the EDX line scans of Pt from Fig. 108(a) are extracted and superimposed by depth alignment at Ni of 30 at. % and concentration normalization with Si bulk.

Fig. 109 shows the superimposition of the EDX line scans of Pt for NiSi_partial and NiSi_laser samples at non-agglomerated stage corresponding to RTAD annealing of 550 °C.

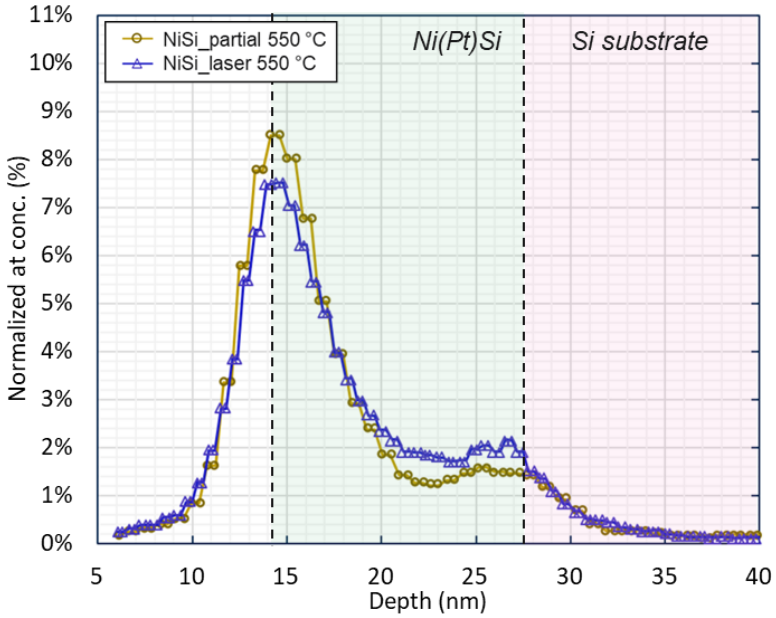


Figure 109. Superimposition of the EDX line scans of Pt after normalization using the concentration in Si bulk, and depth alignment at Ni of 30 at. %, measured for NiSi_partial and NiSi_laser samples after an annealing at 550 °C (extracted from Fig. **109(a) and(b)).**

Indeed, the Pt at the silicide/Si interface appears to be slightly more significant in the case of the NiSi_laser sample. The higher concentration of Pt at the interface can be explained by two principal factors: laser annealing dealing with very high temperature for shorter times and the reduction of the silicide grain size by 50 % as compared to the case of the NiSi_partial samples. The former factor implies that the laser annealing provides a more significant overall energy to the system, increasing the driving force of the diffusion of Pt.

In addition, following this hypothesis, lattice diffusion with higher activation energies may also participate in the overall Pt diffusion towards the silicide/Si interface. However, the short dwell time may also mean that higher rate of nucleation is involved with relatively lower rate of lateral growth. The second factor relating to the grain size confirms our initial hypothesis suggesting an increase of the density of fast diffusion pathways (grain boundaries) in silicide film formed using the laser annealing. This further facilitates Pt diffusion enhancing the silicide thermal stability.

4.2.5 Modelling of the redistribution of Pt

Based on the observation of the Pt redistribution characterized using the TEM-EDX line scan and STEM-EDX mapping, a model is developed to further provide understanding on the role of Pt atom in the agglomeration of the Ni(Pt)Si thin film.

We propose this new model based on the previous work of Luo *et al.* [53] on the role of the slow diffusing Si in the agglomeration of NiSi films. In this new model, we consider the previously presented peculiar redistribution of Pt.

The previous model [53] is developed to describe the redistribution of Si isotopes during the grooving and agglomeration of NiSi, without considering Pt as an alloying element. Based on experimental observations by SEM and atom probe tomography [53], the model assumes that Ni and Si atoms diffuse away from the top NiSi layer near a grain boundary (GB) and form new NiSi beneath the film. This leads to the exposure of some Si regions and a change in the NiSi shape, with an increase in thickness. The model assumes the following main conditions [53]: (i) The volume of the NiSi grain is assumed to be constant during agglomeration (*i.e.*, no grain growth), (ii) The atomic volume of Si is taken as double that of NiSi, while the exact atomic volumes are 20 nm³ and 12 nm³, respectively, (iii) The surface of the Ni(Pt)Si grain remains flat, as roughly observed in the TEM images. Concerning atomic transport, the following additional assumptions are made: (iv) Ni diffusion is fast in NiSi, (iv) Lattice diffusion of Si in both NiSi and Si is limited, and (v) Si diffusion is fast at the NiSi/Si interface.

In the present model, the same assumptions are made, with additional ones for Pt: (vi) Initially, Pt is uniformly distributed with a concentration x_{Pt}^{0} in a slab of thickness h_{Pt}, at the subsurface region of the silicide (vii) Finally, Pt is uniformly redistributed with a concentration x_{Pt} in the new NiSi volume, and (viii) Redistribution of Pt occurs primarily through diffusion at the NiSi/Si interface.

Under the above assumptions, the redistribution of Pt during grooving and agglomeration can be modeled using the mass conservation law. Given the first two assumptions, the law of conservation of mass is equivalent to the conservation of volume (*i.e.*, the volume of Si released by agglomeration is equal to the volume of newly formed

NiSi). Various geometries are considered for the agglomerated grains, including two-dimensional shapes (faceted grain, circular segment) and three-dimensional shapes (spherical cap from columnar grains with different base shapes such as square, hexagon, or circle). It is found that the geometry that best fits the shape and Pt concentration of the islands is a 3D spherical cap starting from hexagonal-based columnar grains, as illustrated in Fig. 110.

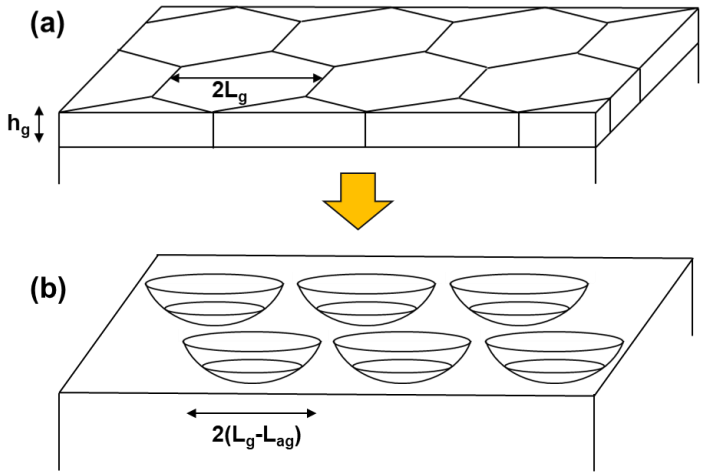


Figure 110. Schematics of the geometry used for the redistribution model: (a) initial columnar grains with a hexagonal base, (b) islands with a spherical cap shape after agglomeration.

Using Eq. 31 to 44 (**see appendix A.iii**), the shape of the Ni(Pt)Si grains observed by TEM (Fig. 103(c) and (d)) were fitted by varying several parameters: L_g , L_{ag}, h_{gr} while the following parameters were fixed for all grains: $h_g = 15\ nm$, $h_{Pt} = 6\ nm$, $x_{Pt}^0 = 9\ at.\%$. Fig. 111 shows the fit obtained for the second grain from the left in Fig. 106(e) (RTAD 700°C).

Fig. 111(a) displays the fitted shape, which is superimposed in Fig. 111(b), and, in Fig. 111(c), the Pt-rich regions are colored in blue. The same type of fitting was performed for several grains, and the results are shown in Figure 112 for grooving (RTAD 600°C) and in Figure 113 for agglomeration (RTAD 700°C).

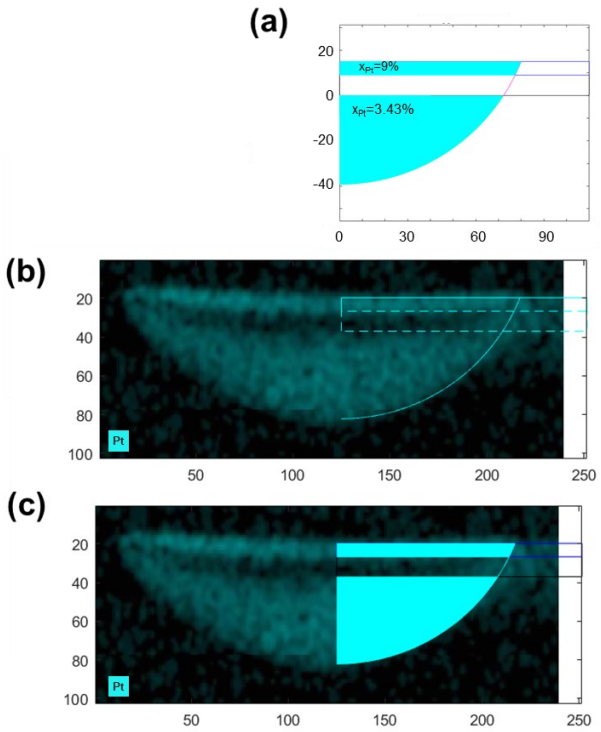


Figure 111. Example of fit of the EDX map for Pt for a grain after agglomeration (second whole grain from the right in Fig. 105(e)) using the present model: (a) fitted shape and Pt-rich region, (b) EDX map for Pt with the fitted shape and Pt-rich region superimposed, (c) same as (b) with the Pt-rich regions highlighted in blue.

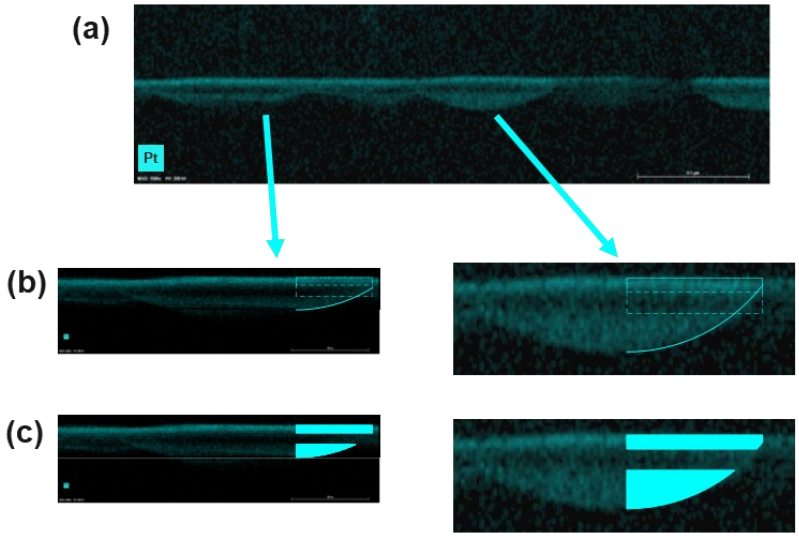


Figure 112. Fit of the EDX map for Pt for two grains after grooving (RTAD 600°C, Fig. **105(d)) using the present model: (a) whole EDX map for Pt, (b) EDX map for Pt with the fitted shape and Pt-rich region superimposed, (c) same as (b) with the Pt-rich regions highlighted in blue.**

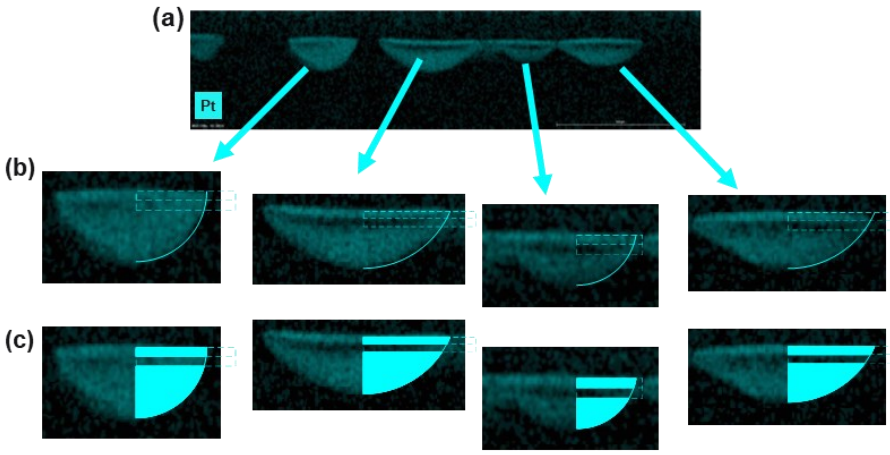


Figure 113. Fit of the EDX map for Pt for four grains after agglomeration (RTAD 700°C, Fig. **105(e)) using the present model: (a) whole EDX map for Pt, (b) EDX map for Pt with the fitted shape and Pt-rich region superimposed, (c) same as (b) with the Pt-rich regions highlighted in blue.**

Although the fit is more challenging for RTAD 600°C, as the grains in this sample are at mixed stages of grooving and agglomeration, the 3D model still provides a very good match to the shape of the grains and the redistribution of Pt, including the different Pt concentration regions. This is particularly true for RTAD 700°C, where there is excellent agreement between the simulation and TEM images, despite the grains exhibiting varying degrees of agglomeration, as evidenced by the different curvatures of the Ni(Pt)Si/Si interface. This agreement validates the main assumptions of the model for grooving and for agglomeration.

From the model, the Pt concentration in the displaced Ni(Pt)Si (V_2) can be calculated. These calculated concentrations, $x_{Pt}^{gr/ag}(V_2)$, are reported in Table 22 alongside the measured concentrations from EDX, $x_{Pt}^{EDX}(V_2)$. The fitted parameters, L_g , L_{ag}, h_{gr} , are also included in the Table. It can be observed that the calculated values are systematically lower than the measured ones.

Table 22. Comparison between the measured EDX concentrations, $x_{Pt}^{EDX}(V_2)$, $x_{Pt}^{EDX}(V_6)$, and the calculated ones, $x_{Pt}^{gr/ag}(V_2)$, $x_{Pt}^{total}(V_2)$. The fitted parameters, L_g , L_{ag}, h_{gr} , are also included.

RTAD	Grain n°	L_g	h_{gr}	L_{ag}	$x_{Pt}^{EDX}(V_6)$	$x_{Pt}^{EDX}(V_2)$	$x_{Pt}^{gr/ag}(V_2)$	$x_{Pt}^{total}(V_2)$
600°C	1	80	10	-	8.6	3	0.35	2.4
600°C	2	60	10	-	8.3	3.6	3.5	4.5
700°C	1	90	-	30	4.3	4	3.5	4.7
700°C	2	110	-	30	5.2	4.5	3.4	4.7
700°C	3	55	-	7	5	4	3	5.8
700°C	4	100	-	20	5.5	3.9	3.3	4.8

Furthermore, Table 22 shows that the Pt concentration in the subsurface region, $x_{Pt}^{EDX}(V_6)$, decreases drastically from the 600°C RTAD to the 700°C RTAD. As discussed previously, this decrease might be due to volume diffusion from the Pt-rich subsurface region towards the surface, and then to fast diffusion along the surface, grain boundaries (GB), and the silicide/Si interface towards the bottom of the grain.

This transport of Pt will contribute to enriching the Ni(Pt)Si region displaced during grooving and agglomeration. The model developed above does not take into account this transport. To account for it, we assume that the change in Pt concentration inside the subsurface region, $\Delta x_{Pt}^{S} = x_{Pt}^{0} - x_{Pt}^{EDX}(V_6)$, has been transferred to the displaced region, as it should be from the conservation of matter.

The additional contribution of Pt for grooving can be expressed as:

$$\mathbf{x_{Pt}^{dif} = \Delta x_{Pt}^{s} \frac{V_6^{gr}}{V_2^{gr}}} \qquad \textbf{Equation 27}$$

where the volume V_6^{gr} is denoted by :

$$\mathbf{V_6^{gr} = a_{sh} L_g^2 h_g - V_4^{gr}} \qquad \textbf{Equation 28}$$

For agglomeration, the volume V_6 is formulated as:

$$\mathbf{V_6^{ag} = V_3^{ag} - V_5^{ag}} \qquad \textbf{Equation 29}$$

The total Pt concentration in the displaced Ni(Pt)Si region is then given by :

$$\mathbf{x_{Pt}^{total}(V_2) = x_{Pt}^{gr/ag}(V_2) + x_{Pt}^{dif}} \qquad \textbf{Equation 30}$$

Table 22 shows relatively good agreement between the Pt concentration measured by EDX, $x_{Pt}^{EDX}(V_2)$, and the total Pt concentration, $x_{Pt}^{total}(V_2)$, calculated using Eq. 30. This calculation takes into account the transport due to grooving and agglomeration, as well as the transport due to Pt diffusion from the subsurface region. The concentrations measured by EDX are generally slightly lower than the calculated ones. This discrepancy can be attributed to the EDX signal integrating over the entire width of the TEM lamella, while the Ni(Pt)Si grain may not extend through the whole width of the lamella. This effect can lead to measured concentrations that are lower than the actual ones.

Nevertheless, the agreement between experiments and simulation is quite good, validating the model and assumptions developed here. Since there is a relatively large contribution of Pt transport from the subsurface region at 700°C, volume diffusion, which should be the limiting diffusion process, should not be negligible at this temperature. The driving force behind this diffusion of Pt at the silicide/Si interface is likely the reduction of the Pt concentration gradient, whereas the driving force for grooving and agglomeration is the reduction of interface energy.

The redistribution of Pt during grooving and agglomeration is relatively similar to that of the Si isotopes observed by Luo *et al.* [53]. As these phenomena lead to a change in grain shape, the displacement of all species is required. Therefore, the transport of the least mobile species may control the kinetics of these phenomena. For pure NiSi compounds, the slow species is Si, but its transport becomes non-negligible at the fastest diffusion path, the silicide/Si interface, when grooving and agglomeration become active. For Ni(Pt)**Si**, the slowest diffusing species may be Pt, or Pt may slow down the diffusion of Si, as Pt is known to delay grooving and agglomeration. The present model confirms that the silicide/Si interface is the predominant diffusion path during grooving and agglomeration, even though some surface and volume diffusion also occur.

Agglomeration is undoubtedly a more complex process than the simplified model presented here. Even in model systems like epitaxial films on mono-crystalline substrates,

intricate phenomena such as Rayleigh instabilities and fractal behavior have been observed. For polycrystalline films, the behavior is even more complex, involving grain growth and the evolution of grain assembly. Additionally, the film's texture is expected to play a significant role. In a polycrystalline film, grains can be randomly oriented or exhibit special relationships with the substrate, such as epitaxy and axiotaxy. Each of these texture components may respond differently to grooving and agglomeration. Notably, it has been demonstrated that axiotaxy can efficiently promote agglomeration because the interface can bend with minimal energy cost. The model featuring a spherical cap geometry aligns with axiotaxy, which typically leads to two-dimensional interface bending along the matching plane's direction with constant curvature.

The addition of alloying elements is typically used to delay agglomeration, and our work provides insight into how these elements are redistributed during this process. This understanding can help elucidate how alloying elements influence agglomeration, also known as dewetting in applications where it is relevant. Our research indicates that the diffusion of the slower-diffusing species along the fast diffusion path must be incorporated into dewetting models for compounds. Understanding the dewetting of compound films is crucial for the nanostructuring of thin films and the growth of nanostructures.

4.2.6 Chemical environment

4.2.6.1 Residual fluoride, F and oxygen, O

Surface preparation and pre-clean cycles can significantly affect the thermal stability of Ni(Pt)Si films. The presence of impurities such as oxygen and fluorine at the interface can lead to increased sheet resistance [100], [106], [108], [109]. During the SiCoNi treatments, residual fluoride and oxygen may remain on top of the Si substrate but in very low concentrations.

The XPS analyses demonstrated higher oxygen content in the surface region of the NiPt layer for the SiCoNi 80 process, indicated by the Ni-O peaks in the O-1s and Ni2p3 spectra. Tavernier *et al.* [150] reported that accumulation of the fluoride salts may result in half-transformed SiO_2 and/or remaining salt that is not well sublimated. We hypothesized that the long exposure time to the plasma in the SiCoNi 80 process may lead to a more significant salt accumulation compared to the SiCoNi 2x40 one illustrated by the Fig. 114 below.

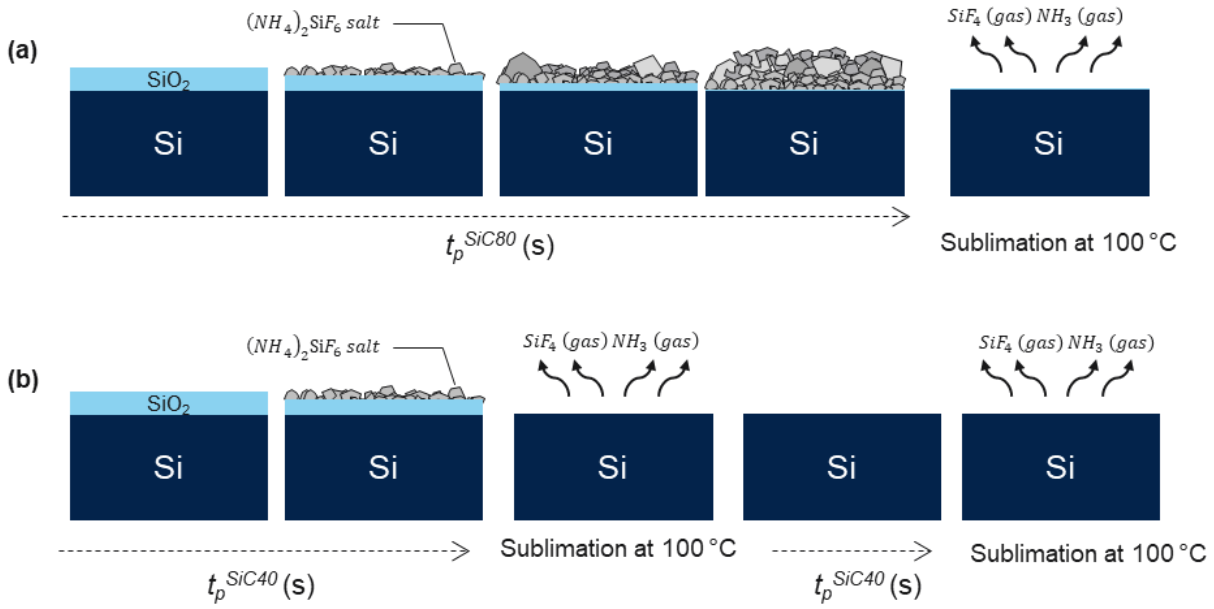


Figure 114. Visual representation of the accumulation of the fluoride salt prior to the sublimation at around 100 °C for (a) SiCoNi 80 and (b) SiCoNi 2x40 process.

The thick accumulated salts on the surface of the substrate could reduce the efficiency of the plasma etching due to the thicker accumulated salt on the Si surface

(potentially reducing the diffusion of the NH_4F species). Under these conditions, a higher content of residual oxygen could be expected, particularly for the SiCoNi 80 case.

Nevertheless, an extensive number of literatures also reported on the benefits of fluorine in improving the thermal stability of the NiSi film [107], [108], [109]. As shown by the XPS measurements in Table 10, the fluorine content is higher in the NiPt_SiC2x40 sample compared to the that of the NiPt_SiC80 one. Fig. 58 also demonstrates the presence of a peak at 684 eV corresponding to the metal-fluoride type of bonding. This peak appears to be significantly more intense for the NiPt_SiC2x40 sample.

In addition to the higher F content in the NiPt layer when the SiCoNi 2x40 treatment is used, our results also demonstrate a clear difference in both the redistribution of the residual fluorine, and the chemical environment depending on the choice of the SiCoNi treatments (either SiCoNi 2x40 or SiCoNi 80). Firstly, the ToF-SIMS depth profiles in Fig. 60, demonstrated that fluorine are mostly redistributed towards the NiPt/intermixing and intermixing/Si interfaces in the case of the NiPt_SiC80 sample. When SiCoNi 2x40 is utilized, the F atoms showed a more homogenous redistribution within the intermixing layer.

A visual representation of the fluorine atoms in the intermixing layer is presented in Fig. 115. The fluorine atoms are represented by the bright orange color with the difference in color gradient representing the concentration variation of F within the intermixing layer.

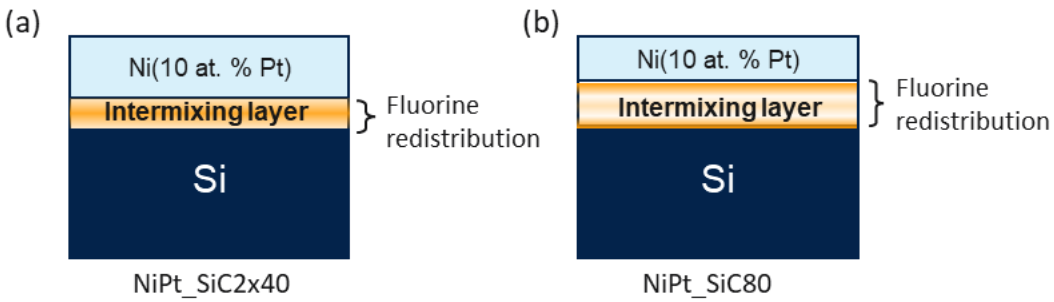


Figure 115. Visual representation of the fluorine redistribution using color gradient, in the intermixing layer (NiSi) for (a) NiPt_SiC2x40 and (b) NiPt_SiC80 samples.

This clearly indicates there are two different possible redistributions of fluorine depending on SiCoNi treatments. In the case of a single-step SiCoNi treatment (SiCoNi 80), fluorine redistributes towards the interfaces with NiPt and Si substrates. For SiCoNi 2x40,

fluorine atom may redistribute by means of incorporation within the intermixing layer. At the current stage, a clear explanation on the different redistribution of F remains difficult.

The EELs spectra in Fig. 61 provide further information regarding the residual fluorine, indicating the presence of Ni-F and/or Si-F bonding environments as shown by the additional peaks (cyan arrow in Fig. 61(a)). The absence of this additional peak in the case of the SiCoNi 80 clearly suggests that the fluorine atoms redistributed towards the NiPt/intermixing and intermixing/Si interfaces, may not be bonded to either the Ni or the Si.

As previously illustrated in Fig. 114(b), the SiCoNi 2x40 process involves a first sublimation annealing after a plasma exposition of duration $t_p^{SiC2x40}$ in the first cycle leading to a thinner salt accumulation at the surface. Since there is no salt accumulation, the plasma efficiency is also not reduced. Furthermore, assuming that the native oxide layer is completely etched in the first cycle, the etchants generated from the plasma, NH_4F will be in interaction only with the surface of the Si substrate. This is not the case in SiCoNi 80 since, there is no fluoride salt sublimation (removal) done before a plasma exposition. **This implies that when the surface of Si free of native oxide, is exposed to the SiCoNi etchants, potential Si-F bonds may be formed.**

4.2.6.2 SiCoNi treatments and Ni(Pt)Si agglomeration

Both the Rs measurements and the fraction of exposed Si, f_{si}(%) showed that the agglomeration is slightly delayed in the case of the NiSi_SiC2x40 sample compared to the NiSi_SiC80 one. Indeed, one may conclude that such improvements could be attributed to mostly the Ni(Pt)Si thickness differences between the two samples. However, further inspection may suggest a more relevant finding on the importance of the SiCoNi 2x40 process.

As illustrated by the Fig. 63, the thicknesses of the Ni(Pt)Si films formed on Si substrate treated by the different SiCoNi processes are identical at least up to the tenth measurement points *i.e.,* near to the center of the wafer. The f_{Si}(%) in Fig. 67 (refer to the inset), indicates that exposed Si is slightly higher in the case of the SiCoNi 80 process compared to the SiCoNi 2x40 one despite the similar thickness. Additionally, as reported in

Table 13, the f_{Si_center} (%) for NiSi_SiC2x40 is at 0.32 % whereas for NiSi_SiC80, the f_{Si_center} (%) is 0.84 %. This clearly suggests that the nucleation of holes may be more significant in the case of the NiSi_SiC80 highlighting the importance of the initial redistribution of fluorine, oxygen, and chemical environments of the intermixing layer, since Ni(Pt)Si thicknesses are identical at the center.

Moreover, Wong *et al.* [107] demonstrated a delay in the agglomeration of the NiSi film from 650 to 750 °C when the Si substrate is implanted with BF_2^+ ions, attributed to the presence of fluorine. Definitely, similar results may not be achieved in our case since the concentration of fluorine is significantly lower post SiCoNi treatments compared to the implanted ones. Indeed, a finer analysis of the residual fluorine remains very complex particularly in the case where the remaining fluorine are expected to completely transform into SiF_6 gas during the sublimation annealings in the SiCoNi treatments.

Nonetheless, these findings highlight the importance of the redistribution of F and potentially their bonding to either Ni or Si, as demonstrated in the case of the SiCoNi 2x40 treatment, on the final thermal stability of the Ni(Pt)Si film. **Indeed, the homogenous fluorine redistribution and the peculiar chemical environments within the intermixing layer, clearly improve the final properties of the Ni(Pt)Si film (overall thickness, thickness uniformity, and thermal stability).** This further underlines the interest of the SiCoNi 2x40 process for industrial wafer processing compared to the single-step SiCoNi treatments (SiCoNi 80).

General conclusions

In the latest 3D Imager technology, the thickness of the Ni(Pt)Si film has been constrained to the ultra-thin regime *i.e.,* around 11 nm thick. The co-integration of the ultra-thin Ni(Pt)Si film and the $TiSi_X$- based contacts constitutes a great technological challenge. The significant thermal budget needed for $TiSi_x$ silicide further exacerbated the sensitivity of the Ni(Pt)Si film to the agglomeration phenomenon leading to severe yield loss, and drastic Rs increase. In this Ph.D. thesis, we have studied the agglomeration phenomenon of the ultra-thin Ni(Pt)Si film on blanket and patterned wafers.

In particular, four major studies are conducted. Firstly, the impact of surface preparation treatments on the formation and agglomeration of 11 nm-Ni(Pt)Si thin film. In this study, we observed a thicker intermixing layer when the Si substrate surface is treated with the SiCoNi 80 process prior to NiPt layer deposition. We found that when the Si substrate is treated using the SiCoNi 2x40 process, there is a higher concentration of fluorine, F, withing the NiPt and intermixing layers. As the presence of F has been demonstrated to slow down the diffusion of Ni, the thinner intermixing layer in the case of the SiCoNi 2x40 may be understood to be due to this effect.

Combined analyses using ToF-SIMS and TEM-EELS techniques demonstrate a clear difference in both the residual fluor redistribution and the chemical bonding environment within the intermixing layers depending on the SiCoNi surface preparation treatments. Homogeneous F redistribution is obtained in the case of the SiCoNi 2x40 and EELS spectra reveal an additional peak (not seen in the case of SiCoNi 80) which might be related to novel Ni-F or Si-F chemical bonds. In addition to these differences, the thickness uniformity of the Ni(Pt)Si film is dramatically improved in the case of the SiCoNi 2x40 treatment compared to the SiCoNi 80 sample.

The second study demonstrates the impact of the different annealing schemes used in the formation of the Ni(Pt)Si thin film on its thermal stability. The different annealing schemes studied are the partial and the total annealing, milliseconds laser annealing (Dynamic Surface Annealing, DSA), and finally the one-step annealing. The different annealing schemes are shown to significantly influence the final microstructure properties of the Ni(Pt)Si film resulting different thermal stability. The laser annealing, in particular,

demonstrates a drastic reduction of the silicide grain size allowing to a delay of the onset of the agglomeration by at least 50 °C. This observation is well aligned on Thompson and Nolan theories [83], [84] on dewetting phenomenon in thin films. In other words, Ni(Pt)Si films with large grain size is reported to have a higher tendency to agglomerate at relatively lower temperature (between 500-550 °C in the case of the total annealing scheme).

EBSD mappings show that the Ni(Pt)Si films exhibit two preferred orientations along the NiSi(013) and NiSi(010) directions. The pole figure analyses reveal that all of the sample exhibit fiber texture regardless of the annealing schemes used. Further inspections of the agglomerated state shows that the grains with (013) orientations represent a large part of agglomerates. This observation suggests that agglomeration phenomenon induces “the consumption” or the “disappearance” of the grains oriented along 010) directions. Furthermore, when comparing the NiSi(103) pole figure, a presence of the axiotaxy ring segments are detected in all of the agglomerated samples.

A third study focuses on the impact of the nano-confinement of the Ni(Pt)Si film on the agglomeration phenomenon using four main structures of varying pitches of 110, 250, 500 nm, and dielectric dots. These results are compared to the blanket wafer ones. The Ni(Pt)Si films formed in the structure with regular lines show a more severe agglomeration as compared to the ones formed in the least confined structures, meaning with the dielectric dots and on blanket wafers. The comparative analyses of the fraction of the exposed Si, f_{Si}(%) exposed an unexpected trend of agglomeration for samples with the regular lines.

A more advanced stages of agglomeration are then observed in the least confined structure with a pitch of 500 nm compared to that of the most confined ones (p=110 nm), attributed to a difference in their grain size. The lateral growth of the Ni(Pt)Si grains in the most confined sample is assumed to be hindered physically leading to smaller grains, and thus a better thermal stability. Moreover, the agglomerated states of the Ni(Pt)Si film in majority of the samples showed a peculiar, elongated shape of agglomerates along the directions of the lines. This clearly reveals the non-negligible impact of the Ni(Pt)Si/SiN interface (meaning with the walls of the dielectric structure) on the agglomeration of the Ni(Pt)Si film. This finding further explains the difference in the agglomeration of the Ni(Pt)Si film formed on blanket wafer and on wafer including dielectric dots. Pole figure analyses

performed using laboratory equipment and ESRF Synchrotron beamline, on both blanket wafer and one of the samples with line structures with pitch of 250 nm show no significant difference in their texture at the non-agglomerated stage. Both pole figures demonstrate the axiotaxy texture, however a finer analysis is required to identify any potential change in texture upon agglomeration in the confined structures.

Finally, the fourth study is conducted on the feasibility of the use laser annealing for silicidation in real integrated circuits. This is achieved through TEM cross-sections and electrical characterizations. Indeed, the normalized resistance increases drastically when RTA2 is used instead of the DSA laser annealing after the thermal budget needed to form $TiSi_x$ contacts. The TEM cross-sections showed a more pronounced groove in the case of the RTA annealing compared to the laser annealing after an $TiSi_x$ anneal at 550 °C. Such results are coherent with blanket results and confirm the interest of using DSA annealing for innovative 3D integrations, mainly for imager technologies.

Moreover, we have also provided observations and discussions on the redistribution of Pt during the agglomeration phenomenon of the Ni(Pt)Si thin film. The initial redistribution of the Pt is evidenced by both STEM-EDX mapping and EDX line scans. The initial redistribution of Pt is characterized by a high concentration of Pt in the upper part of the silicide films. This is a consequence of the phase formation going from θ-Ni_2Si to NiSi phase that leads to high Pt concentration at the top surface. At higher temperatures corresponding to grooving and agglomeration, the Pt shows a specific and complex redistribution. Three distinct regions are identified in the silicide: a Pt-rich region near the surface, a Pt-depleted region within the silicide, and another Pt-rich region corresponding to the displaced NiSi at the silicide/Si interface.

During the agglomeration of the Ni(Pt)Si film there is an increase in the concentration of Pt at the lower part of the silicide grains and/or the newly formed islets. This Pt redistribution is explained by two main phenomena: (i) matter transport linked to the change in shape of the NiSi grains *or* agglomerates associated with grooving and agglomeration (thus, Pt will be displaced along with the Ni and Si atoms), and (ii) a classical diffusion driven by the gradient of Pt concentration between the upper and lower portion of the Ni(Pt)Si grains *or* islets.

In this work, we also propose a model for the redistribution of Pt during the grooving and agglomeration phenomena. Building upon the previous works by Luo *et al.* [25], for the general assumptions regarding the change in shape of the Ni(Pt)Si grains during these processes, our model additionally considers the redistribution of Pt by diffusion at the silicide/Si interface. Using a spherical cap geometry, this model successfully reproduces the change in island shape of the Ni(Pt)Si grains as well as the Pt redistribution during the boundary grooving and agglomeration phenomena.

The good agreement between experimental results and the model confirms that the silicide/Si is the predominant path during the grooving and agglomeration. However, at higher temperatures, changes in Pt concentration suggest that the volume and surface diffusion may not be negligible. In the case of the Ni(Pt)Si agglomeration compared to that of NiSi, Pt may be the slowest diffusing species or may slow down the diffusion of Si as Pt has been shown to retard the agglomeration of the Ni(Pt)Si thin film.

In the framework of the Ph. D thesis presented here, we have covered the impact of the several factors relating to the formation and agglomeration of the ultra-thin Ni(Pt)Si film for 3D integration devices. This includes the control of the microstructural properties, such as grain size, thickness, textures, elements redistributions that may contribute to a more thermally stable silicide film. Several perspectives may thus be considered for future works:

- **A deeper investigation of the chemical bonds present at NiPt/Si interface may be required for a large variety of surface treatments including chemical and physical Si surface etching.**
- **In the case of different surface treatments, a finer analysis is required to explain the different redistribution of fluorine, F, in the intermixing layer.**
- **An explanation of the significant intermixing/Si interface roughness remains complex since the intermixing layer is formed during the PVD deposition step. This means that potentially rough interface may also be a consequence of the PVD sputtering step.**
- **Quantitative analyses remain necessary to properly extract the fraction between of the NiSi(013) to NiSi(010) orientations and in particular the**

problematics concerning the significant signal coming from the Si substrate appears to be a real concern after deep analyses of our ESRF results.

- **The presence of the axiotaxial ring segments are observed in all samples regardless of the annealing schemes used. A finer analysis of the intensity of these rings may be required in order to better compare the impact of the different annealing schemes on the texture.**
- **At the current stage, we hypothesize that the confinement of the Ni(Pt)Si film induces the grain size reduction. However, further investigations may be required to better account the impact of the silicide/SiN interface which is obviously demonstrated during this Ph. D work but needs to be formerly quantify.**
- **Finally, at the non-agglomerated stage, Ni(Pt)Si film formed in confined structures appears to show the same textures like on blanket wafers. A more complete analysis is necessary in order to evaluate the evolution of these textures when the film is agglomerated, in particular in the confined structures.**

List of bibliography

[1] R. R. Schaller *et al.,* “Moore’s law: past, present and future”, IEEE Spectrum, vol. 34, no. 6, pp. 52–59, 1997.

[2] T. N. Theis *et al.,* “The end of Moore’s law: A new beginning for information technology”, Computing in Science & Engineering, vol. 19, no. 2, pp. 41–50, 2017.

[3] K. Cheng *et al.,* “Fully depleted SOI (FDSOI) technology”, Science China Information Sciences, vol. 59, pp. 1–15, 2016.

[4] M. Jurczak *et al.,* “Review of FINFET technology”, presented at the 2009 IEEE International SOI Conference, IEEE, 2009, pp. 1–4.

[5] Z. Shi, D. Onsongo, and S. K. Banerjee, “Mobility and performance enhancement in compressively strained SiGe channel PMOSFETs”, Applied Surface Science, vol. 224, no. 1–4, pp. 248–253, 2004.

[6] J. Choi, Y. Mao *et al.,* “Development of hafnium based high-k materials—A review”, Materials Science and Engineering: R: Reports, vol. 72, no. 6, pp. 97–136, 2011.

[7] D. Mangelinck *et al.,* “Enhancements of thermal stability of NiSi films on (100) Si and (111) Si by Pt addition”, Applied Physics Letters, vol. 75, no. 12, pp. 1736–1738, 1999.

[8] D. Mangelinck *et al.,* “Effect of Co, Pt, and Au additions on the stability and epitaxy of $NiSi_2$ films on (111) Si”, Journal of Applied Physics, vol. 84, no. 5, pp. 2583–2590, 1998.

[9] N. Planes *et al.,* “28nm FDSOI technology platform for high-speed low-voltage digital applications”, in 2012 Symposium on VLSI Technology (VLSIT), Jun. 2012, pp. 133–134. doi: 10.1109/VLSIT.2012.6242497.

[10] C. Cavalcante *et al.,* “28nm FDSOI CMOS Technology (FEOL and BEOL) Thermal Stability for 3D Sequential Integration: Yield and Reliability Analysis”, in 2020 IEEE Symposium on VLSI Technology, Jun. 2020, pp. 1–2. doi: 10.1109/VLSITechnology18217.2020.9265075.

[11] D. James, “IEDM 2017: Intel’s 10nm platform process”, Solid State Technology, 2017.

[12] R. Nelson, “IEDM sees transistor, memory, laser innovations”, EE: Evaluation Engineering, vol. 57, no. 3, 2018.

[13] P. Batude *et al.,* “Enabling 3D monolithic integration”, ECS Transactions, vol. 16, no. 8, p. 47, 2008.

[14] O. Chamirian *et al.,* “Thickness scaling issues of Ni silicide”, Microelectronic Engineering, vol. 70, no. 2, pp. 201–208, Nov. 2003, doi: 10.1016/S0167-9317(03)00366-6.

[15] C. Jahan *et al.,* “Agglomeration control during the selective epitaxial growth of Si raised sources and drains on ultra-thin silicon-on-insulator substrates”, Journal of Crystal Growth, vol. 280, no. 3–4, pp. 530–538, 2005.

[16] O. Nakatsuka *et al.,* “Improvement in NiSi/Si contact properties with C-implantation”, Microelectronic Engineering, vol. 82, no. 3, pp. 479–484, Dec. 2005, doi: 10.1016/j.mee.2005.07.046.

[17] K. De Keyser *et al.,* “Phase formation and thermal stability of ultrathin Nickel-silicides on Si(100)”, Applied Physics Letters, vol. 96, no. 17, p. 173503, Apr. 2010, doi: 10.1063/1.3384997.

[18] S. Kudo *et al.,* "Study of formation mechanism of Nickel silicide discontinuities in high-performance complementary metal–oxide–semiconductor devices", Japanese Journal of Applied Physics, vol. 53, no. 2, p. 021301, Jan. 2014, doi: 10.7567/JJAP.53.021301.

[19] F. A. Geenen *et al.,* "Controlling the formation and stability of ultra-thin Nickel silicides - An alloying strategy for preventing agglomeration", Journal of Applied Physics, vol. 123, no. 7, p. 075303, Feb. 2018, doi: 10.1063/1.5009641.

[20] J. Ohta, Smart CMOS Image Sensors and Applications. CRC Press, 2020.

[21] R. Beica, "3D integration: Applications and market trends", presented at the 2015 International 3D Systems Integration Conference (3DIC), IEEE, 2015, pp. TS5-1.

[22] P. R. Betz *et al.,* American National Biography: Supplement, no. v. 2. Oxford University Press, 2002. [Online]. Available: https://books.google.fr/books?id=wZczV8ZxgL4C

[23] J. Bardeen *et al.,* "Physical principles involved in transistor action", Physical Review, vol. 75, no. 8, p. 1208, 1949.

[24] K. Dawon, "Electric field-controlled semiconductor device", Aug. 1963.

[25] T. Luo, "Study of the mechanisms of silicide formation by isotope diffusion and atom probe tomography", Aix-Marseille, 2018.

[26] Y. Taur and T. H. Ning, "FEOL technology trend", Materials Chemistry and Physics, vol. 52, no. 3, pp. 191–199, 1998.

[27] H. Radamson *et al.,* CMOS Past, Present and Future. Woodhead Publishing, 2018.

[28] M. Gregoire, "HDR Magali Grégoire Silicide in Microelectronics: phase sequence, nanoscale effect, and degradation", 2022.

[29] P. Coudrain *et al.,* "Setting up 3D sequential integration for back-illuminated CMOS image sensors with highly miniaturized pixels with low temperature fully depleted SOI transistors", presented at the 2008 IEEE International Electron Devices Meeting, IEEE, 2008, pp. 1–4.

[30] B. Davari, R. H. Dennard, and G. G. Shahidi, "CMOS scaling for high performance and low power-the next ten years", Proceedings of the IEEE, vol. 83, no. 4, pp. 595–606, 1995.

[31] D. J. Frank *et al.,* "Device scaling limits of Si MOSFETs and their application dependencies", Proceedings of the IEEE, vol. 89, no. 3, pp. 259–288, 2001.

[32] N. Z. Haron *et al.,* "Why is CMOS scaling coming to an END?", presented at the 2008 3rd International Design and Test Workshop, IEEE, 2008, pp. 98–103.

[33] H. Iwai, "CMOS downsizing toward sub-10 nm", Solid-State Electronic, vol. 48, no. 4, pp. 497–503, 2004.

[34] A. Chaudhry *et al.,* "Controlling short-channel effects in deep-submicron SOI MOSFETs for improved reliability: a review", IEEE Transactions on Device and Materials Reliability, vol. 4, no. 1, pp. 99–109, 2004.

[35] A. Chen, "Emerging research devices and architectures for more-than-Moore applications", ECS Transactions, vol. 50, no. 14, p. 3, 2013.

[36] H. Iwai *et al.,* "NiSi salicide technology for scaled CMOS", Microelectronic Engineering, vol. 60, no. 1, pp. 157–169, Jan. 2002, doi: 10.1016/S0167-9317(01)00684-0.

[37] C. Lavoie *et al.,* "Towards implementation of a Nickel silicide process for CMOS technologies", Microelectronic Engineering, vol. 70, no. 2, pp. 144–157, Nov. 2003, doi: 10.1016/S0167-9317(03)00380-0.

[38] C. Osburn, J. Tsai, and J. Sun, "Metal silicides: Active elements of ULSI contacts", Journal of Electronic Materials, vol. 25, pp. 1725–1739, 1996.

[39] S.-L. Zhang *et al.,* "Metal silicides in CMOS technology: Past, present, and future trends", Critical Reviews in Solid State and Materials Sciences, vol. 28, no. 1, pp. 1–129, 2003.

[40] F. d'Heurle, "Silicide interfaces in silicon technology", Journal of Electronic Materials, vol. 27, pp. 1138–1147, 1998.

[41] R. Maddox, "On the optimization of VLSI contacts", IEEE Transactions on Electron Devices, vol. 32, no. 3, pp. 682–690, 1985.

[42] J. A. Kittl *et al.,* "Silicides for 65 nm CMOS and Beyond", MRS Online Proceedings Library (OPL), vol. 765, p. D7.5, 2003, doi: 10.1557/PROC-765-D7.5.

[43] C. Lavoie, "Contacts in Advanced CMOS: History and Emerging Challenges", 2017.

[44] C. Lavoie *et al.,* "Contacts in advanced CMOS: History and emerging challenges", ECS Transactions, vol. 77, no. 5, p. 59, 2017.

[45] C. Detavernier *et al.,* "Low-temperature formation of $CoSi_2$ in the presence of Au", Journal of Applied Physics, vol. 95, no. 10, pp. 5340–5346, 2004.

[46] R. Donaton *et al.,* "Co silicide formation on SiGeC/Si and SiGe/Si layers", Applied Physics Letters, vol. 70, no. 10, pp. 1266–1268, 1997.

[47] J. Strane *et al.,* "Implementation of Robust Nickel Alloy Salicide Process for High-Performance 65nm SOI CMOS Manufacturing", in 2007 International Symposium on VLSI Technology, Systems and Applications (VLSI-TSA), Apr. 2007, pp. 1–2. doi: 10.1109/VTSA.2007.378955.

[48] J. A. Kittl *et al.,* "Ni- and Co-based silicides for advanced CMOS applications", Microelectronic Engineering, vol. 70, no. 2, pp. 158–165, Nov. 2003, doi: 10.1016/S0167-9317(03)00370-8.

[49] P. S. Lee *et al.,* "New salicidation technology with Ni(Pt) alloy for MOSFETs", IEEE Electron Device Letters, vol. 22, no. 12, pp. 568–570, Dec. 2001, doi: 10.1109/55.974579.

[50] K. Maex *et al.,* Properties of Metal Silicides. Oxford University Press, 1995. [Online]. Available: https://books.google.fr/books?id=9P6hDjZ0nCoC

[51] Z. Ma, L. H. Allen, *et al.,* "Effect of dimension scaling on the nucleation of C54 TiSi2", Thin Solid Films, vol. 253, no. 1, pp. 451–455, Dec. 1994, doi: 10.1016/0040-6090(94)90365-4.

[52] B. Imbert *et al.,* "Nickel silicide encroachment formation and characterization", Microelectronic Engineering, vol. 87, no. 3, pp. 245–248, 2010.

[53] T. Luo *et al.,* "Role of the slow diffusion species in the dewetting of compounds: The case of NiSi on a Si isotope multilayer studied by atom probe tomography", Acta Materialia, vol. 165, pp. 192–202, Feb. 2019, doi: 10.1016/j.actamat.2018.11.042.

[54] M. El Kousseifi *et al.,* "Selection of the first Ni silicide phase by controlling the Pt incorporation in the intermixed layer", Acta Materialia, vol. 106, pp. 193–198, 2016.

[55] P. Nash and A. Nash, “The Ni− Si (Nickel-silicon) system”, Bulletin of Alloy Phase Diagrams, vol. 8, no. 1, pp. 6–14, 1987.

[56] F. Geenen *et al.,* “The influence of alloying on the phase formation sequence of ultra-thin Nickel silicide films and on the inheritance of texture”, Journal of Applied Physics, vol. 123, no. 18, 2018.

[57] C. Coia, Microstructure and Growth Kinetics of Nickel Silicide Ultra-Thin Films Synthesized by Solid-State Reactions. École Polytechnique de Montréal, 2008.

[58] M. El Kousseifi *et al.,* “Nucleation and lateral growth kinetics of the NiSi phase at the epitaxial θ-Ni_2Si/Si interface”, Acta Materialia, vol. 198, pp. 100–110, 2020.

[59] C. Van Bockstael *et al.,* “In situ study of the formation of silicide phases in amorphous Ni–Si mixed layers”, Journal of Applied Physics, vol. 106, no. 6, 2009.

[60] T. Futase *et al.,* “Pattern-independent, fine-morphology Ni-Pt silicide formation by partial conversion with low metal-consumption ratio”, presented at the 2010 IEEE International Reliability Physics Symposium, IEEE, 2010, pp. 988–994.

[61] D. Mangelinck, “Effect of a third element on the stability of NiSi thin films on Si”, presented at the Defect and Diffusion Forum, Trans Tech Publ, 2006, pp. 127–134.

[62] N. Breil *et al.,* “Challenges of Nickel silicidation in CMOS technologies”, Microelectronic Engineering, vol. 137, pp. 79–87, Apr. 2015, doi: 10.1016/j.mee.2014.12.013.

[63] D. Deduytsche *et al.,* “High-temperature degradation of NiSi films: Agglomeration versus $NiSi_2$ nucleation”, Journal of Applied Physics, vol. 98, no. 3, p. 033526, Aug. 2005, doi: 10.1063/1.2005380.

[64] P. S. Lee *et al.,* “On the Morphological Changes of Ni- and Ni(Pt)-Silicides”, Journal of The Electrochemical Society, vol. 152, no. 4, p. G305, Mar. 2005, doi: 10.1149/1.1862255.

[65] D. Mangelinck *et al.,* “Progress in the understanding of Ni silicide formation for advanced MOS structures”, Physica Status Solidi (a), vol. 211, no. 1, pp. 152–165, 2014.

[66] O. Chamirian *et al.,* “Ni silicide morphology on small features”, MRS Online Proceedings Library (OPL), vol. 810, pp. C4-4, 2004.

[67] H. Hsu *et al.,* “Epitaxial growth of uniform $NiSi_2$ layers with atomically flat silicide/Si interface by solid-phase reaction in Ni–P/Si (1 0 0) systems”, Applied Surface Science, vol. 257, no. 17, pp. 7422–7426, 2011.

[68] J. A. Kittl *et al.,* “Applications of Ni-based silicides to 45 nm CMOS and beyond”, MRS Online Proceedings Library (OPL), vol. 810, pp. C2-1, 2004.

[69] A. Lauwers *et al.,* “Materials aspects, electrical performance, and scalability of Ni silicide towards sub-0.13 µm technologies”, Journal of Vacuum Science & Technology B: Microelectronics and Nanometer Structures Processing, Measurement, and Phenomena, vol. 19, no. 6, pp. 2026–2037, 2001.

[70] O. Nakatsuka *et al.,* “Low-temperature formation of epitaxial $NiSi_2$ layers with solid-phase reaction in Ni/Ti/Si (001) systems”, Japanese Journal of Applied Physics, vol. 44, no. 5R, p. 2945, 2005.

[71] O. Nakatsuka *et al.,* “Dependence of electrical characteristics on interfacial structure of epitaxial $NiSi_2$/Si Schottky contacts formed from Ni/Ti/Si system”, Japanese Journal of Applied Physics, vol. 47, no. 4S, p. 2402, 2008.

[72] R. N. Wang *et al.,* "Comparison of the thermal stabilities of NiSi films in Ni/Si, Ni/Pd/Si and Ni/Pt/Si systems", Journal of Physics: Condensed Matter, vol. 15, no. 12, p. 1935, Mar. 2003, doi: 10.1088/0953-8984/15/12/310.

[73] T. L. Lee *et al.,* "Highly reliable Nickel silicide formation with a Zr capping layer", Electrochemical and Solid-State Letters, vol. 6, no. 5, p. G66, 2003.

[74] D. Deduytsche *et al.,* "Formation and morphological stability of NiSi in the presence of W, Ti, and Ta alloying elements", Journal of Applied Physics, vol. 101, no. 4, 2007.

[75] J. Foggiato *et al.,* "Optimizing the formation of Nickel silicide", Materials Science and Engineering: B, vol. 114–115, pp. 56–60, Dec. 2004, doi: 10.1016/j.mseb.2004.07.033.

[76] D. Mangelinck, "Addition of third element on NiSi", 1999.

[77] C. Detavernier *et al.,* "An off-normal fibre-like texture in thin films on single-crystal substrates", vol. 426, p. 5, 2003.

[78] T. Shibata *et al.,* "An optimally designed process for submicron MOSFETs", presented at the 1981 International Electron Devices Meeting, IEEE, 1981, pp. 647–650.

[79] C. Delwail, "Etude de l'impact de la pré-amorphisation par implantation ionique pour l'optimisation des contacts siliciurés", 2022.

[80] P. Jacquet *et al.,* "On the solid-state dewetting of polycrystalline thin films: Capillary versus grain growth approach", Acta Materialia, vol. 143, pp. 281–290, 2018.

[81] P. Jacquet *et al.,* "Grain growth: The key to understand solid-state dewetting of silver thin films", Scripta Materialia, vol. 115, pp. 128–132, 2016.

[82] A. Newman *et al.,* "Influence of Si surface preparation on $CoSi_2$ formation and agglomeration", Materials Science in Semiconductor Processing, vol. 162, p. 107488, Aug. 2023, doi: 10.1016/j.mssp.2023.107488.

[83] C. V. Thompson, "Solid-State Dewetting of Thin Films", Annual Review of Materials Research, vol. 42, no. 1, pp. 399–434, Aug. 2012, doi: 10.1146/annurev-matsci-070511-155048.

[84] T. P. Nolan *et al.,* "Modeling of agglomeration in polycrystalline thin films: Application to TiSi2 on a silicon substrate", Journal of Applied Physics, vol. 71, no. 2, pp. 720–724, Jan. 1992, doi: 10.1063/1.351333.

[85] H. Barda *et al.,* "The role of interface diffusion in solid state dewetting of thin films: The nano-marker experiment", Acta Materialia, vol. 177, pp. 121–130, Sep. 2019, doi: 10.1016/j.actamat.2019.07.042.

[86] D. Z. Chi *et al.,* "Nickel silicide as a contact material for submicron CMOS devices", Journal of Electronic Materials, vol. 30, no. 12, pp. 1483–1488, Dec. 2001, doi: 10.1007/s11664-001-0162-4.

[87] D. J. Srolovitz *et al.,* "Capillary instabilities in thin films. II. Kinetics", Journal of Applied Physics, vol. 60, no. 1, pp. 255–260, 1986.

[88] D. Srolovitz and S. Safran, "Capillary instabilities in thin films. I. Energetics", Journal of Applied Physics, vol. 60, no. 1, pp. 247–254, 1986.

[89] G. J. Bailey *et al.,* "Surface tensions in the system solid copper-molten lead", Proceedings of the Physical Society. Section B, vol. 63, no. 5, p. 350, 1950.

[90] W. W. Mullins, “Theory of thermal grooving”, Journal of Applied Physics, vol. 28, no. 3, pp. 333–339, 1957.

[91] D. Amram *et al.,* “Grain boundary grooving in thin films revisited: the role of interface diffusion”, Acta Materialia, vol. 69, pp. 386–396, 2014.

[92] D. Chi *et al.,* “Reverse current transport mechanism in shallow junctions containing silicide spikes”, Journal of Applied Physics, vol. 92, no. 12, pp. 7532–7535, 2002.

[93] T. Yamaguchi *et al.,* “A novel low leakage-current Ni SALICIDE process in nMOSFETs on Si (110) substrate”, presented at the 2007 IEEE International Electron Devices Meeting, IEEE, 2007, pp. 139–142.

[94] J. Demeulemeester *et al.,* “The influence of Pt redistribution on $Ni_{1-x}Pt_xSi$ growth properties”, Journal of Applied Physics, vol. 108, no. 4, 2010.

[95] C. Feautrier *et al.,* “Impact of laser anneal on NiPt silicide texture and chemical composition”, Journal of Applied Physics, vol. 121, no. 22, p. 225109, Jun. 2017, doi: 10.1063/1.4985279.

[96] D. Mangelinck *et al.,* “Enhancement of thermal stability of NiSi films on (100)Si and (111)Si by Pt addition”, Applied Physics Letters, vol. 75, no. 12, pp. 1736–1738, Sep. 1999, doi: 10.1063/1.124803.

[97] C. Detavernier *et al.,* “Influence of Pt addition on the texture of NiSi on Si(001)”, Applied Physics Letters, vol. 84, no. 18, pp. 3549–3551, Apr. 2004, doi: 10.1063/1.1719276.

[98] D. Mangelinck *et al.,* “Effect of Co, Pt, and Au additions on the stability and epitaxy of $NiSi_2$ films on (111)Si”, Journal of Applied Physics, vol. 84, no. 5, pp. 2583–2590, Sep. 1998, doi: 10.1063/1.368611.

[99] T. Futase *et al.,* “Spike Annealing as Second Rapid Thermal Annealing to Prevent Pure Nickel Silicide from Decomposing on a Gate”, IEEE Transactions on Semiconductor Manufacturing, vol. 22, no. 4, pp. 475–481, Nov. 2009, doi: 10.1109/TSM.2009.2031769.

[100] J.-Y. Huang *et al.,* “Impact of Surface Preparation on Ni(Pt) Silicide Oxidation”, p. 4.

[101] J. Luo *et al.,* “Effects of carbon pre-silicidation implant into Si substrate on NiSi”, Microelectronic Engineering, vol. 120, pp. 178–181, May 2014, doi: 10.1016/j.mee.2013.08.010.

[102] D. J. Dingley *et al.,* “Microtexture determination by electron back-scatter diffraction”, Journal of Materials Science, vol. 27, pp. 4545–4566, 1992.

[103] B. De Schutter *et al.,* “Texture in thin film silicides and germanides: A review”, Applied Physics Reviews, vol. 3, no. 3, p. 031302, Aug. 2016, doi: 10.1063/1.4960122.

[104] C. Detavernier *et al.,* “An off-normal fibre-like texture in thin films on single-crystal substrates”, Nature, vol. 426, no. 6967, pp. 641–645, Dec. 2003, doi: 10.1038/nature02198.

[105] S. Gaudet *et al.,* “Three-dimensional reciprocal space measurement by x-ray diffraction using linear and area detectors: Applications to texture and defects determination in oriented thin films and nanoprecipitates”, Journal of Vacuum Science & Technology A, vol. 31, no. 2, 2013.

[106] T. Futase *et al.,* "Removing imperceptible fluoride residue after chemical dry-cleaning to fabricate uniform low-resistance NiSi film", Journal of Vacuum Science & Technology B, vol. 29, no. 5, p. 5, 2011.

[107] A. S. W. Wong *et al.,* "F-enhanced morphological and thermal stability of NiSi films on BF2+-implanted Si(001)", p. 4, 2014.

[108] M. Tsuchiaki, K. Ohuchi, and A. Nishiyama, "Suppression of Thermally Induced Leakage of NiSi-Silicided Shallow Junctions by Pre-Silicide Fluorine Implantation", p. 10.

[109] J. Lei, "Advantage of SiCoNi pre-clean over wet clean for pre-salicide applications beyond 65 nm node", 2006.

[110] K. van Stiphout *et al.,* "Impurity-enhanced solid-state amorphization: the Ni–Si thin film reaction altered by Nitrogen", Applied Physics, p. 13, 2019.

[111] L. Laurent *et al.,* "Effects of Pre-amorphization Thickness and Carbon Implantation on NiPt/Si Silicidation Process", p. 4.

[112] C. Ortolland *et al.,* "Optimized ultra-low thermal budget process flow for advanced High-K/Metal gate first CMOS using laser-annealing technology", presented at the 2009 Symposium on VLSI Technology, IEEE, 2009, pp. 38–39.

[113] C. Ortolland *et al.,* "Junction anneal sequence optimization for advanced high-k/metal gate CMOS technology", presented at the 2009 International Workshop on Junction Technology, IEEE, 2009, pp. 54–57.

[114] C. Ortolland *et al.,* "Silicide yield improvement with NiPtSi formation by laser anneal for advanced low power platform CMOS technology", presented at the 2009 IEEE International Electron Devices Meeting (IEDM), IEEE, 2009, pp. 1–4.

[115] H. Nishino, N. Hayasaka, and H. Okano, "Damage-free selective etching of Si native oxides using NH_3/NF_3 and SF_6/H_2O downflow etching", p. 5, 2014.

[116] C. Ortolland, "New carbon-based thermal stability improvement technique for NiPtSi used in CMOS technology", Microelectronic Engineering, p. 5, 2011.

[117] S. Y. Chen *et al.,* "Excimer Laser-Induced Ti Silicidation to Eliminate the Fine-Line Effect for Integrated Circuit Device Fabrication", Journal of The Electrochemical Society, p. 4.

[118] R. B. Fair, "Junction formation in silicon by rapid thermal annealing", MRS Online Proceedings Library (OPL), vol. 303, p. 311, 1993.

[119] R. Yang *et al.,* "Advanced in situ pre-Ni silicide (SiCoNi) cleaning at 65nm to resolve defects in $NiSi_x$ modules", Journal of Vacuum Science & Technology B, vol. 28, no. 1, pp. 56–61, 2010.

[120] H. Ogawa *et al.,* "Dry Cleaning Technology for Removal of Silicon Native Oxide Employing Hot NH_3/NF_3 Exposure", vol. 41, no. 8, p. 11, 2002.

[121] M. Grégoire *et al.,* "On the influence of Ni(Pt)Si thin film formation on agglomeration threshold temperature and its impact on 3D imaging technology integration", Microelectronic Engineering, vol. 271–272, p. 111937, Mar. 2023, doi: 10.1016/j.mee.2023.111937.

[122] Applied Materials, "Vantage Radiance Plus RTP", Products library Applied Materials. Accessed: Jun. 30, 2024. [Online]. Available: https://www.appliedmaterials.com/us/en/product-library/vantage-radiance-plus-rtp.html

[123] Applied Materials, “Vantage ASTRA DSA”, Products library Applied Materials. Accessed: Jun. 30, 2024. [Online]. Available: https://www.appliedmaterials.com/eu/en/product-library/vantage-astra-dsa.html

[124] D. M. Knotter, “The chemistry of wet cleaning”, Handbook of cleaning in Semiconductor Manufacturing: Fundamental and Applications, pp. 39–94, 2010.

[125] D. K. Schroder, Semiconductor Material and Device Characterization. John Wiley & Sons, 2015.

[126] J. C. Lindon, G. E. Tranter, and D. Koppenaal, Encyclopedia of Spectroscopy and Spectrometry. Academic Press, 2016.

[127] Y. Harold Robinson *et al.,* “Study and Develop an Effective Interfaces to Upload Data into Enterprise Resource Planning System”, in Multimedia Technologies in the Internet of Things Environment, Volume 2, R. Kumar, R. Sharma, and P. K. Pattnaik, Eds., Singapore: Springer Singapore, 2022, pp. 217–234. doi: 10.1007/978-981-16-3828-2_12.

[128] R. W. Collins, “Measurement technique of ellipsometry”, Spectroscopic Ellipsometry for Photovoltaics: Volume 1: Fundamental Principles and Solar Cell Characterization, pp. 19–58, 2018.

[129] E. F. Garman, “Modern methods for rapid X-ray diffraction data collection from crystals of macromolecules”, Crystallographic Methods and Protocols, pp. 87–126, 1996.

[130] G. F. Harrington *et al.,* “Back-to-Basics tutorial: X-ray diffraction of thin films”, Journal of Electroceramics, vol. 47, no. 4, pp. 141–163, 2021.

[131] K. Takayuki, “X-ray diffraction Techniques for thin films”. Accessed: Jun. 30, 2024. [Online]. Available: https://homepage.ntu.edu.tw/~kcyuan/form/For-Rigaku-Upload_thinfilm.pdf

[132] M. Lemang *et al.,* “Redistribution of phosphorus during $Ni_{0.9}Pt_{0.1}$-based silicide formation on phosphorus implanted Si substrates”, p. 7.

[133] S. Gaudet, “L’impact de la texture sur la Reaction en phase solide du Ni avec le Si”, 2011.

[134] R. Tung *et al.,* “Epitaxial silicides”, Thin Solid Films, vol. 93, no. 1–2, pp. 77–90, 1982.

[135] S. Henning *et al.,* “Chapter 1 - Scanning Electron Microscopy, ESEM, and X-ray Microanalysis”, in Microscopy Methods in Nanomaterials Characterization, S. Thomas, R. Thomas, A. K. Zachariah, and R. K. Mishra, Eds., Elsevier, 2017, pp. 1–30. doi: 10.1016/B978-0-323-46141-2.00001-8.

[136] A. Winkelmann *et al.,* “EBSD orientation analysis based on experimental Kikuchi reference patterns”, Acta Materialia, vol. 188, pp. 376–385, Apr. 2020, doi: 10.1016/j.actamat.2020.01.053.

[137] Y. Zhang *et al.,* “Twinning–Detwinning Deformation Mechanism in Ti–15Mo Alloy and Its Effect on the Microstructure Evolution and Yield Strength”, Advanced Engineering Materials, vol. 24, Aug. 2022, doi: 10.1002/adem.202200563.

[138] S. Courtas *et al.,* “Electron BackScattered Diffraction (EBSD) use and applications in newest technologies development”, Microelectronics Reliability, vol. 46, no. 9, pp. 1530–1535, Sep. 2006, doi: 10.1016/j.microrel.2006.07.031.

[139] E. Drouillas *et al.,* “Advanced EELS spectroscopy characterization of AlGaN/GaN materials”, Litterature, vol. 4, p. 5.

[140] F. Battegay and P. Florian, “Defectivity reduction for TiN PVD film”. ST Internal, 2006.

[141] F. M. Anak *et al.,* “Influence of the annealing schemes on the formation and stability of Ni(Pt)Si thin films: Partial, laser, total, and one-step annealings”, Materials Science in Semiconductor Processing, vol. 184, p. 108806, 2024.

[142] F. Guyader *et al.,* “3-Tier BSI CIS with 3D Sequential & Hybrid Bonding Enabling a1.4um pitch,106dB HDR Flicker Free Pixel”, in 2022 International Electron Devices Meeting (IEDM), Dec. 2022, pp. 37.4.1–37.4.4. doi: 10.1109/IEDM45625.2022.10019432.

[143] L. Clevenger and C. Thompson, “Nucleation-limited phase selection during reactions in Nickel/amorphous-silicon multilayer thin films”, Journal of Applied Physics, vol. 67, no. 3, pp. 1325–1333, 1990.

[144] L. Clevenger *et al.,* “Reaction kinetics of Nickel/silicon multilayer films”, Applied Physics Letters, vol. 52, no. 10, pp. 795–797, 1988.

[145] J. Gao *et al.,* “Dewetting of Ni silicide thin film on Si substrate: In-situ experimental study and phase-field modeling”, Acta Materialia, vol. 223, p. 117491, Jan. 2022, doi: 10.1016/j.actamat.2021.117491.

[146] F. Panciera *et al.,* “Pt redistribution in N-MOS transistors during Ni salicide process”, Microelectronic Engineering, vol. 107, pp. 173–177, Jul. 2013, doi: 10.1016/j.mee.2013.01.029.

[147] F. Corni *et al.,* “Dilute NiPt alloy interactions with Si”, Applied Surface Science, Minist. Econom. Affairs, Nov. 1993, pp. 197–202. [Online]. Available: http://gate4.inist.fr/login?url=http://search.ebscohost.com/login.aspx?direct=true&db=inh&AN=4580939&lang=fr&site=eds-live

[148] J. Demeulemeester *et al.,* “On the growth kinetics of Ni(Pt) silicide thin films”, Journal of Applied Physics, vol. 113, no. 16, p. 163504, Apr. 2013, doi: 10.1063/1.4802738.

[149] O. Cojocaru-Mirédin *et al.,* “Snowplow effect and reactive diffusion in the Pt doped Ni–Si system”, Scripta Materialia, vol. 57, no. 5, pp. 373–376, Sep. 2007, doi: 10.1016/j.scriptamat.2007.05.007.

[150] A. Tavernier, “Développement d’un procédé innovant pour le remplissage des tranchées d’isolation entre transistors des technologies CMOS avancées”, 2014.

Table of Figures

Figure 1. Schematic diagram of (a) an n-type MOSFET formed on a p-doped Si substrate and (b) its equivalent electrical diagram, from [25]. 36

Figure 2. (a) Schematics of CMOS Image Sensor (CIS) including micro-lens and color filters on the top of the photodiode inside the pixel area. (b) Schematics of the photodiode as a vertical pn-junction in which the photo-electronic current is generated under illumination and then gathered by the transfer gate to the sense node [28]. 37

Figure 3. Evolution of imager technologies with (a) Front-side illuminated (FSI), (b) Back-side illuminated (BSI), and (c) a more recent 3D stacked BSI (3D-BSI) [28]. 38

Figure 4. Process flows of the 3D sequential integration involving (1) fabrication of the embedded photodiode, (2-4) transfer of a second SOI layer by direct bonding, (5) processing of the low temperature transistor, (6) contacts formation and BEOL steps, and (7-9) Backside illumination is performed [29]. 39

Figure 5. (a) Schematics of the FDSOI architecture with corresponding (b) TEM cross-section views between B-B' from [9]. 41

Figure 6. TEM cross-section of a 28 nm FDSOI technology with silicided gate and source/drain terminals (STMicroelectronics internal data). 42

Figure 7. Evolution of "salicide" integration from C54-$TiSi_2$ to Ni(Pt)Si and recent Ti-based contacts dedicated to 3D integrations based on [44], [52], and STMicroelectronics internal data. The X-axis presents the technology node and the referred integration. The Y-axis shows the metal diffusion coefficient in silicide at 500 °C is given for Ti, Co and Ni silicide. The dominant diffusing species for each system are Si for Ti-Si, Co for Co-Si, and Ni for Ni(Pt)-Si respectively, based on [44]. 45

Figure 8. Phase diagram of Ni-Si system [55]. 47

Figure 9. TEM cross-sections of NiPt layer showing the presence of the amorphous NiSi interlayer (also called intermixing layer) after metal deposition steps (STMicroelectronics internal data). 48

Figure 10. Example of the inverted pyramidal $NiSi_2$ formed on Si(100) substrate from [67]. 49

Figure 11. In-situ XPS analysis as function of the annealing temperature showing the variation of the Ni 2p peak position comparing Ni and Ni(5 at.% Pt) films on Si(100) substrates [61]. 50

Figure 12. Sheet resistance, Rs, evolution of NiSi and Ni(Pt)Si thin films for increasing annealing temperatures post silicide films formation [48]. 50

Figure 13. SEM images of the reaction of (a) 10 nm Ni and of (b) 10 nm Ni–Pt with p+ (100)Si after submitted to an annealing of 700 °C/30 s [48]; 51

Figure 14. Steps in the salicide first process flow for the formation of the Ni(Pt)Si layer on the terminals of a transistor with SOI substrate. The Ni(Pt)Si layer is formed before contact patterning as opposed to the salicide last process for Ti-based silicide (Adapted from [79]). 52

Figure 15. Steps of salicide last process flow for the formation of $TiSi_X$ layer on the terminals of a transistor for bulk Si-substrate. The $TiSi_X$ is formed after the contact patterning from [28]. 53

Figure 16. Schematics of the formation of isolated small islands (blue islets) on the top of rigid substrate (green) due the agglomeration phenomenon [83]. 54

Figure 17. (a) Agglomerates formed on a rigid substrate and (b) agglomerates formed at the interface of two materials [83]. 55

Figure 18. 2D illustration of the cross-section of two grains with diameter D on a rigid substrate at the equilibrium state during the development of grooves adapted from [83]. 56

Figure 19. Mullins first model of a grain boundary grooving with (a) the boundary grooving and (b) the normalized profile shape of the surface [90]. 58

Figure 20. Mass shedding mechanisms: (a) Retraction of the thin film edge described by flux J due to chemical potential gradient. (b-c) The retraction continues and thickens the rim causing a deepening of the valley in front of the rim. (d) The valley achieved a maximum depth and in contact with the substrate, isolating the thin film, creating discontinuities [83]. 58

Figure 21. STEM cross-section of a Ni film on a sapphire, Al_2O_3 substrate, annealed at 700 °C for a duration of 6 mins from [91]. 59

Figure 22. (a) Non-elevated rim during grain boundaries grooving, (b) Extension of Mullins original model of a grain boundary grooving with the consideration of interface diffusion [91]. 59

Figure 23. (a) Initial state (in pink, the Kirkendall marker). (b) Initial stage of boundary grooving without interface diffusion. (c) The presence of interface diffusion increases the height of the Kirkendall marker from [85]. 60

Figure 24. Cross-sectional TEM image of inverted NiSi islands formed on Si substrate post thermal annealing at 750 °C for 30 s [16]. 60

Figure 25. (a) Top-view SEM images showing agglomerated NiSi film on Si substrate. b) Cross-section schematic of the inverse agglomeration of NiSi film [53] 61

Figure 26. Sheet resistance measurements of 13 nm Ni films on Silicon-on-insulator (SOI) substrates. The samples were annealed at 1 °C/s up to 750 °C and kept at this temperature for 10 minutes. (a) A Ni film on Si(100), with and without an amorphous Si interlayer. (b) Ni films on Si(100), implanted with 20 keV/atom of nitrogen [110]. 65

Figure 27. Evolution of the NiPt-silicide resistivity with the a-Si thickness generated for both types of PAI, Si and Ge atoms [111]. 66

Figure 28. (i) Pole Figure of NiSi thin film with F1 and F2 representing fiber texture and E1 and E2 epitaxial one. (ii) Electron backscattered diffraction (EBSD) analysis demonstrating reduction in grain size between a) RTA and b) DSA-type annealing [95]. 67

Figure 29. (i) Annealing profile of RTA2 comparison between conventional RTA2 and spike RTA2. (ii) The morphology of NiSi film for spike and soak RTA annealings at 550 and 590 °C [99]. 68

Figure 30. Co-integration of nickel silicide, Ni(Pt)Si and titanium silicide, TiSi for imager technologies. (a) TEM cross-section image of the CMOS part of the device with Ni(Pt)Si layer highlighted in yellow, (b) Schematics of the integration of silicides in CMOS on the

left and in imager on the right, and (c) TEM cross-section of a part of the imager containing the TiSi layer (reproduced from [95]). 69

Figure 31. Square resistance, Rs, of the Ni(Pt)Si layer with increasing thermal budget for line width, (a) w=2 µm and (b) w=0.1 µm on the right [10]. 70

Figure 32. Schematics of the SiCoNi process illustrating (a) the generation of ammonium fluoride, NH_4F, by remote plasma and the subsequent reaction with SiO_2 to form fluoride salts. (b) Sublimation process of the $(NH4)2SiF6$ salts [121]. 76

Figure 33. Schematics of the Endura equipment by *Applied Materials* illustrating the process sequence for the deposition of NiPt film (denoted by blue arrow). 78

Figure 34. (a) RTA chamber for silicidation of *Radiance* by *Applied Materials* [122]. (b) Cross-sectional schematics of RTA chamber. 79

Figure 35. 3D schematics of the "Vantage Astra" chamber [123]. 80

Figure 36. Schematic of "laser strips" for uncompleted coverage on a wafer during the DSA annealing. 81

Figure 37. (a) 3D schematics of the typical setup of the four-point probe measurement. (b) Electrical representation of the contribution of the different resistances [125]. 82

Figure 38. Apparent resistance with resistance in series model where R1 represents the resistance of Si and R2 of Ni(Pt)Si layer after the agglomeration of Ni(Pt)Si thin film. 84

Figure 39. (a) Schematics of the working principle of ellipsometry [126]. (b) Data processing for thickness determination by comparison with mathematical model [127]. 84

Figure 40. Schematics of x-ray diffraction concept. 86

Figure 41. XRD θ-2θ geometry experimental setup [130]. 87

Figure 42. Schematics of the (a) out-of-plane XRD scan and (b) in-plane XRD scan adapted from [131]. 88

Figure 43. (a) Schematical representation of the setup of in-plane XRD with (b) side view of the setup, (c) top view and inset showing planes perpendicular to sample surface, from [132]. 89

Figure 44. Schematics of a sample with four degrees of freedom in the case where four-axis goniometer is used during XRD scan [130]. 90

Figure 45. (a) Schematics of a polycrystalline material with grains rotating along the axis normal to the sample surface and (b) the corresponding pole figure showing a concentric ring [133]. 91

Figure 46. Schematics of polycrystalline materials with grains showing the grains orientations in top row for (a) random texture, (b) axiotaxy texture, (c) epitaxy texture, and their corresponding pole figure in bottom row (d), (e), and (f) respectively [17], [133]. 91

Figure 47. Interactions between electrons and matter including backscattered electrons (BSE), secondary electrons (SE), Auger electrons adapted from [135] 93

Figure 48. (a) Representation of the EBSD setup with electron beam hitting the surface of the tilted sample. (b) Example of Kikuchi bands formed from the intersection of wide-angle Kossel cones and phosphor screen [136]. 95

Figure 49. Example of an electron backscatter diffraction (EBSD) map of Ti-Mo alloy solution treated at 850 °C for 1 h [137]. A color code indicator is included to indicate the crystal orientation. 96

Figure 50. Study 1: Impact of different types of SiCoNi treatments on the agglomeration of the 11 nm Ni(Pt)Si thin film. In this figure the rounded rectangle refers to the main processes, words in italics to the process description, steps in bullet points to other related process, words in bold to the sample names and rectangle to different characterization techniques. 103

Figure 51. Study 2: Impact of the annealing schemes on the agglomeration of the 11 nm Ni(Pt)Si thin film. In this figure the rounded rectangle refers to the main processes, words in italics to the process description, steps in bullet points to other related process, words in bold to the sample names and rectangle to different characterization techniques. 105

Figure 52. Study 3: Impact of confinement on the agglomeration of the 11 nm Ni(Pt)Si thin film. In this figure the rounded rectangle refers to the main processes, words in italics to the process description, steps in bullet points to other related process, words in bold to the sample names and rectangle to different characterization techniques. 107

Figure 53. Study 4: Results on industrial wafers following the process flows of the integrated circuits. In this figure the rounded rectangle refers to the main processes, words in italics to the process description, steps in bullet points to other related process, words in bold to the sample names and rectangle to different characterization techniques. 109

Figure 54. Schematics for the formation of 11 nm Ni(Pt)Si thin film using two different SiCoNi treatments: SiCoNi 80 (left) and 2x40 (right). 111

Figure 55. Thickness profile of as-dep NiPt layer on Si(100) for a 49-points measurement mapping on 300 mm wafer measured from NiPt_SiC2x40 and NiPt_SiC80 samples. Sites 1 and 49 correspond respectively to the center and the extreme edge of wafer. A 3 mm edge exclusion is considered for such mapping. 114

Figure 56. TEM cross-sections obtained after NiPt deposition on Si substrate for (a) NiPt_SiC2x40 and (b) NiPt_SiC80 samples. 115

Figure 57. XPS spectra of (a) O-1s and (b) Ni-2p3 measured from NiPt layers on Si substrates for both NiPt_SiC2x40 and NiPt_SiC80 samples with a circular inset zoomed on Ni-O peaks. 116

Figure 58. XPS spectra of F1s measured from NiPt layers deposited on Si substrates for NiPt_SiC2x40 and NiPt_SiC80 samples. 117

Figure 59. Concentration profiles of Ni, Pt, Si, O and F in as-dep NiPt layer for (a) NiPt_SiC2x40, and (b) NiPt_SiC80 samples measured using TEM-EDX. The corresponding zoom in (c) and (d) to better visualize both the Pt and F atoms. 119

Figure 60. ToF-SIMS depth profiles of as-dep NiPt layer deposited on Si substrate for (a) NiPt_SiC2x40 and (b) NiPt_SiC80 samples. 121

Figure 61. EELS spectra of nickel $L_{2,3}$ ionization edge extracted from line profiles at different regions: interfaces between the NiPt/NiSi/Si bulk and in the core of each layer for (a) NiPt_SiC2x40 and (b) NiPt_SiC80 samples. Cyan-colored arrow is used to indicate the presence of additional peak. 122

Figure 62. The thickness uniformity of Ni(Pt)Si film measured by ellipsometry after RTA2 annealing for (a) NiSi_SiC2x40, and (b) NiSi_SiC80 samples. 126

Figure 63. Thickness profile of the Ni(Pt)Si film formed on Si(100) substrate for a 49-points measurement mapping on the 300 mm wafer for the different SiCoNi treatments: SiCoNi 2x40 and SiCoNi 80. Site 1 corresponds to the center of the wafer and site 49, to the edge. 126

Figure 64. Sheet resistance of the 11 nm Ni(Pt)Si films formed on Si for NiSi_SiC2x40 and NiSi_SiC80 after high-temperature annealing, RTAD. 127

Figure 65. Top view tilted-SEM images of 11 nm Ni(Pt)Si films formed on Si substrate for (i) NiSi_SiC2x40, and (ii) NiSi_SiC80 samples, measured the (a) center and (b) edge of the 300 mm blanket wafers. 129

Figure 66. Examples of precise segmentation using the Smart Segmentation feature of the IP-SDK software. The surface area of exposed Si substrate, $S_{exposed_Si}$ (μm^2) is extracted for 11 nm Ni(Pt)Si film post RTAD 600 °C (NiSi_SiC2x40). 130

Figure 67. Top view tilted-SEM images measured the (a) center and (b) edge of the wafer for the NiSi_SiC2x40 and NiSi_SiC80 sample. An inset corresponding to a zoom of f_{Si}(%) between 550 and 600 °C is included. 131

Figure 68. Schematics of the different annealing schemes studied for the formation of 11±1 nm Ni(Pt)Si films. The obtained silicide films are then subjected to additional high-temperature annealing (RTAD) between 500 and 700 °C/30 s for agglomeration assessment. 135

Figure 69. Sheet resistance, Rs, of 11±1 nm Ni(Pt)Si films formed by the four types of annealing schemes (NiSi_partial, NiSi_laser, NiSi_total, and NiSi_onestep) after high-temperature annealing, RTAD. 138

Figure 70. Top view tilted-SEM images of 11±1 nm Ni(Pt)Si films after RTAD treatments (i) 500 °C, (ii) 550 °C, (iii) 600 °C, (iv) 650 °C, for all of the samples: (a) NiSi_partial, (b) NiSi_laser, (c) NiSi_total, (d) NiSi_onestep. Light grey and dark grey contrasts represent Ni(Pt)Si and exposed Si substrate/holes respectively. 140

Figure 71. Evolution of the fraction of exposed Si, f_{Si}(%), during the agglomeration of 11±1 nm Ni(Pt)Si films formed by different annealing schemes (NiSi_partial, NiSi_laser, NiSi_total, and NiSi_onestep) extracted from IPSDK software. 142

Figure 72. High-resolution SEM (HRSEM) images showing grains and grain boundaries for 11±1 nm-thick Ni(Pt)Si films formed by different annealing schemes in two states: (a) non-agglomerated and (b) agglomerated. 144

Figure 73. EBSD orientation map for (a) non-agglomerated, and (b) agglomerated 11±1 nm-thick Ni(Pt)Si films on Si(100) substrate formed by the different annealing schemes (NiSi_partial, NiSi_laser, NiSi_total, and NiSi_onestep). Pink-colored grains represent Ni(Pt)Si-(013) planes, blue-colored grains represent Ni(Pt)Si-(010) planes, and dark areas correspond to unindexable areas due to very fine grains (detection limits ≈ 40 nm). 146

Figure 74. (a) Inverse pole figures (IPF) of Ni(Pt)Si thin films on Si(100) substrate at two different states (non-agglomerated and agglomerated) showing an evolution along the (013) orientation (red circle), while the intensity of the (010) orientation is reduced. 148

Figure 75. Pole figures (PF) of Ni(Pt)Si-(103) on Si(100) substrate at two different states: (a) non-agglomerated and (b) agglomerated illustrating the presence of fiber-like texture with off-normal axis. The color scale marker indicates red for maximum intensity, and blue for minimum. 149

Figure 76. Schematics of the process steps used to form the regular silicided lines based on classical photolithography and SALICIDE process for the formation of 11 nm Ni(Pt)Si film on Si(100) substrate (for process details please refer to section 1.2.3). 153

Figure 77. Top-view optical image of (a) dielectrics dots and (a) dielectrics lines regularly spaced by a pitch of *p*, repeated over an area of 2x2 mm² on a 300 mm Si wafer after patterning by DIVA mask. 154

Figure 78. SEM images of two types of structures featured in the DIVA mask design presenting a regular patterning of dielectric and silicided lines in (a) and (b), and silicided substrate including some dielectrics squares in (c) and (d). Note that the (a) and (c) images are obtained through tilted SEM apparatus and (b) and (d) with a classical tool set. 154

Figure 79. Top view HRSEM images of the four types of structures formed by regular silicided lines (a), (b) and (c) presenting different pitch dimensions respectively 110, 250 and 500 nm and dielectric dots (d). In the following sections these structures are named NiSi_Lines_110, NiSi_Lines_250, NiSi_Lines_500, and NiSi_Diel_dots. 155

Figure 80. Top-view HRSEM images of 11 nm Ni(Pt)Si formed on confined structures (NiSi_Lines_110, NiSi_Lines_250, NiSi_Lines_500, and NiSi_Diel_dots) and top view tilted-SEM images measured on blanket wafer for different annealing temperatures (a) 390, (b) 500, (c) 550, (d) 650, and (e) 700 °C. 156

Figure 81. Evolution of the fraction of exposed Si, f_{Si}(%) during the agglomeration of 11 nm Ni(Pt)Si film formed in (in ascending order of degree of confinement) NiSi_blanket, NiSi_Diel_dots, NiSi_Lines_500, NiSi_Lines_250, and NiSi_Lines_110. 158

Figure 82. Pole figure of non-agglomerated 11 nm Ni(Pt)Si film formed on blanket wafer for (a) 2θ=31.20 ° (002/011), (b) 2θ=45.47 ° (112), (c) 2θ=46.65 ° (202/211), and (d) 2θ=51.5 ° (103). Dashed lines are drawn on top of the pole figure of NiSi(103) indicating the presence of ring segments. 160

Figure 83. (a) Angular mapping of intensity, ϕ (°) vs. $2\theta_\chi$ (°) radially integrated for values of χ (°), and (b) extracted XRD θ-$2\theta_\chi$ scans performed on each ϕ (°) value measured from the NiSi_Lines_250 sample after RTAD of 500 °C. 162

Figure 84. Extracted θ-$2\theta_\chi$ scans for (a) ϕ between -100 and -90 °, and (b) ϕ between 86 and 100 ° measured from the NiSi_Lines_250 sample after a RTAD annealing at 500 °C. 163

Figure 85. Extracted pole figures (PF) for (a) 2θ=14.70°, (b) 2θ=20°, (c) 2θ=22°, and (d) 2θ=24° measured from the NiSi_Lines_250 sample. 164

Figure 86. Superimposition of the dashed lines drawn in the NiSi(103) PF in Fig. 82(d), related to blanket experiment, on top of the pole Figures of the NiSi(103) determined for the NiSi_Lines_250 one. 165

Figure 87. Pole Figures of NiSi(103) after a RTAD annealing at 500 °C of (a) NiSi_Diel_dots, (b) NiSi_Lines_500, (c) NiSi_Lines_250, and (d) NiSi_Lines_110 with normalized intensity. 165

Figure 88. Description of a part of the process flow used to fabricate the integrated circuit involving the co-integration of Ni-silicide, Ni(Pt)Si and Ti-silicide, $TiSi_X$ presenting thermal budget incompatibility due to premature agglomeration of Ni(Pt)Si film during $TiSi_x$ formation. 169

Figure 89. SALICIDE process flows illustrating two studied pathways for the formation of Ni(Pt)Si thin film dealing with millisecond laser annealing (DSA). 170

Figure 90. Thickness of Ni(Pt)Si film formed on terminals of the transistor for two types of annealing: standard RTA annealing, named NiSi_circuit, and milliseconds laser annealing, NiSi_circuit_laser. 172

Figure 91. Normalized resistance, R (Ω), extracted from parametric tests on N-doped gates, source/drain, and P-doped source/drain for NiSi_circuit and NiSi_circuit_laser after $TiSi_x$ annealings at 550 and 650 °C. 174

Figure 92. TEM cross-sections obtained after $TiSi_x$ annealings at 550 °C for (a) NiSi_circuit, and (b) NiSi_circuit_laser samples. White dashed lines are included to indicate the boundary grooving phenomenon, with δ, the depth of the groove. 175

Figure 93. TEM cross-sections obtained for NiSi_circuit sample for $TiSi_x$ annealings at (a) 550 °C, and (b) 650 °C. 176

Figure 94. TEM cross-sections obtained for NiSi_circuit_laser sample for $TiSi_x$ annealings at (a) 550 °C, and (b) 650 °C. 177

Figure 95. EDX line scan of oxygen, O and platinum, Pt for the two SiCoNi treatments: (a) SiCoNi 2x40, and (b) SiCoNi 80 treatments. 182

Figure 96. Illustration of the 1D periodic interface achieved for NiSi(103), NiSi(211), NiSi(202), and NiSi(112), planes parallel to Si(220), adapted from [104]. 186

Figure 97. Pole Figures (PF) of Ni(Pt)Si-(103) on Si(100) substrate for an agglomerated silicide sample formed by one-step annealing with a superimposition of calculated axiotaxial lines from [104]. 188

Figure 98. Schematics of the supposed of Ni(Pt)Si grains inside one trench for (a) NiSi_Lines_110, (b) NiSi_Lines_250, and (c) NiSi_Lines_500 samples. 190

Figure 99. Top-view schematics of the (a) NiSi_blanket and (b) NiSi_Diel_dots samples with $D_{blanket} = D_{Diel_dots}$. 192

Figure 100. TEM cross sections of a 11 nm Ni(Pt)Si thin film formed using the standard SALICIDE process (identical to the NiSi_partial sample) and an additional annealing at400 °C. Three different magnifications are shown: (a) low magnification, (b) high magnification between adjacent grains, and (c) at the middle of a grain. The yellow line indicates EDX line scan. 194

Figure 101. (a) STEM-EDX cross-sections of 11 nm Ni(Pt)Si thin film formed using standard SALICIDE (NiSi_partial) after RTAD 400 °C with the STEM image, (b) Ni EDX map, (c) Si EDX map, and (d) Pt EDX map. 195

Figure 102. (a) EDX line scans of Pt concentration measured along the yellow lines in Fig. 100 and (b) zoom EDX line of the same sample for better visualization of Pt redistribution. Regions shaded in green correspond to the Ni(Pt)Si layer and pink to the Si substrate. 196

Figure 103. TEM cross-sections of the morphological evolution of the 11 nm Ni(Pt)Si thin film at each of the RTAD annealings, (a) 500, (b) 550, (c) 600, and (d) 700 °C, taken at (i) lower magnification, (ii) between adjacent grains, and (iii) at the center of a grain/islet. Note that all of the silicide films are formed using the standard SALICIDE process (equivalent to that of the NiSi_partial sample). Yellow, cyan and pink lines indicate EDX line scans. _ 197

Figure 104. EDX line scans of Pt concentration measured along the yellow lines in Fig. 4.4 for each of the RTAD temperatures: (a) 500, and (b) 550 °C. Two lines scans are provided for RTAD at 600 °C corresponding to grains with boundary grooving (cyan line) (c), and grains near a hole (pink line) (d). Similarly for 700 °C: line scan for isolated islet (cyan line) (e), connected islet (pink line) (f). Regions shaded in green corresponds to Ni(Pt)Si layer and pink to Si substrate. _____ 199

Figure 105. EDX maps of Pt measured on Ni(Pt)Si thin films after RTAD annealing at (a) 500, (b) 550, (c) 600 °C zone 1, (d) 600 °C zone 2, and (e)700 °C. _____ 200

Figure 106. Evolution of the Pt concentration at the top surface of the Ni(Pt)Si thin film and at the Ni(Pt)Si/Si interface and their corresponding ratio (Pt_interface/Pt_surface) at each of the RTAD temperatures (°C). _____ 201

Figure 107. Schematics illustrating diffusion paths during different processing steps: (a) Formation of NiPtSi at 380 °C (b) Grooving during RTAD at 600 °C (c) Agglomeration during RTAD at 700 °C. Arrows indicate the direction of diffusion, with corresponding diffusion coefficients provided. _____ 204

Figure 108. EDX line scans of Pt measured at the center of silicide grains/islets for (a) NiSi_partial sample, and (b) NiSi_laser sample after annealing at two RTAD temperatures corresponding to the agglomerated (650 °C) and non-agglomerated (550 °C) stage. _ 206

Figure 109. Superimposition of the EDX line scans of Pt after normalization using the concentration in Si bulk, and depth alignment at Ni of 30 at. %, measured for NiSi_partial and NiSi_laser samples after an annealing at 550 °C (extracted from Fig. 109(a) and(b)). _____ 207

Figure 110. Schematics of the geometry used for the redistribution model: (a) initial columnar grains with a hexagonal base, (b) islands with a spherical cap shape after agglomeration. _____ 209

Figure 111. Example of fit of the EDX map for Pt for a grain after agglomeration (second whole grain from the right in Fig. 105(e)) using the present model: (a) fitted shape and Pt-rich region, (b) EDX map for Pt with the fitted shape and Pt-rich region superimposed, (c) same as (b) with the Pt-rich regions highlighted in blue. _____ 210

Figure 112. Fit of the EDX map for Pt for two grains after grooving (RTAD 600°C, Fig. 105(d)) using the present model: (a) whole EDX map for Pt, (b) EDX map for Pt with the fitted shape and Pt-rich region superimposed, (c) same as (b) with the Pt-rich regions highlighted in blue. _____ 210

Figure 113. Fit of the EDX map for Pt for four grains after agglomeration (RTAD 700°C, Fig. 105(e)) using the present model: (a) whole EDX map for Pt, (b) EDX map for Pt with the fitted shape and Pt-rich region superimposed, (c) same as (b) with the Pt-rich regions highlighted in blue. _____ 211

Figure 114. Visual representation of the accumulation of the fluoride salt prior to the sublimation at around 100 °C for (a) SiCoNi 80 and (b) SiCoNi 2x40 process. _____ 215

Figure 115. Visual representation of the fluorine redistribution using color gradient, in the intermixing layer (NiSi) for (a) NiPt_SiC2x40 and (b) NiPt_SiC80 samples. _____ 216

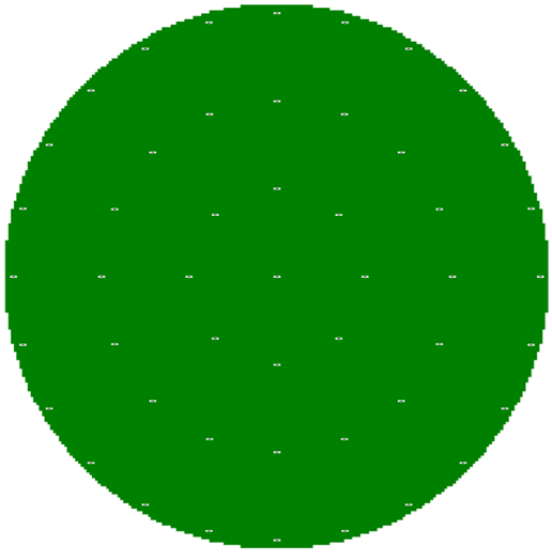
Figure 116. Schematic of the model used to simulate grooving based on the geometry shown in Figure 110. (a) Change in grain shape, (b) redistribution of Pt. R and θ_i correspond to the radius of the NiSi/Si interface curvature and the angles defining the different spherical caps (i=2, 3, 5), respectively. L_g and h_g are the half-size of the Ni(Pt)Si grain and the original thickness of the non-agglomerated NiSi film, respectively. h_{gr} is the depth of the grain boundary grooving. Only half of the annotated volumes is shown for clarity. _____ 249

Figure 117. Schematic of the model used to simulate the agglomeration (a) change in the grain shape (b) redistribution of Pt. L_{ag} is the agglomerated length. Only half of the annotated volumes is shown for clarity. _____ 251

Appendices

A.i 49-points measurements mapping coordinates

a. <u>Measurement sites are indicated with the dashed lines.</u>



X	Y
0	0
0	48.499952
-34.294645	34.294645
-48.499952	0
-34.294645	-34.294645
0	-48.499952
34.294645	-34.294645
48.499952	0
34.294645	34.294645
0	97.000049
-37.120311	89.616359
-68.589392	68.589392
-89.616359	37.120311
-97.000049	0
-89.616359	-37.120311
-68.589392	-68.589392
-37.120311	-89.616359
0	-97.000049
37.120311	-89.616359
68.589392	-68.589392
89.616359	-37.120311
97.000049	0
89.616359	37.120311
68.589392	68.589392
37.120311	89.616359
0	145.5
-37.658171	140.542208
-72.75	126.006696
-102.884037	102.884037
-126.006696	72.75
-140.542208	37.658171
-145.5	0
-140.542208	-37.658171
-126.006696	-72.75
-102.884037	-102.884037
-72.75	-126.006696
-37.658171	-140.542208
0	-145.5
37.658171	-140.542208
72.75	-126.006696
102.884037	-102.884037
126.006696	-72.75
140.542208	-37.658171
145.5	0
140.542208	37.658171
126.006696	72.75
102.884037	102.884037
72.75	126.006696
37.658171	140.542208

A.ii X-ray powder diffraction reference files (PDF)

a. Ni (Cu K1 1.540456 A)

00-004-0850 May 9, 2016 3:55 PM (sz240884)

Status Primary QM: Star Pressure/Temperature: Ambient Chemical Formula: Ni
Empirical Formula: Ni Weight %: Ni100.00 Atomic %: Ni100.00 Compound Name: Nickel
Mineral Name: Nickel, syn

Radiation: CuKa1 : 1.5405 Å Filter: Ni Beta Intensity: Diffractometer

SYS: Cubic SPGR: Fm-3m (225)
Author's Cell [AuthCell a: 3.5238 Å AuthCell Vol: 43.76 Å³ AuthCell Z: 4.00 AuthCell MolVol: 10.94]
Density [Dcalc: 8.911 g/cm³] SS/FOM: F(8) = 87.9(0.0114, 8) Temp: 299.000 K (Author provided temperature)
Color: White

Space Group: Fm-3m (225) Molecular Weight: 58.70
Crystal Data [XtlCell a: 3.524 Å XtlCell b: 3.524 Å XtlCell c: 3.524 Å XtlCell : 90.00°
XtlCell : 90.00° XtlCell : 90.00° XtlCell Vol: 43.76 Å³ XtlCell Z: 4.00]
Crystal Data Axial Ratio [a/b: 1.000 c/b: 1.000]
Reduced Cell [RedCell a: 2.492 Å RedCell b: 2.492 Å RedCell c: 2.492 Å RedCell : 60.00°
RedCell : 60.00° RedCell : 60.00° RedCell Vol: 10.94 Å³]

Atomic parameters are cross-referenced from PDF entry 04-011-9061
Crystal (Symmetry Allowed): Centrosymmetric

SG Symmetry Operators:

Seq	Operator	Seq	Operator	Seq	Operator	Seq	Operator	Seq	Operator	Seq	Operator	Seq	Operator
1	x,y,z	8	-x,-z,-y	15	z,-x,-y	22	-y,x,z	29	-y,z,-x	36	z,-y,x	43	-x,-z,y
2	-x,-y,-z	9	y,x,z	16	-z,x,y	23	z,-y,-x	30	y,-z,x	37	-x,-y,z	44	x,z,-y
3	z,x,y	10	-y,-x,-z	17	y,-z,-x	24	-z,y,x	31	-x,z,-y	38	x,y,-z	45	-y,-x,z
4	-z,-x,-y	11	z,y,x	18	-y,z,x	25	-x,y,-z	32	x,-z,y	39	-z,-x,y	46	y,x,-z
5	y,z,x	12	-z,-y,-x	19	x,-z,-y	26	x,-y,z	33	-y,x,-z	40	z,x,-y	47	-z,-y,x
6	-y,-z,-x	13	x,-y,-z	20	-x,z,y	27	-z,x,-y	34	y,-x,z	41	-y,-z,x	48	z,y,-x
7	x,z,y	14	-x,y,z	21	y,-x,-z	28	z,-x,y	35	-z,y,-x	42	y,z,-x		

Atomic Coordinates:

Atom	Num	Wyckoff	Symmetry	x	y	z	SOF	IDP	AET
Ni	1	4a	m-3m	0.0	0.0	0.0	1.0		

Subfile(s): Common Phase, Educational Pattern, Forensic, Inorganic, Metals & Alloys, Mineral Related (Mineral , Synthetic), NBS Pattern

Prototype Structure: Cu Prototype Structure [Alpha Order]: Cu LPF Prototype Structure: Cu,cF4,225
LPF Prototype Structure [Alpha Order]: Cu,cF4,225
Mineral Classification: Gold (Supergroup), 1C-disordered (Group) Pearson: cF4.00
Cross-Ref PDF #'s: 01-087-0712 (Alternate), 04-001-0091 (Alternate), 04-010-6148 (Primary), 04-011-9061 (Alternate)
CAS: 7440-02-0 Entry Date: 09/01/1954

References:

Type	DOI	Reference
Primary Reference		Swanson, Tatge. Natl. Bur. Stand. (U. S.), Circ. 539 I, 13 (1953).
Crystal Structure		Crystal Structure Source: LPF.

Database Comments: Additional Patterns: See PDF 01-087-0712. Analysis: Spectrographic analysis show <0.01% each of Mg, Si and Ca. Color: White. Sample Source or Locality: Sample obtained from Johnson Matthey Company, Ltd. Temperature of Data Collection: Pattern taken at 299 K. Unit Cell Data Source: Powder Diffraction.

d-Spacings (8) - 00-004-0850 (Fixed Slit Intensity) - Cu K1 1.54056 Å

2 (°)	d (Å)	I	h	k	l	*	2 (°)	d (Å)	I	h	k	l	*	2 (°)	d (Å)	I	h	k	l	*
44.5066	2.034000	100	1	1	1		92.9440	1.062400	20	3	1	1		144.6693	0.808400	14	3	3	1	
51.8459	1.762000	42	2	0	0		98.4456	1.017200	7	2	2	2		155.6525	0.788000	15	4	2	0	
76.3699	1.246000	21	2	2	0		121.9303	0.881000	4	4	0	0								

b. NiSi (Cu K1 1.540456 A)

01-070-9169 May 9, 2016 3:35 PM (sz240884)

Status Alternate QM: Star Pressure/Temperature: Ambient Chemical Formula: Ni Si
Empirical Formula: Ni Si Weight %: Ni67.63 Si32.37 Atomic %: Ni50.00 Si50.00 ANX: NO
Compound Name: Nickel Silicon

Radiation: CuKa1 : 1.5406 Å d-Spacing: Calculated Intensity: Calculated I/Ic: 2.35

SYS: Orthorhombic SPGR: Pnma (62)
Author's Cell [AuthCell a: 5.1752(7) Å AuthCell b: 3.3321(5) Å AuthCell c: 5.6094(9) Å
AuthCell Vol: 96.73 Å³ AuthCell Z: 4.00 AuthCell MolVol: 24.18]
Author's Cell Axial Ratio [c/a: 1.084 a/b: 1.553 c/b: 1.683]
Density [Dcalc: 5.959 g/cm³ Dstruc: 5.96 g/cm³] SS/FOM: F(30) = 146.5(0.0058, 35)
Temp: 295.000 K (Author provided temperature)

Space Group: Pnam (62) Molecular Weight: 86.79
Crystal Data [XtlCell a: 5.175 Å XtlCell b: 5.609 Å XtlCell c: 3.332 Å XtlCell : 90.00°
XtlCell : 90.00° XtlCell : 90.00° XtlCell Vol: 96.73 Å³ XtlCell Z: 4.00]
Crystal Data Axial Ratio [c/a: 0.644 a/b: 0.923 c/b: 0.594]
Reduced Cell [RedCell a: 3.332 Å RedCell b: 5.175 Å RedCell c: 5.609 Å RedCell : 90.00°
RedCell : 90.00° RedCell : 90.00° RedCell Vol: 96.73 Å³]

Atomic parameters are cross-referenced from PDF entry 04-003-0573
Crystal (Symmetry Allowed): Centrosymmetric

SG Symmetry Operators:

Seq	Operator	Seq	Operator	Seq	Operator	Seq	Operator
1	x,y,z	3	-x+1/2,y+1/2,-z+1/2	5	-x,-y,z+1/2	7	x+1/2,-y+1/2,-z
2	-x,-y,-z	4	x+1/2,-y+1/2,z+1/2	6	x,y,-z+1/2	8	-x+1/2,y+1/2,z

Atomic Coordinates:

Atom	Num	Wyckoff	Symmetry	x	y	z	SOF	IDP	AET
Ni	1	4c	..m	0.184	0.006	0.25	1.0		6-a
Si	2	4c	..m	0.08	0.33	0.75	1.0		6-b

Subfile(s): Inorganic, Metals & Alloys Prototype Structure: Fe As Prototype Structure [Alpha Order]: As Fe
LPF Prototype Structure: Fe As,oP8,62 LPF Prototype Structure [Alpha Order]: As Fe,oP8,62
Pearson: oP8.00

Cross-Ref PDF #'s: 00-038-0844 (Primary), 01-070-2626 (Alternate), 01-070-9170 (Alternate), 01-070-9249 (Deleted), 01-078-2570 (Alternate), 01-078-2571 (Alternate), 01-078-3100 (Alternate), 04-001-3267 (Alternate), 04-003-0573 (Primary), 04-004-7095 (Alternate), 04-004-7130 (Alternate), 04-006-9131 (Alternate), 04-010-6144 (Alternate), 04-016-5667 (Alternate), 04-017-6382 (Alternate)

Entry Date: 09/01/2005 Last Modification Date: 09/01/2011 Last Modifications: Reflections

References:

Type	DOI	Reference
Primary Reference		Calculated from ICSD using POWD-12++.
Additional Reference		Rabadanov, M.Kh., Ataev, M.B. Crystallogr. Rep. 47, 33 (2002).
Crystal Structure		Crystal Structure Source: LPF.
Structure		"Atomic structure and enormous anisotropy of thermal expansion in Ni Si single crystals. I. Refinement of structure models". Rabadanov, M.Kh., Ataev, M.B. Kristallografiya 47, 40 (2002).

Database Comments: ANX: NO. Analysis: Ni1 Si1. Formula from original source: Ni Si. ICSD Collection Code: 095448. Temperature of Data Collection: 295 K. Wyckoff Sequence: c2(PNMA). Unit Cell Data Source: Single Crystal.

d-Spacings (107) - 01-070-9169 (Fixed Slit Intensity) - Cu K1 1.54056 Å

2 (°)	d (Å)	I	h	k	l	*	2 (°)	d (Å)	I	h	k	l	*	2 (°)	d (Å)	I	h	k	l	*
23.3675	3.803670	118	1	0	1		61.0953	1.515540	34	2	0	3		79.3853	1.206070	11	4	1	0	
31.1952	2.864780	710	0	1	1		62.8292	1.477820	8	3	1	1		81.0870	1.185000	3	3	1	3	
31.8810	2.804700	144	0	0	2		65.0624	1.432390	22	0	2	2		81.5759	1.179130	101	4	1	1	
34.6368	2.587600	269	2	0	0		66.7178	1.400810	49m	0	0	4		81.9383	1.174830	34	4	0	2	
35.7964	2.506390	316	1	1	1		66.7178	1.400810	m	2	2	0		82.1830	1.171950	82	3	2	1	
36.4052	2.465860	184	1	0	2		67.8319	1.380490	47m	1	2	2		83.5418	1.156310	4	2	1	4	
38.2739	2.349650	10	2	0	1		67.8319	1.380490	m	2	1	3		86.7990	1.121090	21	2	2	3	
44.2835	2.043730	136	2	1	0		69.0506	1.359070	4	2	2	1		88.0881	1.107980	16	4	1	2	
45.7364	1.982130	768	1	1	2		69.3730	1.353540	15	1	0	4		89.2635	1.096410	44	1	0	5	
47.2983	1.920250	999	2	1	1		69.9094	1.344460	10	3	1	2		89.9780	1.089550	14	0	3	1	
47.7848	1.901830	311	2	0	2		73.0770	1.293800	29	4	0	0		90.1244	1.088160	4	3	0	4	
51.9555	1.758540	255	1	0	3		74.8221	1.267890	57	3	0	3		91.7719	1.072880	3	0	2	4	
55.0763	1.666050	291	0	2	0		75.3228	1.260700	17	4	0	1		92.5182	1.066170	16	1	3	1	
55.7001	1.648860	167	3	0	1		75.8531	1.253200	141m	1	1	4		92.8498	1.063230	18m	0	1	5	
56.3788	1.630610	181	0	1	3		75.8531	1.253200	m	2	2	2		92.8498	1.063230	m	4	0	3	
59.3765	1.555240	1	1	1	3		77.3285	1.232930	2	2	0	4		94.3145	1.050540	12	1	2	4	
60.6287	1.526080	11	1	2	1		79.1198	1.209450	99	1	2	3		95.3949	1.041480	15	1	1	5	

© 2016 International Centre for Diffraction Data. All rights reserved.

c. $NiSi_2$ (Cu K1 1.540456 A)

Name and formula

Reference code:	00-043-0989
Compound name:	Nickel Silicon
PDF index name:	Nickel Silicon
Empirical formula:	$NiSi_2$
Chemical formula:	$NiSi_2$

Crystallographic parameters

Crystal system:	Cubic
Space group:	Fm3m
Space group number:	225
a (Å):	5,4160
b (Å):	5,4160
c (Å):	5,4160
Alpha (°):	90,0000
Beta (°):	90,0000
Gamma (°):	90,0000
Volume of cell (10^6 pm^3):	158,87
Z:	4,00
RIR:	-

Subfiles and quality

Subfiles:	Alloy, metal or intermetalic Inorganic
Quality:	Blank (B)

Comments

Creation Date:	01/01/1970
Modification Date:	01/01/1970
Sample Preparation:	Vacuum-deposition of pure Ni film on (111) Si single-crystals. Cell parameter generated by least squares refinement
Unit Cell:	Reference reports: a=5.406.

References

Primary reference: Yoon, K., Jpn. J. Appl. Phys. Part 1, **21**, L779, (1982)

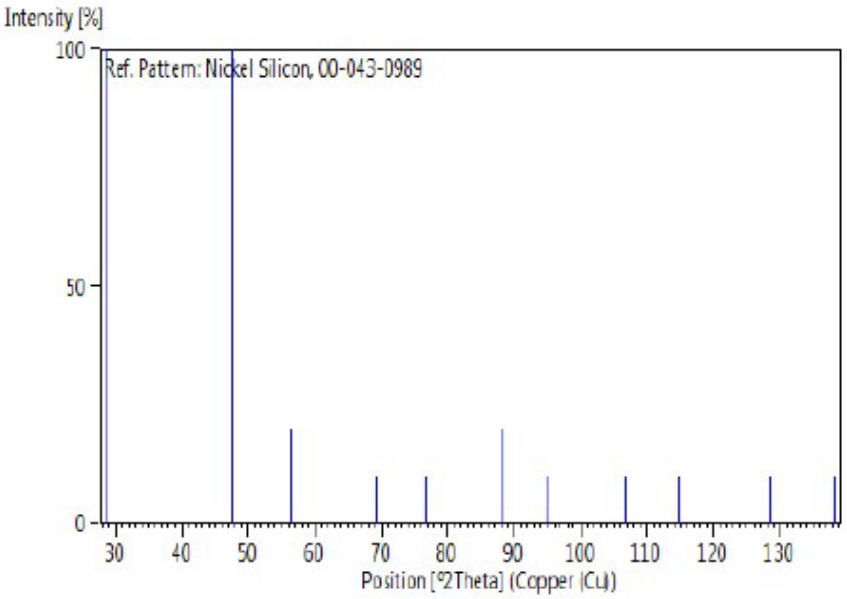
Peak list

No.	h	k	l	d [A]	2Theta[deg]	I [%]
1	1	1	1	3,11900	28,597	100,0
2	2	2	0	1,91600	47,411	100,0
3	3	1	1	1,63200	56,328	20,0
4	4	0	0	1,35400	69,348	10,0
5	3	3	1	1,24300	76,590	10,0

1 Of 2

6	4	2	2	1,10500	88,390	20,0
7	5	1	1	1,04500	94,975	10,0
8	4	4	0	0,96000	106,719	10,0
9	5	3	1	0,91430	114,811	10,0
10	6	2	0	0,85500	128,563	10,0
11	5	3	3	0,82500	138,037	10,0

Stick Pattern



d. NiSi for beam energy of 17 keV (wavelength 0.719319 A) – monochromatic source

01-070-9169 Jun 21. 2024 11:02 AM (AF271119)

Status Alternate **Quality Mark:** Star **Environment:** Ambient **Temp:** 295.0 K **Chemical Formula:** Ni Si
Empirical Formula: Ni Si **Refined Formula:** Ni Si **Weight %:** Ni67.63 Si32.37 **Atomic %:** Ni50.00 Si50.00
Compound Name: Nickel Silicon **Entry Date:** 09/01/2005 **Modification Date:** 09/01/2020 **Modifications:** Update

Radiation: CuKα1 (1.5406 Å) **d-spacing:** Calculated **Intensity:** Calculated - Peak

Crystal System: Orthorhombic **SPGR:** Pnma (62)
Author's Unit Cell [a: 5.1752(7) Å **b:** 3.3321(5) Å **c:** 5.6094(9) Å **Volume:** 96.73 Å³ **Z:** 4.00
MolVol: 24.18 **c/a:** 1.084 **a/b:** 1.553 **c/b:** 1.683] **Calculated Density:** 5.959 g/cm³
Structural Density: 5.959 g/cm³ **SS/FOM:** F(30) = 144.2(0.0059, 35) **R-factor:** 0.009 **I/Ic:** 2.35
I/Ic - CW ND: 0.62

Space Group: Pnam (62) **Molecular Wt:** 86.78 g/mol
Crystal Data [a: 5.175 Å **b:** 5.609 Å **c:** 3.332 Å **α:** 90.00° **β:** 90.00° **γ:** 90.00° **XtlCell Vol:** 96.73 Å³
XtlCell Z: 4.00 **c/a:** 0.644 **a/b:** 0.923 **c/b:** 0.594]
Reduced Cell [a: 3.332 Å **b:** 5.175 Å **c:** 5.609 Å **α:** 90.00° **β:** 90.00° **γ:** 90.00° **RedCell Vol:** 96.73 Å³]

Atomic parameters are cross-referenced from PDF entry 04-016-5667 **AC Space Group:** Pnma (62)
AC Unit Cell [a: 5.1818 Å **b:** 3.334 Å **c:** 5.619 Å **α:** 90° **β:** 90° **γ:** 90°]

Space Group Symmetry Operators:

Seq	Operator	Seq	Operator	Seq	Operator	Seq	Operator
1	x,y,z	3	x+1/2,-y+1/2,-z+1/2	5	-x,y+1/2,-z	7	-x+1/2,-y,z+1/2
2	-x,-y,-z	4	-x+1/2,y+1/2,z+1/2	6	x,-y+1/2,z	8	x+1/2,y,-z+1/2

Atomic Coordinates:

Atom	Num	Wyckoff	Symmetry	x	y	z	SOF	IDP	AET
Ni	1	4c	.m.	0.0069	0.25	0.1879	1.0		
Si	2	4c	.m.	0.3122	0.75	0.1041	1.0		

Crystal (Symmetry Allowed): Centrosymmetric

Subfiles: Inorganic, Metal & Alloy **Pearson Symbol:** oP8.00 **Prototype Structure (Formula Order):** Fe As
Prototype Structure (Alpha Order): As Fe **LPF Prototype Structure (Formula Order):** Fe As,oP8,62
LPF Prototype Structure (Alpha Order): As Fe,oP8,62 **ANX:** NO **Wyckoff Sequence:** c2

Cross-Ref PDF #'s: 01-070-2626 (Alternate), 01-070-9170 (Alternate), 01-078-2570 (Alternate), 01-078-2571 (Alternate), 01-078-3100 (Alternate), 01-083-3118 (Alternate), 04-001-3267 (Alternate), 04-003-0573 (Alternate), 04-004-7095 (Alternate), 04-004-7130 (Alternate), 04-006-9131 (Alternate), 04-010-6144 (Alternate), 04-016-5667 (Primary), 04-017-6382 (Alternate), 04-019-2898 (Alternate), 04-019-2900 (Alternate), 04-019-2905 (Alternate)

References:

Type	DOI	Reference
Primary Reference		Calculated from ICSD using POWD-12++.
Crystal Structure		Crystal Structure Source: LPF.
Structure		Rabadanov, M.Kh., Ataev, M.B. "Atomic structure and enormous anisotropy of thermal expansion in Ni Si single crystals. I. Refinement of structure models". Kristallografiya 2002, 47 (1), 40.

Database Comments: ANX: NO. Analysis: Ni1 Si1. Formula from original source: Ni Si. ICSD Collection Code: 95448. Calculated Pattern Original Remarks: (See translation) CYSTE3 (2002) 47 p.33-38 iss*. Temperature of Data Collection: 295 K. Wyckoff Sequence: c2. Unit Cell Data Source: Single Crystal.

d-spacings (97) - Ni Si - 01-070-9169 (Stick, fixed slit intensity) - X-ray (0.729319 Å)

2θ (°)	d (Å)	I	h	k	l	*	2θ (°)	d (Å)	I	h	k	l	*	2θ (°)	d (Å)	I	h	k	l	*
11.003	3.803670	118	1	0	1		25.845	1.630610	181	0	1	3		33.430	1.267890	57	3	0	3	
14.626	**2.864780**	710	0	1	1		27.121	1.555240	1	1	1	3		33.626	1.260700	17	4	0	1	
14.941	2.804700	144	0	0	2		27.649	1.526080	11	1	2	1		33.834	1.253200	141m	1	1	4	
16.203	2.587600	269	2	0	0		27.846	1.515540	34	2	0	3		33.834	1.253200	141m	2	2	2	
16.732	2.506390	316	1	1	1		28.571	1.477820	8	3	1	1		34.407	1.232930	2	2	0	4	
17.009	2.465860	184	1	0	2		29.498	1.432390	22	0	2	2		35.096	1.209450	99	1	2	3	
17.856	2.349650	10	2	0	1		30.178	1.400810	49m	0	0	4		35.198	1.206070	11	4	1	0	
20.556	2.043730	136	2	1	0		30.178	1.400810	49m	2	2	0		35.845	1.185000	3	3	1	3	
21.203	**1.982130**	768	1	1	2		30.633	1.380490	47m	1	2	2		36.029	1.179130	101	4	1	1	
21.894	**1.920250**	1000	2	1	1		30.633	1.380490	47m	2	1	3		36.166	1.174830	34	4	0	2	
22.109	1.901830	311	2	0	2		31.108	1.359070	4	2	2	1		36.258	1.171950	82	3	2	1	
23.936	1.758540	255	1	0	3		31.259	1.353540	15	1	0	4		36.766	1.156310	4	2	1	4	
25.286	1.666050	291	0	2	0		31.475	1.344460	10	3	1	2		37.964	1.121090	21	2	2	3	
25.554	1.648860	167	3	0	1		32.741	1.293800	29	4	0	0		38.431	1.107980	16	4	1	2	

© 2024 International Centre for Diffraction Data. All rights reserved.

e. Si for beam energy of 17 keV (wavelength 0.719319 A) – monochromatic source

00-005-0565 Jun 21. 2024 11:05 AM (AF271119)

Status Alternate **Quality Mark:** Star **Environment:** Ambient **Temp:** 299.0 K **Chemical Formula:** Si
Empirical Formula: Si **Weight %:** Si100.00 **Atomic %:** Si100.00 **Compound Name:** Silicon
Mineral Name: Silicon, syn **CAS Number:** 7440-21-3 **Entry Date:** 09/01/1955

Radiation: CuKα1 (1.5405 Å) **Filter:** Ni Beta **Intensity:** Diffractometer - Peak

Crystal System: Cubic **SPGR:** Fd-3m (227)
Author's Unit Cell [a: 5.4301 Å **Volume:** 160.11 Å³ **Z:** 8.00 **MolVol:** 20.01] **Calculated Density:** 2.33 g/cm³
Color: Black, gray **SS/FOM:** F(11) = 62.5(0.0135, 13) **I/Ic:** 4.7

Space Group: Fd-3m (227) **Molecular Wt:** 28.09 g/mol
Crystal Data [a: 5.430 Å **b:** 5.430 Å **c:** 5.430 Å **α:** 90.00° **β:** 90.00° **γ:** 90.00° **XtlCell Vol:** 160.11 Å³
XtlCell Z: 8.00 **a/b:** 1.000 **c/b:** 1.000]
Reduced Cell [a: 3.840 Å **b:** 3.840 Å **c:** 3.840 Å **α:** 60.00° **β:** 60.00° **γ:** 60.00° **RedCell Vol:** 40.03 Å³]

Atomic parameters are cross-referenced from PDF entry 04-012-7888 **AC Space Group:** Fd-3m (227)
AC Unit Cell [a: 5.4317(6) Å **b:** 5.4317(6) Å **c:** 5.4317(6) Å **α:** 90° **β:** 90° **γ:** 90°]
Space Group Symmetry Operators:

Seq	Operator	Seq	Operator	Seq	Operator	Seq	Operator	Seq	Operator
1	x,y,z	11	z,-x+1/4,-y+1/4	21	-y+1/4,z,-x+1/4	31	-x+1/4,-z+1/4,y	41	z,y,x
2	-x,-y,-z	12	-z,x+3/4,y+3/4	22	y+3/4,-z,x+3/4	32	x+3/4,z+3/4,-y	42	-z,-y,-x
3	x,-y+1/4,-z+1/4	13	-z+1/4,x,-y+1/4	23	-y+1/4,-z+1/4,x	33	y,x,z	43	z,-y+1/4,-x+1/4
4	-x,y+3/4,z+3/4	14	z+3/4,-x,y+3/4	24	y+3/4,z+3/4,-x	34	-y,-x,-z	44	-z,y+3/4,x+3/4
5	-x+1/4,y,-z+1/4	15	-z+1/4,-x+1/4,y	25	x,z,y	35	y,-x+1/4,-z+1/4	45	-z+1/4,y,-x+1/4
6	x+3/4,-y,z+3/4	16	z+3/4,x+3/4,-y	26	-x,-z,-y	36	-y,x+3/4,z+3/4	46	z+3/4,-y,x+3/4
7	-x+1/4,-y+1/4,z	17	y,z,x	27	x,-z+1/4,-y+1/4	37	-y+1/4,x,-z+1/4	47	-z+1/4,-y+1/4,x
8	x+3/4,y+3/4,-z	18	-y,-z,-x	28	-x,z+3/4,y+3/4	38	y+3/4,-x,z+3/4	48	z+3/4,y+3/4,-x
9	z,x,y	19	y,-z+1/4,-x+1/4	29	-x+1/4,z,-y+1/4	39	-y+1/4,-x+1/4,z		
10	-z,-x,-y	20	-y,z+3/4,x+3/4	30	x+3/4,-z,y+3/4	40	y+3/4,x+3/4,-z		

Origin: O2
Atomic Coordinates:

Atom	Num	Wyckoff	Symmetry	x	y	z	SOF	IDP	AET
Si	1	8a	-43m	0.125	0.125	0.125	1.0		

Crystal (Symmetry Allowed): Centrosymmetric

Subfiles: Ceramic (Semiconductor), Common Phase, Forensic, Inorganic, Metal & Alloy, Mineral Related (Mineral, Synthetic), NBS Pattern
Mineral Classification: Diamond (supergroup), 2C-diamond (group) **Pearson Symbol:** cF8.00
Prototype Structure (Formula Order): C **Prototype Structure (Alpha Order):** C
LPF Prototype Structure (Formula Order): C,cF8,227 **LPF Prototype Structure (Alpha Order):** C,cF8,227 **ANX:** N

Cross-Ref PDF #'s: 00-026-1481 (Alternate), 00-027-1402 (Primary), 04-001-7247 (Alternate), 04-002-0118 (Alternate), 04-002-0891 (Alternate), 04-003-1456 (Alternate), 04-003-3352 (Alternate), 04-003-3353 (Alternate), 04-003-4734 (Alternate), 04-004-5099 (Alternate), 04-004-6896 (Alternate), 04-005-9699 (Alternate), 04-006-2527 (Alternate), 04-006-2591 (Alternate), 04-006-4528 (Alternate), 04-006-6436 (Alternate), 04-007-5232 (Alternate), 04-007-8736 (Alternate), 04-012-7888 (Alternate)

References:

Type	DOI	Reference
Primary Reference Crystal Structure		Swanson, Fuyat. Natl. Bur. Stand. (U. S.), Circ. 539 1953, II, 6. Crystal Structure Source: LPF.

Database Comments: Additional Patterns: See PDF 00-027-1402. ANX: N. Analysis: Spectroscopic analysis: <0.001% Cu, Ag, Zn, Sn, Mg, Fe. Sample Source or Locality: Sample from Johnson Matthey Company. Temperature of Data Collection: 299 K. Unit Cell Data Source: Powder Diffraction.

d-spacings (11) - Si - 00-005-0565 (Stick, fixed slit intensity) - X-ray (0.729319 Å)

2θ (°)	d (Å)	I	h	k	l	*	2θ (°)	d (Å)	I	h	k	l	*	2θ (°)	d (Å)	I	h	k	l	*
13.347	**3.1380**	100	1	1	1		34.035	1.2460	13	3	3	1		46.821	0.9178	11	5	3	1	
21.897	**1.9200**	60	2	2	0		38.419	1.1083	17	4	2	2		50.265	0.8586	9	6	2	0	
25.726	**1.6380**	35	3	1	1		40.847	1.0450	9	5	1	1		52.253	0.8281	5	5	3	3	
31.177	1.3570	8	4	0	0		44.654	0.9599	5	4	4	0								

© 2024 International Centre for Diffraction Data. All rights reserved. Page 1 / 1

A.iii Detailed equations used in the modelisation of the redistribution of Pt

Figure 116 illustrates the geometrical parameters and the different volumes used to simulate the change in grain shape (Fig. 116(a)) and the redistribution of Pt (Fig. 116(b)) during grooving.

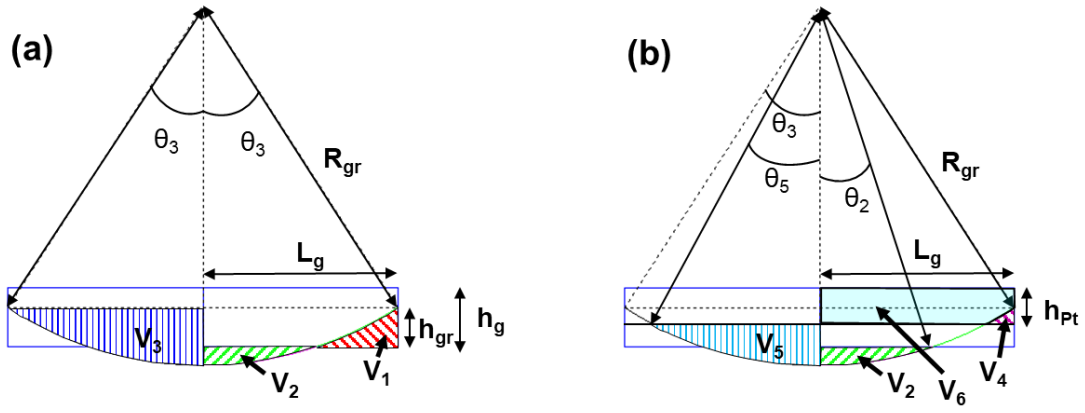


Figure 116. Schematic of the model used to simulate grooving based on the geometry shown in Figure 110. (a) Change in grain shape, (b) redistribution of Pt. R and θ_i correspond to the radius of the NiSi/Si interface curvature and the angles defining the different spherical caps (i=2, 3, 5), respectively. L_g and h_g are the half-size of the Ni(Pt)Si grain and the original thickness of the non-agglomerated NiSi film, respectively. h_{gr} is the depth of the grain boundary grooving. Only half of the annotated volumes is shown for clarity.

Based on Fig. 116, the conservation of the Ni(Pt)Si volume affected by grooving can be expressed as:

$$V_{gr}^{0} = V_3 \qquad \textbf{Equation 31}$$

where V_3 is the volume of the spherical cap after grooving.

V_{gr}^{0} is the part of the initial grain volume before grooving which has a height equal to the grooving height, h_{gr} , and can be formulated as:

$$V_{gr}^{0} = a_{sh} L_g^2 h_{gr} \qquad \textbf{Equation 32}$$

where L_g is the half size of the NiSi grain, and h_{gr} is the depth of the grain boundary grooving (Figure 116(a)). The constant a_{sh} depends on the initial shape and takes the value of $2\sqrt{3}$ for grain with a hexagonal base. The volume of a spherical cap is given by :

$$\boldsymbol{V = \pi \frac{R^3}{3}(1 - cos\,\theta)^2(2 + cos\,\theta)} \qquad \textbf{Equation 33}$$

In Eq. 33, R_{gr} can be denoted as (see Figure 116(a)):

$$\boldsymbol{R_{gr} = \frac{L_g}{sin\,\theta_3}} \qquad \textbf{Equation 34}$$

Consequently, the value of θ_3 can be obtained by solving the following equation numerically since there is no analytical solution:

$$\boldsymbol{\frac{3a_{sh}h_{gr}}{\pi L_g} - (sin\,\theta_3)^{-3}(1 - cos\,\theta_3)^2(2 + cos\,\theta_3) = 0} \qquad \textbf{Equation 35}$$

As shown in Fig. 116(b), the redistribution of Pt can be expressed as:

$$\boldsymbol{x_{Pt}^{gr} = x_{Pt}^{0}\frac{V_4}{V_2}} \qquad \textbf{Equation 36}$$

The volume V_4 is given by :

$$\boldsymbol{V_4 = a_{sh}L_g^2(h_{gr} - h_g + h_{Pt}) + V_5 - V_3} \qquad \textbf{Equation 37}$$

where h_g is the initial thickness of the non-agglomerated Ni(Pt)Si film and h_{Pt} is the thickness of the subsurface region with uniform Pt concentration before grooving (Figure 116b).As V_2 and V_5 are spherical caps of radius R_{gr}, their volumes are given by Eq. 33 with angles defined by the relationships:

$$\boldsymbol{cos\,\theta_2 = \frac{h_{gr} + R_{gr}\,cos\,\theta_3}{R_{gr}}} \qquad \textbf{Equation 38}$$

$$\boldsymbol{cos\,\theta_5 = \frac{h_{gr} + h_{Pt} - h_{Pt} + R_{gr}\,cos\,\theta_3}{R_{gr}}} \qquad \textbf{Equation 39}$$

Similar equations can be derived for agglomeration based on Figure 117. The conservation of Ni(Pt)Si volume is expressed by:

$$V_3 = a_{sh} L_g^2 h_g$$ **Equation 40**

This equation allows for the determination of the angle θ_3 through numerical solving of the following equation:

$$\frac{3a_{sh}L_g^2 h_g}{\pi} - \left(\frac{L_g - L_{ag}}{sin\,\theta_3}\right)^3 (1 - cos\,\theta_3)^2(2 + cos\,\theta_3) = 0$$ **Equation 41**

where R_{ag} is equal to:

$$R_{ag} = \frac{L_g - L_{ag}}{sin\,\theta_3}$$ **Equation 42**

The redistribution of Pt after agglomeration is also obtained using Eq. 36 with the following parameters:

$$cos\,\theta_2 = \frac{h_g + R_{ag}\,cos\,\theta_3}{R_{ag}}$$ **Equation 43**

$$cos\,\theta_5 = \frac{h_{Pt} + R_{ag}\,cos\,\theta_3}{R_{ag}}$$ **Equation 44**

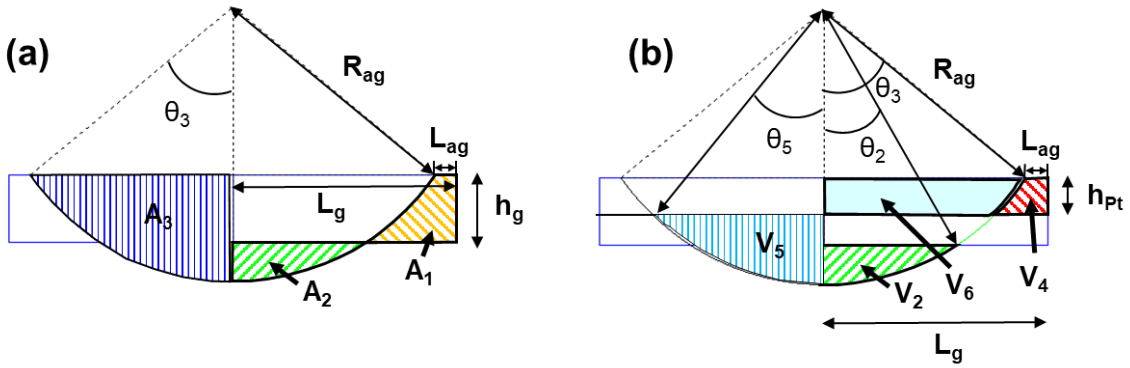


Figure 117. Schematic of the model used to simulate the agglomeration (a) change in the grain shape (b) redistribution of Pt. L_{ag} is the agglomerated length. Only half of the annotated volumes is shown for clarity.